



Contribution à l'étude du comportement mécanique de voies ferrées, composants à caractère dissipatif non-linéaire : semelle sous rail et sous-couche de grave bitumineuse.

Roman Zhuravlev

► To cite this version:

Roman Zhuravlev. Contribution à l'étude du comportement mécanique de voies ferrées, composants à caractère dissipatif non-linéaire : semelle sous rail et sous-couche de grave bitumineuse.. Mécanique des matériaux [physics.class-ph]. Ecole nationale supérieure d'arts et métiers - ENSAM, 2017. Français. NNT : 2017ENAM0039 . tel-01744302

HAL Id: tel-01744302

<https://pastel.hal.science/tel-01744302>

Submitted on 27 Mar 2018

HAL is a multi-disciplinary open access archive for the deposit and dissemination of scientific research documents, whether they are published or not. The documents may come from teaching and research institutions in France or abroad, or from public or private research centers.

L'archive ouverte pluridisciplinaire **HAL**, est destinée au dépôt et à la diffusion de documents scientifiques de niveau recherche, publiés ou non, émanant des établissements d'enseignement et de recherche français ou étrangers, des laboratoires publics ou privés.

2017-ENAM-0039



École doctorale n° 432 : Sciences des Métiers de l'ingénieur

Doctorat ParisTech

THÈSE

pour obtenir le grade de docteur délivré par

l'École Nationale Supérieure d'Arts et Métiers

Spécialité “ Mécanique-Matériaux ”

présentée et soutenue publiquement par

Roman ZHURAVLEV

le 14 décembre 2017

Contribution à l'étude du comportement mécanique de voies ferrées

Composants à caractère dissipatif non-linéaire : semelle sous rail et sous-couche de grave bitumineuse

Directeur de thèse : **Philippe VIOT**

Co-encadrement de la thèse : **Sandra GUERARD, Catherine FROUSTEY**

Jury

M. Oleg B. NAIMARK, Professeur des universités, RAS UB Continuum Mechanics Institute

Président

M. Erwan VERRON, Professeur des universités, GeM, Centrale Nantes

Rapporteur

M. Moussa NAIT-ABDELAZIZ, Professeur des universités, LMSFC, Polytech Lille

Rapporteur

M. Philippe VIOT, Professeur des universités, I2M, Arts et Métiers - ParishTech

Examinateur

Mme. Sandra GUERARD, Maître de conférences, I2M, Arts et Métiers - ParishTech

Examinateur

Mme. Catherine FROUSTEY, Maître de conférences HdR, I2M, Université de Bordeaux

Examinateur

M. Pierre-Emmanuel LAURENS, Ingénieur, Direction Ingénierie & Projets SNCF

Invité

T
H
È
S
E

Acknowledgements

The work presented in this PhD dissertation was completed at the Institute of Mechanics and Engineering (Bordeaux, France) in the laboratory of Dumas department in the industrial partnership with SNCF railway company.

I would like to thank Philippe Viot, university professor and former director of Arts et Métiers-ParisTech Campus of Bordeaux-Talence, who has accepted the official direction of my thesis.

My gratitude goes to the scientific advisors of my thesis project Sandra Guérard, a maître de conférences at I2M and Arts et Métiers-ParisTech, and Catherine Froustey, a maître de conférences and HdR at I2M and University of Bordeaux, for their time contributions, patience and encouragement as well as for giving me the benefit of their immense knowledge, ideas and advice. I thank them both for choosing my candidature for this project and for their confidence in my knowledge and abilities.

My sincerest thanks to Oleg B. Naimark, a professor at Perm State University and laboratory director at RAS UB Continuum Mechanics Institute, for giving me the honour of chairing my thesis jury and for making a long trip to take place in the examining committee. I want also to thank Erwan Verron, a professor at the Ecole Centrale de Nantes, and to Moussa Nait-Abdelaziz, a professor at the University of Lille 1, for kindly accept the invitation to examine my PhD dissertation and be the referee during my thesis defence. A special thank goes to Pierre-Emmanuel Laurens, an engineer at Direction Ingénierie & Projets SNCF, who was always available for discussions and additional information about the project and who agreed to be the member of my thesis committee. I am grateful to the members of the examining committee for their insightful comments and interesting questions.

A big thanks to all my colleagues (PhDs, interns and researchers) and the staff of I2M and ENSAM for their sympathy, their availability and willingness to help. I particularly thank Jonathan Merzeau whose help was indispensable during the realization of the experiments.

Finally, I thank my family and, in particular, my wife Daria Zhuravleva, whose attention, support and belief in me have been a great source of encouragement during the years, which contributed a lot to the success of this work. Many thanks to my friends Alexandre Nikitin, Dmitrii Ilin and Bertrand Canetti for their friendship, support and help, especially at the beginning of my stay in France.

Remerciements

Le travail présenté dans ce mémoire a été réalisé au sein du laboratoire du « Institut de Mécanique et d'Ingénierie » (I2M) au département DuMAS rattaché à l'École Nationale Supérieure des Arts et Métiers (ENSA) Bordeaux.

Je remercie M. Philippe Viot, professeur à Arts et Métiers-ParishTech et ancien directeur du Campus Arts et Métiers-ParishTech de Bordeaux-Talence, d'avoir accepté de prendre la direction officielle de ma thèse.

Toute ma gratitude va aux responsables scientifiques de mon projet de thèse M^{me} Sandra Guérard, maître de conférences chez I2M et Arts et Métiers-ParishTech, et M^{me} Catherine Froustey, maître de conférences et HdR chez I2M et Université de Bordeaux, pour leurs disponibilités, patience et encouragements ainsi que pour m'avoir fait profiter de leurs connaissances, de leurs conseils et de leurs réflexions. Je les remercie tous deux pour m'avoir d'abord accueillie au sein du I2M-DuMAS, leur confiance qu'ils m'ont accordée en m'acceptant dans leur équipe.

J'adresse mes remerciements les plus sincères à M. Oleg B. Naimark professeur à l'Université d'État de Perm et directeur de laboratoire chez RAS UB Continuum Mechanics Institute, de m'avoir fait l'honneur de présider mon jury de thèse et d'avoir fait un long déplacement pour pouvoir participer à mon jury de thèse. Tous mes remerciements également à M. Erwan Verron, professeur à l'Ecole Centrale de Nantes, et à M. Moussa Nait-Abdelaziz, professeur à l'Université de Lille 1, qui m'ont fait la faveur d'accepter de juger ce travail et d'en être rapporteurs. Je tiens aussi à remercier particulièrement M. Pierre-Emmanuel Laurens, ingénieur chez Direction Ingénierie & Projets SNCF, qui a su être disponible pour les discussions et pouvoir me fournir l'information complémentaire sur le projet et qui a accepté d'en être le membre de mon jury de thèse. Merci à toutes ces personnes pour l'intérêt qu'ils ont porté à mon travail.

Un grand merci à toutes mes collègues (doctorants, stagiaires et chercheurs) et au personnel de l'I2M et l'ENSA pour leur sympathie, leur disponibilité et disposition à apporter leur sollicitude. Je remercie en particulier, M. Jonathan Merzeau dont l'aide a été irremplaçable lors de la réalisation des expériences.

Je remercie enfin ma famille et, en particulier, ma femme Daria Zhuravleva dont la confiance en moi, l'attention et le soutien ont été une grande source d'encouragement pour moi et contribué à l'aboutissement de ce travail. Grand merci également à mes amis Alexandre Nikitin, Dmitrii Ilin et Bertrand Canetti pour leur compagnie, leur soutien et leur aide, surtout au début de mon séjour en France.

Table of contents

Table of contents	iii
List of figures	v
List of Tables	ix
Introduction	1
Chapter 1: Constitutive models for elastomers. Theoretical approach.....	5
1. Introduction	5
2. Nonlinear elasticity (Hyperelasticity)	7
2.1. General theory of hyperelasticity	7
2.2. Hyperelastic models	9
2.3. Identification of parameters of hyperelastic models	12
2. Linear Viscoelasticity.....	14
2.1. Creep and Stress Relaxation.....	15
2.2. Boltzmann Superposition Principle.....	17
2.3. Mechanical models of linear viscoelasticity	19
2.4. Complex modulus and complex compliance.....	20
3. Nonlinear viscoelasticity or Visco-hyperelasticity.....	21
3.1. Convolution integral approach (CI-model)	21
3.2. Internal variables approach (IV-model)	24
3.3. Identification of parameters of visco-hyperelastic models.....	26
3.4. Conclusions on visco-hyperelasticity	27
4. Conclusions to Chapter 1	27
Chapter 2: Experimental and numerical study of elastomeric rail pad subjected to compression load	29
1. Introduction	29
2. Study of on-track loads relatively to rail pads.....	30
2.1. <i>In-situ</i> measurements and experimental approach	30
2.2. Analytical study of loads acting on rail pads.....	33
3. Materials and instrumentations	40
3.1. Materials and specimens	40
3.2. Instrumentations (experimental study).....	41
3.3. Methods of a material model constants set optimization	42
4. Modelling of elastomeric material of the rail pad	43
4.1. Validation of the material incompressibility	43
4.2. Quasi-static compression and tension experiments.....	43
4.3. Choosing an appropriate hyperelastic model	44

4.4. Constants identification of the visco-hyperelastic model (CI-model).....	47
5. Investigation of the rail pad structure.....	49
5.1. Experimental investigation of the rail pad structure.....	49
5.2. Description of the rail pad FE model	50
5.3. Results of FE simulation using the full-structure 3D model	51
5.4. Results of FE simulation using simplified model approaches.....	54
6. Simulation of the rail pad subjected to repetitive load.....	55
6.1. FE simulation results	55
7. Conclusions to Chapter 2	57
Chapter 3: Influence of heterogeneities on mechanical properties: Virtual Material concept	59
1. Introduction.....	59
2. Virtual material concept.....	62
2.1. General approach.....	63
2.2. Doehlert experimental design and parameters of VM specimens	64
2.3. Numerical development of an inclusions skeleton.....	65
2.4. Manufacturing of a real specimen.....	68
3. Mechanical behaviour of VM specimens.....	70
3.1. Mechanical behaviour of the silicone material.....	71
3.2. Experimental investigation of VM specimens	72
3.3. Discussion of experimental results.....	77
3.4. Finite element simulation	87
3.5. Comparison between FE and experimental results. Discussion.....	96
4. Conclusions to Chapter 3	97
General conclusions. Remarks and perspectives	101
Bibliography	103
Appendix	111
Appendix A.....	111
Appendix B	113
Document résumé en français du manuscrit de thèse	115

List of figures

Figure 1: Schematic representation of the TGV ballasted railway track structure	1
Figure 1.1: (a) Schematic diagram of a cross-linked polymer; (b) Schematic diagrams of undeformed and deformed polymer (images are taken from [17]).....	5
Figure 1.2: (a) Typical load-elongation curves for a polymer at different temperatures/strain rates[17]; (b) Stress-strain curves illustrating Mullins softening effect (numbers indicate a cycle number and location of maximum load for this cycle)	6
Figure 1.3: Typical tests which provide pure homogeneous deformations for incompressible material: (a) uniaxial tension, (b) uniaxial compression, (c) biaxial tension, (d) pure shear [37].....	13
Figure 1.4: Two load programs to represent (a) creep effect at applied constant stress and (b) relaxation effect at applied constant strain.....	16
Figure 1.5: The creep compliance J_t (a) and the relaxation modulus G_t (b) as functions of time t (from [17])	16
Figure 1.6: Illustration of the two-step (a) loading and (b) loading-unloading experiment (from [17])	17
Figure 1.7: The creep behaviour of a linear viscoelastic solid (from [17]).....	18
Figure 1.8: Classical mechanical models of linear viscoelasticity	19
Figure 1.9: The complex modulus $G = G_1 + iG_2$ and $\tan\delta = G_2/G_1$	20
Figure 1.10: Concept of an intermediate configuration S_{t-s} at a time $t-s$ between the initial S_0 and the final S configurations.	22
Figure 1.11: Schematic representation of deformation split in IV-model approach	25
Figure 1.12: Applicability domains for constitutive approaches, appropriate for the modelling of the mechanical behaviour of elastomers (from [44]).....	28
Figure 2.1: Rail pad location on the ballasted railway track	29
Figure 2.2: TGV train with two power cars, bar/restaurant car, two end and five intermediate passenger cars	30
Figure 2.3: Measurement of a wheel force using the set of strain gauges connected to a Wheatstone bridge: (a) location of strain gauges on a rail; (b) an example of signal of one wheel obtained using data from strain gauges	31
Figure 2.4: The common wheel force signal caused by passing of a TGV-PSE train plotted in a time domain (a); superimposed peaks of a wheel force signal (b).....	32
Figure 2.5: Experimental setup for the measurement of a rail pad compression displacement	32

Figure 2.6: The common rail pad compression displacement signal caused by passing of a TGV-PSE train plotted in a time domain (a); superimposed peaks of a rail pad compression displacement signal (b)	33
Figure 2.7: Dimensions of a TGV train (in metres) [1].....	34
Figure 2.8: Construction of a fastening system “Nabla” [1].....	36
Figure 2.9: Distribution of the wheel load among the sleepers (from [58])	36
Figure 2.10: Rail on a Winkler foundation subjected to concentrated load Q_w	37
Figure 2.11: Dependence of distributed reaction force $r(x, t)$ on distance x from a wheel load moving with the speed $v = 87.8$ m/s	37
Figure 2.12: Dependence of av^2 on the value of a train speed compared with the value of b	38
Figure 2.13: Dependence of distributed reaction force $r(x, t)$ (blue curve) on position of a wheel load moving with the speed $v = 87.8$ m/s and sleepers’ reaction forces R_i (red arrows)	38
Figure 2.14: Reaction force of a sleeper of interest depends on a distance between centres of this sleeper and approaching bogie	39
Figure 2.15: Time signals of the forces acting on a rail and a rail pad generated by a bogie passing with the speed $v = 87.8$ m/s.....	40
Figure 2.16: Dimensions of: (a) a cylindrical specimen; (b) a dumbbell specimen [112]; (c) a rail pad specimen.....	41
Figure 2.17: Hydrostatic compression experiment testing set: (a) schematic representation of a hydrostatic chamber; (b) specimen on a supporting rig	42
Figure 2.18: Pressure dependences on change in volume during hydrostatic compression experiment.....	43
Figure 2.19: Profiles of the Engineering Stress and Strain vs Time in compression (a) and tension (b) experiments	44
Figure 2.20: Fitting of different hyperelastic models to experimental data: (a) Neo-Hookean, Mooney-Rivlin and Yeoh models; (b) Ogden models with strict and relaxed condition (Eq. 2.11); (c) Arruda-Boyce model	46
Figure 2.21: (a) Comparison between experimental data and prediction of fitted CI-model; (b) convergence curves for different values of the Prony’s series order	49
Figure 2.22: Force vs Displacement curve obtained during QS compression experiment of a rail pad in the second cycle.....	49
Figure 2.23: 3D and 2D FE models of the rail pad (a-b); planes of symmetry (a-b); boundary conditions applied on rigid compression plates (b); mesh refinement near groove (c)	50
Figure 2.24: Force vs Displacement curves obtained in the experiment and calculated by FE simulation using values of friction in the range of 0.17 to 0.3	52

Figure 2.25: Comparison between displacement maps in horizontal direction obtained in FE simulation (a) and experiment (b)	52
Figure 2.26: True strain YY-field calculated in different cross-sections in the Z-direction (from face to the middle of the specimen) and true strain fields obtained in 2D plane strain (PE) and plane stress (PS) models. Rail pad is under compressive displacement of 1.08 mm.....	53
Figure 2.27: True shear strain (XY), von Mises stress and hydrostatic stress maps calculated at the cross-section located in the middle of the specimen. Rail pad is under compressive displacement of 1.08 mm	54
Figure 2.28: Comparison between experimental data and response from FE model of a rail pad: (a) 2D plane strain and plane stress; (b) 3D grooveless	55
Figure 2.29: Force vs Time curve of a dynamic impact, applied on the numerically studied structure, and Displacement vs Time curve obtained as a result of FE simulation (a); and comparison between dependences of the compression displacement value on time obtained from FE simulation results and by averaging <i>in-situ</i> experimental data (b).....	56
Figure 3.1: Grading curve and composition by mass for a GB3 mixture [4].....	59
Figure 3.2: Schematic representation of process of development of numerical and real specimens	63
Figure 3.3: Parameters of specimens on the scale of the Doehlert diagram (a); variation function for the Doehlert experimental design (b)	65
Figure 3.4: Scheme representing algorithm of inclusions locations calculation	66
Figure 3.5: Optimization schemes for links number and length.....	67
Figure 3.6: Inclusions skeleton designed for 3D printing of the specimen V0075-D08 reinforced by links: (a) isometric view, (b) XZ-plane view	68
Figure 3.7: Inclusions skeleton of the specimen V7.5-D08: numerical (a) and printed using ABS plastic material (b). Stair-like surface of a 3D printed geometry (c).....	69
Figure 3.8: Moulding of the specimen Vo225-D12 into a silicone matrix	70
Figure 3.9: Experimental investigation of the mechanical behaviour of silicone material: (a) Cylindrical specimen; (b) Pressure dependences on change in volume during hydrostatic compression experiment; (c) Stress vs Stretch curve obtained during QS compression experiment.....	71
Figure 3.10: VM loading scheme (a) and cycling influence (b).....	72
Figure 3.11: Calculation of dissipated energy	73
Figure 3.12: Force vs Macroscopic strain curves obtained during QS-compression experiment of VM specimens subjected to load in X-, Y- and Z-directions	75
Figure 3.13: Force vs Macroscopic strain curves obtained during experimental investigation of VM specimens subjected to compression load in the Y-direction	76

Figure 3.14: F_{max} (a,c) and $E\%$ (b,d) output parameters obtained during QS-compression experiment as functions of inclusions' volume fraction and diameter	77
Figure 3.15: Dependences of F_{max} (a) and $E\%$ (b) on total inclusions' surface area.....	78
Figure 3.16: Porosities in the structure of real VM specimens: (a) rigid links and (b) voids in regions of inclusions-matrix separation. (c) Stair-like surface of inclusions and links.....	79
Figure 3.17: The values of coordinates of centroid of spherical inclusions (a) and moment of inertia of inclusions set in relation to the three main axes of the cube (b) as function of total inclusions surface. Results obtained for inclusions arrangements were compared to the central line of the cube (a) and the moment of inertia of an equivalent homogeneous solid (b)	80
Figure 3.18: Schematic representation of a load-bearing chain in a composite material (a); construction of a surface of projections (b).....	81
Figure 3.19 a-b: Surfaces of projections for specimens Voo75-Do8 (a) and Voo75-D12 (b)..	83
Figure 3.20: Orientations of links of the specimen V7.5-D8 inclined by less than 45° towards coordinate axes.....	86
Figure 3.21: (a) Fitting of different hyperelastic models to QS compression data of a cylindrical silicone specimen; (b) prediction by FE simulation of the mechanical behaviour of Voo-D10 specimen using previously fitted Arruda-Boyce hyperelastic model	88
Figure 3.22: Scheme of inverse identification process.....	89
Figure 3.23: Meshing of the matrix (a) and the inclusions skeleton (b) of Vo3-D10 specimen	90
Figure 3.24: Boundary conditions for VM finite element model	91
Figure 3.25: Influence of a friction coefficient value on the mechanical response of the FE model of V15-D10 specimen.....	92
Figure 3.26: F_{max} (a) and $E\%$ (b) output parameters obtained during FE simulations as functions of inclusions' volume fraction and diameter.....	94
Figure 3.27: Force vs Macroscopic strain curves obtained during FE simulations of VM specimens subjected to compression load in the Y-direction	95
Figure 3.28: Maps of (a) Von Mises stress and (b)Y-uniaxial true strain at $x = 5$ mm and $x = 35.5$ mm cross sections (relatively to the central, 60x60x60 mm ³ , part) of V22.5-D8 FE model subjected to compression displacement of 10 mm.....	96
Figure 3.29: Dependences of F_{max} (a) and $E\%$ (b) on total inclusions' surface area obtained during experimental and FE investigations	97

List of Tables

Table 2.1: Parameters of a railway track	35
Table 2.2: Constraints ensuring consistency of hyperelastic models with the theory of linear elasticity.....	45
Table 2.3: Constants of the CI-model identified by the least-square fitting process.....	48
Table 3.1: Parameters of inclusions skeletons obtained after packing procedure	65
Table 3.2: Maximum force and Dissipated energy fraction data obtained during experimental investigation of VM specimens subjected to compression load.....	74
Table 3.3a: $Sfrn$ [%] calculated for each of the main directions and for different n	82
Table 3.4: Links volume fraction (calculated relative to the volume of RVE and the volume of inclusions) and orientation	87
Table 3.5: Constants of Arruda-Boyce hyperelastic model	89
Table 3.6: Maximum force and Dissipated energy fraction data obtained during FE simulation of VM specimens subjected to compression load	93

Introduction

The efforts of railway engineers have always been focused on improving the efficiency of railway transportation, which generally involves increasing train's operational speed and a lifetime of the railway track. Nowadays, train speed is mostly limited by the ability of a railway track to sustain the load generated by passing cars with an acceptable safety level. For example, in 2007, a French high-speed train TGV set the world speed record of 574.8 km/h for trains on conventional rails, whereas the maximum operational speed for this type of train is no higher than 320 km/h [1]. Repetitive dynamic loads caused by passing trains can damage railway track, especially at high speeds. In addition, the existence of defects at the wheel-rail interface (wheel flats, worn rail surface) or on the railway bed (voids under sleepers, ballast fouling, insufficient drainage, etc.) can increase the dynamic component of a train wheel load [2]. Investigation of the mechanical behaviour of the railway track structure (as the whole and by parts) can have a great influence on the progress in safety and efficiency of railway transportation.

The modern railway track is a complex multilayer structure, made of different materials, which help to improve the railway bed's resistance to external factors and increase its lifetime. The structure of a standard ballasted railway track is schematically represented in Figure 1. Longitudinal stainless steel rails are designed to guide and support train wheels while distributing concentrated wheel loads along the supporting sleepers. Rail pads, made of elastomeric material, are designed to damp vibrations and decrease the dynamic part of the wheel load in order to reduce and simplify impact on further layers. The supporting sleepers, made of reinforced concrete, are evenly spaced along the length of the track, supporting the rails and keeping them spaced to the correct gauge. Sleeper's geometry (an increased surface of the sleepers' base in the first place) allows an additional decrease in a load magnitude, transferred to the next layers. Track ballast forms the track-bed, made from rocks, which

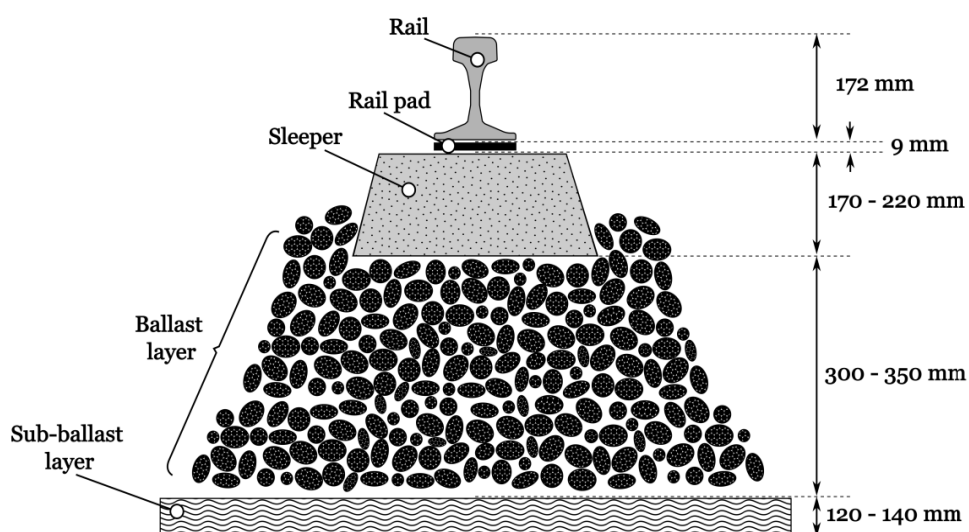


Figure 1: Schematic representation of the TGV ballasted railway track structure

provide a stable load-bearing platform and support the sleepers uniformly. The ballast layer is designed to transmit the load from the sleeper/ballast interface to the sub-ballast/subgrade layers at a reduced and acceptable level and provide the required degree of elasticity and dynamic resiliency. The sub-ballast layer provides additional protection of the subgrade (the foundation of the track) in the meaning of reduction of the transferred load, preventing interpenetration of the ballast (separating function), protection from precipitation, etc. Recently, improvements in the mechanical properties and the lifetime of the track were obtained with the use of bituminous (asphalt) mixture (BM) in a sub-ballast layer instead of the classically used well-crushed and compacted stones. The whole railway track structure is built on the subgrade which is a ground layer made of natural soil or sand. A more detailed description of railway track structure could be found in the following book [2].

Using such a complex structure makes it very difficult to predict the mechanical behaviour of the railway track. Experimental investigations in this field (performed both in laboratory and *in-situ*) are usually expensive, complicated and time-consuming. Thus, progress in numerical approach in the investigation of the whole railway track as well as its different layers taken separately has a great significance in today's railroad science.

For the earliest wooden and, starting from the 18th century, iron rails, the rigid fixation to a support (sleepers) by rail spikes and, more lately, by screw spikes was used. A significant progress in the railroad transportation along with increased demands (speed, carrying capacity, etc.) in the late 1940's lead to a revision of a rails' profile shape and, consequently, fastening system. It was found that the rigid fixation does not provide a sufficient level of resilience and results in loose of a fixating tight under vibrations [3]. The problem was resolved by the implementation of elastomeric rail pads, characterized by high ageing resistance, the capability to sustain high deformations and damp the energy of an external load. Nowadays, an increase in operational speed of trains can require optimization of a rail pads contribution to the mechanical behaviour of the modern railway track. The mechanical behaviour of a rail pad structure (material + geometry) influences the rigidity of the whole railway track and has a greater influence on the distribution of a wheel load among adjacent sleepers. Thus, possibility to predict mechanical properties of such structures has a great importance for the railroad science, while a lack of numerical studies concerning this subject can be found in the literature.

Classical sub-ballast layer, constituted of well-crushed and compacted stones, was initially designed to sustain only compressive loads in a vertical direction. The lack of binding between particles in such a structure and constant influence of precipitation, temperature changes and cyclic loading inevitably lead to degradation of the layer and accumulation of deformation. Moreover, recent *in-situ* measurements have shown that tensile deformation of the sub-ballast layer, caused by a passing train, in longitudinal and transversal directions cannot be neglected [4]. In attempts to improve mechanical properties of the sub-ballast layer, the BM material was suggested in the early 1970's. Viscoelastic properties of such a material allow damping noise and vibration, while rigid particles, bound together by asphalt, form a stable support for upper layers. Despite obvious advantages of such approach, there is still not much experience in this field, and experimental investigations and modelling of BM are commonly based on the macroscopic behaviour of the material. However, investigation of heterogeneous materials cannot be full apart from the mesoscopic approach.

The present work is devoted to study of rail pad and bituminous sub-ballast layers. These parts of the track were chosen for their similarities in the mechanical behaviour (nonlinearity

and energy dissipation) and function (reduction of the dynamic part of the load, influence on the load distribution). The work is divided into three chapters.

The first chapter reviews the main aspects of the mechanical behaviour of elastomeric materials and covers the common theoretical approaches, appropriate for the modelling of such behaviour. This study is necessary and used in second and third chapters.

The second chapter is devoted to study of elastomeric material of a rail pad and to numerical modelling of a whole elastomeric rail pad structure subjected to common track loads. Special attention was given to the possibility of the model to describe the nonlinearity of the mechanical behaviour and capability of energy dissipation (hysteretic load-deformation loop). Finite element model proposed in this chapter, *inter-alia*, can be used for the calculation of engineering parameters of a rail pad (*e.g.* stiffness, loss modulus, etc.). Moreover, numerical optimization of a rail pad geometry/material can be carried out with the help of the FE model to find the best compromise between dissipative properties and rigidity of the structure and complexity of the model realization. Additionally, possible ways to simplify the numerical model were also covered and discussed.

The third chapter of the thesis is connected to the study of an asphalt mixture material, which is used on a railway track as a sub-ballast layer. Generally, works concerning numerical study of a composite structure can be divided on two groups: studies based on a theoretically developed representative volume element (RVE) (2D [5], [6] or 3D [6]–[10]); and studies ([11]–[15]) considering a real specimen geometry obtained using experimental technique (X-ray tomography, optical surface scanning, etc.). Obviously, the former lack some connection with real cases, while the latter is lacking generality. In this chapter, the influence of the material heterogeneity on its mechanical behaviour was studied using a new “Virtual Material” (VM) concept, which allows keeping the connection between numerical and real specimens without losing generality. It can be found that such approach is insufficiently covered in the literature [16].

Chapter 1: Constitutive models for elastomers. Theoretical approach

1. Introduction

The mechanical behaviour of elastomeric materials cannot be strictly referred to one of particular types of matter, such as elastic solid or viscous liquid, and must be described in terms of viscoelasticity, which is a complex of these both states. This concept is based on both polymers microstructure and the observed macroscopic behaviour.

From the microscopic point of view, elastomers consist of randomly oriented molecular chains, which are connected (cross-linked) between each other at some points (Figure 1.1a). Thus, deformation of a polymeric material can be presented as a stretching or relaxation of these chains (Figure 1.1b).

From the macroscopic point of view, the mechanical behaviour of elastomers is highly dependent on a loading history and testing conditions, among which are temperature, rate (frequency) of the load and its amplitude. It was found by many authors [17], [18], that a decrease in the value of temperature as well as an increase in the value of load rate cause material to behave more as a solid and increase its stiffness and fragility (Figure 1.2a). On the opposite, at high temperatures or low rate of load, the same material can demonstrate more viscous, rubber-like behaviour with low stiffness and possibility to withstand large elongations (more than 100 %) without accumulation of irreversible strains. Due to its viscoelastic nature, elastomers subjected to a cycling load show a significant loop of hysteresis and, as a result, dissipate energy in each load cycle.

The dependency of the mechanical behaviour of elastomers on a loading history can be observed in phenomena of creep, stress relaxation and the Mullin's effect. The phenomenon

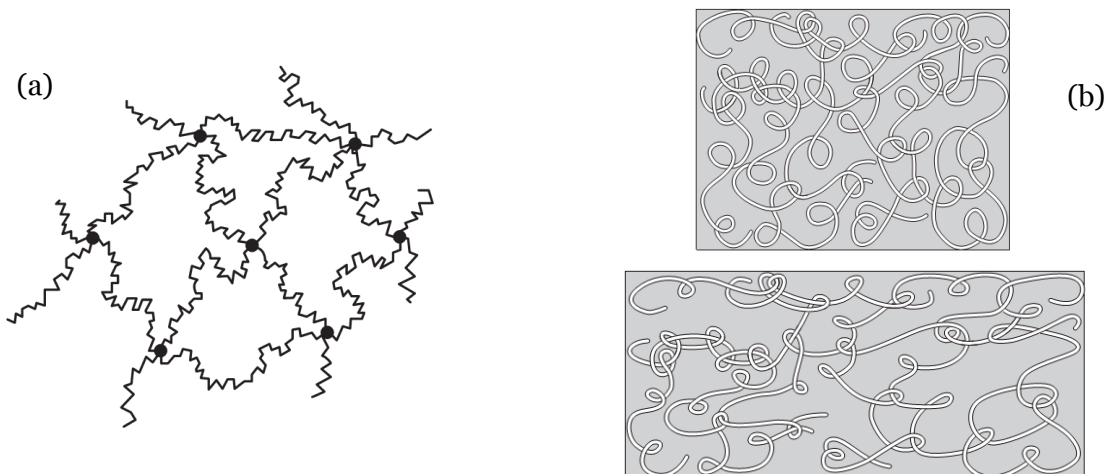


Figure 1.1: (a) Schematic diagram of a cross-linked polymer; (b) Schematic diagrams of undeformed and deformed polymer (images are taken from [17])

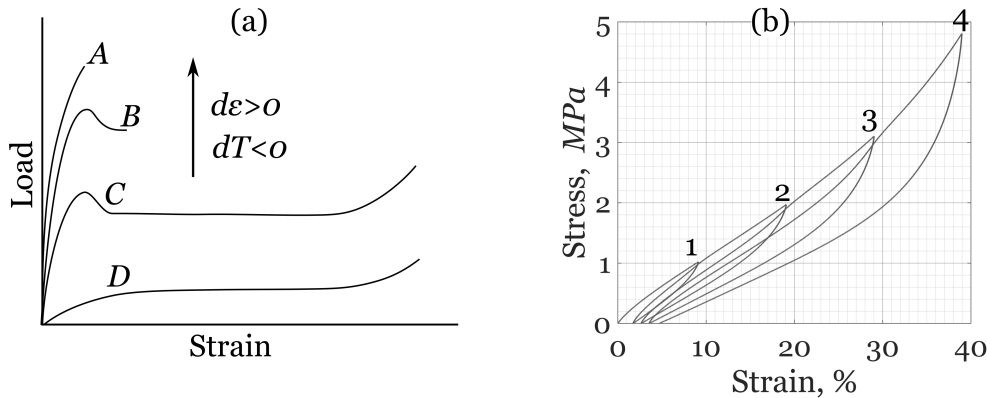


Figure 1.2: (a) Typical load-elongation curves for a polymer at different temperatures/strain rates[17]; (b) Stress-strain curves illustrating Mullins softening effect (numbers indicate a cycle number and location of maximum load for this cycle)

of creep takes place when the strain in the polymer increases due to the action of a constant stress. Subjecting of an elastomeric specimen to a constant strain will result in a decrease or relaxation of the stress value with time. The Mullin's (softening) effect can be observed during cycling of a polymer material and can be described by the following aspects [19]:

- The resulting value of the stress at the same value of strain is decreasing with the cycle number (if cycling is performed with the same strain amplitude);
- The Mullin's softening is less in each following cycle. Generally, continuing cycling leads to stabilization of the material behaviour
- If the second cycle is performed with an increased level of the maximum strain, then the Mullin's effect can be observed only in a range of deformation of the first cycle. In other words, loading part of the experimental curve obtained in the second cycle can be split into two parts (see Figure 1.2b): 1) in the first part (from zero stress to point "1") material response is softer than in the corresponding part of the first cycle; 2) in the second part (from the point "1" to the point "2") material behaves as if it was the first cycle.
- The Mullin's effect is not permanent, and material properties can be recovered with time (which depends on material and temperature).

Generally, elastomers subjected to hydrostatic loading undergo a negligible change in volume. Thus, in applications, it is common to consider the material behaviour of such materials as incompressible. However, this assumption must be verified experimentally and be adequate for the studied problem.

Thus, despite the fact that the quantitative behaviour of elastomeric materials is greatly influenced by its composition, the qualitative behaviour of all elastomers, in general, can be described by means of the following aspects:

- Nonlinear elasticity (usually based on the approach of hyperelasticity);
- Strain rate and frequency dependency (phenomenon of viscoelasticity);
- Dependency from loading history (including Mullins effect);
- Temperature dependency;
- Incompressibility

The present chapter reviews the main theoretical approaches for modelling the mechanical behaviour of elastomers. Temperature dependence of the material, as well as the Mullin's effect, were not taken into account during modelling and considered only during the experimental investigation (pre-cycling and constant temperature during testing were ensured).

2. Nonlinear elasticity (Hyperelasticity)

2.1. General theory of hyperelasticity

Modelling of the large strain nonlinear behaviour of elastomeric materials is commonly based on the approach of hyperelasticity, which implies the existence of a strain energy density function $W [J/m^3]$ (Helmholtz free energy function defined per unit of volume), which depends on an actual state of deformation [20]. Generally speaking, it is a scalar-valued function:

$$W = W(\underline{\underline{F}}) = W_I(I_B, II_B, III_B) = W_\lambda(\lambda_1, \lambda_2, \lambda_3) \quad (1.1)$$

written in terms of either invariants I_B, II_B, III_B (strain invariants) of the left Cauchy-Green deformation tensor $\underline{\underline{B}}$ or in terms of eigenvalues λ_i of the deformation gradient tensor $\underline{\underline{F}}$, also called the principal stretches. Invariants of the tensor $\underline{\underline{B}}$ can be defined through the principal stretches:

$$\begin{aligned} I_B &= B_{ii} = \lambda_1^2 + \lambda_2^2 + \lambda_3^2 \\ II_B &= \frac{1}{2} (B_{ii}B_{jj} - B_{ji}B_{ij}) = \lambda_1^2\lambda_2^2 + \lambda_2^2\lambda_3^2 + \lambda_1^2\lambda_3^2 \\ III_B &= \det \underline{\underline{B}} = \lambda_1^2\lambda_2^2\lambda_3^2 \end{aligned} \quad (1.2)$$

For simplicity, further, in the text, the index “ B ” will be omitted in the invariants’ notation (only invariants of the left Cauchy-Green deformation tensor $\underline{\underline{B}}$ will be considered).

In the most of applications, elastomeric materials are considered to be incompressible and isotropic: these approaches help to simplify material model equations. Incompressibility constraint means invariability of the volume during material deformation. The nonlinear mechanics of solids postulates that the change in a volume during deformation of the continuum is defined by the Jacobian J , which is equal to the determinant of the deformation gradient tensor $\underline{\underline{F}}$ [20]. Thus, in terms of the principal stretches the condition of incompressibility can be defined in the following form:

$$J = \det \underline{\underline{F}} = \lambda_1\lambda_2\lambda_3 = 1 \quad (1.3)$$

Incompressibility constraint (1.3) must be taken into account when formulating the strain energy density function W . This can be done by the help of the Lagrange multiplier p , which

is defined as a hydrostatic pressure and determined subsequently from the equilibrium equation and boundary conditions:

$$W = W(\underline{\underline{F}}) - p(J - 1) \quad (1.4)$$

Actual stress can be now calculated by taking a partial derivative of W by a strain tensor. Particularly, the Cauchy stress for an incompressible material can be found using a chain rule of differentiation [20]:

$$\text{in terms of invariants: } \underline{\underline{\sigma}} = -p\underline{\underline{1}} + 2\left(\frac{\partial W}{\partial I}\underline{\underline{B}} - \frac{\partial W}{\partial II}\underline{\underline{B}}^{-1}\right) \quad (1.5a)$$

$$\text{in terms of principal stretches: } \sigma_i = \lambda_i \frac{\partial W}{\partial \lambda_i} - p \quad (1.5b)$$

where $\underline{\underline{1}}$ is the unit tensor.

Since the assumption of the material incompressibility (1.3) the number of independent variables (stretches or invariants) in the proposed dependency could be decreased down to two ($\lambda_3 = (\lambda_1 \lambda_2)^{-1}$). For simplicity reasons the strain energy function W will be further defined as a function of two variables ($W = W_I(I_B, II_B) = W_\lambda(\lambda_1, \lambda_2)$). Elimination of the constant p from (1.5a) and (1.5b) results in the following:

$$\sigma_i - \sigma_3 = 2\left[\frac{\partial W}{\partial I}(\lambda_i^2 - (\lambda_1 \lambda_2)^{-2}) - \frac{\partial W}{\partial II}(\lambda_i^{-2} - (\lambda_1 \lambda_2)^2)\right], \text{ for } i=1,2 \quad (1.6a)$$

$$\sigma_i - \sigma_3 = \lambda_i \frac{\partial W}{\partial \lambda_i}, \text{ for } i=1,2 \quad (1.6b)$$

To ensure consistency with the classical theory of incompressible isotropic elasticity and provide zero values of energy and stresses at the chosen reference configuration, the strain energy density function must satisfy the following conditions [21]:

$$W|_{\lambda_i=1} = 0, \quad \frac{\partial W}{\partial \lambda_i}|_{\lambda_i=1} = 0, \quad (1.7a)$$

$$\frac{\partial^2 W}{\partial \lambda_i \partial \lambda_j}|_{\lambda_i=\lambda_j=1} = 2\mu, \quad \frac{\partial^2 W}{\partial \lambda_i^2}|_{\lambda_i=1} = 4\mu, \quad (1.7b)$$

Here $\mu > 0$ is the shear modulus of the material in the reference configuration (at low strain value).

The Cauchy stress tensor $\underline{\underline{\sigma}}$ is a symmetrical tensor defined in the actual material configuration, so it is convenient to use it during development of material model equations. However, the non-symmetrical first Piola-Kirchhoff stress tensor $\underline{\underline{P}}$ (also called engineering stress) is commonly used during fitting of model equations to the experimental data. The first Piola-Kirchhoff stress tensor is related to the Cauchy stress tensor by the following expression:

$$\underline{\underline{P}} = J \underline{\underline{\sigma}} \underline{\underline{F}}^{-T} \quad (1.8)$$

2.2. Hyperelastic models

Hyperelastic models consider the static response of a material and do not take into account loading history and any of strain rate or frequency effects. Formulations of the potential W is commonly developed using phenomenological and/or micro-mechanical approach [22]–[24]. The former are designed to mathematically describe the observed macroscopic behaviour of elastomers and generally have an explicit connection with the classical theory of elasticity through constraints, defined in the form of mathematical equations. The latter are derived using statistical mechanics and idealized molecular chains representation of the material structure. This makes some parameters of micro-mechanical models to have (in some way) a real physical meaning for the studied material.

Generally speaking, there is no strict strategy of choosing the appropriate hyperelastic model for a studied material. However, according to [22], some aspects of an efficient and realistic hyperelastic material model can be proposed:

- The hyperelastic model should be able to fit the complex nonlinear behaviour of the material. For example, the S-shaped stress-strain curve, which is typical for rubbers deformed up to high strain level [25], cannot be fully described by low-order polynomial models (*e.g.* Neo-Hookean or Mooney-Rivlin models, see Section 2.2.1). More complicated high-order polynomial (*e.g.* Yeoh or Generalized Polynomial models, see Section 2.2.1), molecular-based (*e.g.* Arruda-Boyce model, see Section 2.2.1) or power-based (*e.g.* Ogden model, see Section 2.2.1) models can, in most of the cases, successfully fit the material nonlinearity [24].
- Applicability domain of the model has to be well known and appropriate for the studied problem, *i.e.* all parameters calculation has to be done inside this domain.
- An increase in the model complexity generally leads to an increase in the number of constants to identify. This can result in non-uniqueness of the optimal constants set issue, mentioned in a number of works [21], [22], [26]. In order to control this non-uniqueness and ensure physically reasonable response of the model, constraint conditions for the parameter calculation process have to be defined. As an example, it could be an incompressibility criterion (1.3), conditions (1.7ab) and the Hill's stability criterion [26].
- To prevent convergence problems and non-uniqueness of parameters, the chosen model has to be as simple as possible and comprise as few as possible numbers of constants.

The contradiction between some statements of this list is obvious: from the one side, an increase in the fitting accuracy requires more complex formulation for the strain energy potential; on the other side an increase in complexity of the model equation generally results in an increase in number of constants to identify, leads to computational difficulties and model instability. Thus, choosing the right hyperelastic model for each elastomeric material has to be based on a compromise between all parameters mentioned above.

Many hyperelastic models have been proposed so far (comparative review of most of them can be found in works of Marckmann and Verron [23], Steinmann *et al.* [24] and Beda [22]), moreover, some recent works devoted to development of new hyperelastic potentials can be found in literature (*e.g.* [27], [28]). Analysis of all existing hyperelastic models was not a

concern of the present study, therefore, only a few of the most known and commonly used models will be reviewed further in this section.

As it was mentioned above, the corresponding strain energy functions of all hyperelastic models are commonly defined in terms of invariants I, II, III or the principal stretches λ_i . Thus, hyperelastic models can be classified into invariant-based and stretch-based.

2.2.1. Invariant-based hyperelastic models

It is convenient to begin this review with the Generalized Rivlin (or sometimes called the Polynomial) hyperelastic model. This invariant-based strain energy function was proposed by R.S. Rivlin [29] in 1951, and it can be considered as a generalized form of all invariant-based phenomenological models:

$$W_R = \sum_{p,q=0}^N C_{pq}(I - 3)^p(II - 3)^q \quad (1.9)$$

where C_{pq} are material parameter constants. The polynomial form of the model makes it very flexible and provides good capabilities of accurate fitting of experimental data (especially for high values of p and q). However, using of this model is not common, because of its complexity, big number of parameters and low stability. Simplified versions of this model were proposed by different authors in attempts to solve these problems. Particular cases of the Generalized Rivlin strain energy potential are reviewed further in this chapter.

a) The Neo-Hookean model (1948) [30]

The Neo-Hookean model (the simplest model of the Generalized Rivlin family) can be obtained by considering only one constant $C_{10} \neq 0$, or alternatively taking only one member $p = 1$ and $q = 0$ in (1.9). Thus, resulting strain energy function has the following form:

$$W_{NH} = C_{10}(I - 3) \quad (1.10)$$

It was found by different authors [23], [24], [31] that the first order I-based equation has an insufficient accuracy to predict the nonlinear behaviour of elastomers, especially at strains higher than 50 %.

This model was initially derived by Treloar [30] using the Gaussian statistics for molecular chain network. In his notation $C_{10} = \frac{1}{2}nkT$, where n is the chain density per unit volume, k is the Boltzmann constant and T is the absolute temperature. It can be noted that limitations of the Gaussian statistics theory make the Neo-Hookean model to be adequate only in a range of small strains (as it was mentioned above). However, the physical basis of the model and the only one parameter to identify can be marked as positive points of the model.

Consistency with the linear theory of elasticity (1.7) leads to relation $C_{10} = \mu/2$

b) The Mooney-Rivlin model (1940-1948) [32], [33]

This model was initially derived by Mooney [33], assuming that the behaviour of elastomeric material has to be linear under shear loading conditions. After him, Rivlin [32] had expressed the model in terms of invariants:

$$W_{MR} = C_{10}(I - 3) + C_{01}(II - 3) \quad (1.11)$$

The Mooney-Rivlin model is widely used in applications at moderate strain range (less than 200 %) due to its simplicity and improved accuracy in predicting the mechanical behaviour of rubber-like materials compared to the Neo-Hookean model.

c) The Yeoh model (1990) [34]

Experimental investigation of carbon-black filled rubbers in simple shear, performed by Yeoh [34], had shown that assumption of a linear stress-strain relation proposed by Mooney do not represent the actual nonlinear behaviour of the material. In order to fix this problem, it was suggested to consider non-zero terms up to the third order in equation (1.9). Moreover, Yeoh had found that the term $\partial W/\partial I$ makes a much greater contribution to the final value of the stress than $\partial W/\partial II$, and the later can be neglected. Finally the strain energy potential was proposed as follows:

$$W_Y = \sum_{p=1}^3 C_p(I - 3)^p \quad (1.12)$$

The cubic character of the strain energy function allows the Yeoh model to reproduce the S-shape stress-strain curve behaviour at large strains. Moreover, few authors stated that the optimal set of model parameters C_p , identified using only one type of experiment (*e.g.* uniaxial tension), yields qualitatively reasonable prediction for the complementary deformation modes (*e.g.* pure shear and equibiaxial tension) [24], [34].

d) Arruda-Boyce (8-chain) model (1993) [35]

To eliminate limitations of the Gaussian statistics theory and extend the micromechanical approach on a range of big deformations, the non-Gaussian statistical method, based on a use of the inverse Langevin's function, was suggested [17]. One of the models using this method was proposed by Arruda and Boyce in 1993 [35]. The authors assumed that the molecular structure of a material can be locally represented by the eight chains network: a cubic RVE with eight chains of the same separation (end-to-end distance), oriented from the centre to the cube vertices. Deformation of the molecular network leads to stretching/relaxing of these chains, which results in the entropy change. This change in entropy is proportional to the work spent on deformation of the network. Since the inverse of the Langevin's function does not have an analytical representation, the Taylor approximation was used in order to obtain the final expression for the strain energy potential [35]:

$$W_{AB} = C_1 \sum_{i=1}^5 \alpha_i \beta^{i-1} (I_B^i - 3^i), \quad (1.13)$$

with $\beta = \frac{1}{N}$; $\alpha = [\frac{1}{2}, \frac{1}{20}, \frac{11}{1050}, \frac{19}{7000}, \frac{519}{673750}]$

where C_1 can be defined as a shear modulus and N is a material constant related to the micro-structure of a polymer.

The polynomial form of equation (1.13) governs possibility of the Arruda-Boyce model to predict the S-shape behaviour. A small number of constants reduces possible instability of the optimal constants set. It was shown in [24] that the Arruda-Boyce model has both good

capabilities of fitting experimental data and predicting material behaviour in deformation modes not used in constant identification.

2.2.2. Stretch-based hyperelastic models

The class of stretch-based hyperelastic models could be generalized by the strain energy function proposed by Ogden [36]:

$$W_O = \sum_{p=1}^N \frac{\mu_p}{\alpha_p} (\lambda_1^{\alpha_p} + \lambda_2^{\alpha_p} + \lambda_3^{\alpha_p} - 3) \quad (1.14)$$

$$\mu_p \alpha_p > 0 \text{ (no sum over the } p \text{)} \quad (1.15)$$

$$\sum_{p=1}^N \mu_p \alpha_p = 2\mu \quad (1.16)$$

Here N is the model order, μ_p, α_p are material constants to be determined through the process of fitting to experimental data and $\mu > 0$ is the shear modulus of the material in the reference configuration (at a small strain). It must be noted that the big number of model parameters ($2N$) can result in instability of optimal constants set. Constraint conditions (1.15) (derived from mentioned above Hill's stability criterion [26], [36]) and (1.16) (obtained in accordance with (1.7)) can help to find unique a set of constants. The Ogden model provides a good accuracy for fitting test data especially for $N \geq 3$, while ability the to predict material behaviour in deformation modes different from used in constant search process remains weak [24].

2.3. Identification of parameters of hyperelastic models

Identification of material constants of a chosen hyperelastic model is classically done by fitting corresponding stress-strain equation to the experimental data. It is common to apply pure homogeneous state of deformation to the studied material, because simplifies experimental measurements and ensures a simplified form of mathematical equations. When the material is deformed homogeneously, the strain magnitude does not vary with the position in the body and the principal axes of the strain tensor do not change their direction with both position in the body and variation in strain. Typical pure homogeneous deformations for incompressible material are uniaxial (simple) tension/compression, (equi-)biaxial tension, and pure shear (also called planar tension) [31], [36]–[38].

It was mentioned above that some elastomeric materials could have load-rate behaviour due to their viscoelastic properties. Thus, it is important to use quasi-static experimental data for calibration of a hyperelastic material model in order to decrease an influence of the rate dependent viscoelasticity [21], [36], [39]–[41].

2.3.1. The uniaxial (simple) tension/compression

The stress-strain state created by external forces, in which the only one principal stress has a non-zero value, is called uniaxial stress-strain state. This condition can be created by either tension of a long thin specimen along the longest direction or compression of a cylindrical specimen in a direction perpendicular to its base (Figure 1.3a-b). Considering that the load is acting in the third principal direction ($\lambda_3 = \lambda$), assumptions of the material incompressibility

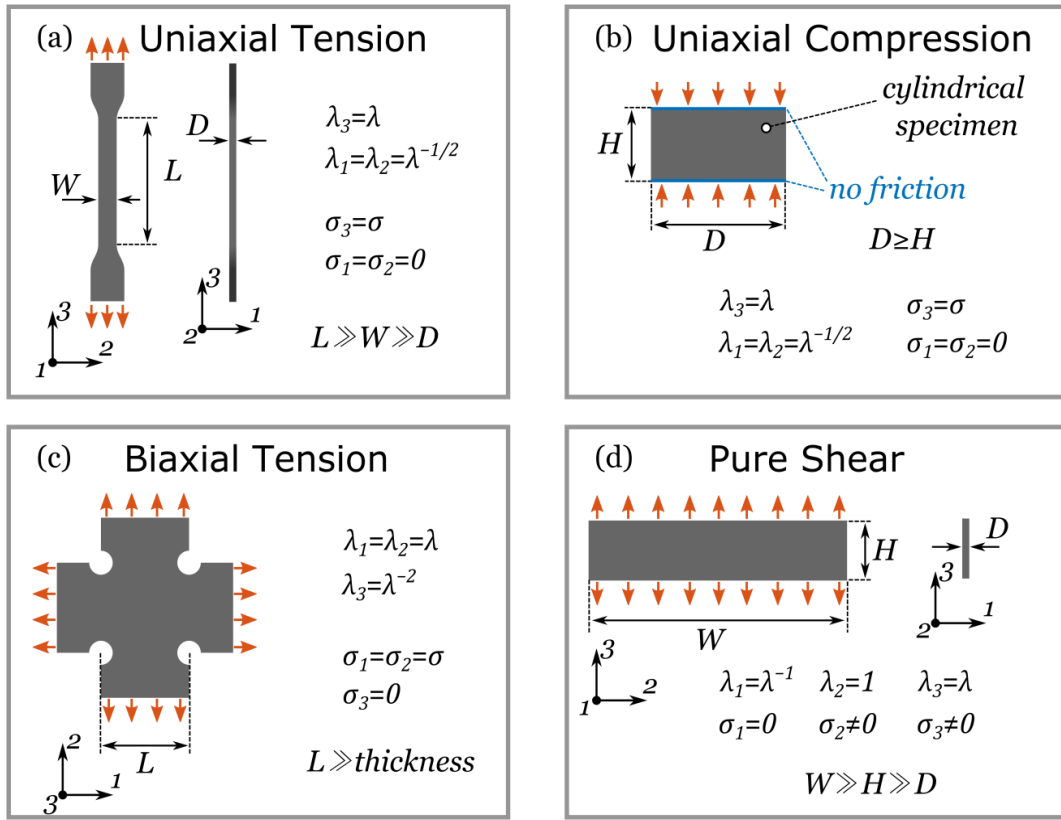


Figure 1.3: Typical tests which provide pure homogeneous deformations for incompressible material: (a) uniaxial tension, (b) uniaxial compression, (c) biaxial tension, (d) pure shear [37].

($III = \lambda_1^2 \lambda_2^2 \lambda_3^2 = 1$) and isotropy ($\lambda_1 = \lambda_2 = \lambda^{-1/2}$) lead to the following expressions for the deformation gradient $\underline{\underline{F}}$ and invariants of the left Cauchy-Green deformation tensor $\underline{\underline{B}}$:

$$\underline{\underline{F}} = \begin{bmatrix} \lambda^{-1/2} & 0 & 0 \\ 0 & \lambda^{-1/2} & 0 \\ 0 & 0 & \lambda \end{bmatrix}, \quad I = 2\lambda^{-1} + \lambda^2, \quad II = \lambda^{-2} + 2\lambda \quad (1.17)$$

In this case only stress $\sigma_3 = \sigma$ remains non-zero, while the other two principal stresses are equal to zero since there is no lateral force applied ($\sigma_1 = \sigma_2 = 0$).

The uniaxial tension and uniaxial compression tests are very popular, because of their simplicity. However, there are some difficulties and restrictions can be found and it is important to add several notes relatively to the experimental procedure. In order to provide required homogeneous stress-strain state in the uniaxial tension experiment, the length of the specimen for simple tension test has to be at least 8-10 times bigger than width and thickness [37]. Presence of the friction between the cylindrical specimen and compression plates does not allow the specimen to expand freely during uniaxial compression. Even small values of friction can cause substantial shearing strains, which will result in the non-homogeneous stress-strain state. Usually, a special lubrication is used in order to reduce the influence of the friction.

2.3.2. The (equi-)biaxial tension

In the biaxial tension, experiment specimen is equally stretched along two directions, which are orthogonal to each other (Figure 1.3c). Consideration of conditions of the incompressibility and material isotropy leads to $\lambda_1 = \lambda_2 = \lambda$ and $\lambda_3 = \lambda^{-2}$. The corresponding deformation gradient tensor and strain invariants will take the following form:

$$\underline{\underline{F}} = \begin{bmatrix} \lambda & 0 & 0 \\ 0 & \lambda & 0 \\ 0 & 0 & \lambda^{-2} \end{bmatrix}, I = \lambda^{-4} + 2\lambda^2, II = 2\lambda^{-2} + \lambda^4 \quad (1.18)$$

Biaxial stress state can be characterized by two non-vanishing principal stresses of equal magnitude ($\sigma_1 = \sigma_2 = \sigma$). The third principal stress is equal to zero ($\sigma_3 = 0$).

It can be noted that in the case of incompressible materials, the biaxial tension test creates a state of strain equivalent to the pure compression (compression with no friction influence) [38]: biaxial extension of a specimen in directions 1 and 2 leads to compression in the direction 3 and *vice versa*. The above statement will be more obvious if take $\lambda_1 = \lambda_2 = \lambda^{-1/2}$ and $\lambda_3 = \lambda$ in (1.18). In this case, expression (1.18) will be equivalent to (1.17). The actual type of test has a higher complexity, however, there is no problem with friction anymore and pure the homogeneous stress-strain state can be easily achieved.

2.3.3. The pure shear (or the planar tension)

Another type of experiment, which is creating a close-to-homogeneous stress-strain state, is the pure shear (planar tension) test. The pure shear experiment requires a thin rectangular sheet specimen, which is at least 10 times shorter in height (direction of stretching) than in width [31], [37]. In order to reach the necessary stress-strain condition, lateral deformation in the specimen must be prevented and, thereby, the sample must be well constrained along its long edges (Figure 1.3d).

In accordance with the material incompressibility and isotropy, a state of pure shear can be defined in terms of principal stretches with $\lambda_1 = \lambda^{-1}$, $\lambda_2 = 1$ and $\lambda_3 = \lambda$. Deformation gradient and strain invariants in this case can be expressed in the following form:

$$\underline{\underline{F}} = \begin{bmatrix} \lambda^{-1} & 0 & 0 \\ 0 & 1 & 0 \\ 0 & 0 & \lambda \end{bmatrix}, I = II = \lambda^2 + \lambda^{-2} + 1 \quad (1.19)$$

The pure shear is a special case of a state of plane stress ($\sigma_1 = 0$), in which two remaining principal stresses σ_2 and σ_3 have non-zero values.

3. Linear Viscoelasticity

The material behaviour can be generally distinguished between two pure material states: the elastic solid and the viscous liquid [17]. The elastic solid has a definite shape, which can be changed by external forces in order to achieve the equilibrium state. In an ideal elastic solid, all the energy spent on deformation by external forces is stored in the material and released, when the forces are removed, to restore the original shape of the body, thus, no energy

dissipation occurs. On the other hand, a viscous liquid has no definite shape and deforms irreversibly, when subjected to external forces. The behaviour of elastic solid can be described in terms of the Hooke's Law and the behaviour of viscous liquid is defined by Newton's Law of Viscosity [18]:

$$\sigma = \eta \frac{d\varepsilon}{dt} \quad (1.20)$$

Here η is the coefficient of viscosity. In an elastic body a stress value linearly depends on the actual value of a strain. It is seen from expression (1.20) that unlike the elastic case, the stress state in a viscous body has a linear dependency on speed of deformation.

It was mentioned in the introduction to the present chapter that the behaviour of elastomers can show attributes inherent to both of those two ideal types of matter depending on external conditions. There is no theory, which can completely describe such behaviour on the physical basis. Theory of viscoelasticity is mostly based on constitutive equations, which represent the macroscopic behaviour of elastomers when the time is taken into account.

The approach of linear viscoelasticity assumes that differential equations, which associate the value of stress with the value of strain, are always linear. In other words, it can be said that a linearly viscoelastic material has a linear relationship between its strain history and its current value of stress. In addition, linear viscoelasticity postulates the assumption of small strains, which allows considering the same material coordinates for the initial and final configurations of the deformable body (equality up to sign between Green-Lagrange and Euler-Almansi strain measures [20]).

3.1. Creep and Stress Relaxation

Viscoelasticity of materials can be observed in macroscopic phenomena of creep and stress relaxation. To demonstrate these phenomena, let us assume two simple one-dimensional tests. In the first one, the viscoelastic material is subjected to a constant load and in the second to a constant deformation (Figure 1.4a-b).

Application of the constant stress σ_0 results in accumulation of strain in two stages: (1) accumulation of elastic strain corresponding to applied load; (2) slow accumulation of additional strain with time. This effect is called *Creep* and it defines the creep compliance $J(t)$:

$$J(t) = \varepsilon(t)/\sigma_0 \quad (1.21)$$

If the material is subjected to the constant strain load ε_0 , the value of stress varies in two stages: (1) accumulation of stress corresponding to applied strain; (2) a slow decrease in the value of stress with time. This effect is called *Stress Relaxation* and it defines the relaxation modulus $G(t)$:

$$G(t) = \sigma(t)/\varepsilon_0 \quad (1.22)$$

The mechanical behaviour of the elastomeric material is highly dependent on conditions of the experiment and can vary from glassy rigid to a viscous liquid. Connecting these

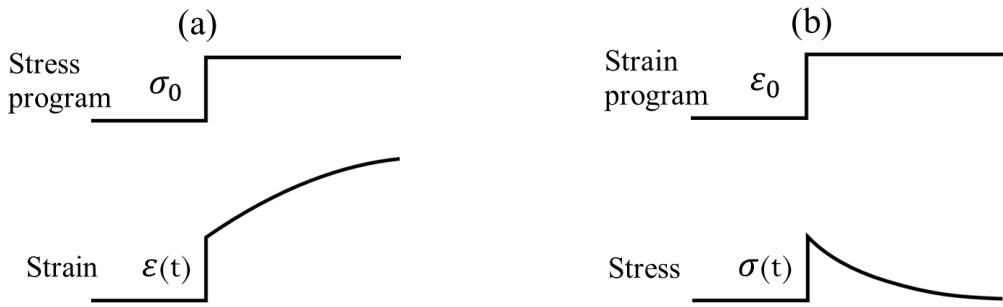


Figure 1.4: Two load programs to represent (a) creep effect at applied constant stress and (b) relaxation effect at applied constant strain

observations of the macroscopic behaviour of polymers with the definition of the creep compliance and the relaxation modulus, approximate variation diagrams for these functions can be proposed as presented in Figure 1.5a-b. It is seen from these diagrams that, in the region of short times, values of $J(t)$ and $G(t)$ correspond to the glassy behaviour of the material. At a very long times, values of these functions correspond to the pure rubber-like behaviour of elastomers. It must be mentioned that, in these two regions (glassy and rubbery behaviour), material is almost time independent. At intermediate times, behaviour of material can be characterized as viscoelastic, and so time dependent. In this time region, the material behaviour is characterized by characteristic time τ , called retardation time for $J(t)$ and relaxation time for $G(t)$.

For convenience, the short-time (or unrelaxed) and the long-time (or relaxed) values of the creep compliance and the relaxation modulus are usually distinguished and denoted as J_0/J_∞ and G_0/G_∞ respectively.

The “Flow” region mentioned on diagrams in Figure 1.5a-b for infinity times is connected with uncontrolled strain accumulation/stress relaxation due to fatigue processes. The same behaviour can be found in polymers at high temperatures near the melting point.

In practical applications, it is common to use an exponential function or a sum of exponents (which is often called the Prony's Series or the Generalized Maxwell model [17]) to represent

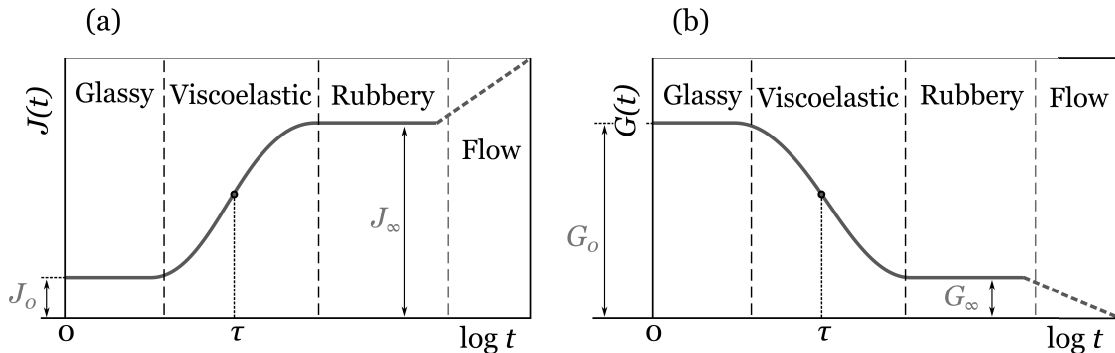


Figure 1.5: The creep compliance $J(t)$ (a) and the relaxation modulus $G(t)$ (b) as functions of time t (from [17])

functions $G(t)$ and $J(t)$. For example, the relaxation modulus can be defined as follows:

$$G(t) = G_0 - \sum_{i=1}^N G_i(1 - e^{-t/\tau_i}) = G_\infty + \sum_{i=1}^N G_i e^{-t/\tau_i} \quad (1.23)$$

Here N is the order of the Prony's Series, $G_0 = G(0)$ and $G_\infty = G(t \rightarrow \infty)$ are short-term and long-term moduli of the material respectively, G_i and τ_i are relaxation moduli and relaxation times of the i -th Prony's Series respectively. Parameters $(N, G_\infty, \tau_i, G_i)$ are material model constants. It needs to be highlighted that material constants G_0 and G_∞ can be related to each other through the expression $G_\infty = G_0 - \sum_{i=1}^N G_i$.

3.2. Boltzmann Superposition Principle

The theory of linear viscoelasticity is based on the mathematical statement, called the Boltzmann Superposition Principle, which postulates the following: 1) stress-relaxation (and creep) is a function of entire loading history; 2) each loading step makes an independent contribution to the final deformation (or value of stress) [17]. In order to illustrate statements of the Boltzmann Superposition Principle consider a number of specific loading program cases:

a) Two-step loading experiment

Let us assume that the load is increased by the value σ_0 at time $\tau = 0$ and by the value σ_1 at time $\tau = \tau_1$. Then, the total strain accumulated in the material due to the action of two loading steps can be calculated as follows:

$$\varepsilon(t) = \varepsilon_0(t) + \varepsilon_1(t) = \sigma_0 J(t) + \sigma_1 J(t - \tau_1) \quad (1.24)$$

It must be noted that the stress σ_0 continues acting at time period $[\tau_1, t]$, which results in accumulation of additional creep:

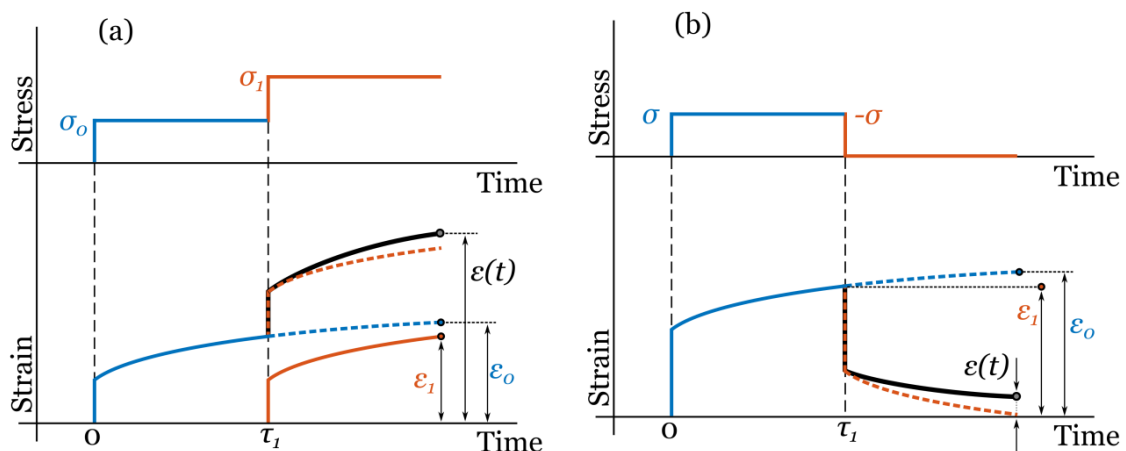


Figure 1.6: Illustration of the two-step (a) loading and (b) loading-unloading experiment (from [17])

$$\varepsilon'_0 = \sigma_0 J(t) - \sigma_0 J(\tau_1) \quad (1.25)$$

The scheme of the examined loading case is presented in Figure 1.6a

b) Two-step loading-unloading experiment

Let us consider experiment, in which a stress σ is applied at time $\tau = 0$ and then removed at time $\tau = \tau_1$. This problem can be solved in the same way as the two-step loading case by taking $\sigma_0 = \sigma$ and $\sigma_1 = -\sigma$

$$\varepsilon(t) = \varepsilon_0(t) - \varepsilon_1(t) = \sigma J(t) - \sigma J(t - \tau_1) \quad (1.26)$$

A stress $\sigma_0 = \sigma$, applied at the beginning of the experiment, continues its influence on a creep strain accumulation even after it is released (Figure 1.6b). The strain function $\varepsilon_1(t)$ in (1.26) tends to recover material to its initial state.

To generalize the above two-step approach, consider loading program with N steps in which the stress is increased by the value of $\Delta\sigma_i$ at discrete times τ_i (Figure 1.7). Using (1.21) and similarly to (1.24) the total strain, accumulated due to creep, can be calculated in the following way:

$$\varepsilon(t) = \Delta\sigma_1 J(t - \tau_1) + \Delta\sigma_2 J(t - \tau_2) + \Delta\sigma_3 J(t - \tau_3) + \dots \quad (1.27)$$

where $J(t - \tau_i)$ is a creep compliance function corresponding to i -th load. Taking a sum of all components, equation (1.27) can be generalized in the form of Duhamel integral [17], [18]:

$$\varepsilon(t) = \int_{-\infty}^t J(t - s) d\sigma(s) = \quad (1.28a)$$

$$\varepsilon_0 + \int_{-\infty}^t \hat{J}(t - s) \frac{d\sigma(s)}{ds} ds = \quad (1.28b)$$

$$= J_0 \sigma + \int_{-\infty}^t \hat{J}(t - s) \frac{d\sigma(s)}{ds} ds \quad (1.28c)$$

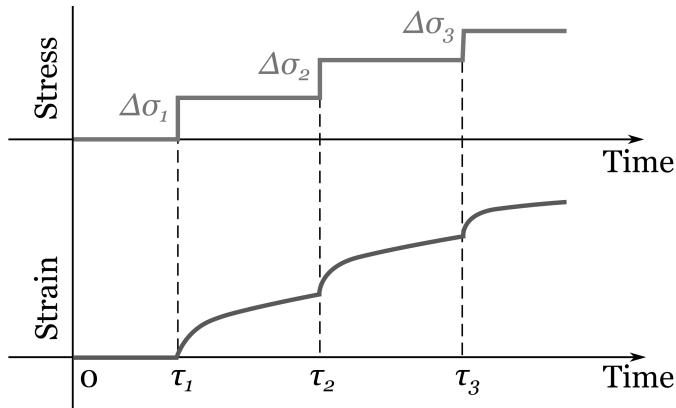


Figure 1.7: The creep behaviour of a linear viscoelastic solid (from [17])

In equation (1.28b), the instantaneous response ε_0 was separated from the time dependent part of equation. Expression for $\varepsilon(t)$ can be also written in terms of the short-term ($t \rightarrow 0$) compliance J_0 and the total stress $\sigma = \sum \Delta\sigma_i$ at the end of the experiment. In equations (1.28b) and (1.28c) $J(t) = J_0 + \hat{J}(t)$.

The stress relaxation behaviour of rubber-like materials can be generalized in the exact same way using strain increments $\Delta\varepsilon_i$ at times τ_i . Then the total stress can be expressed in the form of Duhamel integral as in the case of a creep strain:

$$\sigma(t) = \int_{-\infty}^t G(t-s) \frac{d\varepsilon(s)}{ds} ds = G_\infty \varepsilon + \int_{-\infty}^t \hat{G}(t-s) \frac{d\varepsilon(s)}{ds} ds \quad (1.29)$$

In equation (1.29), relaxed response was distinguished from time-dependent part of the equation and written in terms of the relaxed (long-term) modulus G_∞ and the total applied strain $\varepsilon = \sum \Delta\varepsilon_i$.

3.3. Mechanical models of linear viscoelasticity

The alternative way of representing the linear viscoelasticity is to consider dependency between stress and strain in the form of linear differential equation [17]. In the most general case, this equation has the following form:

$$a_0\sigma + a_1 \frac{d\sigma}{dt} + a_2 \frac{d^2\sigma}{dt^2} + \dots = b_0\varepsilon + b_1 \frac{d\varepsilon}{dt} + b_2 \frac{d^2\varepsilon}{dt^2} + \dots \quad (1.30)$$

Equation (1.30) generalizes the class of phenomenological models, which are trying to describe the observed behaviour of viscoelastic materials using a set of elastic springs and viscous dashpots.

Classically three typical model approaches are considered: the Maxwell model, the Kelvin-Voigt model and the Standard Linear Solid (also known as Zener) model. Taking only one term on either stress or strain side of the equation (1.30) corresponds to the Maxwell (spring

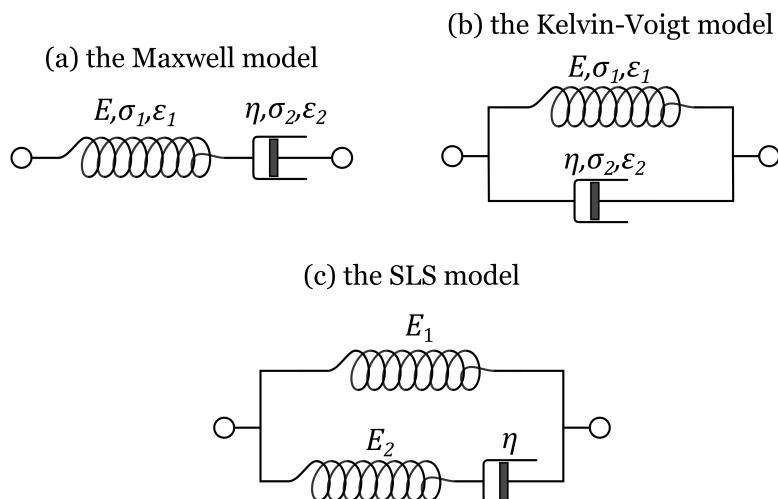


Figure 1.8: Classical mechanical models of linear viscoelasticity

and dashpot set in series, Figure 1.8a) or the Kelvin-Voigt (spring and dashpot set in parallel, Figure 1.8b) elementary models [17], which have limitations and can describe only stress relaxation or creep phenomena respectively. It can be shown that the Standard Linear Solid (SLS) model (spring and a Maxwell element set in parallel, Figure 1.8c), proposed in order to overcome limitations of the previous two models, is adequate for creep (when $d\sigma/dt = 0$) and for stress relaxation (when $d\varepsilon/dt = 0$), giving an exponential response in both cases [17].

It should be noted that all three models can predict only exponential response, but in a real application, it is not always sufficient. For a better representation of the observed viscoelastic behaviour, additional terms in linear differential equation (1.30) can be required. Equations which can be obtained in this way are equivalent to either a large number of Maxwell elements in parallel or a large number of Kelvin-Voigt elements in series.

3.4. Complex modulus and complex compliance

Static experiment with a fixed value of stress or strain is not the only way to observe the influence of viscoelastic effects on the material behaviour of elastomers. Alternatively, the specimen can be subjected to an alternating strain, while the stress is simultaneously measured. In this case and within the framework of linear viscoelasticity, stress and strain values will both vary sinusoidally with the same period but different phase angle:

$$\text{Strain: } \varepsilon = \varepsilon_0 \sin(\omega t) \quad \text{Stress: } \sigma = \sigma_0 \sin(\omega t + \delta) \quad (1.31)$$

Here, ω is the angular frequency and δ is the phase angle. The expression for the stress can be expanded to $\sigma = \sigma_0 \cos(\delta) \sin(\omega t) + \sigma_0 \sin(\delta) \cos(\omega t)$. Thus, the stress can be considered as a sum of two components: (1) the first has the magnitude of $\sigma_0 \cos(\delta)$ and is in phase with the strain and (2) the second has the magnitude of $\sigma_0 \sin(\delta)$ and is 90° out of phase with the strain. In order to obtain stress-strain relationship, above representation of the stress can be rewritten in the following form:

$$\sigma = \varepsilon_0 G_1 \sin(\omega t) + \varepsilon_0 G_2 \cos(\omega t) \quad (1.32a)$$

where

$$G_1 = \frac{\sigma_0}{\varepsilon_0} \cos(\delta) \quad G_2 = \frac{\sigma_0}{\varepsilon_0} \sin(\delta) \quad (1.32b)$$

Moduli G_1 and G_2 form the complex modulus of a material $\tilde{G} = G_1 + iG_2$ (Figure 1.9). If assumed that $\varepsilon = \varepsilon_0 \exp(i\omega t)$ and $\sigma = \sigma_0 \exp i(\omega t + \delta)$, then

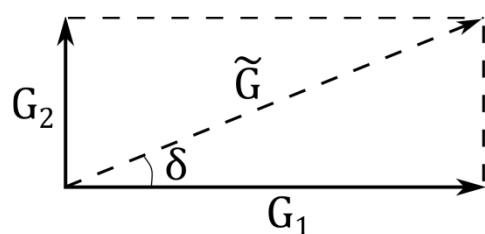


Figure 1.9: The complex modulus $\tilde{G} = G_1 + iG_2$ and $\tan(\delta) = G_2/G_1$

$$\tilde{G} = \frac{\sigma}{\varepsilon} = \frac{\sigma_0}{\varepsilon_0} e^{i\delta} = \frac{\sigma_0}{\varepsilon_0} (\cos \delta + i \sin \delta) = G_1 + iG_2 \quad (1.33)$$

The real part G_1 of the complex modulus \tilde{G} , which is in phase with the strain, is often called the storage modulus. It defines the energy stored in the specimen due to applied strain. The imaginary part, which is 90° out of phase with the strain, defines the dissipation of energy and is often called the loss modulus. Using the same method, a complex compliance can be defined:

$$\tilde{J} = J_1 - iJ_2 \quad \tilde{G} = \frac{1}{\tilde{J}} \quad (1.34)$$

4. Nonlinear viscoelasticity or Visco-hyperelasticity

All models and approaches to describe viscoelasticity of rubber-like materials, proposed so far, were based on two assumptions: 1) differential equations, which associate the value of stress with the value of strain, are always linear; 2) all strains are small. However, in real applications, it is common to consider high strains, which, generally, have a nonlinear dependency on the value of stress. In order to have the possibility to describe the viscoelastic behaviour of elastomers at a wide range of strains, it is necessary to extend the theory of linear viscoelasticity to the domain of finite strains.

Visco-hyperelastic models are generally derived from one of two different frameworks: the convolution integral (CI-model) approach [42]–[45] or the internal variables (IV-model) approach [44], [46]–[50]. The first approach (CI-model) is based on an extension of the Boltzmann principle of the theory of linear viscoelasticity into the domain of large nonlinear strains. The CI-model approach can be described as a separation of total stress on hyperelastic and viscoelastic parts. The hyperelastic part, in this case, corresponds to a strain-rate-independent response of the material (sometimes called relaxed or long-term behaviour). The viscoelastic part, in its turn, describes a deviation of the material behaviour from pure hyperelastic. This part depends on strain rate and loading history.

The second framework, the so-called internal variables model (IV-model), considers that the total deformation of a material is composed of two independent states: pure viscoelastic and pure hyperelastic. More detailed description of both approaches in terms of equations is discussed further in this section.

For additional information on this subject, readers are referred to works of Amin *et al.* [46] and Haupt and Lion [42] presenting overall introductions to the development of visco-hyperelastic models. Analytical comparison of both CI-model and IV-model frameworks can be found in the work of Petiteau *et al.* [44].

4.1. Convolution integral approach (CI-model)

4.1.1. General approach

Using equation (1.23) and integration by parts, equation (1.29) can be rewritten as follows:

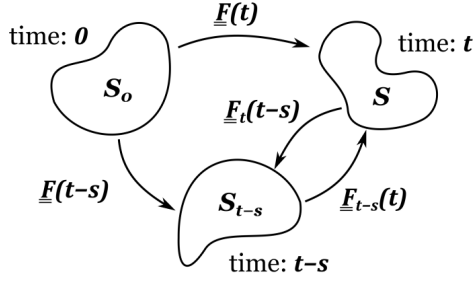


Figure 1.10: Concept of an intermediate configuration S_{t-s} at a time $t - s$ between the initial S_0 and the final S configurations.

$$\sigma(t) = G(t-s)\varepsilon(t)|_{-\infty}^t - \int_{-\infty}^t \dot{G}(t-s)\varepsilon_0(s)ds = \sigma_0(t) + \int_{-\infty}^t \frac{\dot{G}(s)}{G_0}\sigma_0(t-s) ds \quad (1.35)$$

Here $\sigma_0(t) = G_0\varepsilon(t)$ defines the short-term behaviour of the material connected with initial ($t \rightarrow 0$) modulus G_0 (if material is loaded infinitely fast).

Extension of the linear viscoelasticity approach (1.35) to a finite strain domain has been proposed by Bernstein *et al.* [51]. As in the linear case, continuous deformation of the body from the initial configuration S_0 at time 0 to the final configuration S at time t can be discretized by intermediate states S_{t-s} at times $t - s$ (Figure 1.10). Thus, in notations of the nonlinear continuum mechanics, this assumption can be described in terms of following strain gradient tensors:

- $\underline{\underline{F}}(t-s)$ transforms S_0 to S_{t-s} . Particularly $\underline{\underline{F}}(t)$ defines deformation between the initial S_0 and the final S configurations.
- $\underline{\underline{F}}_t(t-s)$ defines deformation from S to S_{t-s} .
- $\underline{\underline{F}}_{t-s}(t)$ defines deformation from S_{t-s} to S . Thus, it can be written that $\underline{\underline{F}}_{t-s}(t) = \underline{\underline{F}}_t^{-1}(t-s)$

In accordance with the superposition principle, each intermediate state S_{t-s} influence continuously on the final configuration S . In other words, the value of stress at the final configuration S is calculated as the sum (integral) of contributions from all intermediate configurations S_{t-s} .

Since the assumption of small strains is not considered, the same tensors, defined in different material configurations, must be distinguished. Thus, the stress tensor $\underline{\underline{\sigma}}_0(t-s)$, defined in the coordinate system connected with the state S_{t-s} , must be rewritten in accordance with the coordinate system of the final state S . For this purpose, the “push-forward” operator $\chi_*\{\cdot\} = \underline{\underline{F}}\{\cdot\}\underline{\underline{F}}^T$ ([20]) must be applied on the $\underline{\underline{\sigma}}_0(t-s)$. Finally, in accordance with [51], the Cauchy stress tensor can be expressed by analogy with (1.35):

$$\underline{\underline{\sigma}}(t) = \underline{\underline{\sigma}}_0(t) + \int_{-\infty}^t \frac{\dot{G}(s)}{G_0} \underline{\underline{F}}_{t-s}(t) \underline{\underline{\sigma}}_0(t-s) \underline{\underline{F}}_{t-s}^T(t) ds \quad (1.36)$$

The integral expression (1.36) is called convolution (or hereditary) integral of the material history [44]. Convolution integral models for viscoelasticity have been widely used in

rheology ([51], [52]) and solids ([42], [44], [53]). Additional details on hereditary integral models for viscoelasticity can be found in a comparative study by Ciambella *et al.* [54].

4.1.2. The CI-model for the incompressible material

The Cauchy stress $\underline{\underline{\sigma}}(t)$ can be split into deviatoric and hydrostatic parts:

$$\underline{\underline{\sigma}}(t) = [\underline{\underline{\sigma}}(t)]^D - p(t) \cdot \underline{\underline{1}} \quad (1.37a)$$

$$p(t) = -\frac{1}{3} \underline{\underline{1}} : [\underline{\underline{\sigma}}(t)]^H \quad (1.37b)$$

where $[\cdot]^D = dev(\cdot)$ and $[\cdot]^H = tr(\cdot)$ are deviatoric and spherical parts of the tensor respectively. If assumption of incompressibility is considered, then $p(t) = p = constant$ can be considered in (1.37). Thus, substituting (1.36) into (1.37a) results in:

$$\underline{\underline{\sigma}}(t) = -p \cdot \underline{\underline{1}} + [\underline{\underline{\sigma}}(t)]^D + dev \left\{ \int_0^t \left(\frac{\dot{G}(s)}{G_0} \underline{\underline{F}}_{t-s}(t) [\underline{\underline{\sigma}}_0(t-s)]^D \underline{\underline{F}}_{t-s}^T(t) \right) ds \right\} \quad (1.38)$$

The short-term stress $\underline{\underline{\sigma}}_0(t)$ is derived from the hyperelastic strain energy potential $W(\underline{\underline{B}}(t))$ using equation (1.5a) or (1.5b). Hyperelastic model must be chosen in accordance with criteria listed in Section 2.2.

Equation (1.38) is a general expression of the Cauchy stress tensor for the CI-model approach. However, in order to use (1.38) in the fitting process, it has to be rewritten to be consistent with the loading scheme used in the experiment (uniaxial, biaxial, shear, etc.).

From positive points of the CI-model, it can be highlighted its numerical simplicity (the only integral must be calculated numerically) and direct connection with the well-established Boltzmann Superposition Principle. Moreover, the split of stress, proposed by this model, has experimental evidence observed by a number of authors [48], [55] during stress multi-relaxation experiments. According to these works, pure hyperelastic part of the total stress defines a relaxation limit for the stress value at each level of strain. These limiting values form an intermediate curve inside of the Stress vs Strain loop, which corresponds to the long-term pure hyperelastic behaviour of material:

$$\underline{\underline{\sigma}}_\infty(t) = \underline{\underline{\sigma}}_0(t) \cdot \left(1 - \sum_{i=1}^N \frac{G_i}{G_0} \right) \quad (1.39)$$

From weak points of the present approach, it can be mentioned a possible inaccuracy in the prediction of the long-term relaxation behaviour of rubber using one exponential function in the expression for the relaxation function $G(t)$ (1.23). An increase in order of the Prony's series N generally can improve model response; however, this can result in a large number of constants to identify. This problem can be solved, though, by proposing a different expression for the $G(t)$ [42].

4.2. Internal variables approach (IV-model)

As it was mentioned above, the IV-model is based on a split of the total strain on pure viscoelastic and pure hyperelastic parts. In terms of nonlinear mechanics, it is assumed that the gradient of the total deformation $\underline{\underline{F}}$ can be written in the following way:

$$\underline{\underline{F}} = \underline{\underline{F}_e} \underline{\underline{F}_i} \quad (1.40)$$

where $\underline{\underline{F}_e}$ and $\underline{\underline{F}_i}$ are elastic and inelastic parts of $\underline{\underline{F}}$ respectively. It must be noted that the subscript “elastic” is used to distinguish strain rate independent part of deformation from the strain rate dependent and does not mean that the strain defined by $\underline{\underline{F}_e}$ must be linear.

Schematically, this split of deformation gradient is illustrated in Figure 1.11a. Inelastic deformation gradient $\underline{\underline{F}_i}$ transforms material from initial configuration S_0 to an intermediate, pure viscoelastic, state S_i . After, the elastic deformation gradient $\underline{\underline{F}_e}$ transforms material to the final configuration S . Alternatively, this approach can be represented as an extension of the SLS model, described in the Section 3.3. In the opposite to the linear viscoelastic case, here strain is defined by deformation gradient tensor $\underline{\underline{F}}$ in the strain rate independent network “A” and deformation gradients $\underline{\underline{F}_e}$ and $\underline{\underline{F}_i}$ in the strain rate dependent network “B” (Figure 1.11b). Thus, in accordance to the fact that energy can be stored only in two springs, assume that the strain energy density function of the whole element described in Figure 1.11b can be defined as a sum of energy potentials of these springs:

$$W(\underline{\underline{F}}, \underline{\underline{F}_e}) = W_1(\underline{\underline{F}}) + W_2(\underline{\underline{F}_e}) \equiv W_1(\underline{\underline{B}}) + W_2(\underline{\underline{B}_e}) \quad (1.41)$$

The Second Principle of thermodynamics postulates that the total production of entropy within the solid body must be non-negative. In practice, it is often assumed that the heat flow through a solid is sufficiently rapid to ensure that the temperature remains approximately uniform and stable. Under this condition and in accordance with the Second Principle of thermodynamics, the following inequality (also called Clausius-Duhem inequality) can be postulated:

$$\mathcal{D}_{int} = \underline{\underline{\sigma}} : \underline{\underline{D}} - \dot{W} \geq 0 \quad (1.42)$$

where \mathcal{D}_{int} is the internal dissipation and $\underline{\underline{D}} = \frac{1}{2}(\underline{\underline{L}} + \underline{\underline{L}}^T)$ is the deformation rate tensor ($\underline{\underline{L}}$ is the velocity gradient tensor, defined as $\underline{\underline{L}} = \underline{\underline{F}} \underline{\underline{F}}^{-1}$). Physically, inequality (1.42) states that the rate of work done by the stress must always be equal or exceed the rate of change of free energy of the solid, which is defined by W . Substituting (1.41) into (1.42) leads to:

$$\underline{\underline{\sigma}} : \underline{\underline{D}} - \frac{\partial W_1}{\partial \underline{\underline{B}}} : \dot{\underline{\underline{B}}} - \frac{\partial W_2}{\partial \underline{\underline{B}_e}} : \dot{\underline{\underline{B}}_e} \geq 0 \quad (1.43)$$

Time derivative of the left Cauchy-Green deformation tensor $\underline{\underline{B}} = \underline{\underline{F}} \underline{\underline{F}}^T$ can be expressed using $\underline{\underline{L}}$:

$$\dot{\underline{\underline{B}}} = \underline{\underline{L}} \underline{\underline{B}} + \underline{\underline{B}} \underline{\underline{L}}^T \quad (1.44)$$

In order to derive expression for $\dot{\underline{\underline{B}}}_e$, define firstly the velocity gradient tensor $\underline{\underline{L}}$ in terms of tensors $\underline{\underline{L}}_e$ and $\underline{\underline{L}}_i$:

$$\underline{\underline{L}} = \dot{\underline{\underline{F}}} \underline{\underline{F}}^{-1} = \left(\dot{\underline{\underline{F}}}_e \underline{\underline{F}}_i + \dot{\underline{\underline{F}}}_i \underline{\underline{F}}_e \right) \cdot \underline{\underline{F}}_i^{-1} \underline{\underline{F}}_e^{-1} = \underline{\underline{L}}_e + \underline{\underline{F}}_e \underline{\underline{L}}_i \underline{\underline{F}}_e^{-1} \quad (1.45)$$

Finally, expressing $\underline{\underline{L}}_e$ from (1.45) it is easy to obtain the following relationship:

$$\dot{\underline{\underline{B}}}_e = \underline{\underline{L}} \underline{\underline{B}}_e + \underline{\underline{B}}_e \underline{\underline{L}}^T - 2 \underline{\underline{F}}_e \underline{\underline{D}}_i \underline{\underline{F}}_e^T \quad (1.46)$$

Substituting expressions for $\dot{\underline{\underline{B}}}$ and $\dot{\underline{\underline{B}}}_e$ to Clausius-Duhem inequality (1.43) and using properties of the double contraction it can be obtained:

$$\left(\underline{\underline{\sigma}} - 2 \frac{\partial W_1}{\partial \underline{\underline{B}}} \underline{\underline{B}} - 2 \frac{\partial W_2}{\partial \underline{\underline{B}}_e} \underline{\underline{B}}_e \right) : \underline{\underline{D}} + 2 \left(\underline{\underline{F}}_e^T \frac{\partial W_2}{\partial \underline{\underline{B}}_e} \underline{\underline{F}}_e \right) : \underline{\underline{D}}_i \geq 0 \quad (1.47)$$

Following procedure proposed by Coleman and Noll [56], it can be shown that inequality (1.47) is valid if and only if both two following expressions are true:

$$\text{Stress relation: } \underline{\underline{\sigma}} = 2 \frac{\partial W_1}{\partial \underline{\underline{B}}} \underline{\underline{B}} + 2 \frac{\partial W_2}{\partial \underline{\underline{B}}_e} \underline{\underline{B}}_e \quad (1.48a)$$

$$\text{Dissipation inequality: } 2 \left(\underline{\underline{F}}_e^T \frac{\partial W_2}{\partial \underline{\underline{B}}_e} \underline{\underline{F}}_e \right) : \underline{\underline{D}}_i \geq 0 \quad (1.48b)$$

The simplest expression for $\underline{\underline{D}}_i$, sufficient to satisfy (1.48b), was proposed by Huber and Tsakmakis [57] and used by Amin *et al.* [46] and Petiteau *et al.* [44]. It can be expressed as follows:

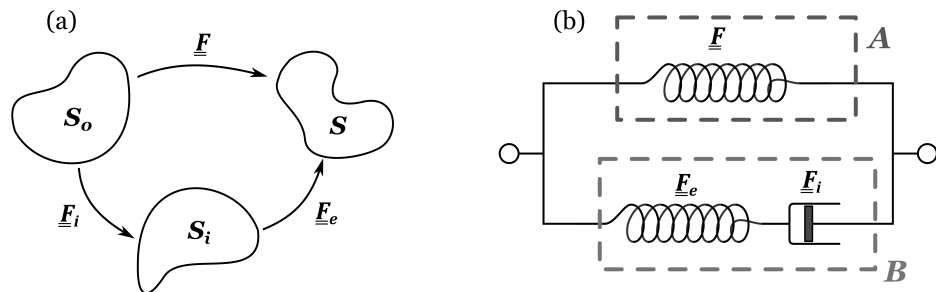


Figure 1.11: Schematic representation of deformation split in IV-model approach

$$\underline{\underline{D}_i} = \frac{1}{\eta} \left[\underline{\underline{F}_e}^T \frac{\partial W_2}{\partial \underline{\underline{B}_e}} \underline{\underline{F}_e} \right]^D \geq 0 \quad (1.49)$$

where η is a material constant connected with viscoelasticity. Substituting (1.49) to (1.46) gives the evolution equation for the strain in the elastic part of the network “B”:

$$\dot{\underline{\underline{B}_e}} = \underline{\underline{L}} \underline{\underline{B}_e} + \underline{\underline{B}_e} \underline{\underline{L}}^T - \frac{2}{\eta} \underline{\underline{B}_e} \left[\frac{\partial W_2}{\partial \underline{\underline{B}_e}} \underline{\underline{B}_e} \right]^D \quad (1.50)$$

Constitutive behaviour of the IV-model can be fully described by equations (1.48a) and (1.50). Thus, in order to determine stress $\underline{\underline{\sigma}}$ at each deformation state defined by $\underline{\underline{B}}$, firstly, tensor $\underline{\underline{B}_e}$ must be calculated by solving the differential equation (1.50). Numerically, this can lead to an increase in computational time and accumulation of the error.

The IV-model for the incompressible material can be obtained in the similar with the CI-model way using split of the total stress into deviatoric and hydrostatic parts.

The main advantage of the IV-model is an explicit consistency of the model with the second principle of thermodynamics: the model equations are directly derived on its basis. It must be highlighted that the IV-approach assumes existence of an independent pure viscoelastic equilibrium state of the material S_i . However, this assumption is not based on any physical considerations or experimental evidence. Additionally, the lack of a straight definition for the expression of $\underline{\underline{D}_i}$ (1.49) increases complexity of the modelling process.

4.3. Identification of parameters of visco-hyperelastic models

Many authors have found that it is convenient to separate the parameters identification of the long-term behaviour of the model (pure hyperelastic stress $\underline{\underline{\sigma}}_\infty$ in (1.39)) and the stress relaxation (e.g. [17], [47], [49]). This strategy can provide an easier way of identification of model constants using different experimental data. Indeed, consideration of the pure hyperelastic behaviour reduces equation (1.36) of the CI-model to $\underline{\underline{\sigma}}(t) = \underline{\underline{\sigma}}(\underline{\underline{B}}) = \underline{\underline{\sigma}}_\infty(\underline{\underline{B}})$ and results in $\underline{\underline{B}_e} = \underline{\underline{B}}$ for the IV-model. Stress relaxation experiment can be defined using the CI-model by taking $\underline{\underline{\sigma}_0} = \text{const}$, so the total value of stress become dependent only on parameters of the relaxation function $G(t)$ (the value of $\underline{\underline{\sigma}_0}$ in this case can be identified from boundary conditions). For the case of the IV-model this type of experiment results in $\underline{\underline{B}} = \text{const}$ and $\underline{\underline{L}} = 0$, thus, equation (1.50) become homogeneous, and the value of the total stress depends only on parameter of viscosity.

However, in reality, viscoelastic and hyperelastic mechanics act simultaneously, and pure state of the material cannot be obtained experimentally. According to Kossa *et al.* [24], separate fitting of hyperelastic and/or viscoelastic parts raises multiple errors:

- Location of an intermediate hyperelastic response on the Stress vs Strain curve is approximated and cannot be clearly identified experimentally;
- The equation of the stress relaxation considers a step loading program, which means that a specimen is loaded instantaneously before relaxation. Stress relaxation experiment, in the opposite, implies loading of a specimen at constant strain rate. Thus, the starting point of the relaxation curve in the experiment depends on the strain rate, which doesn't coincide with the theoretical initial stress.

Thus, the visco-hyperelastic model must be fitted to experimental data without separation of long-term and relaxation behaviour of the studied material.

4.4. Conclusions on visco-hyperelasticity

In the present work CI-model approach was chosen for modelling the mechanical behaviour of the elastomeric material of rail pad. The reason for choosing this approach can be explained as follows. First of all, the CI-model is a natural extension of the theory of linear viscoelasticity, as it is based on an extension of the well-established Boltzmann Superposition Principle. Additionally, the split of stress, proposed by this model, has experimental evidence observed by a number of authors [48], [55] during stress multi-relaxation experiments. In the opposite of CI-model, the IV-model approach assumes the existence of an independent pure viscoelastic state of the material, which cannot be proved experimentally or justified by any physical considerations.

Moreover, the CI-model approach is already implemented in most of FE codes, which makes it easier to use.

5. Conclusions to Chapter 1

The macroscopic mechanical behaviour of elastomeric materials was overviewed in accordance with experimental evidence found in the literature. In general, elastomers have the very complex mechanical behaviour, which depends, *inter alia*, on a wide range of external factors (among which are strain rate, loading frequency and temperature). The literature review of the most common approaches, appropriate for the modelling of different aspects of the mechanical behaviour of such materials (Figure 1.12), was carried out.

Additionally, experimental procedures, required for the identification of parameters of models were reviewed and discussed. It was found that the quality of model fit can be increased using complex experimental data, without separation of the long- and short-term behaviour of elastomer.

Two approaches (CI-model and IV-model) extending the theory of linear viscoelasticity to the domain of finite strains were reviewed. The CI-model approach was chosen to represent the mechanical behaviour of a rail pad material in the following chapter.

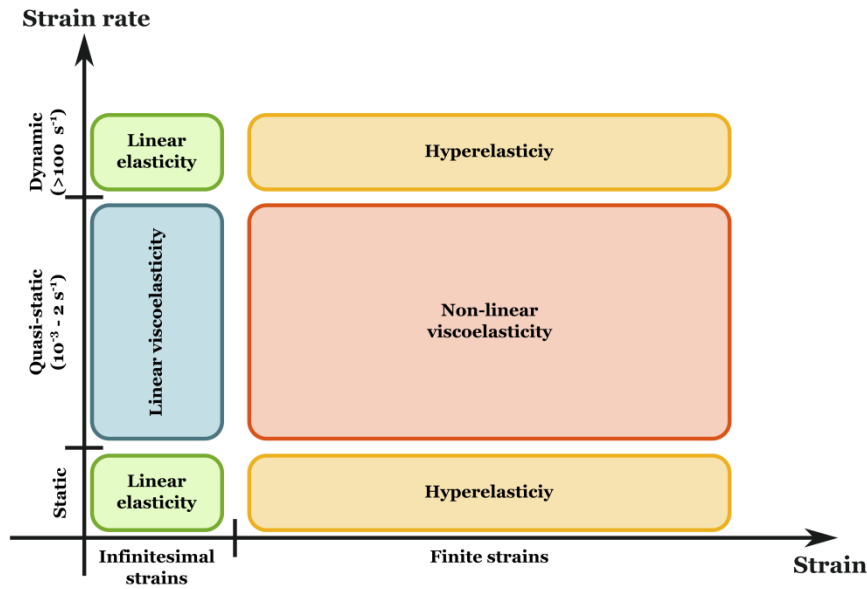


Figure 1.12: Applicability domains for constitutive approaches, appropriate for the modelling of the mechanical behaviour of elastomers (from [44])

Chapter 2: Experimental and numerical study of elastomeric rail pad subjected to compression load

1. Introduction

Elastomeric rail pads, located between the rail and the sleeper (Figure 2.1), appear to be an essential part of the modern railway track. The main purpose of rail pads is to provide a smooth contact between the rail and the sleeper. Dissipative properties of rubber combined with adapted geometry make rail pads indispensable when considering reduction of noise, vibrations and dynamic component of wheel load. Low stiffness of rail pads (compared to rail and sleeper) and possibility to sustain big deformations lead to bending of a rail under wheel load of the train, which allow separating this load between few sleepers [58], [59] (see Section 2.2.4Figure 2.9). Thus, mechanical properties of elastomeric rail pad have a direct influence on railway track stiffness and define the distribution of wheel load between sleepers. However, investigations of rail pad contribution to the mechanical behaviour of a railway track are mostly limited to experimental ones [60]–[63]. Numerical studies in the field of railroad engineering are usually devoted to modelling a whole railway track structure and mostly performed using a simplified representation of a rail pad. In these works, rail pads are mainly represented by one-dimensional spring [64]–[67] or spring-dashpot connector [68]–[73] between the rail and the sleeper. Their mechanical behaviour, in this case, is defined by stiffness and damping factor constants, which must be identified experimentally for each type of a rail pad (material and geometry). Moreover, it was found in works [74] and [75] that considering the longitudinal and/or lateral dimensions of the rail pad significantly influences the mechanical response of the railway track model, although, the influence of the pad geometry hasn't been studied numerically. Besides the works mentioned above, a lack of numerical studies concerning the whole rail pad structure can be found in the literature. Thus, development of numerical model representing the complex 3D geometry of a rail pad can be useful for a number of tasks, among which are:

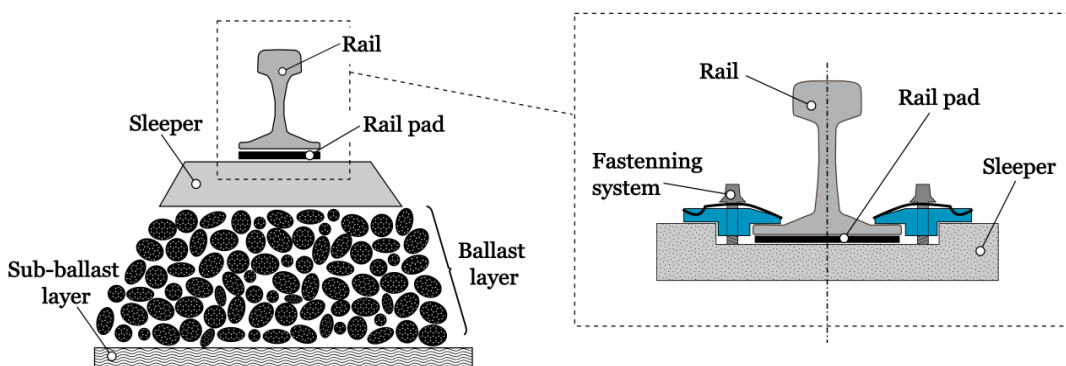


Figure 2.1: Rail pad location on the ballasted railway track

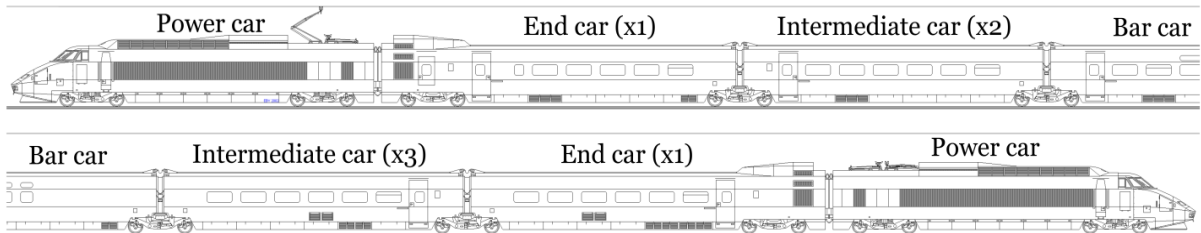


Figure 2.2: TGV train with two power cars, bar/restaurant car, two end and five intermediate passenger cars

- Identification of the exact contribution of a rail pad to the mechanical behaviour of the railway track
- Identification of stiffness and damping factor constants for the chosen rail pad material and geometry
- Optimization of rail pad geometry and material parameters.

The aim of the study presented in this chapter was to provide a complete strategy of modelling a whole elastomeric rail pad structure subjected to compressive load and investigate the importance of accounting its whole 3D geometry.

2. Study of on-track loads relatively to rail pads

Loading conditions, intrinsic to a rail pad located on a ballasted railway track, must be defined before starting an investigation of the mechanical behaviour of its material and structure (both experimentally and numerically). It can be done using *in-situ* experimental data and analytical approximation.

The first part of this section presents an analysis of *in-situ* measurements carried out by SNCF between 2005 and 2009. This data can give an idea of speeds and magnitudes of the load acting on the pad when the train passes over.

In the second part, loads acting on the rail pad are studied analytically. In this way, their contribution to the total load can be investigated. Moreover, an analytical approach is more flexible and allows to consider different loading cases.

2.1. *In-situ* measurements and experimental approach

Experimental validation is an essential part of any modelling process. Experimentally, the mechanical behaviour of a rail pad can be studied both in laboratory and *in-situ* on a real railway track. The first approach provides greater flexibility and control of the loading and measuring processes. Conversely, *in-situ* measurements can be influenced by many factors (like temperature, track and train conditions and others), which are hard to control and accurately predict. Nevertheless, since laboratory experiments, as well as numerical studies, intended to simulate the real loading cases for the structure studied, *in-situ* data measured on a real railway track can be required.

On the railway track, rail pads are mainly subjected to compressive loads, when a train passes over. In order to investigate precisely the loading conditions for a rail pad, *in-situ* measurements were carried out on a railway track by SNCF railway company. During several

experimental campaigns performed by SNCF between 2005 and 2009 on the real high-speed railway tracks (on straight and curved railway lines), wheel load acting on a rail (Q_w) and a compression displacement (d_{cd}) of a rail pad, caused by passing trains, were measured *in-situ* [76]. In the present study, data obtained for a TGV train (Figure 2.2) passing over a straight railway line is presented and analyzed. It must be highlighted beforehand that *in-situ* measurements of a rail pad compression and force acting on a rail were carried out during different experimental campaigns. It happened that the experimental data corresponding to the same train and the same measurement line was available for a slightly different train speeds: 296 km/h for the compression displacement data and 316 km/h for the wheel force data. TGV train consists of two power cars, two end cars (connecting a power car with intermediate wagons) and 6 intermediate cars. All train cars are supported by a total of 10 bogies (20 wheel axles). Due to the difference in the mass of different car types, as well as non-uniform distribution of wheel axles (see Figure 2.2) along the train, it was expected to observe some variance in recorded signals.

The measurement of a wheel load was performed using the set of strain gauges connected to a Wheatstone bridge. It can be shown that the value of the wheel load Q_w , located between two points A and B (Figure 2.3a), is proportional to the output signal of a Wheatstone bridge:

$$Q_w = \frac{V_{out}}{V_{in}} KE \quad (2.1)$$

where V_{in} and V_{out} are input and output voltage signals of a Wheatstone bridge, K is the area of a rail cross section and E is the Young's modulus of a rail material. An example of signal, obtained for one wheel using data from a Wheatstone bridge, is presented in Figure 2.3b. It must be noted that the value of Q_w calculated by this method is constant between points A and B (to within the error of measurement). The common wheel force signal, caused by passing of a TGV train, is shown in Figure 2.4a. The value of the wheel force was averaged by superimposing peak signals as it is shown in Figure 2.4b. Only signals from wheel axles with

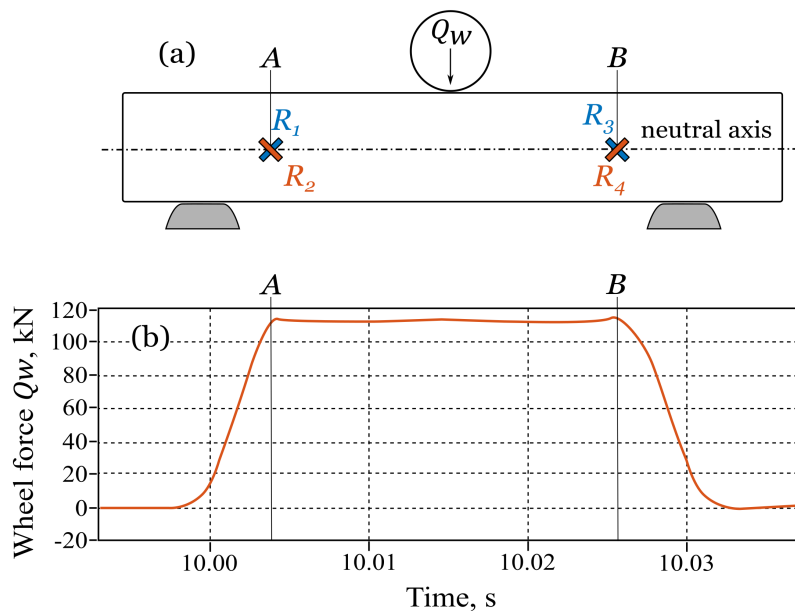


Figure 2.3: Measurement of a wheel force using the set of strain gauges connected to a Wheatstone bridge: (a) location of strain gauges on a rail; (b) an example of signal of one wheel obtained using data from strain gauges

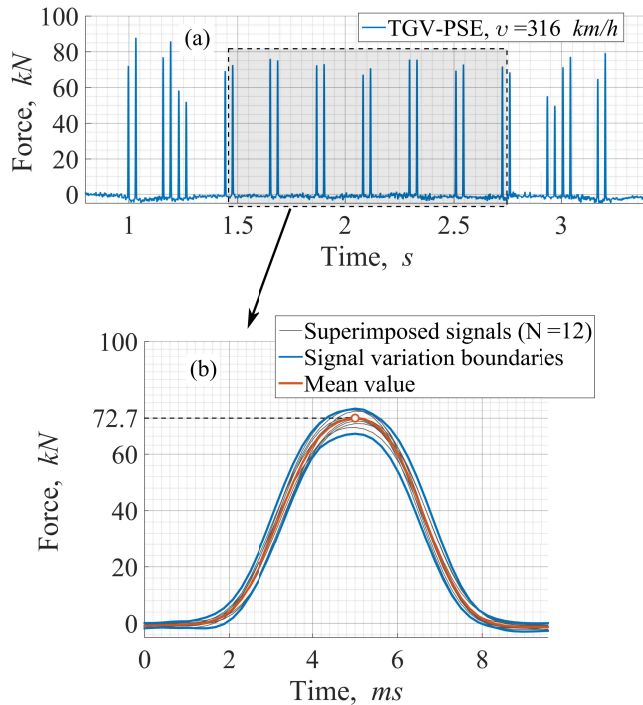


Figure 2.4: The common wheel force signal caused by passing of a TGV-PSE train plotted in a time domain (a); superimposed peaks of a wheel force signal (b)

the same bearing load were used for the averaging (passenger cars in the middle of the train). The average peak value of the wheel load in this case is equal to 72.7 kN.

The measurement of the rail pad compression displacement (d_{cd}) was carried out using a laser displacement sensor installed on a sleeper. Experimental setup is presented in Figure 2.5. Location of the sensor allows to measure vertical displacement of a rail relatively to the position of a sleeper. Thus, as the rail deformation can be considered as negligible, measurements made by the laser sensor provide the compression displacement of a rail pad regardless for the deformation of underlying layers of the track.

The common rail pad compression displacement signal caused by passing TGV train is shown in Figure 2.6a. Similarly to the wheel force signal, an average level of rail pad compression

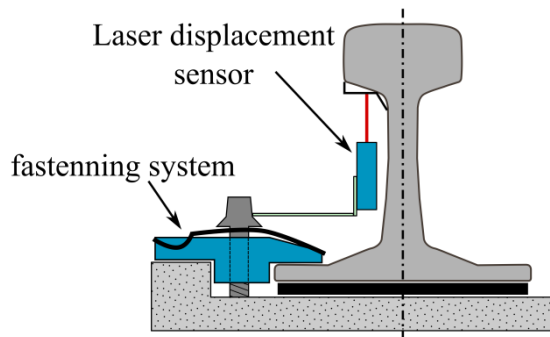


Figure 2.5: Experimental setup for the measurement of a rail pad compression displacement

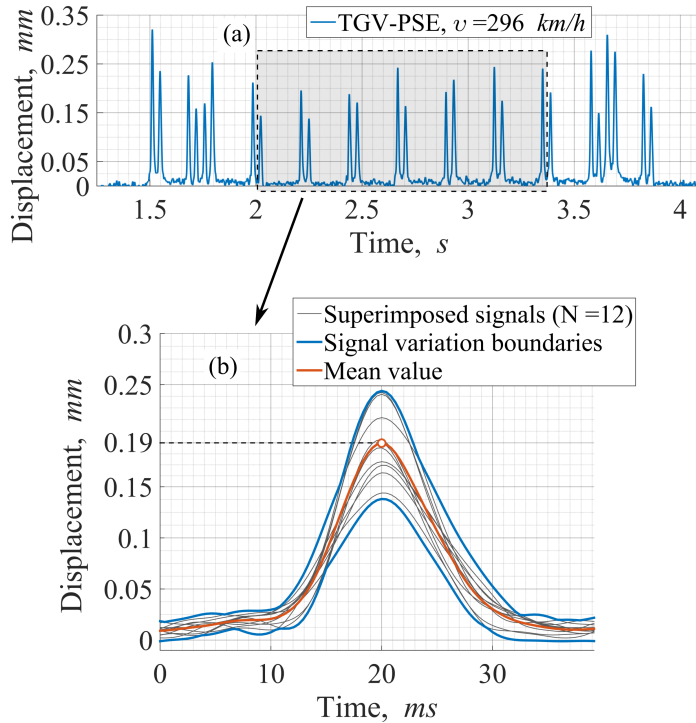


Figure 2.6: The common rail pad compression displacement signal caused by passing of a TGV-PSE train plotted in a time domain (a); superimposed peaks of a rail pad compression displacement signal (b)

displacement was obtained by averaging signals from all bogies of the train located on passengers-type cars in the middle of the train (Figure 2.6ab). The average peak value of the rail pad compression displacement, in this case, is equal to 0.19 mm. In accordance with the load duration (Figure 2.6b) and taking into account that the common thickness of a rail pad is equal to 9-10 mm, it is easy to calculate the macroscopic strain rate ($\dot{\lambda}$) of a compressive load, which does not exceed values in the range of $1-2 \text{ s}^{-1}$. Due to this fact, attention was paid to experimental investigation of the behaviour of rubber material at quasi-static strain rate.

2.2. Analytical study of loads acting on rail pads

Loading profile, required as an input for the numerical study, can be identified analytically by taking a sum of all forces acting on a rail pad at a chosen time. These forces can be divided into static and dynamic parts. The contribution of the first group combines the weight of a rail and the clamping force of a fastening system and can be easily approximated using basic approaches of applied mechanics and simple experiments. On the contrary, the dynamic load of train wheelsets incorporate not only inertial forces of rotating wheel with the mass (easy to calculate), but also additional loads connected with sprung mass of cars and imperfections of the wheel-rail contact zone (corrugations, welds, wheel flats, etc.), which cannot be easily identified and approximated. In the railroad engineering, it is common to consider the dynamic part of the wheel load to be proportional to the static wheel load with the coefficient φ , which depends on the train speed and parameters of the track:

$$Q_{dynamic} = \varphi \cdot Q_{static} \quad (2.2)$$

Different methods of calculation of the impact factor φ were proposed by different authors taking into account track irregularities, vehicle suspension and speed, track curvature, track condition and so on [2], [58], [77]. However, according to a comparative study of Van Dyk *et al.* [77], most of the models developed so far provide satisfactory results only for average train speeds (less than 200 km/h) and usually overestimate the dynamic contribution in the case of high speeds. Additionally, most of recommendations were developed for particular railway tracks and with time became obsolete.

Thus, in order to eliminate the problem of choosing an appropriate model for the dynamic factor φ , an average value of the wheel load measured *in-situ* was used in this study.

2.2.1. Parameters of the studied case

The profile of load acting on a rail pad is obviously dependent on the type of a railway track (with or without ballast), parameters of its structure (type of rails and fastening system, location of sleepers, etc.), speed and type of a train (weight and dimensions of cars, location of wheels, etc.).

Dimensions of a TGV high-speed train are presented in Figure 2.7. The rest of parameters, required for the present study, were found in literature or provided by Direction Ingénierie & Projets of SNCF company (Table 2.1). The coefficient k , indicated in Table 2.1, is referred to a track modulus (index) and defined as the supporting force per unit length of rail per unit deflection [78]

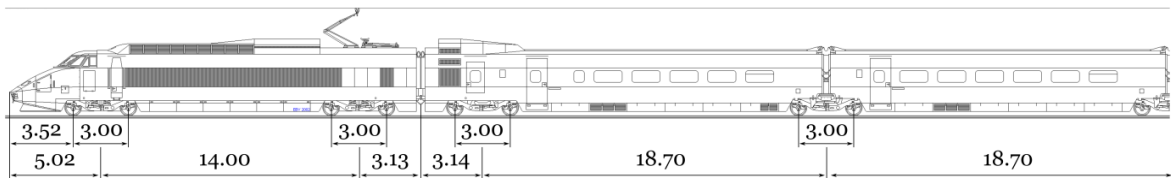


Figure 2.7: Dimensions of a TGV train (in metres) [1]

Speed of a train was chosen to be equal to 316 km/h (87.8 m/s), because the force data, which will be used in the present analytical study, was available for this value of speed.

It was mentioned above that the deformation of rail pads are mostly caused by static preloads of rail and fastening system and dynamic wheel load of a passing train. Further, in this section, analytical study of the dynamic load of a train wheelset (bogie) will be defined. Calculation of the wheel load was done considering the following cases (from simple to complex):

- Dynamic load of a one wheel
- Dynamic load of two wheelsets (bogie)

In this analytical approach, railway track is considered to be horizontal and straight.

2.2.2. Preload from the weight of a rail

On the ballasted railway track, steel rails are located on equally spaced concrete sleepers. Thus, each sleeper supports an equal part of a rail weight. The value of preload, caused by the

rail weight, can be easily calculated following the theory of simply supported beams and use constants from Table 2.1:

$$F_r = \rho g l \cong 360 \text{ N} \quad (2.3)$$

Table 2.1: Parameters of a railway track

Parameter	Value	Comment
Q_w	$72.7 \cdot 10^3 \text{ N}$	The average peak wheel load (in accordance with Section 2.1)
Train		
• model: <i>TGV-PSE</i>		
d	3 m	Distance between wheel centres on one bogie
v	87.8 m/s	TGV speed
Rails		
• material: <i>stainless steel</i>	ρ	Distributed mass of a rail
• model: “ <i>60E1</i> ”	E	Young’s modulus
	J_x	Area moment of inertia
Fastening system		
• model: “ <i>Nabla</i> ”	F_{cf}	The average clamping force, caused by two “Nabla” fasteners (see Figure 2.8)
	d_{cd}^{nabla}	Compression displacement caused by clamping force F_{cf}
Rail pads		
• material: <i>27 phr carbon black filled styrene-butadiene rubber (SBR)</i>		
• geometry: <i>grooved rail pad (Figure 2.2c, Section 1.1)</i>		
• dimensions: <i>156 x 182 x 9 mm³</i>		
Sleepers		
• material: reinforced concrete	l	Sleepers’ spacing distance
Railway track		
• type: <i>ballasted</i>	k	100 · 10 ⁶ N/m ²
		Railway track index

2.2.3. Preload from fastening system

The rail fastening system “Nabla” consists of two fasteners: one from each side of a rail. Construction of a “Nabla” fastener is presented in Figure 2.8. Each fastener consists of a screw spike (1), a steel Nabla clip (2) (transfer load from screw spike) and a plastic insulator (3) (provides a good contact with a rail and a sleeper). Thus, the force from a screw spike is distributed between sleeper and rail through the insulator. The clamping force, applied on a rail pad after installation of the “Nabla” fastening system, was measured by SNCF

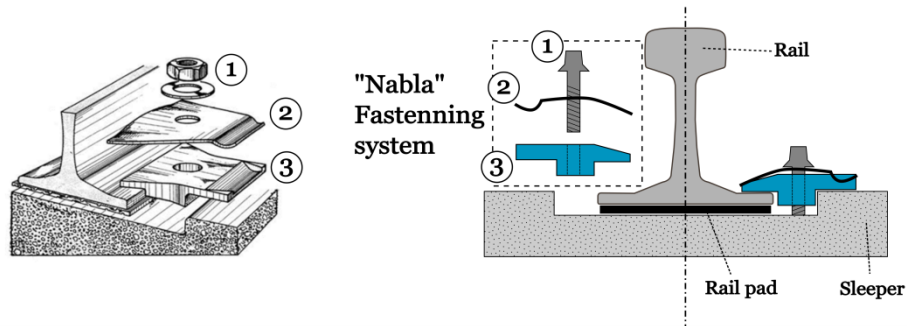


Figure 2.8: Construction of a fastening system “Nabla” [1]

engineering department in accordance with the European norm EN 13146-7 [79]. It was found that on average the clamping force $F_{cf} = 16.9 \text{ kN}$ can be accepted.

2.2.4. Moving load of one wheel

A load signal of a passing train on a railroad structure can be presented as a set of concentrated loads (wheels) moving along the beam (rail), which is located on uniformly spaced supports (sleepers with or without rail pads). Supports are located on a laminated half-space, which represents ballast, sub-ballast, subgrade, etc.

Let us consider one of these loads (one wheel). In the simplest case, when the beam deflection is not considered, one concentrated load will be distributed along all supports holding this beam. In reality, an action of a concentrated force results in deflection of a rail and, consequently, in the non-uniform distribution of this load between a number of supports [58], [59]. An example of such a distribution, obtained using finite element approach, is presented in Figure 2.9. The number of loaded sleepers and the force distribution depend on several factors: rigidity of a railway structure, mechanical properties and geometry of a rail, distance between sleepers, the magnitude of wheel axle loads, train speed, etc. Identification of the force distribution along sleepers is connected with the calculation of rail deflection due to the application of a concentrated load.

The first approach, widely used for calculation of a rail deflection, is referred to Winkler foundation problem: deflection of a beam (rail) due to the moving (wheel) load [80]. In this approach, beam is located on elastic foundation with the distributed stiffness $k [\text{N}/\text{m}^2]$.

Consider the vertical deflection $U(x, t)$ of a rail due to action of the impulse load Q_w . This causes deformation of the elastic foundation and, consequently, counteracting distributed force $r(x, t) = -kU(x, t)$, which is acting back on a rail (Figure 2.10). Expression for the deflection $U(x, t)$ can be derived from the classical beam theory (Euler–Bernoulli theory)

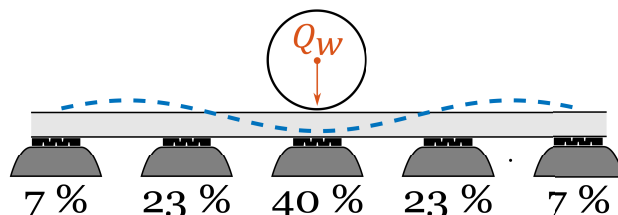


Figure 2.9: Distribution of the wheel load among the sleepers (from [58])

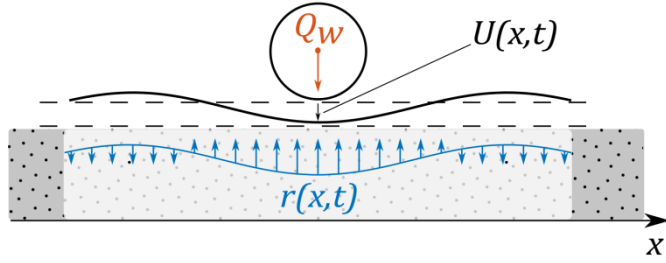


Figure 2.10: Rail on a Winkler foundation subjected to concentrated load Q_w

using the following equation:

$$EJ_x \frac{d^4 U(x, t)}{dx^4} + \rho \frac{d^2 U(x, t)}{dt^2} + kU(x, t) = -Q_w \delta(x - vt) \quad (2.4)$$

Here E , J_x , ρ and v are Young's modulus, the second moment of inertia, distributed mass of a rail and speed of a train respectively (see Table 2.1); $\delta(x)$ is the Dirac function, which is used in order to ensure the impulse impact with the magnitude Q_w . The second term in equation (2.4) is taken to consider inertia of a rail and dependency of $U(x, t)$ on time.

Equation (2.4) can be solved using a double Fourier transformation of the function $U(x, t)$ and methods of a contour integration (solution in details is described in Appendix A). The final solution is written as follows:

$$U(x, t) = -\frac{Q_w b^3 e^{-q|x-vt|}}{4sqk} \cos(s|x-vt| - \operatorname{arctg}(q/s)) \quad (2.5a)$$

with

$$s = \sqrt{0.5(b^2 + av^2)}; q = \sqrt{0.5(b^2 - av^2)} \quad (2.5b)$$

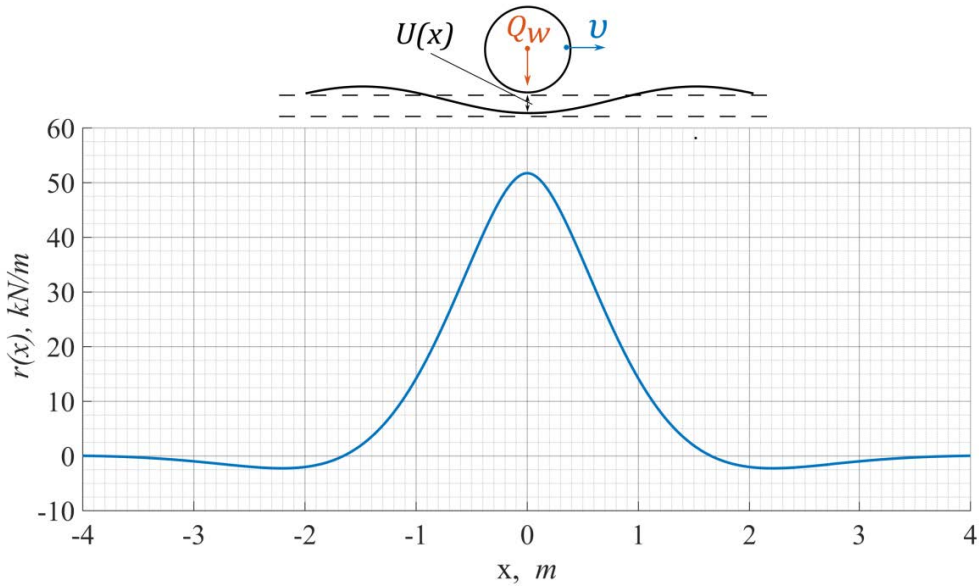


Figure 2.11: Dependence of distributed reaction force $r(x, t)$ on distance x from a wheel load moving with the speed $v = 87.8$ m/s

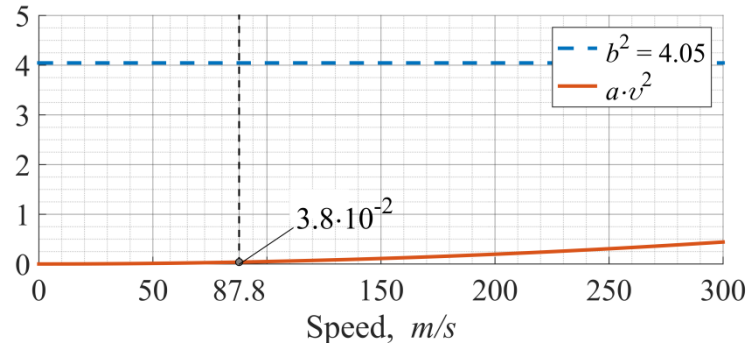


Figure 2.12: Dependence of av^2 on the value of a train speed compared with the value of b^2

$$2a = \rho/EJ_x; b^4 = k/EJ_x \quad (2.5c)$$

Thus, distributed reaction force $r(x, t)$, caused by one moving wheel, can be found as:

$$r(x, t) = \frac{Q_w b^3 e^{-q|x-vt|}}{4sq} \cos(s|x-vt| - \arctg(q/s)) \quad (2.6)$$

Variation of the distributed reaction force $r(x, t)$ relatively to position of a wheel load moving with the speed of 316 km/h is presented in Figure 2.11. The value of $r(x, t)$ becomes zero at 1.75 m away from the point of load application. Negative values of the $r(x, t)$ outside the 1.75 m band mean that the rail tends to bend backwards in these regions.

It needs to be highlighted that inertia forces of a rail have negligible influence on the final shape of the curve presented in Figure 2.11. Indeed, it can be shown, using the above-mentioned constants, that the value of av^2 is negligibly small compared to b^2 for the studied train speed. Figure 2.12 presents dependence of av^2 on the value of a train speed. It is seen

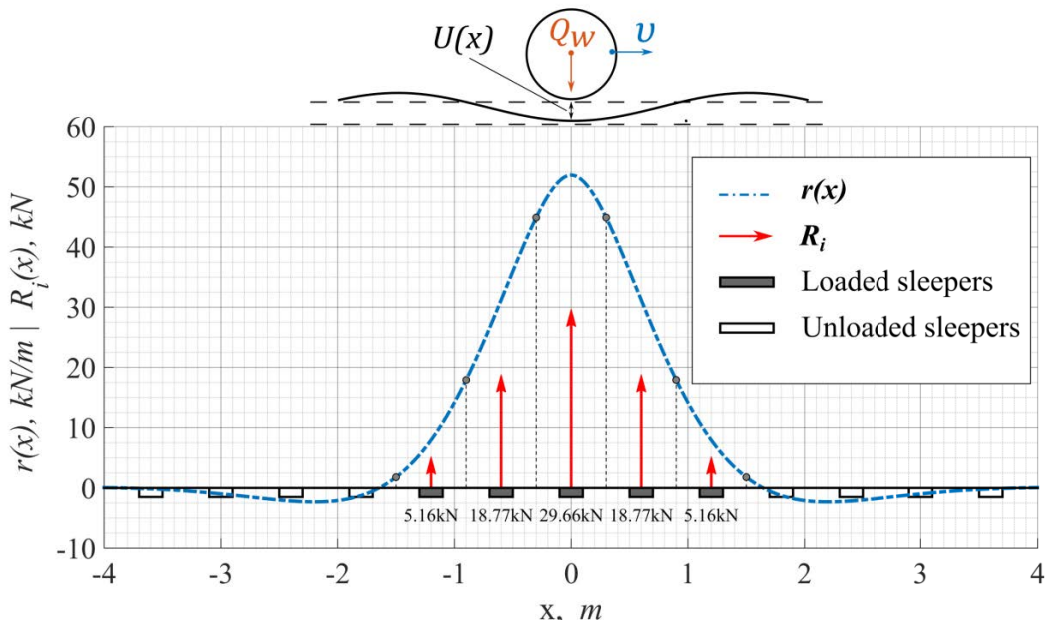


Figure 2.13: Dependence of distributed reaction force $r(x, t)$ (blue curve) on position of a wheel load moving with the speed $v = 87.8$ m/s and sleepers' reaction forces R_i (red arrows)

that an average TGV speed $v = 87.8 \text{ m/s}$ (316 km/h) corresponds to the value of $av^2 = 3.8 \cdot 10^{-2}$, which is approximately 1% of $b^2 = 4.05$.

The distributed force $r(x, t)$ can be discretized by a number of concentrated loads R_i , which are spaced apart by distance l (Figure 2.13). The forces R_i are defined as reaction forces of equally spaced sleepers located under the rail instead of the Winkler foundation. Magnitude of R_i can be calculated for each sleeper as an integral of $r(x)$ over the region $[x_i - \frac{l}{2}, x_i + \frac{l}{2}]$, where x_i is the coordinate of a sleeper centre and l is the spacing between adjacent sleepers:

$$R_i = R(x_i) = \int_{-l/2}^{l/2} r(\xi + x_i) d\xi \quad (2.7)$$

Figure 2.13 represents an example of discretization of a continuous function $r(x, t)$ (blue curve) by discrete values R_i (red arrows, with the length equal to the corresponding force magnitude). It is considered that the position of the wheel load coincides with the centre of one sleeper, which is located at $x = 0$.

2.2.5. Moving load of two wheels (the bogie load)

Wheel pairs of all modern trains are always located on bogies. Each bogie contains four wheels (two per rail), while the distance between two wheels on one side of a bogie usually doesn't exceed 2.5-3 m. Thus, in accordance with observations made in the previous section, it can be assumed that the load profile from the first wheel can overlap the load profile from the second wheel.

If the coordinate $x = 0$ in this case coincides with the centre of a bogie, when the value of distributed reaction force $r_b(x, t)$, caused by the combined load signal generated by two wheels, spaced by distance of 3 m (in accordance to TGV train dimensions presented on Figure 2.7), can be calculated as follows:

$$r_b(x, t) = r_1(x - 1.5, t) + r_2(x + 1.5, t) \quad (2.8)$$

where r_1 and r_2 are distributed reaction forces for the first and the second wheels.

Let us consider a variation of a reaction force $R(X(t))$ of a sleeper of interest, caused by a bogie passing over. The force $R(X(t))$ depends on the distance $X(t)$ between centres of the sleeper and the approaching bogie (Figure 2.14). Force vs Time profile calculated for a rail pad is presented in Figure 2.15. In the presented case, time $t = 0 \text{ ms}$ corresponds to

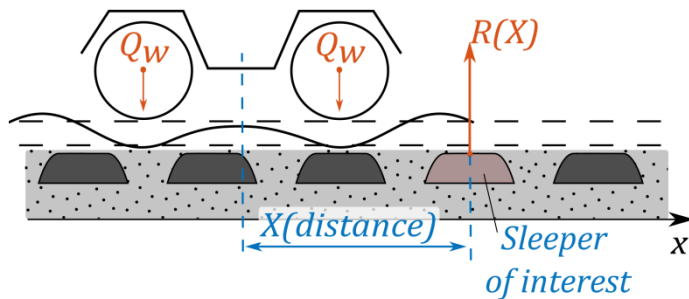


Figure 2.14: Reaction force of a sleeper of interest depends on a distance between centres of this sleeper and approaching bogie

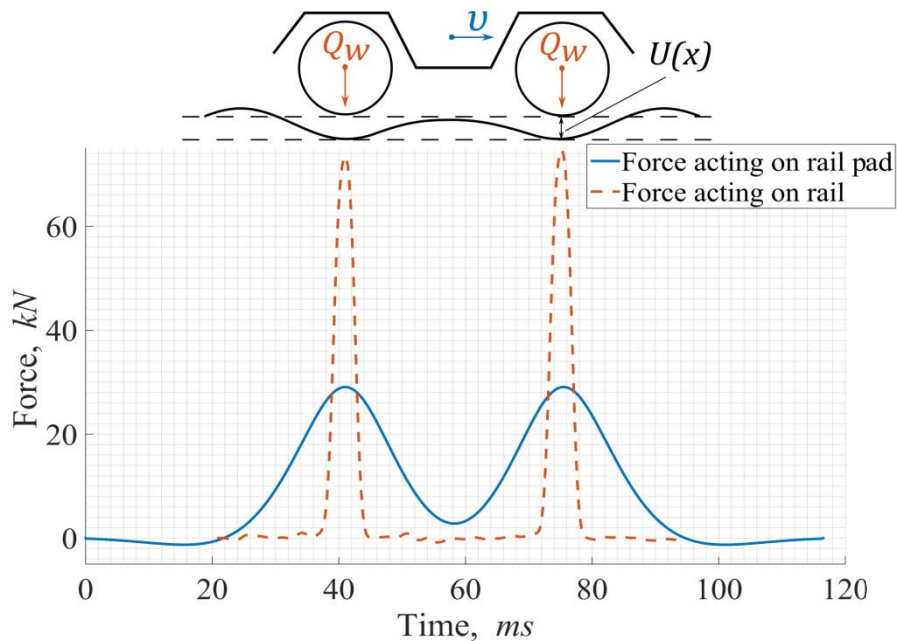


Figure 2.15: Time signals of the forces acting on a rail and a rail pad generated by a bogie passing with the speed $v = 87.8 \text{ m/s}$

$X(0) = 6 \text{ m}$, which is taken as an initial distance between centres of the sleeper and the bogie.

To obtain the final load applied on a rail pad, the dynamic signal presented in Figure 2.15 must be corrected by static preload forces, caused by the weight of a rail (Section 2.2.2) and the clamping force of a fastening system (Section 2.2.3). It can be noted that as well as in the case of the one-wheel load (Section 2.2.4), a rail bends in both negative (opposite to a load direction) and positive directions when the bogie passes over. Bending of a rail in the negative direction leads to a slight unloading of a rail pad below the level of the static preload.

3. Materials and instrumentations

3.1. Materials and specimens

During the work on the presented project, experimental investigations were carried out to study the mechanical behaviour of the elastomeric material of rail pad and the macroscopic behaviour of a rail pad structure.

All specimens were provided by SNCF railway company and were made of a material that is currently used in rail pad production: 27 phr carbon black filled styrene-butadiene rubber (SBR).

Investigation of the material behaviour (Section 4.1 – 4.2) was carried out in compression using cylindrical specimens with a diameter of $25 (\pm 0.1) \text{ mm}$ and height of $20 (\pm 0.1) \text{ mm}$ (Figure 2.16a) and in tension using dumbbell specimens with dimensions described in Figure 2.16b. Incompressibility of the material was verified during hydrostatic compression experiment using cylindrical specimens.

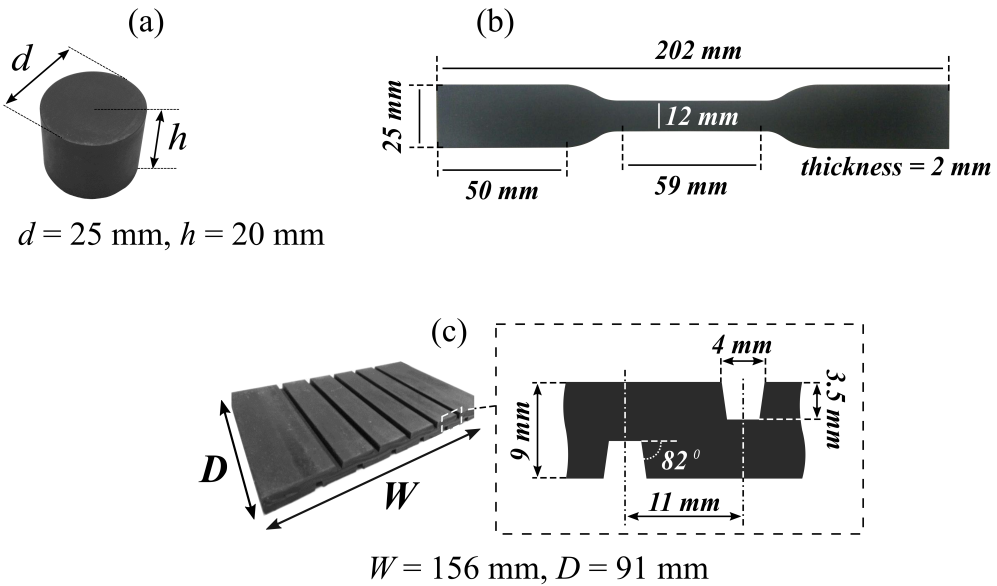


Figure 2.16: Dimensions of: (a) a cylindrical specimen; (b) a dumbbell specimen [112]; (c) a rail pad specimen

Grooved rail pad specimens with dimensions $156 \times 91 \times 9 \text{ mm}$ (Figure 2.16c) were used during the investigation of the mechanical behaviour of the pad structure (Section 5.1). This geometry corresponds to half of the real pad (dimensions $156 \times 182 \times 9 \text{ mm}$) and was chosen in order to reduce sample rigidity.

3.2. Instrumentations (experimental study)

3.2.1. Quasi-static compression/tension experiment

All experimental investigations were carried out on an Instron 5969 testing machine (Instron Ltd, High Wycombe, UK), instrumented with a 50 kN load cell. Force, displacement and deformation data were recorded with a frequency rate of 10 Hz.

Measurements of the strain value were carried out using laser extensometer during tension experiment. The value of strain in compression experiment was calculated as the ratio between applied displacement and the initial height of the specimen. Additionally, laser extensometer was used during experiments on rail pad structure in order to measure the relative vertical displacement of compression plates with increased accuracy. This method was required due to small ($\sim 1 \text{ mm}$) relative displacement of compression plates during the experiment. Digital image correlation (DIC) method was also used for analysis of the rail pad specimen's face deformation (see Section 5.1).

3.2.2. Hydrostatic compression experiment

Hydrostatic compression experiment was performed using hydrostatic chamber presented in Figure 2.17a. Samples of SBR were fixed on a special support (Figure 2.17b), to ensure that the whole surface of the specimen is open for pressure application. The support rig was mounted on a chamber filled with alcohol (which is considered incompressible), and the specimen was located in the centre of this chamber (Figure 2.17a). The pressure in the chamber was increased by displacement of a cylindrical punch (diameter 20 mm) inside the

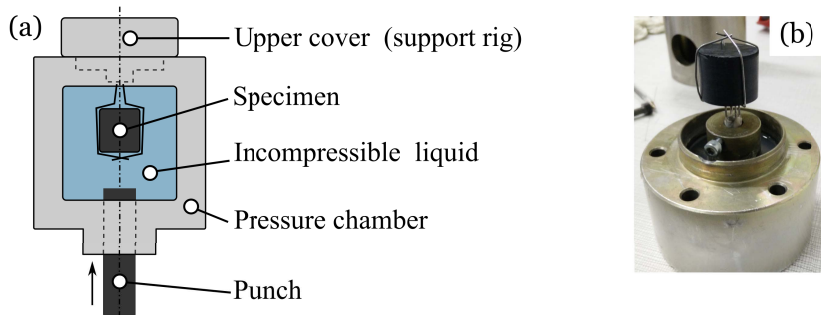


Figure 2.17: Hydrostatic compression experiment testing set: (a) schematic representation of a hydrostatic chamber; (b) specimen on a supporting rig

chamber. Movement of the punch was controlled by a displacement sensor of the testing machine. The pressure was measured by a piezoelectric pressure sensor (Kistler, model 7005, range 60 MPa, the natural frequency of 70 kHz), which was fastened on the inside wall of the chamber.

All experimentations were carried out at a room temperature (25°C).

3.3. Methods of a material model constants set optimization

All functions of material models have been reproduced using MatLab® software. In order to identify constants of proposed models, minimization of the square difference between the model response and the corresponding experimental data was carried out. When the multiple experimental data were used for the model fitting, a sum of square differences was minimized:

$$\min_{C_j \in \Omega} \left[\sum_{i=1}^n (y^i - y_{fit}^i(C_j))^2 \right] \quad (2.9)$$

where C_j are constants, Ω is constraints condition and $i = 1, \dots, n$ is a number of an experimental data set. The minimization problem was solved using *fmincon* function, allowing optimization of nonlinear problems with constraints. Default interior-point minimization algorithm was chosen in accordance with MatLab® documentation. Central form of a finite difference calculation was used in order to increase accuracy.

Two stopping criteria were chosen to control convergence of the optimization function: $TolX = 1e-15$ and $TolFun = 1e-15$ are termination tolerances for the change in the value of constants and objective function respectively.

Initial values of constants C_j were chosen randomly in each optimization run. A constant set was accepted as optimal if it was repeated (to within a 1% relative error) by three independent optimization runs.

4. Modelling of elastomeric material of the rail pad

4.1. Validation of the material incompressibility

It is very common to consider elastomeric materials as nearly incompressible when modelling their mechanical behaviour. In order to verify the incompressibility of the material studied, a hydrostatic compression test was carried out.

Speed of the punch movement (see Figure 2.17b) was equal to 24 mm/min to ensure strain rate of $2 \cdot 10^{-3}\text{ s}^{-1}$. Pressure in the chamber was considered to be uniform due to the quasi-static nature of the experiment. Additionally, the same test was carried out with an empty chamber (with no specimen, chamber filled with alcohol) to evaluate the compressibility of the chamber. A change in volume was considered to be equal to the volume of the punch in the chamber (additional details concerning this hydrostatic chamber can be found in [81]).

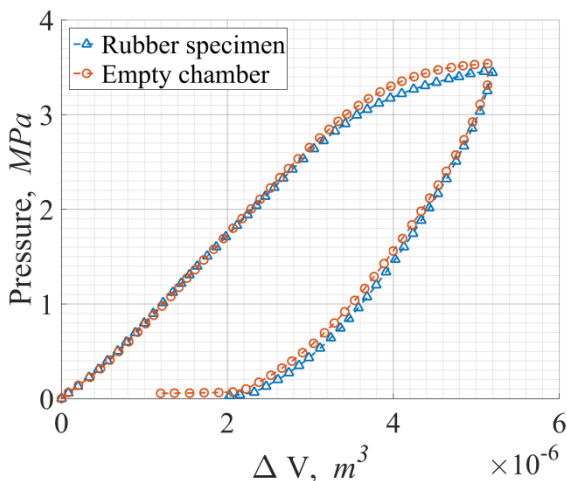


Figure 2.18: Pressure dependences on change in volume during hydrostatic compression experiment

Figure 2.18 shows the evolution of pressure as a function of volume variation during the hydrostatic compression experiment. It can be seen that there is no significant difference between the two curves representing the tests with and without rubber specimen in the chamber.

Hence, the change in volume observed during compression of the SBR specimen is linked only to the compressibility of the experimental chamber. It can then be concluded that the SBR material can be considered as incompressible (Poisson's ratio ~ 0.5).

4.2. Quasi-static compression and tension experiments

Cylindrical and dumbbell specimens were subjected to 2 loading-unloading cycles in uniaxial compression and tension regimes respectively. The first cycle with an increased load magnitude was carried out in order to exclude the influence of the non-destructive Mullins

effect, which was not taken into account in the framework of the present study ([19]). Data obtained in the second loading cycle were used in the following study.

A displacement load was applied with a strain rate of 0.01 s^{-1} (12 mm/min in compression and 60 mm/min in tension). The upper and bottom surfaces of compression specimens were covered with grease in order to reduce the effect of friction, prevent barreling and obtain a more homogeneous stress-strain state in the material. Profiles of the Engineering Stress and Strain vs Time in compression and tension experiments are presented in Figure 2.19. The chosen level of load is sufficient to fully observe nonlinearity of the mechanical behaviour of the material.

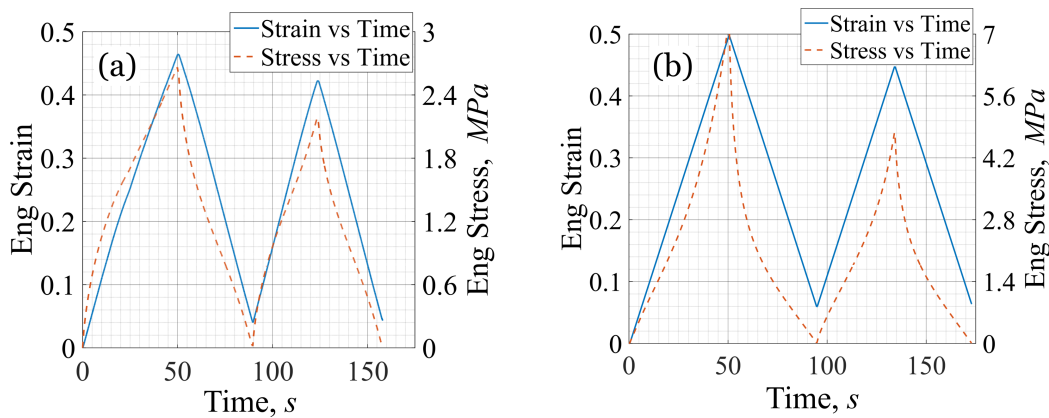


Figure 2.19: Profiles of the Engineering Stress and Strain vs Time in compression (a) and tension (b) experiments

It must be noted that modelling of the strain rate dependent mechanical behaviour of elastomeric materials does not necessarily require experimental investigation at different strain rates: the CI-model explicitly takes into account strain rate dependency (see $d\varepsilon(s)/ds$ in equation (1.29) in Chapter 1). Thus experimental investigations were carried out at only one strain rate.

An accumulation of residual strain due to the Mullins effect leads to a change in the dimensions of the specimen after each loading cycle. These changes must be taken into account when calculating actual strain and stress. Thus, the stretch and stress values in the second loading cycle were calculated with respect to the actual dimensions of the specimen instead of the initial ones.

4.3. Choosing an appropriate hyperelastic model

The list of hyperelastic models reviewed in Chapter 1: Section 2.2 was considered for the present study. First of all, the ability of the hyperelastic models to describe the nonlinear behaviour of the studied material was investigated. Consideration of the uniaxial compression experiment leads to the fact that only σ_{11} has a non-zero value (compression is carried out in the direction \underline{x}_1 of the orthogonal basis $(\underline{x}_1, \underline{x}_2, \underline{x}_3)$). The unknown scalar Lagrange multiplier p in equation (1.5) (Chapter 1) can be excluded using (1.6) and $\sigma_{22} = \sigma_{33} = 0$. Finally, using equation (1.8) and taking $\lambda_1 = \lambda$, the expression for uniaxial engineering stress (used in the process to fit experimental data) can be obtained:

$$P_{11} = \frac{\sigma_{11}}{\lambda} = 2 \left[\frac{\partial W}{\partial I_B} (\lambda - \lambda^{-2}) - \frac{\partial W}{\partial II_B} (\lambda^{-3} - 1) \right] \quad (2.10)$$

As mentioned in Chapter 1: Section 2.1, the hyperelastic model must be consistent with the theory of linear elasticity. Generally, this condition leads to an equation which links model constants and the shear modulus μ of the material at small strains [82] (Table 2.2).

Table 2.2: Constraints ensuring consistency of hyperelastic models with the theory of linear elasticity

Hyperelastic model	Constant constraints according to [82]	Constant constraints used in the present work
1 Neo-Hookean	$2C_1 = \mu$	$3 < 2C_1 \leq 4$
2 Mooney-Rivlin	$2(C_1 + C_2) = \mu$	$3 < 2(C_1 + C_2) \leq 4$
3 Arruda-Boyce	$2C_1 \sum_{i=1}^5 i\alpha_i \beta^{i-1} I_B^{i-1} = \mu$	$3 < 2C_1 \sum_{i=1}^5 i\alpha_i \beta^{i-1} I_B^{i-1} \leq 4$
4 Yeoh	$2C_1 = \mu$	$3 < 2C_1 \leq 4$
5 N th order Ogden's	$\frac{1}{2} \sum_i^N \mu_i \alpha_i = \mu$	$3 < \frac{1}{2} \sum_i^N \mu_i \alpha_i \leq 4$

In the case of linearly elastic materials, the shear modulus can be calculated using Young's modulus E and Poisson's ratio ν of the material ($\nu \approx 0.5$ due to material incompressibility). However, the value of E cannot be strictly identified from experimental data, since the behaviour of the rubbers is nonlinear even at small strains.

Thus, the value of $E = \text{Stress}/\text{Strain}$ was calculated in three points at the beginning, middle and end of the loading part of the experimental curves obtained in tension and compression experiments. A range of obtained values was used instead of a one value for constraining parameters of the models. In this way, a range of $E \in [9, 21] \text{ MPa}$, and therefore $\mu \in [3, 7] \text{ MPa}$, was used, and constraints were expressed in the form of inequalities (Table 2.2). In accordance with [36], satisfying the Hill's stability criterion requires an additional condition to be used for constants of the Ogden hyperelastic model:

$$\mu_i \alpha_i > 0 \text{ (for each } i = 1, \dots, N) \quad (2.11)$$

It was also noted in [36] that not all conditions (2.11) are necessary if the order of the Ogden model $N \geq 3$. However, it was found that relaxing constraints (2.11) at any N (allowing one or more terms to take negative values) makes it impossible to find a unique set of constants.

The results of the fitting procedure obtained for the models from Table 2.2 are presented in Figure 2.20a-c. In order to easily compare models' applicability ranges (in terms of strain values) with strains observed during the finite element simulation of the rail pad structure, the true strain ($\ln(\lambda)$) measure was used in the presented plots. The goodness of fit was measured using the coefficient of determination [83], denoted by R^2 and calculated as follows:

$$R^2 = 1 - \frac{\sum_{i=1}^N (y^i - \bar{y})^2}{\sum_{i=1}^N (y^i - \bar{y})^2} \quad (2.12)$$

where $\bar{y} = \frac{1}{N} \sum_{i=1}^N y^i$ is an average value of experimental response. The coefficient of determination generally ranges from $-\infty$ (bad fit) to 1 (perfect fit). However, the value of $R^2 = 0$ already indicates, that the model response is no better than the strait line $y = \bar{y}$.

Figure 2.20a presents the results of fitting polynomial-based models, such as the Neo-Hookean, the Mooney-Rivlin and the Yeoh, to experimental data. It can be seen that the Mooney-Rivlin and the Yeoh models provide the best fit. Mooney-Rivlin model has a better fit in the tension region, however, it becomes unstable at compressive strains less than -0.6 : the curve changes its curvature and an absolute value of the stress starts decreasing with an increase in strain, which is physically incorrect.

Fitting the Ogden model of orders $N = 1,2,3$ leads to the same solution to the optimization problem: $[\mu_1]_{N=1} = [\mu_1 + \mu_2]_{N=2} = [\mu_1 + \mu_2 + \mu_3]_{N=3}$ and $\alpha_i = \alpha$ for all $i = 1 \dots N$. The coefficient of determination in this case is equal to 0.987, which is worse than results of the Mooney-Rivlin and the Yeoh models. Relaxing of the constraints set (2.11) provides a better solution to the problem (for $N = 3$), although, as mentioned above, it would be non-unique.

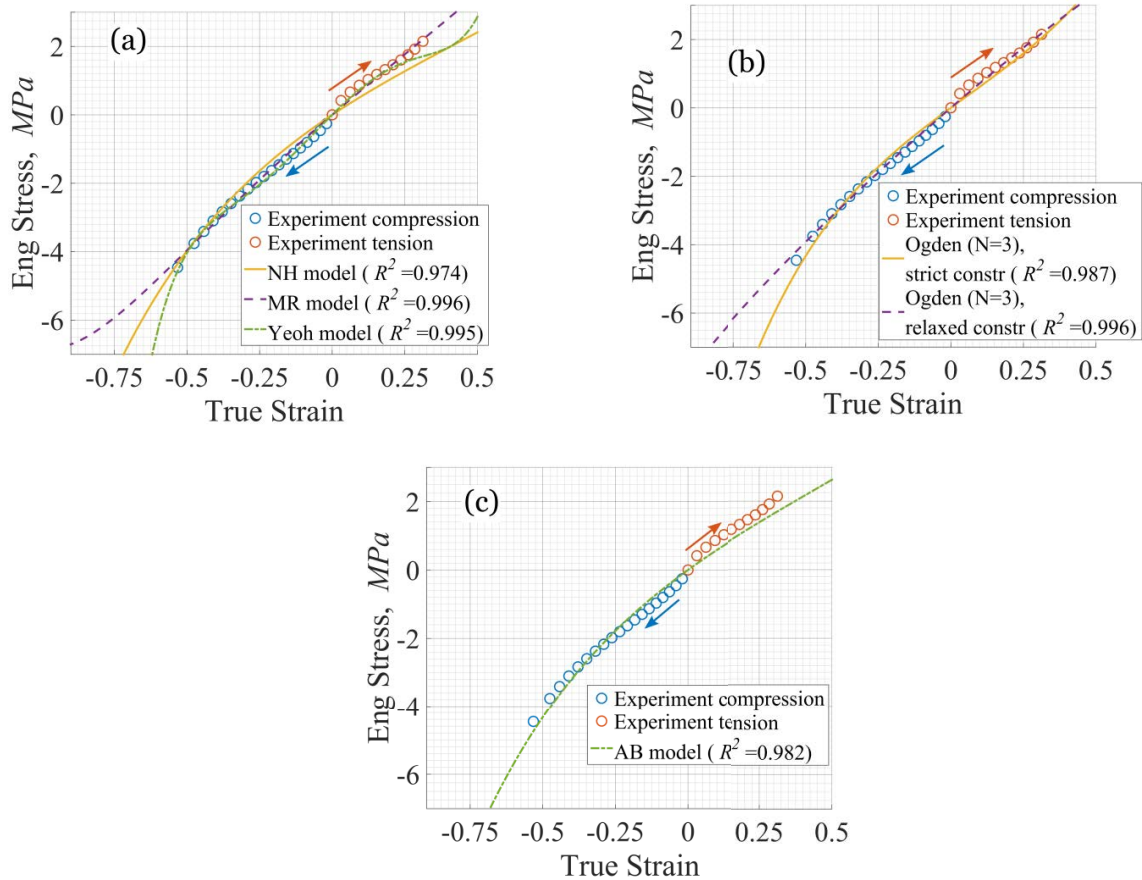


Figure 2.20: Fitting of different hyperelastic models to experimental data: (a) Neo-Hookean, Mooney-Rivlin and Yeoh models; (b) Ogden models with strict and relaxed condition (Eq. 2.11); (c) Arruda-Boyce model

Results of fitting the 3rd order Ogden model with strict and relaxed condition (2.11) are presented in Figure 2.20b. Fitting of the Arruda-Boyce model resulted in the value of R^2 equal to 0.982 (Figure 2.20c).

It was found that all considered hyperelastic models, except for the Yeoh model and the Ogden model with relaxed conditions (2.11), are inaccurate in fitting the beginning of the experimental curves (*i.e.* at strains in the range from -0.2 to 0.2) and to represent its S-shaped behaviour.

Based on the data presented in this paragraph, Yeoh hyperelastic model was chosen to describe hyperelastic phenomena in the studied material as it provides satisfactory prediction capabilities along with a stable and unique set of constants and a relatively simple mathematical expression.

It was shown in works of Marckmann and Verron [23] and Steinmann *et al.* [24] that the constant set ensuring an acceptable prediction in one deformation mode (say uniaxial tension) can provide less accurate and sometimes unacceptable results for complementary deformation modes (say equibiaxial and shear). Thus, verification of model capabilities to predict the mechanical behaviour of a rubber material in various deformation modes (uniaxial, biaxial, shear) can be carried out for the chosen hyperelastic model (*e.g.* [34], [35], [84]). Alternatively, to increase the accuracy of a model, certain authors perform complex fitting procedures, taking into account experimental data from different experiments. However, both approaches require additional experimental investigation, which can be time-consuming as well as cost intensive, while does not guarantee the success (convergence) of the fitting procedure. In accordance with Steinmann *et al.* [24], an effective hyperelastic model must allow the determination of its parameters for a specific material from fitting few simple experiments. It was also shown in [24] that the Yeoh hyperelastic model, fitted to one of the three experimental data sets (uniaxial tension, equibiaxial tension and pure shear), yields qualitatively and quantitatively reasonable prediction results for complementary deformation modes. Moreover, it was concluded in Yeoh [85] that data from any single deformation mode can be sufficient to characterize hyperelastic models expressed in terms of the first strain invariant I_B only. By this and the fact that the uniaxial loading was considered as the main deformation mode for the rail pad, additional experimental investigation for the rubber material of the rail pad was not performed.

4.4. Constants identification of the visco-hyperelastic model (CI-model)

In accordance to the discussion presented in Chapter 1: Section 4.3, optimization of the CI-model was carried out using QS-compression and tension experimental data without separation of long-term and relaxation behaviour of the material.

Equation (1.38) from Chapter 1 has been rewritten for the case of uniaxial loading using (2.10), recalling that decomposition of a stress tensor on deviatoric and hydrostatic parts ($[\cdot]^D = [\cdot] - \frac{1}{3} \underline{\underline{1}} : [\cdot]^H$) and keeping in mind that $\sigma_{22} = \sigma_{33} = 0$ (used to determine the constant p). The strain energy potential of the Yeoh hyperelastic model does not depend on II_B (see equation (1.12) in Chapter 1: Section 2.2.1), therefore the corresponding part in (2.10) is equal to zero. It must be noted that relative moduli $g_\infty = G_\infty/G_0$ and $g_i = G_i/G_0$ are used in the following equations instead of G_∞ and G_i used previously in (1.29) in Chapter I. Relative

moduli must satisfy the relation $g_\infty + \sum_{i=1}^N g_i = 1$. As in the hyperelastic models case (Section 4.3), an expression for engineering stress $P_{11}(t)$ was used during the process of least square fitting to the experimental data:

$$P_{11}(t) = \frac{\sigma_{11}(t)}{\lambda(t)} = 2 \frac{\partial W(t)}{\partial I_B} (\lambda(t) - \lambda^{-2}(t)) - \sum_{i=1}^N \frac{g_i}{\tau_i} \int_0^t \frac{\partial W(t-s)}{\partial I_B} Q(t-s) e^{-s/\tau_i} ds \quad (2.13a)$$

with

$$Q(t-s) = \frac{2}{3} \{ 2\lambda(t)[1 - \lambda^{-3}(t-s)] - \lambda^{-1}(t)[1 - \lambda^3(t-s)] \} \quad (2.13b)$$

$$\frac{\partial W(t)}{\partial I_B} = \sum_{i=1}^3 i C_i (\lambda^2(t) + 2\lambda^{-1}(t) - 3)^{i-1} \quad (2.13c)$$

Additionally, in order to ensure consistency with the theory of linear elasticity the following constraint inequality (by analogy with inequalities in Table 2.2 for hyperelastic models) was used:

$$\mu_0^{\min} g_\infty < 2C_1 g_\infty \leq \mu_0^{\max} g_\infty \quad (2.14)$$

where μ_0 and $\mu_\infty = \mu_0 g_\infty$ are the instantaneous and long-term shear moduli of the material in the reference configuration S_0 (see Figure 1.12 in Chapter 1) and $\mu_\infty \in [\mu_\infty^{\min}, \mu_\infty^{\max}]$. The range of values of $\mu_\infty \in [1.9, 2.3]$ was chosen for consistency with the intermediate, pure hyperelastic state of the material (see Chapter 1: Section 4.1 and equation (1.39)) using the same approach as for the hyperelastic model in Section 4.3. A total of 5 constants were identified by the least-square fitting process (Table 2.3).

Table 2.3: Constants of the CI-model identified by the least-square fitting process

Constant name	C_1 [MPa]	C_2 [MPa]	C_3 [MPa]	g_1 [MPa]	τ_1 [s]
Value	2.5264	-0.9177	0.4711	0.5688	2.635

The mechanical behaviour of the adjusted CI-model is presented in Figure 2.21a. It can be seen that the CI-model with the first order Prony's series provides sufficient conformity between model and the experimental data. The best response of the model can be found in the range of strains between -0.6 and 0.2. The quality of prediction starts to fall outside of this band, which is especially true for tension. Additionally, the pure hyperelastic response of the CI-model, as discussed above, can be calculated using (2.10) multiplied by the long-term relative shear modulus g_∞ . The long-term response of the model is presented by the dashed line in Figure 2.21a.

Efforts to increase the accuracy of the model calibration by increasing the order of Prony's series did not provide any improvement. Figure 2.21b shows convergence curves of successful optimization runs with the Prony's series order $N = 1, 3$ and 10 . It is seen that in all studied cases the objective function tends to the same resulting value. Moreover, it was found that an optimal constants set obtained for $N = 1$ is a linear combination of constants obtained for $N = 3$ and $N = 10$.

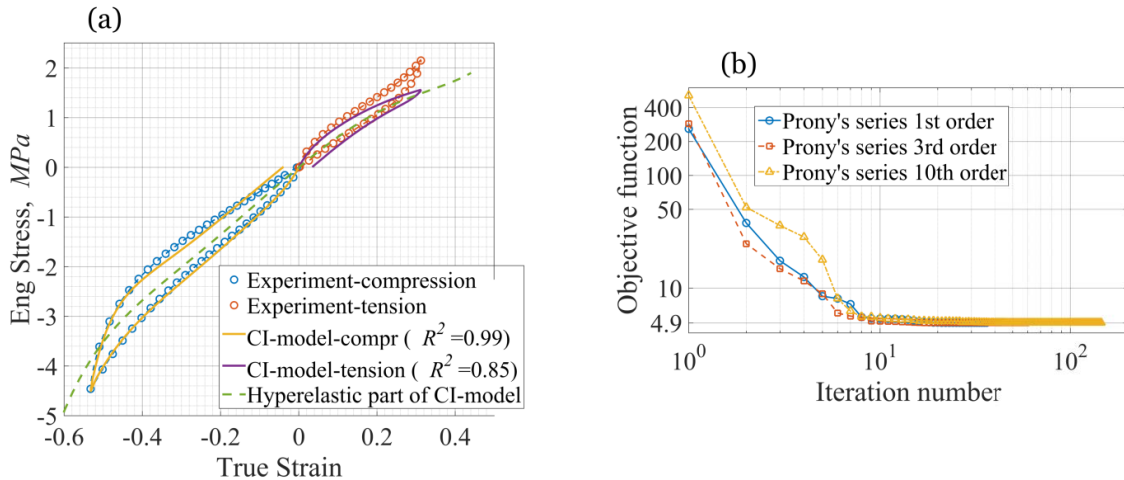


Figure 2.21: (a) Comparison between experimental data and prediction of fitted CI-model;
(b) convergence curves for different values of the Prony's series order

5. Investigation of the rail pad structure

5.1. Experimental investigation of the rail pad structure

The possibility of the described and adjusted CI-model to successfully predict the mechanical behaviour of a rail pad structure under compressive loads can be validated using the corresponding experimental investigations. Firstly, rubber rail pad with the geometry described in Section 3.1 (Figure 2.16c) was preloaded up to 100 N to ensure contact between specimen and compression plates. During the experiment, rail pad was subjected to a compressive load up to 45 kN in the first cycle and up to 40 kN in the second cycle (which corresponds to half of the common on-track wheel load). The first loading cycle with an increased load magnitude was carried out to exclude the Mullins effect influence on the material behaviour and data obtained in the second cycle were used. The speed of load was equal to 6 mm/min, which corresponds to a macroscopic strain rate of 0.01 s^{-1} . The compressive load was applied through rectangular steel plates measuring $150 \times 200 \times 18$

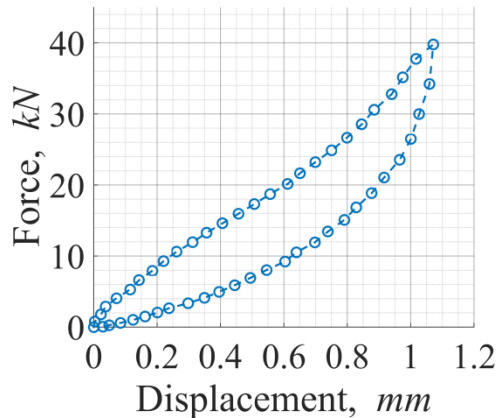


Figure 2.22: Force vs Displacement curve obtained during QS compression experiment of a rail pad in the second cycle

mm³. According to the norm on rubber rail pad testing [79], two pieces of abrasive cloth must be placed between specimen and steel plates. It was found that abrasive paper can be damaged during cycling, and this fact can influence the experimental results. Thus, to avoid this problem, the surfaces of the compression plates were roughened by machine treatment. The experimental procedure was carried out for three identical specimens in order to verify repeatability of results. The Force vs Displacement curve commonly obtained during the experiment is shown in Figure 2.22: Force vs Displacement curve obtained during QS compression experiment of a rail pad in the second cycle. It can be seen that the structure exhibits sufficient nonlinearity as well as energy dissipation (hysteresis loop). The total compression displacement was equal to 1.08 mm (12% of the macroscopic strain).

One side face of the specimen was covered with a speckle pattern and tracked by a video camera (with image acquisition frequency of 10 Hz). Vic-2D™ software (Correlation Studios, Columbia, SC 29063 - USA) was used to calculate the displacement field on the surface of the specimen. Results from 2D DIC were used in the finite element model validation process and can be found in Section 5.2.

5.2. Description of the rail pad FE model

Finite element simulations of the experiment described in Section 5.1 were carried out. For this purpose, 2D and 3D models of the rail pad specimen have been developed in ABAQUS® software. According to the symmetry of the pad geometry, the computational time was significantly reduced by modelling only half of the 2D models and a quarter of the 3D structures (Figure 2.23a-b).

A 3D model representing the exact geometry of half of the rail pad geometry was first used to verify the CI-model, adjusted in Section 4.4. The capabilities of simplified finite element models were examined: 2D approaches were verified using plane strain and plane stress models of the problem studied. The influence of grooves on the mechanical behaviour of the rail pad was also studied by an additional finite element simulation using a 3D grooveless model. 8-node linear brick elements with reduced integration (C3D8RH) were used in 3D models of the rail pad. A total of 205482 elements for the full structure model and 23184 for the simplified, grooveless model were used. 8839 4-node bilinear square elements with

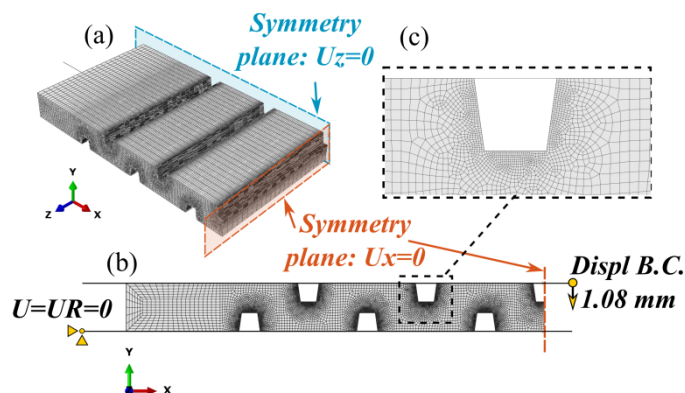


Figure 2.23: 3D and 2D FE models of the rail pad (a-b); planes of symmetry (a-b); boundary conditions applied on rigid compression plates (b); mesh refinement near groove (c)

reduced integration (CPE4RH and CPS4R) were considered in 2D plane strain and plane stress models. In the full-structure 3D model, and all the 2D models, special attention was paid to the refinement of the mesh near the grooves (Figure 2.23c): in these regions, the material exhibits high deformations, which put the specimen into self-contact and contact with compression plates.

A material model, adjusted in Section 4, was used to represent the rubber material of a rail pad. Compression plates were modelled as analytically rigid. The bottom compression plate was fully constrained in displacement ($U = 0$) and rotation ($UR = 0$). Vertical displacement was applied on the top plate in order to simulate loading and unloading of the rail pad (Figure 2.23b). Total displacement of the top plate was equal to 1.08 mm, and total time for the plate to descend was 10.8 s (therefore compression speed was equal to 6 mm/min).

According to the ABAQUS® Analysis User's Manual [86], quasi-static problems can be simulated using explicit or implicit dynamic solvers. The explicit dynamics procedure was originally developed to model high-speed impact events with consideration of mass and inertia effects. Thus, modelling a quasi-static event in its natural time period can require millions of time increments to complete simulation, and is therefore computationally inefficient. Finite element problems were therefore calculated using the implicit dynamic solver. Simulations were carried out on a Dell PowerEdge R820 server equipped with 6 CPUs Intel(R) Xeon(R) E5-4617 @2.90GHz and 64 GB of RAM. Solving a full 3D geometry model took approximately 16 hours.

5.3. Results of FE simulation using the full-structure 3D model

The value of friction coefficient (Coulomb friction model was used in ABAQUS® [87]) between compression plates and rail pad, was optimized comparing the macroscopic response of the structure during the experimental investigation and FE simulation. Figure 2.24 presents Force vs Displacement curves obtained in the experiment and calculated by finite element simulation using different values of friction coefficient (in the range of 0.17 to 0.3). It is seen in Figure 2.24 that the best prediction of the experimental data (especially on the loading part of the curve) can be obtained if the value of the friction coefficient is equal to 0.225. The static stiffness calculated using experimental and numerical data at 1.08 mm displacement, in this case, is equal to 37200 kN/m and 37100 kN/m respectively (error ~ 0.2 %).

The displacement field in the studied structure does not depend on the material model and its parameters, yet it does depend on the friction between the specimen and the compression plates. Thus, the chosen value of friction can be validated by comparing displacement fields on the specimen's side face obtained in simulation and experiment. Figure 2.25a-b presents displacement field maps in a horizontal direction (load is applied in a vertical direction) extracted by the DIC method from experimental data (Figure 2.25b) and calculated using the finite element method (Figure 2.25a).

The same colour map legend is used to represent results of both the experiment and the FE simulation. It can be seen that the maps are in good agreement both qualitatively and quantitatively. During compression experiment, the rail pad structure undergoes considerable barreling on the specimens' edges. The vertical displacement field was not taken into account during this study, due to the inability of the 2D DIC method to recorder this information, when the barreling takes place.

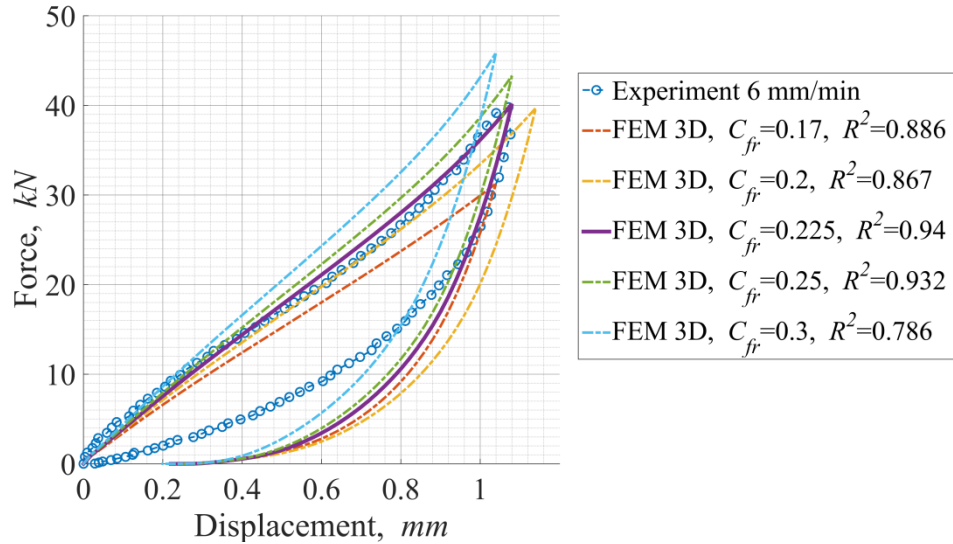


Figure 2.24: Force vs Displacement curves obtained in the experiment and calculated by FE simulation using values of friction in the range of 0.17 to 0.3

The high accuracy of the model prediction was reached on the most of the Force vs Displacement curve. However, it can be seen in Figure 2.24 that the subsequent unloading from 0.94 mm is followed by a gradual increase in the discrepancy between experiment and numerical data, which results in accumulation of a larger residual displacement value: 0.2 mm in FEM against 0.04 mm in the experiment (which corresponds to 2.2% and 0.4% of macroscopic strain respectively). This behaviour of the FE model can be connected with the overestimation of the residual strain value by the CI-model observed in Section 4.4 of the present chapter.

Rail pads with a grooved geometry are commonly used on railways to reduce the rigidity of this type of structure. It makes the use of harder rubbers possible, which are more resistant to ageing and fatigue processes. However, during uniaxial compression, grooves aligned in the Z-direction allow the material to expand freely in the X- and Y-directions. This creates zones of high stress-strain concentrations near the grooves. Finite element approach provides the possibility of a precise study of stress/strain distribution in the structure, allowing visualization and measurement of these concentrations. Maps of true strains, calculated in the direction of loading (Y-direction) are shown in Figure 2.26. Four different cross-sections

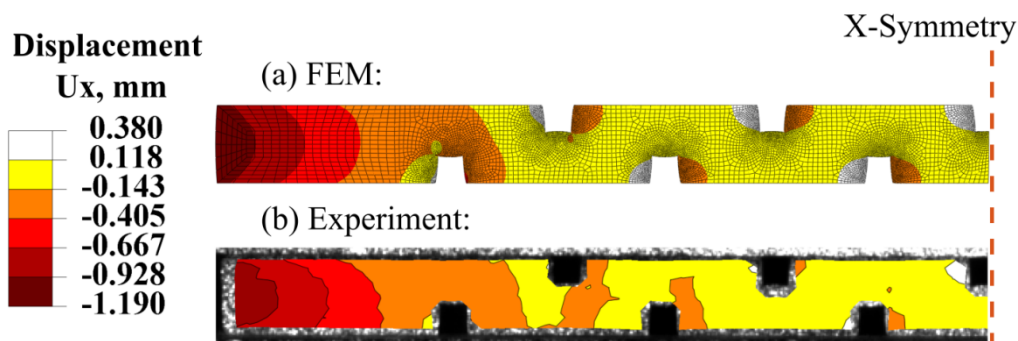


Figure 2.25: Comparison between displacement maps in horizontal direction obtained in FE simulation (a) and experiment (b)

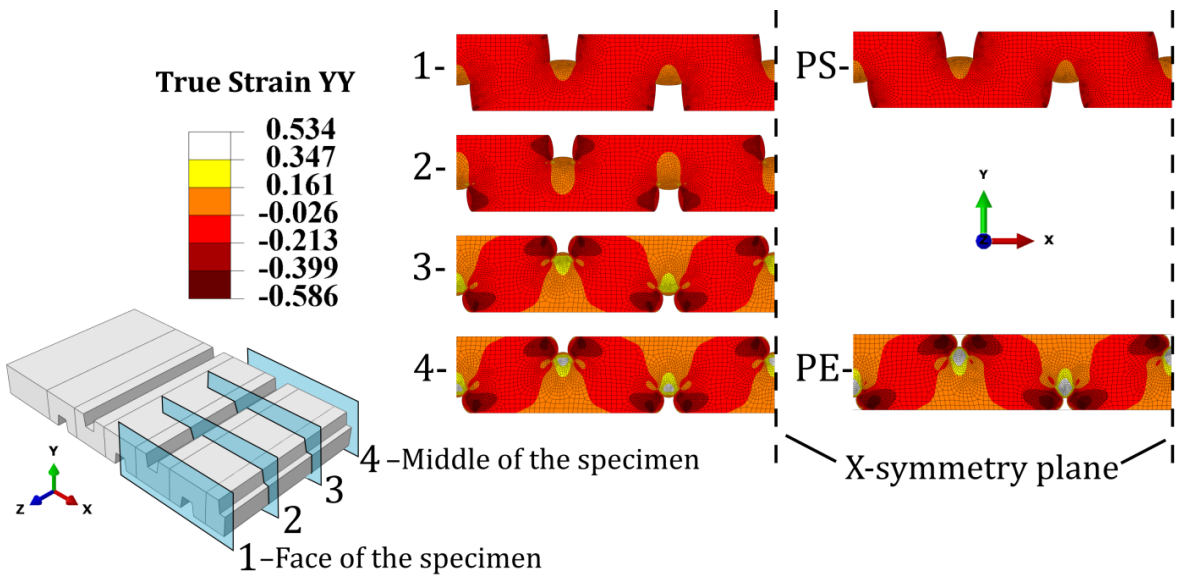


Figure 2.26: True strain YY -field calculated in different cross-sections in the Z-direction (from face to the middle of the specimen) and true strain fields obtained in 2D plane strain (PE) and plane stress (PS) models. Rail pad is under compressive displacement of 1.08 mm

in the Z-direction are presented, from face to the middle of the specimen. The strain field is highly inhomogeneous in the Z-direction: it has almost uniform distribution on the face of the rail pad (slice 1 in Figure 2.26), whereas high levels of strain can be found near the grooves in the middle of the sample (slice 4 in Figure 2.26).

Figure 2.27 presents the true shear strain (XY) map as well as maps of von Mises and hydrostatic stresses calculated at the cross-section located in the middle of the specimen. It can be seen that shear strain (XY) varies from -0.27 to 0.28 in most of the rail pad structure, however, in stress-strain concentration zones these values increase to -0.81 and 0.82. The shear component of the total strain is almost twice as high as uniaxial strain component (see Figure 2.27) and therefore can have a stronger influence on the macroscopic behaviour of the rail pad. However, it is unlikely that this fact can influence the accuracy of the FE model as the Yeoh hyperelastic material model was chosen (see discussion in Section 4.3 of this Chapter).

The von Mises stress map presented in Figure 2.27 shows the contribution of the deviatoric part of the stress to the stress state of the material in the studied region. It is seen that high concentrations can be found near grooves (~6 times higher than average in the section), which can consequently result in degradation of material characteristics in these regions. Optimization of rail pad geometry can reduce stress concentrations and extend its lifetime.

It was found that hydrostatic stress ($p(t)$ in equation (9)) has an almost homogeneous distribution in the specimen's centre (varies between 4 and 5.5 MPa). Concentration zones (values up to 8.5 MPa) can be found near grooves, where self-contact and contact with compression plates are established. Optimization of the rail pad geometry can reduce these concentration zones and increase the lifetime of rail pads. The relatively small size of concentration zones in the studied case allows neglecting their influence on the macroscopic response of the structure.

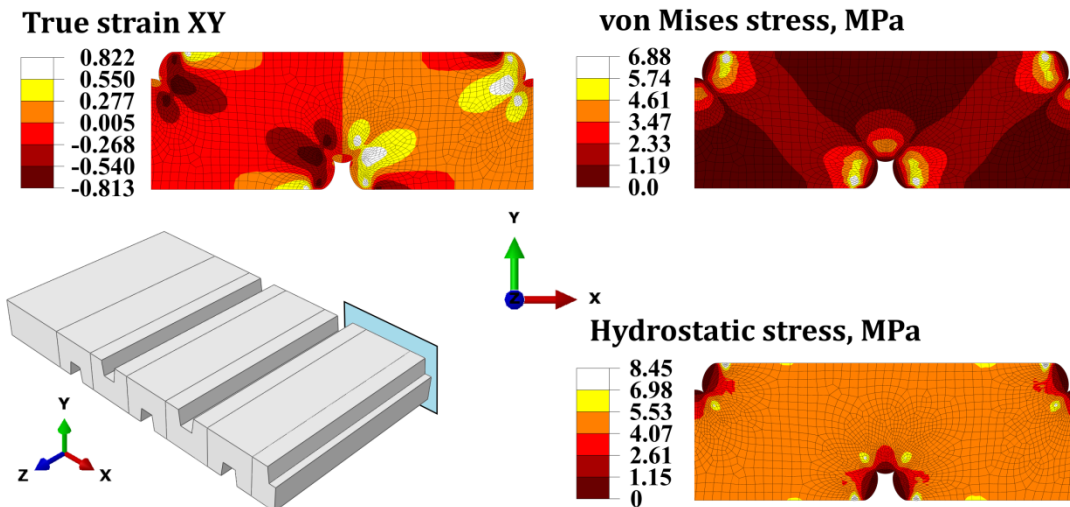


Figure 2.27: True shear strain (XY), von Mises stress and hydrostatic stress maps calculated at the cross-section located in the middle of the specimen. Rail pad is under compressive displacement of 1.08 mm

As mentioned above, one of the most important properties of rubber for industrial applications is its ability to dissipate energy. The value of the energy dissipated in one loading cycle can be calculated as a surface area inside the Force vs Displacement loading-unloading loop. Using experimental data, it was found that the rail pad specimen dissipated 9.45 J during the loading cycle. Simulation of the compression experiment with the full structure 3D model resulted in 12.96 J of dissipated energy, which is 37.5 % higher than the experimental value. This difference is mostly caused by a mismatch between FE model and experimental data on the unloading part.

5.4. Results of FE simulation using simplified model approaches

Figures 2.28a-b presents a comparison of simulation results, obtained using simplified numerical models of the rail pad, with experimental data. It was found that the 2D plane strain approach results in a higher value of force, which is twice that measured in the experiment (Figure 2.28a). Conversely, using a 2D plane stress approach leads to a very soft response of the structure (Figure 2.28a).

These results can be easily explained by comparing strain fields in 3D and 2D models. Figure 2.26 shows that the strain field in the 2D plane stress model (PS) matches that on the face of a 3D model. On the other hand, the strain field in the 2D plane strain model (PE) coincides with the middle cross-section of the 3D model. The plane stress case corresponds to the unconstrained 3D case, which is very similar to the stress-strain state on the face of the specimen. Conversely, the portion of material located in the middle of the specimen is compressed in the Z-direction from in front and behind. This stress-strain state is very similar to that in the 2D plane strain approach.

Results of the simulation using the 3D grooveless model are presented and compared with experimental data in Figure 2.28b. It can be seen that the 3D grooveless model of a rail pad shows very stiff behaviour: the force at the maximum value of compressive displacement is three times greater than in the experiment. As mentioned above, the existence of grooves on the rail pad structure obviously results in a rather softer response.

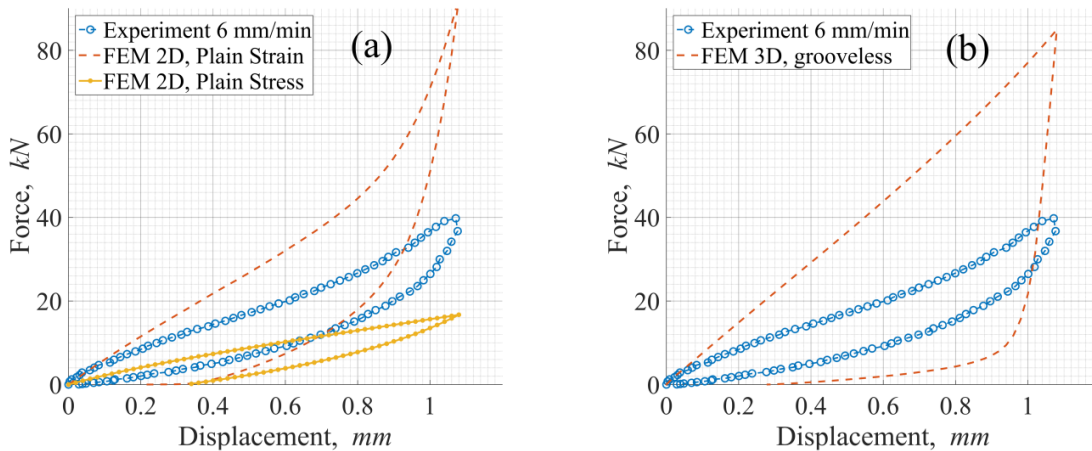


Figure 2.28: Comparison between experimental data and response from FE model of a rail pad: (a) 2D plane strain and plane stress; (b) 3D grooveless

6. Simulation of the rail pad subjected to repetitive load

The mechanical behaviour of a rail pad subjected to the loading regime common for a railway track was studied numerically using the finite element model proposed in Section 5 and the Force vs Time loading profile defined in Section 2.2 of the present chapter. Comparison between rail pad compression displacement data obtained *in-situ* experimentally and using FEM approach allows to study capabilities of the FE model to predict the dynamic behaviour of a rail pad structure.

6.1. FE simulation results

Let us recall that in the previous sections the mechanical behaviour of a rail pad was studied experimentally and numerically using only a half of the real rail pad geometry ($156 \times 91 \times 9$ mm 3 instead of $156 \times 182 \times 9$ mm 3). In order to compare the mechanical behaviour of a finite element model of the pad with *in-situ* experimental data, a numerical model of the whole pad was developed.

The Force vs Time loading profile, identified on the base of *in-situ* data (see Section 2.2) was applied to the rail pad structure through one static and one dynamic steps. In the first step, static preload of the fastening system and the weight of a rail were applied. It was found that installation of a rail and the “Nabla” fastening system results in the force $F_{pr} = F_{cf} + F_r = 17.3$ kN.

It must be highlighted that the clamping force of the fastening system is applied by tightening “Nabla” clip towards the sleeper. This means that after the target force (tightening torque) is reached, the corresponding compression displacement d_{cd}^{nabla} applied on a rail pad remains constant. This results in relaxation of the applied force with time due to mechanical properties of elastomeric material of a rail pad. Thus, it can be assumed that on a real railway track the dynamic load signal of a train is acting on a fully relaxed rail pad structure. Thus,

the first static step was applied in the way to ensure relaxed the initial condition of the numerical specimen after preloading and before application of the dynamic load signal (additional information on this concern can be found in Appendix B).

Figure 2.29a presents the Force vs Time curve of the dynamic impact, applied to the numerically studied structure in the second step, and Displacement vs Time curve obtained as a result of FE simulation. It is seen that the symmetry of the input signal relative to its centre is not repeated for the output signal: the second peak on the Displacement vs Time curve reaches higher magnitude than the first one (0.18 mm against 0.2 mm); additionally, significant value of a residual deformation can be found after unloading ($\sim 20\%$ of a peak displacement magnitude).

The Compression displacement vs Time curve obtained from FE simulation results (d_{cd}^{FEM}) and the averaged *in-situ* experimental curve (d_{cd}^{exp}) are compared in Figure 2.29b. It is seen that a sufficient qualitative correspondence between experimental and numerical results was established: by means of peaks magnitudes and the general evolution of the variable as a function of time. However, few points of criticism for the results of FE simulation have to be mentioned. Firstly, in contradiction to the experimental data, the numerical value d_{cd}^{FEM} grows with different slope and slightly underestimates value of d_{cd}^{exp} at the first peak (10 % lower than the measured *in-situ*). These differences are most likely connected with simplifications of the chosen analytical approach (in reality additional loads, such as sprung mass of cars, imperfections of the wheel-rail contact zone, etc., contribute to the value of studied variable), as well as with uncertainties linked to the choice of constants for the railway track (track stiffness, rail modulus, etc.) and *in-situ* measurements (different train speeds, uncertainty of sensors, etc.). Application of a more advanced approach for the calculation of a force vs time profile (*e.g.* as in [88]) can sufficiently improve the model prediction. Secondly, overestimation of the residual compression displacement at unloading (observed in Section 5.3) leads to overestimation of the value of d_{cd} at the second peak.

Accepting the considered model simplifications, approximations and presented sources of uncertainties it can be concluded that, in general, the FE model successfully predicts the

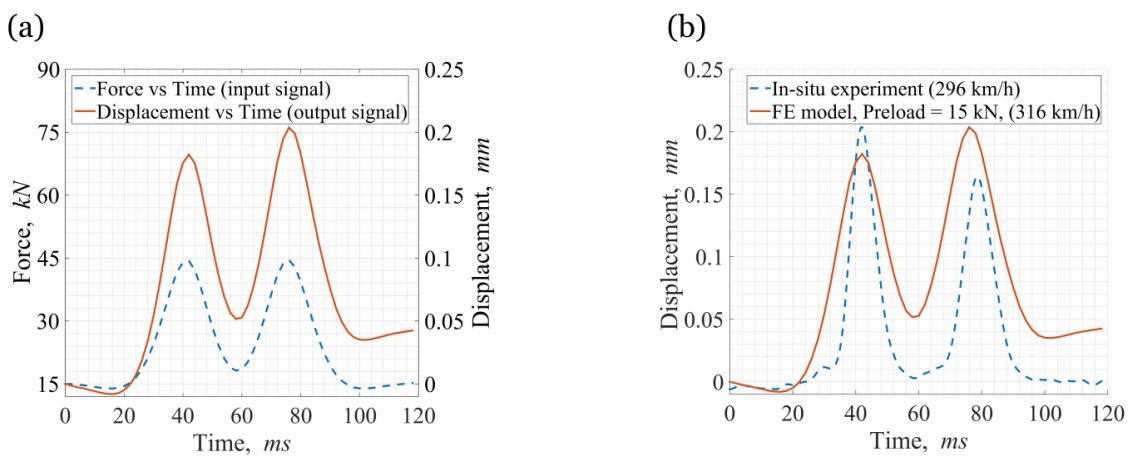


Figure 2.29: Force vs Time curve of a dynamic impact, applied on the numerically studied structure, and Displacement vs Time curve obtained as a result of FE simulation (a); and comparison between dependences of the compression displacement value on time obtained from FE simulation results and by averaging *in-situ* experimental data (b)

behaviour of a rail pad structure subjected to a dynamic load of a passing train.

It can be finally concluded that the CI-model identified using data from the uniaxial experiment at QS strain rate only can successfully predict the global response of a rail pad structure at both QS and dynamic loading rates. Thus, the presented approach can be used for the precise study of the macroscopic behaviour of a rail pad structure at different loading conditions (different preload, varying load rates and frequencies).

7. Conclusions to Chapter 2

The aim of the present chapter was to develop a finite element model, capable to predict the nonlinear behaviour and dissipative properties of a real rail pad structure, subjected to compressive load. Possible ways to simplify the process of the model development were also covered and discussed.

The material behaviour of the rail pad was modelled using a visco-hyperelastic model of the convolution integral type. A set of experimental investigations was carried out in tension and compression using specimens of the material studied in order to: 1) verify consideration of the material incompressibility; 2) choose an appropriate material model; 3) identify the material model constants.

It was shown that the number of experimental investigations of the material behaviour can be reduced to only QS uniaxial tension-compression experiments. First of all, experimental measurements of a rail pad compression displacement carried out *in-situ* by the engineering department of SNCF railway company, allow to conclude that the macroscopic strain rate ($\dot{\lambda}$) of a compressive load does not exceed a quasi-static values of $1-2 \text{ s}^{-1}$. This and the fact the CI-model explicitly takes into account strain rate dependency (by the $d\varepsilon(s)/ds$ term in its formulation), allow to consider only one quasi-static strain rate during experimental investigation, which significantly decreases the complexity of the modelling process. Secondly, in accordance to [24] the Yeoh hyperelastic model yields qualitatively and quantitatively reasonable prediction results for the complementary deformation modes (say equibiaxial tension and pure shear), while fitted using one type of experimental data (say uniaxial tension/compression). Thus, additional experimental investigation of the rubber material of the rail pad (besides uniaxial tension/compression) was not considered.

Finite element analysis of the rail pad specimen (representing half of a rail pad structure) subjected to a quasi-static compressive load was carried out using 3D (grooved and grooveles), 2D plane strain (2D PE) and 2D plane stress (2D PS) approaches. Results of the finite element simulations were compared with corresponding experimental observations in terms of global force-displacement response and displacement maps on one side of the specimen.

Comparison between experimental data and numerical results, obtained using grooved 3D model has shown limitations of the model to predict dissipative properties of the real specimen. It was found that the observed discrepancy can be caused by a poor prediction of a residual compression displacement by the FE model (2.2% of the macroscopic strain against 0.4% in the experiment). However, comparison on the basis of the overall macroscopic behaviour has shown sufficient conformity between Force vs Displacement curves obtained during experiment and numerical simulation (the coefficient of determination $R^2 = 0.94$).

Moreover, it must be highlighted that prediction of the stiffness of the studied specimen resulted in error of less than 1 %.

Compression of the rail pad structure leads to stress-strain concentration zones near the grooves. Stress and strain values in these regions are up to four times higher than the corresponding values in the rest of the volume of the structure. It was also shown that uniaxial compression of a grooved rail pad structure leads to the generation of high shear strains in the material. The shear component of the total strain is almost twice as high as uniaxial tension or compression and therefore can have a strong influence on the macroscopic behaviour of the rail pad. It was assumed that prediction errors observed during analysis of the macroscopic behaviour of the rail pad model can be also connected with the existence of high shear strains, while shear experimental data was not used during material model adjustment.

The importance of taking into account the whole 3D geometry of a rail pad structure when modelling its mechanical behaviour has also been studied. It was shown that using of simplified FE models leads to high overestimation (2D plane strain and 3D grooveless models) or underestimation (2D plane stress model) of the rail pad mechanical behaviour.

In the final part of this chapter capability of the proposed FE model to predict the macroscopic mechanical behaviour of a real rail pad subjected to a complex dynamic load signal was studied. The loading signal (Force vs Time), applied for the FE model of the rail pad, was calculated using analytical approach and *in-situ* experimental data of a wheel load, provided by Direction Ingénierie & Projets of SNCF company. Obtained results of the compression displacement were compared with the corresponding data of *in-situ* experimental measurement. It was shown that the FE model, developed in this Chapter, is capable to describe the dynamic behaviour of a rail pad structure to within the error of prediction of the residual compression displacement. Adaptation of a more advanced model capable to describe the nondestructive Mullins softening effect (*e.g.* [89]–[91]) and elimination of uncertainties linked with the choice of constants and experimental measurements can, probably, resolve this problem.

The choice of a rail pad material and geometry has a direct influence on the mechanical properties of a railway track. Locally this influence is connected with dumping properties and ability to reduce noise, vibrations and dynamic component of a wheel load. Globally, the rigidity of a rail pad structure influence the distribution of a wheel load between adjacent sleepers: softer rail pad response leads to higher rail bending and, therefore, to better load distribution. The presented study shows the potential for the numerical optimization of a rail pad geometry/material, which can be carried out in order to find the best compromise between sufficient level of energy dissipation, an acceptable rigidity of the structure and complexity of the model realization. Additionally, the developed model can be used in the complex 3D simulation of a railway track, taking into account real behaviour of rail pad structures.

Chapter 3: Influence of heterogeneities on mechanical properties: Virtual Material concept

1. Introduction

Nowadays, more and more material engineers are looking in the direction of composites, considering them as an alternative to standard construction materials. This interest is explained by flexibility and diversity of mechanical properties of heterogeneous materials, which can be achieved by varying its composition. As an example of the “revision and modernization” process for construction materials, a new development on a sub-ballast layer of a standard ballasted railway track can be mentioned. It was found that using a bituminous mixture (BM) layer instead of a compacted crushed-stone layer improves the mechanical behaviour of railway track and leads to a significant decrease of maintenance operations [4].

The macroscopic behaviour and physical properties of heterogeneous materials, such as BM, depend directly on characteristics of their composition: mechanical properties of constituent materials and their volume/mass fractions. A BM classically consists of compacted mineral aggregates of different size (~80-85 % of total volume and 90-96 % of total mass) incorporated into bitumen matrix (~10-12 % of total volume and 4-10 % of total mass) with a presence of a low quantity of air bubbles (~3-5 % of total volume). The size distribution of aggregates is usually defined by the grading curve, showing a percentage by weight of particles passed through the certain sieve size. Figure 3.1 presents the grading curve (along with the descriptive table) for the GB3 mixture, which is commonly used for a sub-ballast layer on railroads in France [4].

In engineering applications, it is common to focus experimental studies mainly on

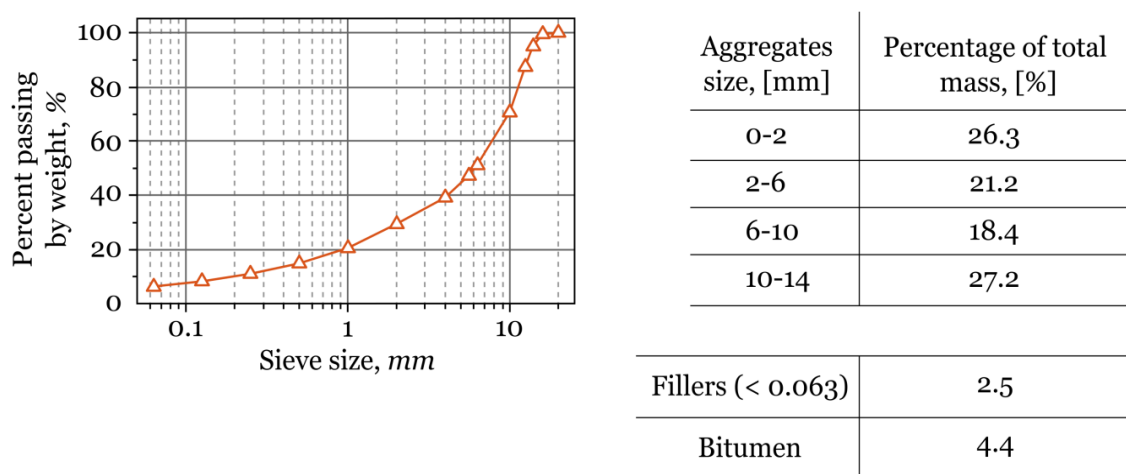


Figure 3.1: Grading curve and composition by mass for a GB3 mixture [4]

macroscopic parameters (such as dynamic modulus, fatigue resistance, etc.) of BMs' mechanical behaviour [92]. It can be also noted that constitutive models of BM are usually proposed on the basis of the macroscopic behaviour of materials [93]–[95] and tend to characterize their behaviour. However, a full investigation of heterogeneous materials cannot be carried out apart from the mesoscopic approach. Analysis of the material behaviour on a meso-scale allows to study precisely the influence of parameters of internal structure on the macroscopic behaviour. However, experimental techniques, gaining access to the internal structure of materials, are very limited to a few methods of nondestructive testing (*e.g.* X-ray tomography) and often apply restrictions on specimen's size, shape and conditions of the experiment. Significant progress in computational capacities allows the use of numerical approaches, such as finite element method (FEM) and less often discrete element method (DEM), to study internal mechanics of composite materials. These methods, however, raise additional sub-tasks, which must be resolved. Among them are:

a) Discretization of the studied problem:

In the first place, the question of discretization is a question of compromise between accuracy and computational efficiency. Representation of a complete material structure even on a meso-scale can result in a very complex numerical model. On the other hand, the very simplified representation can lack details, important for the studied case. First of all, the dimensionality of the studied problem must be chosen. For example, in [12] it was found that a 2D FEM and DEM provide reasonable accuracy in prediction of complex modulus and creep stiffness of an asphalt mixture. A 2D approach can be appropriate when the qualitative characterization of an internal mechanics remains the main subject of a study and prevails over the quantitative one [5]. On the other hand, limitations of a 2D approach connected with the impossibility to describe out-of-plane aggregate-to-aggregate contacts and interlock effects were also mentioned in [12], [15]. Moreover, the comparison between 2D and 3D meso-scale FE models performed in [6] has shown that stress magnitudes computed in the bitumen (matrix) part of a 3D model are generally 2.6 to 3.5 times higher than those in the 2D model.

Secondary, geometrical parameters of inclusions (aggregates) have to be specified. For example, mineral aggregates in a BM have not only a wide range of sizes (Figure 3.1), but also varies by the shape [92]. Depending on the case of study, the shape of aggregates can be described as polyhedrons (polygons in 2D) or simplified by ellipses or spheres. The former approach is mostly used in the study of real structures observed by X-ray tomography (*e.g.* [13]–[15]) or optical surface scanning techniques (*e.g.* [11], [12]). The later uses simplified representation in order to concentrate attention on mechanisms involved, regardless the shape of inclusions (*e.g.* [5], [6], [96]).

Generally, only part of the grading curve is represented in numerical models of BM: particles below the certain size barrier are considered to be a part of the matrix (*e.g.* [9], [13], [14]). This is done to reduce the numerical complexity of the task and increase computational efficiency. It can be also noted here that the high level of inclusions volume fraction (V_{fr}) can influence convergence of numerical packing algorithms, especially for monodisperse composites [97].

Finally, shape and size of the studied numerical specimen must be chosen. The shape of the specimen mostly depends on the case of study: cubic (square) volume for the most general case [9], [12], [14], [98]; cylindrical shape for the correspondence with classical BM

specimens shape [11], [13], [92]; complex geometry can be also suggested for very precise structural studies [5], [6].

The choice of the size of the numerical specimen is connected with the choice of the minimal representative volume element (RVE): a minimal volume, which can be statistically representative of the whole composite, *i.e.*, to effectively include a sampling of all microstructural heterogeneities that occur in the composite [99]. In practice, this condition can be relaxed: in such a way numerical specimen can be less than a minimal RVE for reasons of computational efficiency and predict the overall response of the composite with a certain level of accuracy [100].

b) The size of a representative volume element

The right choice of the size of RVE has a great importance because it influences both the numerical complexity of the model and its prediction capabilities [96], [100]–[102]. A lot of discussions were made so far in the framework of this subject. Theoretical approximations confirmed by numerical simulations show that, in the case of a linear elasticity and for RVE and inclusion characteristic sizes L and D , the ratio of $L/D = 2$ is sufficient to ensure at most a 5 % error in effective composite properties (such as macroscopic Young's modulus, Poisson's ratio and shear modulus) [100], [101]. It was mentioned in [100] that no theoretical estimation of the minimal RVE size were carried out for the framework of nonlinear mechanics. However, it was found in [102], using results of numerical simulations of RVEs with different characteristic sizes, that the value of $L/D = 16$ ensures reasonable relative error well below 5 %. It was shown in [100] that this ratio can be reduced to the value in range the of 3.6 to 6.6, which allows to sufficiently reduce computing costs without great loss of accuracy.

c) Numerical packing of aggregates into a chosen volume

A lot of different 2D and 3D packing algorithms were used recently for purposes of numerical representation of composite materials [5], [8], [10], [97], [98]. Numerical complexity of a packing algorithm mostly depends on factors defining discretization of the studied problem: for example, an increase in the problem dimensionality or inclusions volume fracture would obviously increase packing complexity.

An additional constraint of a minimum distance a between inclusions is often applied during packing. First of all, this condition allows to preserve connection with a real case of the study, when particles are separated by matrix material [9], [10], [98]. Moreover, it was noted by a number of authors [97], [100], [101] that control for the minimum relative distance between inclusions in the case of using FEM approach allows to avoid excessive mesh refinement (which can greatly affect the computational time) and the presence of distorted elements. However, it must be noted that imposing this additional constraint condition can sometimes prevent the particles packing algorithm from convergence [10], [100].

While the value of a minimum distance between inclusions is mostly dependent on the studied problem and computational capabilities, few suggestions can still be found in the literature. For example, Moraleda *et al.* [103] packed monodisperse spherical inclusions with $V_{fr} = 25\%$ into a periodic cubic cell volume using a minimum distance equal to 7% of their radius. During packing of a polydisperse spherical inclusions (with radius in range from 1 to 9.5 mm), Wriggers and Moftah [10] have varied the minimal distance depending on the

target value of V_{fr} and particle radius r : $0.46 r$ for $V_{fr} = 20\%$; $0.18 r$ for $V_{fr} = 30\%$; and $0.02 r$ for $V_{fr} = 40\%$ and $V_{fr} = 50\%$. Guo *et al.* [100] have found that separation of two arbitrary inclusions by distance higher than $0.2 r$ for $V_{fr} \leq 20\%$ and $0.1 r$ for $V_{fr} \geq 20\%$ allows to prevent severely distorted finite elements in the matrix.

d) Search of appropriate material models for aggregates and the matrix

Modelling of the mechanical behaviour of composite materials considering their internal structure obviously requires the material definition of all constituting parts. For this, additional experimental investigations generally must be carried out.

Concluding, it can be said that published works concerning numerical modelling of composite materials can be divided into two groups. Works from the first group are devoted to study of a theoretical RVE using 2D [5], [6] or 3D [6]–[10] approaches. These works usually lack connection with real cases and provide more theoretical and qualitative results at a meso-scale. In the second group, authors have chosen to work with numerical RVE (2D and 3D) developed using X-ray tomography or optical surface scanning techniques [11]–[15]. Contrary to the previous group, these works are devoted to study the one concrete case and are lacking generality.

In this work, the new “Virtual Material” (VM) concept, which allows keeping a connection between numerical and real specimens without losing generality, was suggested.

Main ideas of VM concept can be postulated as follows: 1) development of an artificially heterogeneous material with controlled level of heterogeneity by parameters chosen *a priori*; 2) direct geometrical correspondence between numerical and real specimens in order to exclude influence of the inclusions location and distribution in the matrix; 3) material models for the numerical specimen are based on the mechanical behaviour of materials constituting the real specimen.

Thus, the influence of heterogeneity of a two-component material on its mechanical behaviour was studied using VM concept.

2. Virtual material concept

Among all parameters which influence the mechanical behaviour of VM, the followings can be highlighted:

- Material properties of the matrix
- Material properties of the inclusions
- Distribution of inclusions' sizes and shapes
- Total volume fraction of the inclusions
- Distribution (location) of the inclusions in the matrix

Within the framework of the present study, it was chosen to reduce the very general problem stated above to a more specialized case. Thus, influence of the size (D) and the volume fraction (V_{fr}) of monodisperse spherical inclusions, randomly packed into a cubic hyperelastic matrix, on the mechanical behaviour of obtained composite structure was

investigated. Material parameters of inclusions and matrix are considered to be predefined. Inclusions are assumed to be rigid (non-deformable) compared to the material of the matrix.

An experimental investigation at a quasi-static strain rate was considered for this type of structure since both consisted materials have a strain rate independent behaviour. Additionally, it can be noted, that loads observed on the level of the BM layer of the ballasted railway track have intermediate rates [4].

2.1. General approach

Schematic process of development of VM specimens for a certain pair “diameter-volume fraction” is presented in Figure 3.2. Firstly, inclusions were randomly distributed inside the cubic volume of the size L conserving a minimum distance between particles (Step 1a-b). Thus, influence of inclusions location and distribution was eliminated from the list of variables. Detailed information on this step can be found in Section 2.3.1. Afterwards, inclusions skeleton obtained was located in the centre of a cubic matrix of the size $L + \Delta L$. Increased outer dimensions of the matrix secure inclusions inside the specimen and prevent them from falling out. Numerical geometry of the matrix was developed directly on the base of obtained inclusions coordinates using Boolean operations (Step 2a). Finally, numerical specimen was imported to a finite element software and meshed (Step 3a). Overall information about finite element model of VM specimens is presented in Section 3.4.2.

Manufacturing of a real specimen required additional steps. First of all, links, connecting inclusions between each other, were arranged (Step 2b, see Section 2.3.2): this allows to maintain inclusions in their original locations during moulding process (Step 4b). Obtained inclusions skeletons were printed out using 3D printer and moulded into the matrix (Step 3b-4b). Steps 3b and 4b are explained in details in Section 2.4.

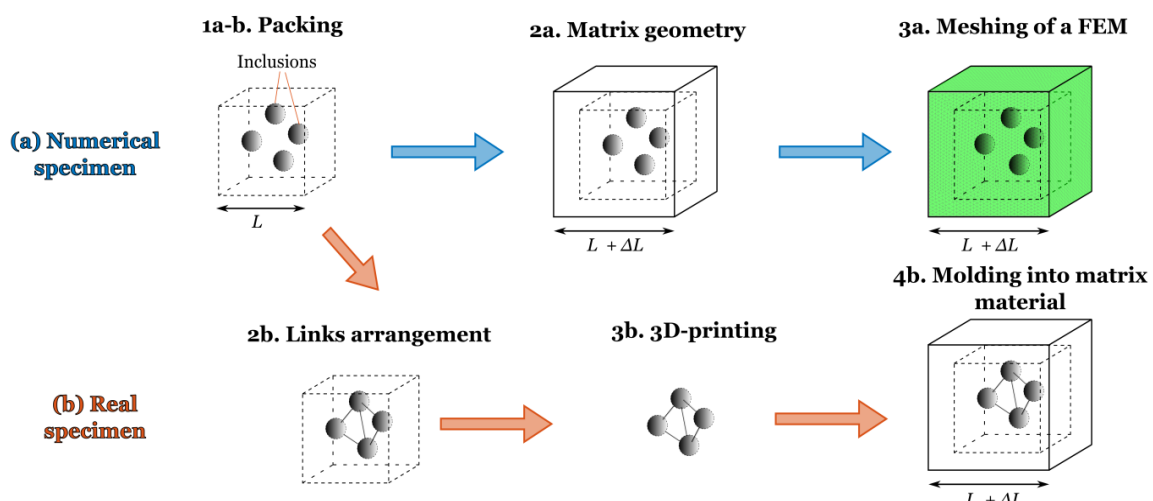


Figure 3.2: Schematic representation of process of development of numerical and real specimens

2.2. Doeblert experimental design and parameters of VM specimens

Methods of experimental design, in general, provide a rule in accordance with which input parameters for each experimental run have to be chosen. The main objectives of the experimental design method can be described as follows [104], [105]:

- Identification of input factors, which have the most significant influence on the resulting value of the studied output response variable
- Qualitative study of variation of the response variable, using polynomial interpolation of experimental data and constructing the “response surface”
- Minimization of experimental runs required

In the framework of the present study parameters of specimens under development (pairs “diameter-volume fraction”) were chosen in accordance with the Doeblert experimental design (Figure 3.3a). The Doeblert experimental design uses the second-degree polynomial model to predict response value and construct the “response surface” [106]:

$$y_{mod}(\mathbf{x}) = b_0 + b_1x_1 + b_2x_2 + b_3x_1x_2 + b_4x_1^2 + b_5x_2^2 \quad (3.1)$$

where x_1 and x_2 are input factors (parameters of an experiment) and b_i ($i=0, \dots, 5$) are parameters of the model. In practice, it is common to place input factors of different orders of magnitude on the same standard scale using the standard scores (standardized variables) approach. Thus, if an input factor $x_j \in [x_j^{min}, x_j^{max}]$ then the standard score z_j can be defined by

$$z_j = \frac{x_j - \mu}{\sigma} \quad (3.2)$$

where μ is the mean value and σ is the standard deviation of the input factor x_j . Identification of parameters of the model (3.1) requires performing 7 experiments and is carried out as a linear least square minimization of the error between experimental results and the model response with the help of the Moore-Penrose pseudoinverse matrix:

$$\mathbf{b} = (\mathbf{Z}^T \mathbf{Z})^{-1} \mathbf{Z}^T \mathbf{y} \quad (3.3)$$

where \mathbf{b} is a column vector of unknown parameters of the model, \mathbf{Z} is the 7×6 matrix of the model and \mathbf{y} is a column vector of 7 experimental measurements.

The Doeblert experimental design has the following advantages:

- Uniform distribution of experimental points: quality of the interpolation for the response surface equally depends on all experimental points
- Possibility of extension of the studied region by adding new experimental points
- Possibility to increase the number of input parameters without loss of previously obtained results
- The high quality of prediction (low variance) in almost all studied domain (Figure 3.3b).

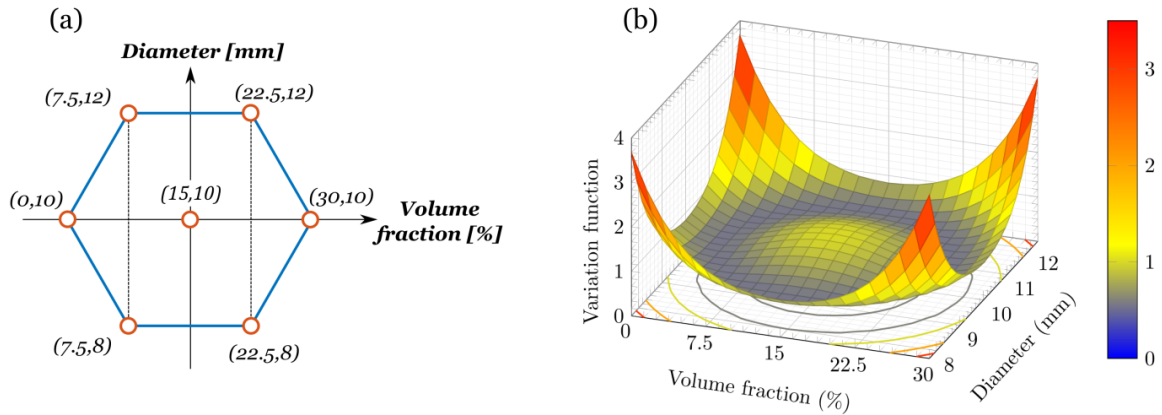


Figure 3.3: Parameters of specimens on the scale of the Doehlert diagram (a); variation function for the Doehlert experimental design (b)

The following pairs of parameters of inclusions “volume fraction-diameter” (V_{fr} [%]; D [mm]) were chosen (Figure 3.3a): (0; 10), (7.5; 8), (7.5; 12), (15; 10), (22.5; 8), (22.5; 12) and (30; 10). Inclusions with characteristic size between 8–12 mm were chosen in accordance with the grading curve in Figure 3.1. In the following text particular specimen will be denoted by the form \mathbf{VxxDxx} (i.e. V15-D10 refers to the specimen with 10 mm diameter inclusions occupying 15 % of 60x60x60 mm³ volume).

2.3. Numerical development of an inclusions skeleton

This section is devoted to the numerical development of an inclusions skeleton for each pair (V_{fr} ; D) by implementation of steps 1 and 2a presented in Figure 3.2.

2.3.1. Packing of inclusions (Step 1)

Spherical inclusions were randomly packed into a cubic volume with $L = 60$ mm using open source software GranOO [107]. The chosen size of the specimen ensures the ratio L/D to be between 5 and 7.5, which is in good accordance with values proposed in the literature (see Section 1). The inclusions packing algorithm is presented schematically in Figure 3.4.

GranOO software tries to pack the predefined number of inclusions while avoiding mutual intersection and intersection with borders of the cubic specimen. In order to ensure a minimal distance between inclusions, the radius of spherical particles was increased during

Table 3.1: Parameters of inclusions skeletons obtained after packing procedure

	V00-D10	V0075-D08	V0075-D12	V015-D10	V0225-D8	V0225-D12	V03-D10
Target V_{fr} [%]	0.0	7.5	7.5	15	22.5	22.5	30
Resulted V_{fr} [%]	0.0	7.45	7.54	15.03	22.46	22.62	30.06
Number of inclusions	0	60	18	62	181	54	124

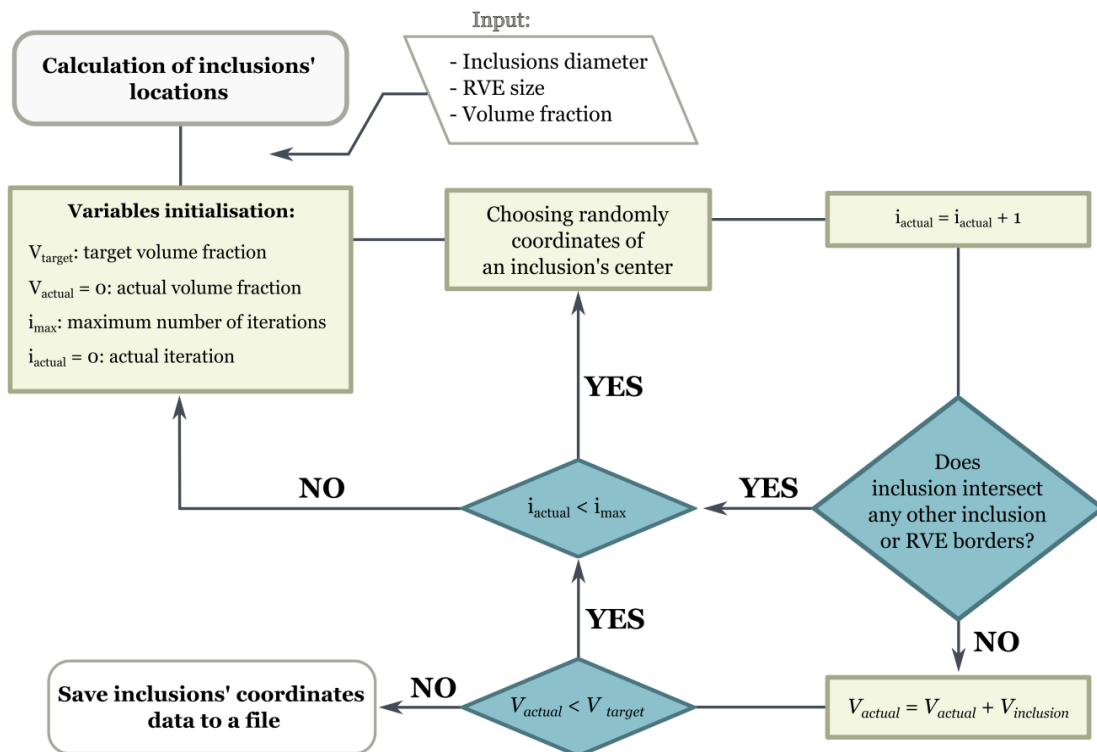


Figure 3.4: Scheme representing algorithm of inclusions locations calculation

the work of the packing algorithm by $\Delta r = 0.5$ mm. Thus, a minimum distance of 1 mm (16–25% of inclusions' radius) between any two inclusions and 0.5 mm between any inclusion and a border of cube was ensured.

Target and resulted volume fractions, as well as the number of inclusions packed during the procedure described above, are presented in Table 3.1 for each of studied specimens. It can be easily found that an average difference between target and resulted volume fractions is less than 0.5 %.

2.3.2. Arrangement of links (Step 2a)

To obtain stable inclusions skeleton and preserve all particles in their initial positions (calculated in the previous step) during 3D printing and moulding processes, inclusions must be connected between each other by a set of rigid links. However, the presence of these links can naturally influence the mechanical behaviour of the final specimen. The stated contradiction was mitigated by optimization of the links number and length using algorithms presented schematically in Figure 3.5.

Firstly, 3D Delaunay triangulation was built on centres of inclusions to connect them by defining tetrahedra. The main advantage of the Delaunay method is that it avoids creating extremely acute and obtuse angles in tetrahedra, which allows, at the end, to delete more links, while keeping the structure of inclusions stable. By building tetrahedra, Delaunay triangulation creates a big number of duplicate links, which were subsequently deleted from the final set.

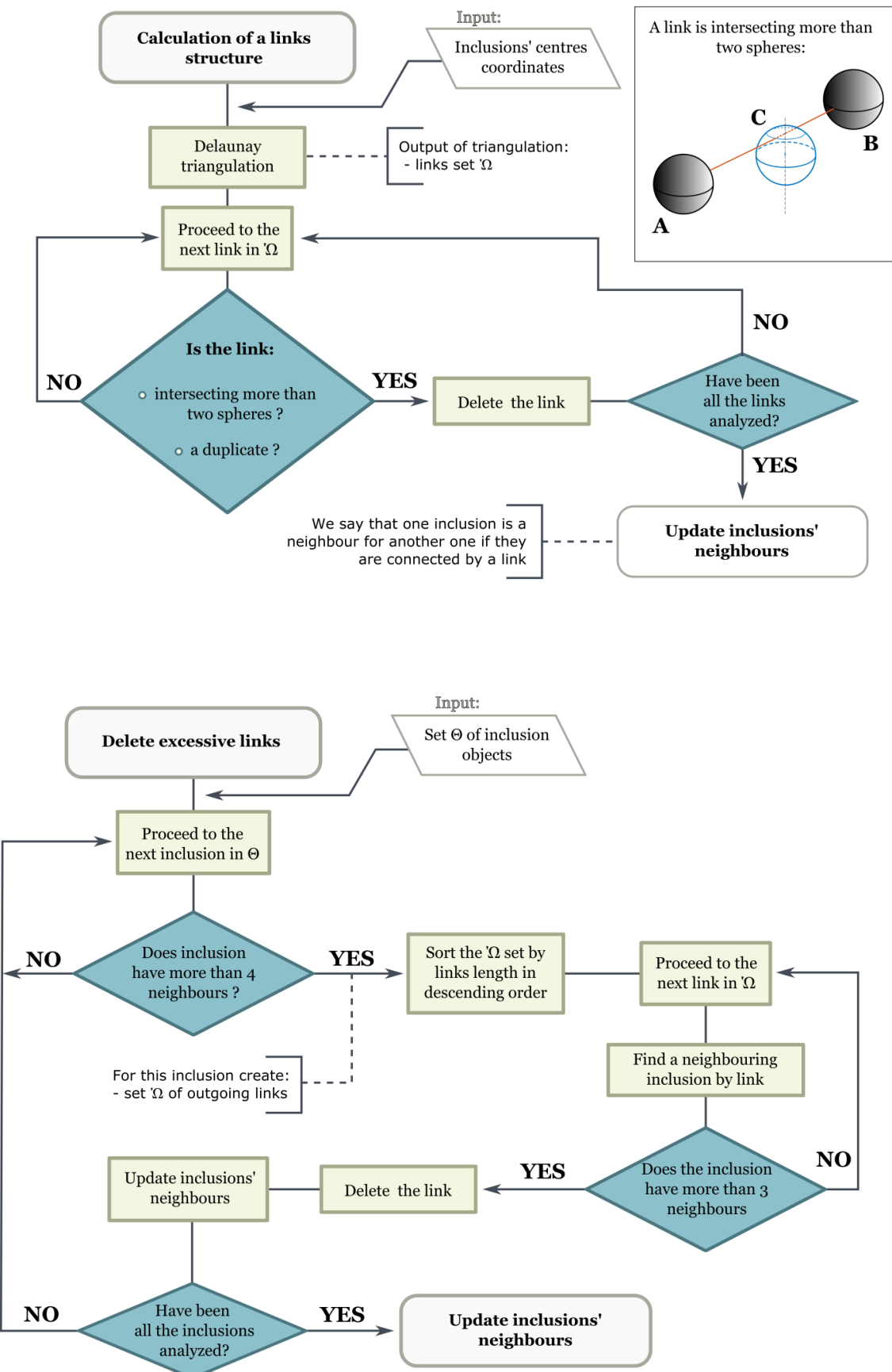


Figure 3.5: Optimization schemes for links number and length

As a sphere occupies some volume around its centre (in the contrary to a point), then a certain link may go from the centre of an inclusion *A* to the centre of an inclusion *B* by intersecting another inclusion *C* (Figure 3.5). Links fitting this definition were removed from the inclusions skeleton.

The second algorithm tries to decrease the number of links outgoing from an inclusion down to 4 while ensuring that each inclusion is connected with at least 3 other inclusions. The algorithm iteratively searches for the longest links among removal candidates and delete them only if it will not decrease the number of outgoing links for any other inclusion below 3.

The choice of the links' diameter was mostly based on the stability of a printed structure and was defined by the printing of a small portion of the final geometry. It was found that links with a diameter of 1 mm provide sufficient rigidity for the structure without an excessive increase in volume fraction of ABS (Acrylonitrile butadiene styrene plastic) material. Additional information concerning 3D printing of developed specimens is presented in Section 2.4.

Final structures of the specimen with and without links were exported to a step format required for a 3D printing machine and finite element software. For this purpose a special script allowing automatic creation of a necessary geometry in CATIA CAD software was developed using Python programming capabilities.

An example of a structure obtained after all described manipulations is presented in Figure 3.6a-b. Inclusions skeletons designed for 3D printing were complemented by four supporting legs (see Figure 3.6a-b). The legs allow locating an inclusions skeleton in the centre of the 70x70x70 mm box and keeping a minimum distance of 5 mm between inclusions and specimen's borders during the moulding process (Figure 3.6b).

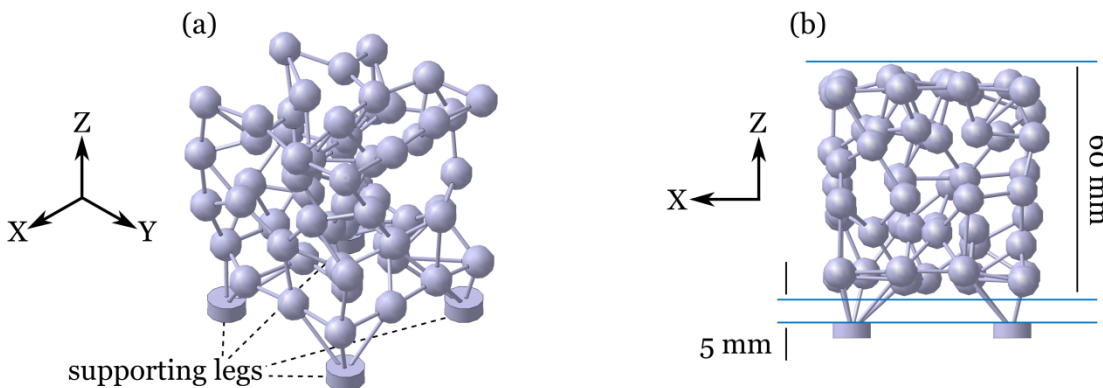


Figure 3.6: Inclusions skeleton designed for 3D printing of the specimen Voo75-D08 reinforced by links: (a) isometric view, (b) XZ-plane view

2.4. Manufacturing of a real specimen

Manufacturing of real specimens on the basis of numerical geometry was carried out in two steps (see Figure 3.2, Steps 3b-4b). Firstly, inclusions skeletons, developed in Section 2.3, were printed out using additive manufacturing. In the next step, obtained structures were moulded into silicone matrix.

2.4.1. 3D printing of the inclusions skeleton

Inclusions skeleton was printed by a Stratasys® uPrint SE Plus 3D professional printer using ABS plastic material (Acrylonitrile butadiene styrene terpolymer with density in the range of 0.9-1.1 g/cm³ and Young modulus between 1700 and 2600 MPa). uPrint SE Plus prints the structure using two materials: space not occupied by inclusions and links is filled by supporting material, which is chemically removed afterwards. The printing resolution is 0.25 mm. An example of a printed inclusions skeleton (V7.5-Do8) is presented in Figure 3.7b along with numerical representation.

Thin geometries (like links of 1 mm in diameter) printed using 3D technic can be very fragile depending on the printing direction. It was found that links oriented in the printing direction have the lowest fracture resistance. In the opposite, links oriented at 90° to the printing direction have the highest possible rigidity. Chemical leaching of a supporting material can be destructive for links especially for those oriented with the printing direction. Thus, the printing direction must be chosen in accordance with the dominant links orientation in the specimen, while no main orientation can be defined for links in studied specimens (see Section 3.3.3). However, the orientation of supporting legs (see Figure 3.6a-b and Figure 3.7a-b), governing the position of the inclusions skeleton, tends to the Z-direction. Thus, X or Y direction of printing will provide the most stable structure with the highest fracture resistance. In order to preserve conformity, all specimens were printed in the X-direction.

Geometries produced by 3D printing technique have a non-smooth, stair-like surface with a step height equal to the printer resolution (Figure 3.7c). It must be kept in mind that such form of inclusions' surface can influence the behaviour of VM specimens, and more precisely, the contact behaviour between inclusions and matrix.

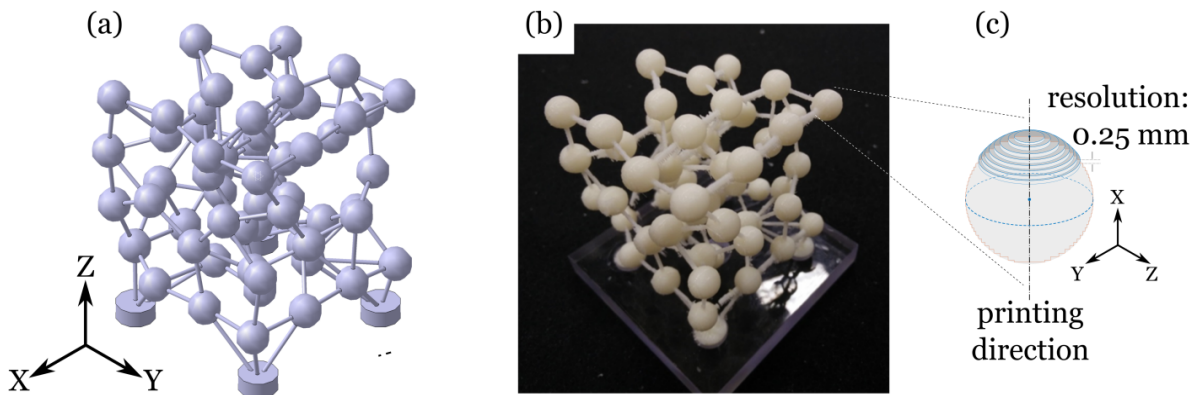


Figure 3.7: Inclusions skeleton of the specimen V7.5-Do8: numerical (a) and printed using ABS plastic material (b). Stair-like surface of a 3D printed geometry (c)

Printing and chemical leaching of each specimen took approximately 12-24 h depending on specimen complexity.

2.4.2. Moulding the inclusions skeleton into silicone matrix

According to the scheme presented in Figure 3.2 manufacturing of a real specimen imply moulding of an inclusions skeleton into the hyperelastic matrix. Soloplast™ silicon material was chosen for this purpose. The silicone is supplied as a liquid viscous substance, which solidifies after mixing with a hardener component in the proportion of 100 to 5 (100 g of a silicone to 5 ml of a hardener). Silicone and hardener components were taken with a precision of 0.1 g and 0.1 ml respectively. Generally, drying takes 1-2 days depending on the quantity of the material.

During moulding process a specially developed moulding boxes with the inner dimensions of 70x70x70 mm³ was used (Figure 3.8). All facets of the box are separable, so the specimen can be easily taken out after silicon is dry. The specimen was mounted on the bottom facet of the box (see Figure 3.7 and Figure 3.8). Thus, moulding of a silicone compound was carried out in the Z-direction of a specimen.

Liquid silicone can contain a certain quantity of air bubbles (especially after mixing with a hardener), which can naturally decrease the rigidity of the dried material. Thus, degassing of the silicone mould is a very important step in the specimen preparation process. Degassing was performed for each silicone mould using the vacuum chamber.

It must be mentioned that preliminary tests have shown no adhesion between dried silicone and ABS plastic (used for 3D printing of inclusions skeletons).

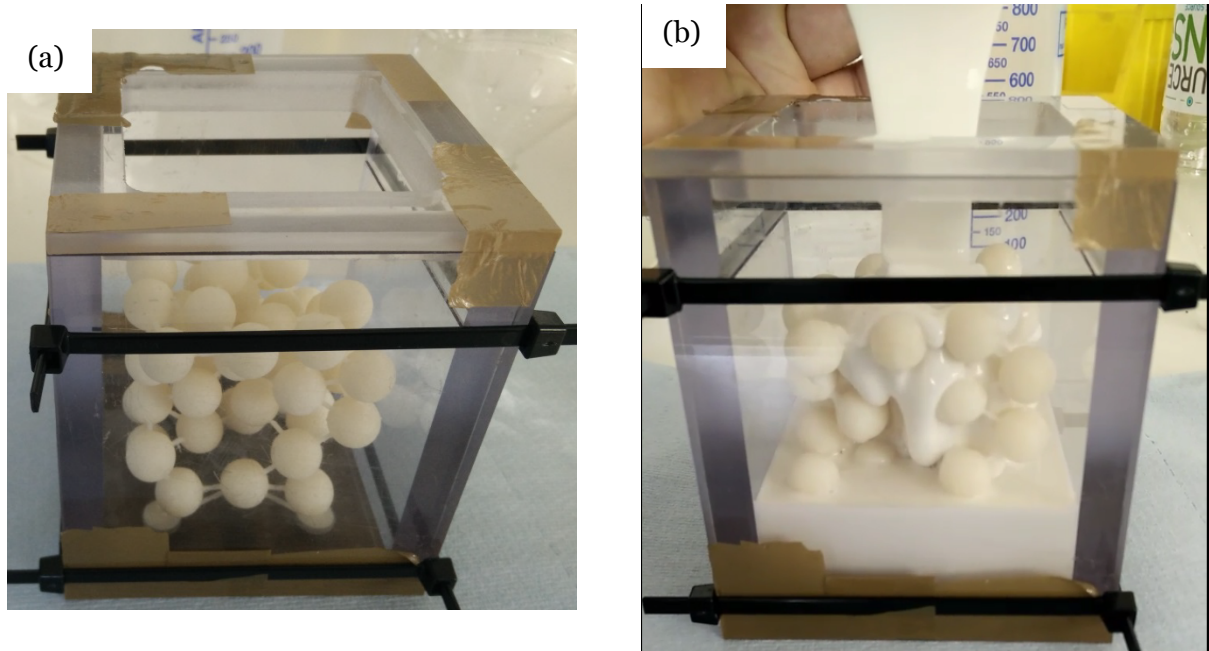


Figure 3.8: Moulding of the specimen Vo225-D12 into a silicone matrix

3. Mechanical behaviour of VM specimens

Mechanical behaviour of developed specimens was studied by following experimental and numerical (Finite Element) approaches.

Firstly, the following aspects of a macroscopic response were investigated using both experimental and FE approaches:

1. Specimens mechanical isotropy (influence of loading direction)
2. Specimens rigidity (Force vs Macroscopic strain response)
3. Energy dissipated for one loading cycle

Secondly, local stress concentrations in the matrix material caused by inclusions movement were studied numerically using FE method. Finally, macroscopic results obtained using experimental and FE approaches were compared.

3.1. Mechanical behaviour of the silicone material

Inclusions were considered as rigid comparing to the silicone matrix ($E_{ABS} \sim 2100$ MPa against $E_{silicone} \sim 0.5$ MPa). Precise investigation of the mechanical behaviour of the silicone material was carried out following methods used for the rubber material of a rail pad (see Chapter 2: Section 3.2). Experimental investigation was done using cylindrical specimens of 31 mm in diameter and 34 mm in height (Figure 3.9a).

3.1.1. Incompressibility of the silicone material

Firstly, incompressibility of the material was verified during hydrostatic compression experiment, described in Chapter 2: Section 3.2. The evolution of pressure as a function of volume variation obtained during this experiment is presented in Figure 3.9b. No significant difference between the two curves representing the tests with and without the silicone specimen in the chamber was found.

Following the same argumentations as in the case of SBR specimen in Chapter 2: Section 4.1, it is concluded that the silicone material can be considered as incompressible.

3.1.2. QS compression experiment

Firstly, it must be noted that preliminary investigation of silicone material at different strain rates has shown no strain rate dependent behaviour. Thus, any observed energy dissipation

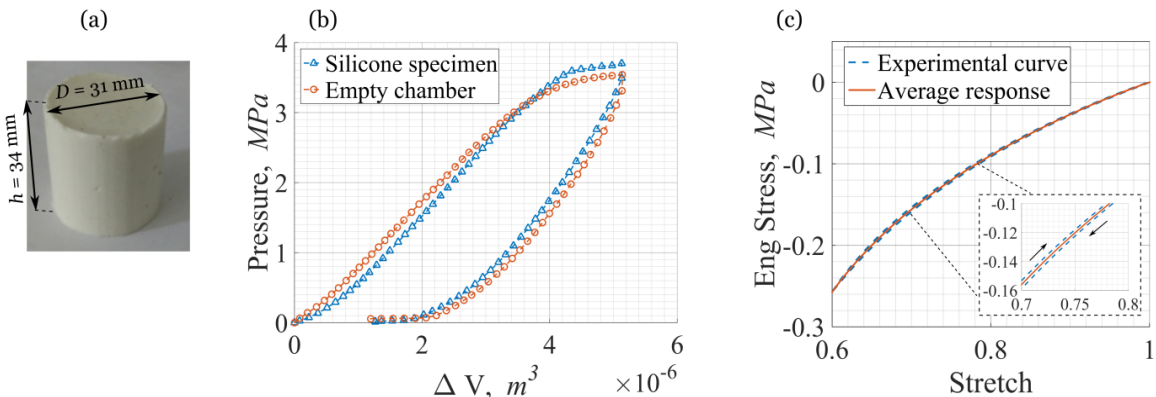


Figure 3.9: Experimental investigation of the mechanical behaviour of silicone material:
 (a) Cylindrical specimen; (b) Pressure dependences on change in volume during hydrostatic compression experiment; (c) Stress vs Stretch curve obtained during QS compression experiment

was explained by residual friction, which cannot be completely eliminated during compression experiment.

Silicone cylindrical specimen was subjected to 3 loading-unloading cycles in the uniaxial compression regime. A displacement load was applied at a low strain rate of 0.002 s^{-1} (4 mm/min). Stainless steel compression plates were covered by a thin layer of grease in order to reduce the influence of friction. First, two cycles were performed in order to exclude the influence of the non-destructive Mullins effect and stabilize the mechanical response of the material. The Stress vs Stretch curve obtained in the third loading cycle is presented in Figure 3.9c. Experimental curve forms a small loop of hysteresis (released energy is only 3% smaller than the accumulated energy), which appears to be an evidence of energy dissipation caused by friction between specimen and compression plates. It was assumed that the real behaviour of the silicone material can be considered as purely hyperelastic and approximated by an averaged response between loading and unloading parts of the Stress vs Stretch loop.

3.2. Experimental investigation of VM specimens

VM specimens with structure developed in previous sections were subjected to compression load with a displacement control. Before the experiment, all specimens were kept in the climate chamber at the temperature of 23°C for 24 hours in order to eliminate the influence of the temperature variation. In order to decrease the influence of links on the mechanical behaviour, all specimens were preliminarily subjected to cyclic loading with an amplitude of 15 mm in each of primary directions (X, Y and Z). It is assumed that all links were broken during this pre-cycling procedure.

Loading scheme was identical for each specimen and each loading direction and is presented in Figure 3.10a. Each specimen was initially preloaded to 5N in order to establish contact between specimen and compression plates. After four loading cycles in series with $\Delta d = 15 \text{ mm}$ (21.5 % of macroscopic strain from the initial state), the fifth cycle with $\Delta d = 10 \text{ mm}$ (14.3 % of macroscopic strain from the initial state) was applied. Displacement load was always applied relatively to the starting point of the following cycle. Pre-cycling eliminates effects of permanent (broken or/and shifted links) and temporary (Mullin's effect)

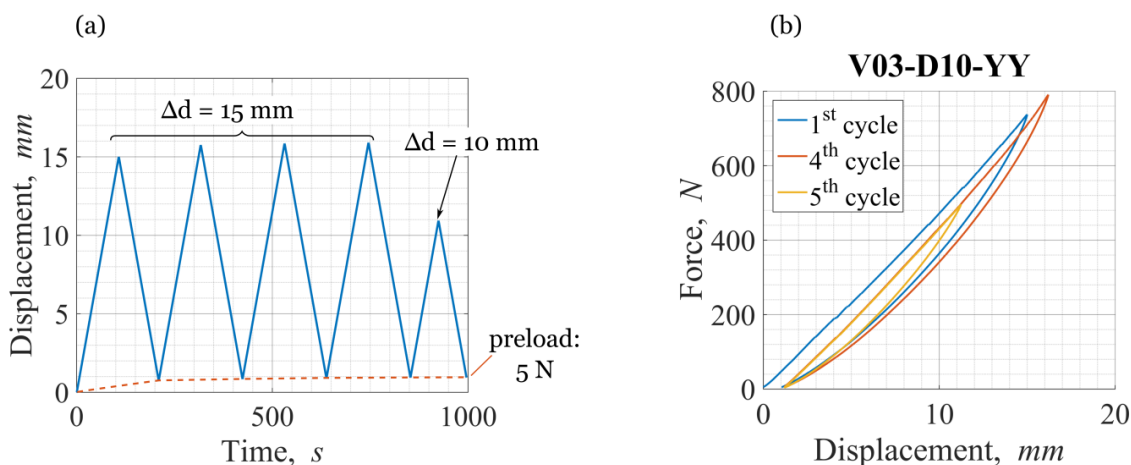


Figure 3.10: VM loading scheme (a) and cycling influence (b)

damage in the material. Experimental data from the 5th cycle was used in the following study.

Pre-cycling effect (presented in Figure 3.10b on the example of the Vo3-D10 specimen) was not the same for all the specimens. Thus, for the better correspondence between experimental data, obtained for different specimens and loading directions, experimental curves were plotted in Force vs Macroscopic strain coordinates, where the macroscopic strain was calculated relative to the final point of the fourth cycle of the pre-cycling procedure. The speed of load was equal to 8.4 mm/min, which corresponds to a macroscopic strain rate equal to $2 \cdot 10^{-3} \text{ s}^{-1}$. Experimental procedure was performed in each of three main directions (Z, Y and X) with 2 hours rest time in the climate chamber between experiments.

Experiments were carried out using an INSTRON 50kN testing machine (Instron Ltd, High Wycombe, UK), instrumented with a 50 kN load cell and stainless still compression plates. No glue or lubricant was applied between specimens' and plates' surfaces, so a small value of frictional sliding was expected.

3.2.1. Maximum force (F_{max}) parameter

VM specimens have a nonlinear dependence of recorded force on applied compressive displacement. Thus, due to this nonlinearity, the value of specimen's stiffness calculated using standard formula (force divided by the corresponding displacement) would directly depend on the level of applied displacement. In order to avoid this problem and have possibility to compare rigidity of different specimens, it was decided to use maximum force (F_{max}) parameter instead of stiffness. The value of F_{max} was calculated as the value of force at the maximum level of applied compressive displacement (10 mm).

3.2.2. Fraction ($E_{\%}$) of dissipated energy from total accumulated energy

Each specimen during cycling shows a hysteresis loop (mismatch between loading and unloading parts of Force vs Displacement curve due to energy dissipation). The value of energy dissipated in one loading cycle can be calculated as the area of hysteresis loop (in Force vs Displacement coordinates) observed in the experiment. Integration of the loading part of the experimental curve gives the energy accumulated in the material during loading (Figure 3.11). Integration of the unloading part, on the other hand, gives the energy released during unloading. The difference between these two values (or simply the area of the hysteresis loop) defines the energy dissipated for one cycle. The capability of studied

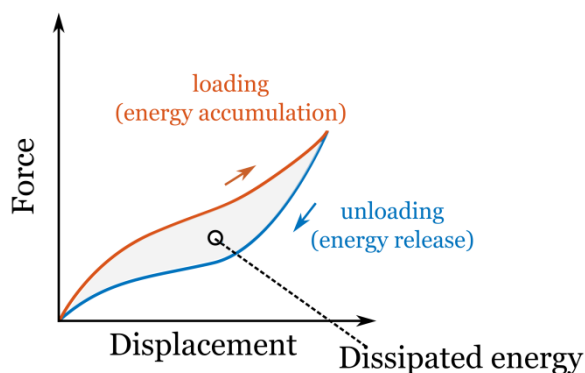


Figure 3.11: Calculation of dissipated energy

specimens to dissipate energy was compared by the parameter $E\%$:

$$E\% = \frac{\text{Energy dissipated}}{\text{Energy accumulated}} \cdot 100 \% \quad (3.4)$$

3.2.3. Results of experimental investigation

All specimens were subjected to compression load in the three main directions (Z, Y and X) in order to study their isotropy. Comparison of specimens macroscopic response in each of three main loading directions is presented in Figure 3.12. More precise comparison was carried out on the base of F_{max} and $E\%$ values (Table 3.2).

The first observation, which must be highlighted, is that Voo-D10 specimen (without inclusions) is dissipating energy during the loading cycle (see loop of hysteresis in Figure 3.12a and values of $E\%$ in Table 3.2). It was found previously, that the silicone material of the matrix has the nonlinear strain rate-independent (hyperelastic) behaviour and does not show any viscoelasticity and energy dissipation phenomena. It can be seen however, that Voo-D10 specimen, which is not containing any inclusion, still dissipates some energy. This observation can be explained by energy dissipation on a relative frictional sliding between specimen's and compression plates' surfaces. The value of $E\%$ connected to this friction will be referred by E_{fr}^r in the following text.

Table 3.2: Maximum force and Dissipated energy fraction data obtained during experimental investigation of VM specimens subjected to compression load

	F_{max} [N]			$E\%$ [%]		
	X	Y	Z	X	Y	Z
Voo-D10	398.2	399.6	371.9	$E_{fr}^r = 2.2$	$E_{fr}^r = 1.8$	$E_{fr}^r = 5.2$
Voo75-Do8	427.2	428.1	401.1	6.6	6.5	7.8
Voo75-D12	394.4	393.4	378.6	6.0	6.3	7.2
Vo15-D10	430.4	436.2	413.6	8.3	8.2	9.3
Vo225-D8	395.6	377.7	388.1	12.4	10.9	11.4
Vo225-D12	397.3	406.2	406.4	12.1	11.0	12.6
Vo3-D10	479.8	489.9	475.5	15.6	15.7	16.5

Let us assume that the value of E_{fr}^r remains constant for all the specimens considered. In this case, it can be found that the value of E_{fr}^r constitutes a significant part of the $E\%$. For example, for X and Y loading directions E_{fr}^r reaches up to 29 % of $E\%$ (for specimens with small inclusions' volume fraction). For the Z-direction this fraction increases up to 70 %. This observation must be kept in mind during the following analysis of the mechanical behaviour of VM specimens.

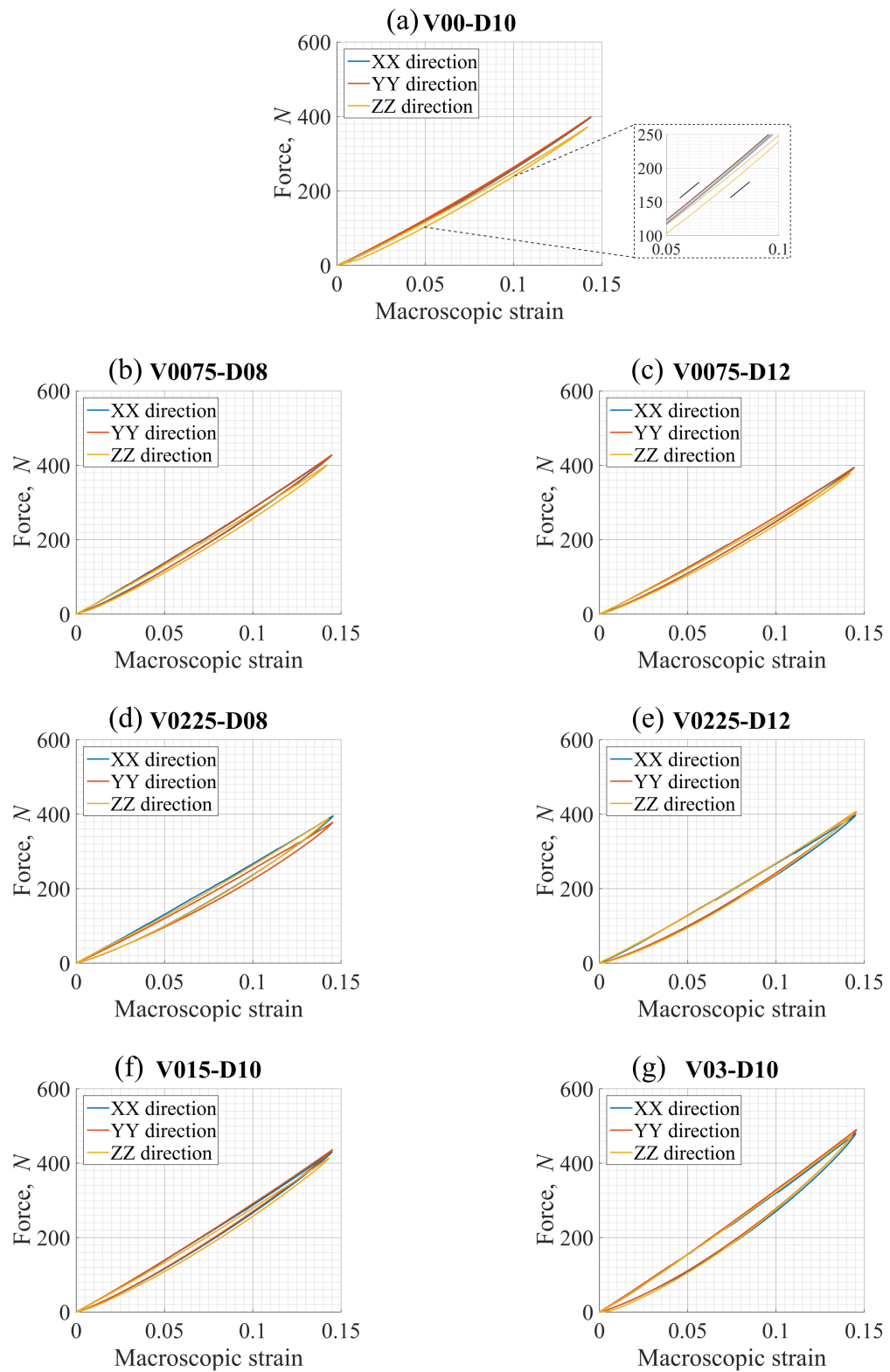


Figure 3.12: Force vs Macroscopic strain curves obtained during QS-compression experiment of VM specimens subjected to load in X-, Y- and Z-directions

It is seen from Figure 3.12 and Table 3.2 that, for almost all VM specimens, Z-load direction is characterized by decreased valued of F_{max} and increased value of $E\%$ compared to other load directions. For example, for the specimen V015-D10 $F_{max}^Z = 413.6$ N, while F_{max}^X and F_{max}^Y equal to 430.4 and 436.2 N respectively. The value of $E\%$ for the same specimen, in its turn, is ~13 % higher in the case of Z-direction of applied load. It can be explained by recalling silicone moulding process and the fact that moulding box was filled by the silicone in the Z-direction. Due to the surface tension, liquid silicon compound tends to “climb” on vertical walls of the moulding box, forming concave meniscus-like effect.

Consequently, after drying, the top surface in the Z-direction of the specimen has a small curvature, which changes contact conditions during the experiment. We believe that this difference in the contact conditions at different loading directions led to the difference in the observed mechanical behaviour, mentioned above. It must be noted that contribution of this concave meniscus cannot be estimated and, as a result, the comparison between Z and X or Z and Y directions becomes difficult. Comparison between data obtained in X and Y directions for a given specimen, on the contrary, have not shown significant anisotropy.

3.2.4. Comparison between different specimens

Force vs Macroscopic strain curves obtained during the experimental investigation of VM specimens subjected to compression load in the Y-direction are presented in Figure 3.13. It is seen that an increase in volume fraction of inclusions leads to a nonlinear increase in capability of a specimen to dissipate energy. For example, an increase in V_{fr} from 0.0 % to 7.5 % and from 22.5 % to 30.0 % leads to an increase in $E\%$ on ~ 4.7-4.8 %. The change of V_{fr} on the same value from 7.5 % up to 15.0 % or from 15.0 % up to 22.5 % leads to an increase in $E\%$ by 1.8 % and 2.8 % respectively. On the other hand, variation of the inclusions size for the same level of V_{fr} has almost no influence on the dissipative properties of VM specimens.

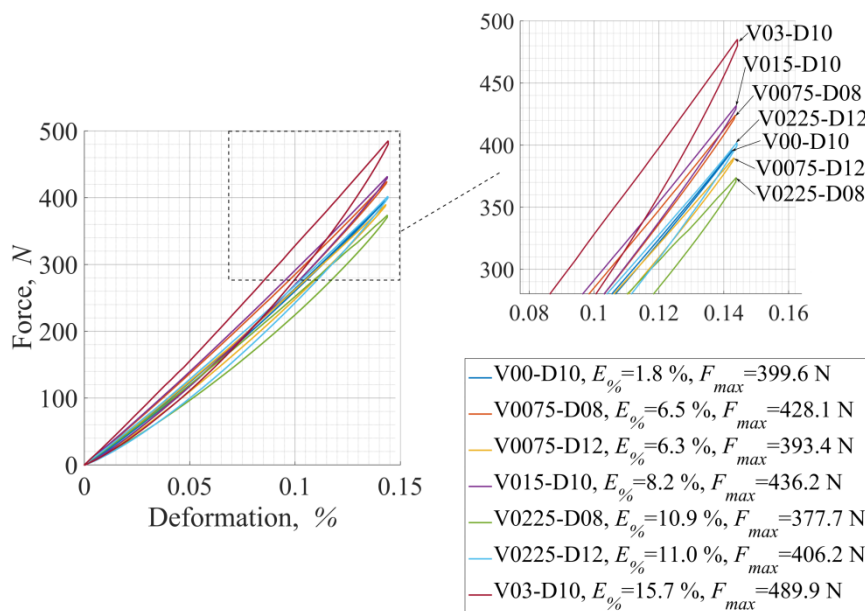


Figure 3.13: Force vs Macroscopic strain curves obtained during experimental investigation of VM specimens subjected to compression load in the Y-direction

3.3. Discussion of experimental results

3.3.1. Response surfaces (experimental study)

Influence of input factors V_{fr} and D on the resulting value of output variables F_{max} and $E\%$ can be studied with more precision using the response surfaces method. Response surfaces for F_{max} and $E\%$ were constructed on the base of experimental data obtained during QS-compression of VM specimens (Figure 3.14). Expressions for these surfaces were obtained using equation (3.3) and are as follows:

$$F_{max}(\hat{V}_{fr}, \hat{D}) = 436.18 + 23.82\hat{V}_{fr} - 1.79\hat{D} + 36.44\hat{V}_{fr}\hat{D} + 8.57\hat{V}_{fr}^2 - 49.3\hat{D}^2 \quad (3.5a)$$

$$E\%(\hat{V}_{fr}, \hat{D}) = 8.18 + 6.15\hat{V}_{fr} - 0.035\hat{D} + 0.208\hat{V}_{fr}\hat{D} + 0.53\hat{V}_{fr}^2 + 0.483\hat{D}^2 \quad (3.5b)$$

where \hat{V}_{fr} and \hat{D} are standardized variables V_{fr} and D respectively. It is seen in Figure 3.14a-c that the value of F_{max} is nonlinearly dependent on both V_{fr} and D . Moreover, a maximum value of F_{max} can be found at each value of V_{fr} . For example, at $V_{fr} = 7.5\%$ the maximum value of $F_{max} = 428.44$ N is reached at $D = 9.53$ mm; at $V_{fr} = 22.5\%$ the maximum value of $F_{max} = 451.6$ N is obtained at $D = 10.38$ mm.

On the opposite to the F_{max} dependence, the value of $E\%$ is monotonically dependent on V_{fr} and has a slight dependency on the value of D (variation of about 2-3 % from the average can

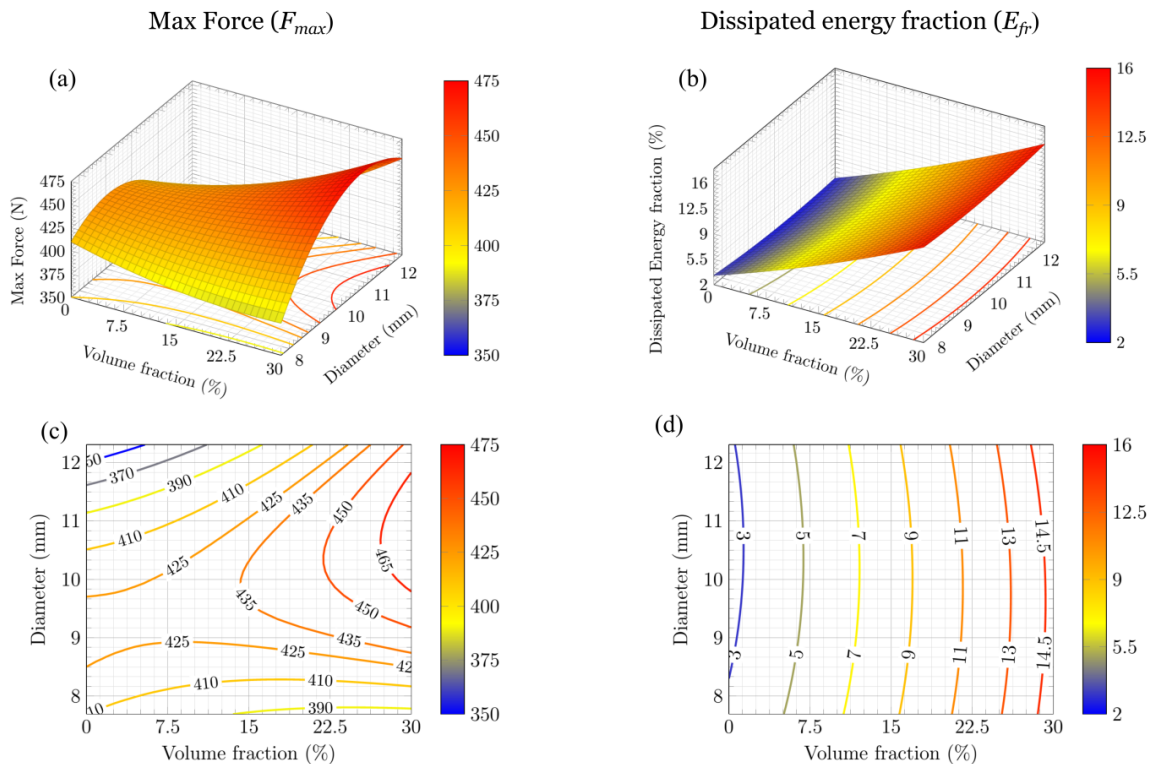


Figure 3.14: F_{max} (a,c) and $E\%$ (b,d) output parameters obtained during QS-compression experiment as functions of inclusions' volume fraction and diameter

found).

3.3.2. The total area of inclusions

The total area of inclusions' surfaces S_{total} can be considered as an integral parameter of VM specimens, because it depends on both the size of inclusions and the volume fraction (number of inclusions). Values of F_{max} and $E\%$ obtained for different VM specimens and different load directions were plotted against the total inclusions' surface area (Figure 3.15a-b). It is seen from Figure 3.15a that the value of F_{max} has a non-monotonic dependence on the value of S_{total} : it grows with an increase in the value of S_{total} for most of the specimens, while results obtained for specimens V0225-D12 and V0225-D08 are falling out from the general tendency. There can be two possible explanations of this behaviour. It was mentioned in Section 2.4.2 that no adhesion between materials of inclusions and the matrix was found. The lack of adhesion between inclusions and matrix can result in a decrease in the total rigidity of a specimen due to: 1) more relaxed state of the material near inclusions; and 2) nucleation of porosities in the regions of inclusions-matrix separation (Figure 3.16). Thus, it can be assumed that in the same time an increase in S_{total} leads to both an increase in specimen's rigidity, due to generation of new load-bearing chains, and to a decrease in specimen's rigidity, due to generation of new porosities.

The second possible explanation of a non-monotonic dependence of F_{max} on S_{total} stands on a possibility of a slight difference in the mechanical behaviour of a silicone matrix for different specimens: no technical details were provided by supplier concerning dried silicone compound. Thus, it is possible that small difference in silicone-hardener proportions, difference in humidity or not sufficient degassing could lead to difference in rigidity of silicone material for different specimens.

Figure 3.15b shows dependency of $E\%$ on S_{total} . Recalling the hyperelastic nature of the matrix material behaviour and elastic nature of the inclusions behaviour, it must be admitted that, besides the friction between specimen and compression plates, the only reason of energy dissipation, observed during experimental study of VM specimens, is the frictional

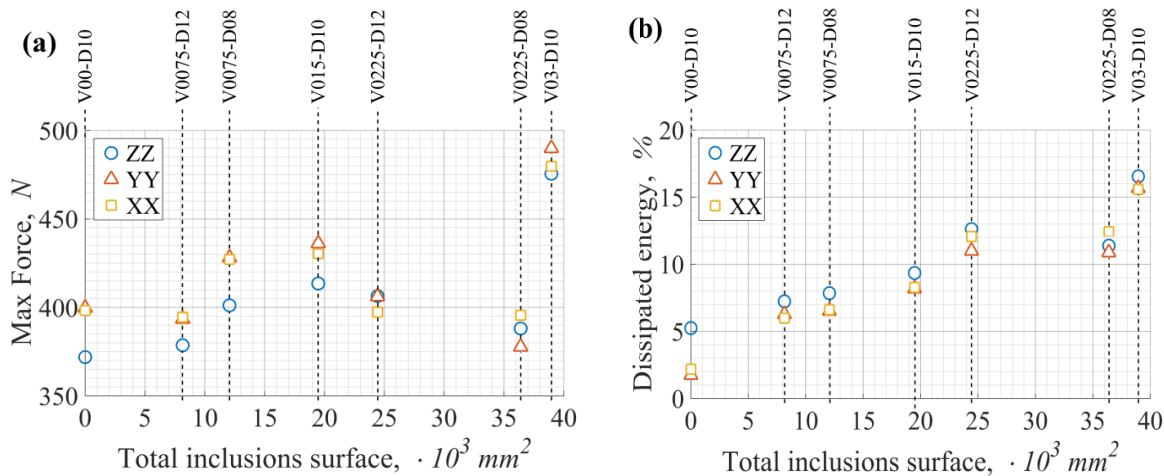


Figure 3.15: Dependences of F_{max} (a) and $E\%$ (b) on total inclusions' surface area

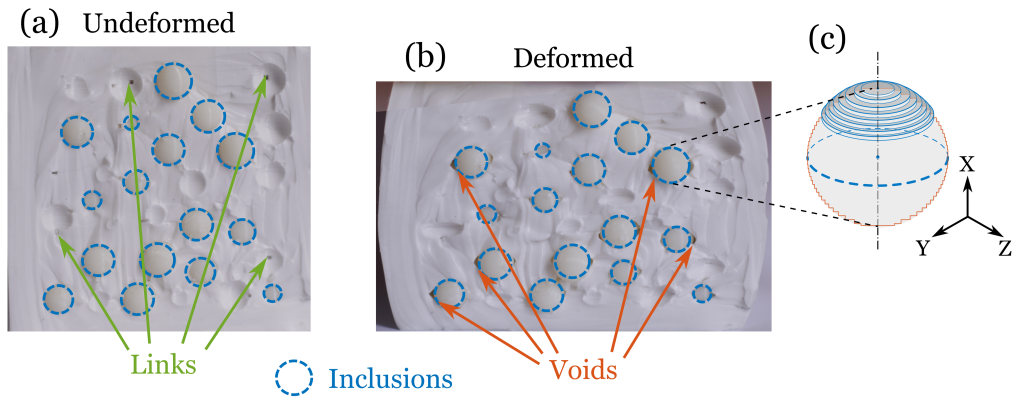


Figure 3.16: Porosities in the structure of real VM specimens: (a) rigid links and (b) voids in regions of inclusions-matrix separation. (c) Stair-like surface of inclusions and links

interaction between inclusions and matrix contact surfaces. Thus, it can be assumed that a higher value of S_{total} must result in a higher values of dissipated energy. However, it is seen in Figure 3.15b that the monotonically increasing dependency of $E\%$ on S_{total} has two “flat” regions for specimens with the same value of V_{fr} . Thus, it can be concluded that experimental investigation of VM specimens has shown that the value of inclusions’ volume fraction has a higher influence on dissipative properties of a composite material than the size of these inclusions.

3.3.3. Analytical study of developed inclusion structures

Experimental results presented in the previous section have shown close to the isotropic behaviour of VM specimens subjected to a compression load. Isotropy is a very important characteristic of composite materials, which can influence the choice of methods utilized for study and modelling of such materials. In this section, the internal structure of developed VM specimens was analyzed analytically in order to study homogeneity of inclusions distribution and estimate volume fraction and orientation of rigid links.

a) Inclusions centroid and the moment of inertia

Firstly, the isotropy of inclusions distribution was analyzed following the procedure proposed by Segurado and Llorca [97]: 1) computing of the coordinates of the centroid of the particles skeleton; and 2) computing its moment of inertia in relation to the three perpendicular axes originated at the centre of the specimen. The results of these calculations are plotted in Figure 3.17a-b against the total inclusions surface (thus data obtained for different specimens with the same value of V_{fr} can be distinguished). For simplicity density of inclusions was assumed to be equal to $\rho = 1 \text{ g/cm}^3$ during calculation of their moments of inertia. Coordinates of centroids were compared to the central line of a cube (Figure 3.17a). The moment of inertia of each inclusions arrangement was compared with the moment of inertia of an equivalent homogeneous cubic specimen, whose mass is equal to the mass of all inclusions ($M_{cube} = V_{fr}L^3\rho$).

It is seen from Figure 3.17a that centroids of inclusions skeletons are always close to the centre of a cube ($L/2 = 30 \text{ mm}$). Moments of inertia of the studied inclusions skeletons are very close to the case of the homogeneous cubic specimen (~7 % of difference in average).

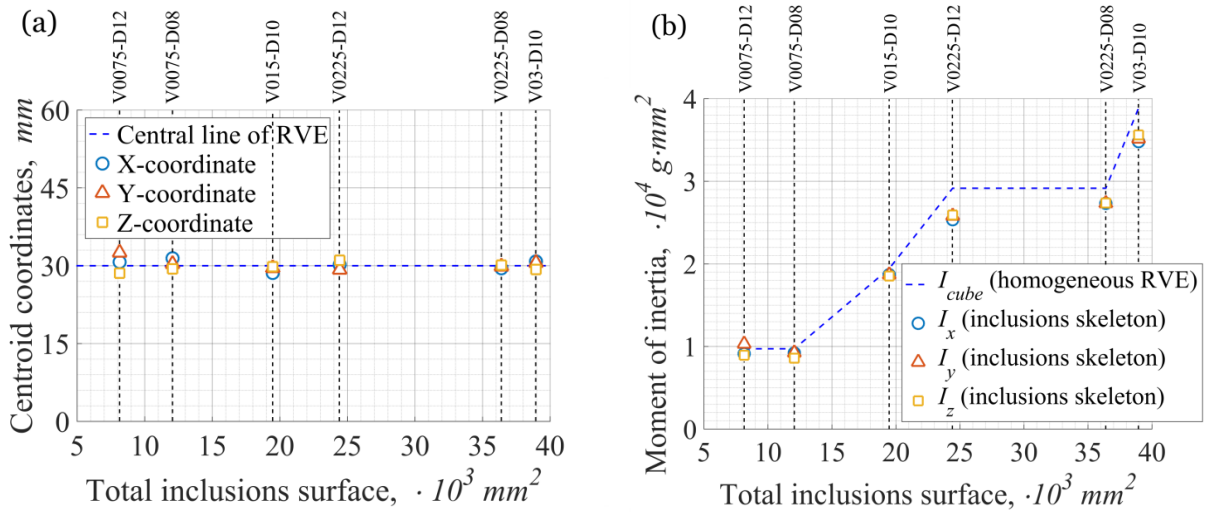


Figure 3 17: The values of coordinates of centroid of spherical inclusions (a) and moment of inertia of inclusions set in relation to the three main axes of the cube (b) as function of total inclusions surface. Results obtained for inclusions arrangements were compared to the central line of the cube (a) and the moment of inertia of an equivalent homogeneous solid (b)

Moreover, the standard deviation of moments of inertia does not exceed 1 % from the average for specimens with $V_{fr} \geq 0.15$ and 6.5 % for specimens with $V_{fr} = 0.075$ (Figure 3 17b). Thus, it can be concluded that, in accordance with the presented analysis, no axial preferential directions can be found for studied inclusions arrangements and the distribution of inclusions in the cube is close to homogeneous.

b) Surface of projections (force paths)

In powders/granular materials the external axial load is inhomogeneously transmitted through contacts between particles, forming so-called load-bearing chains (or force networks) which are going through the material in the direction of load [108]. A similar mechanism can be assumed for composite materials reinforced by rigid particles. Schematically, this type of load transmission is presented in Figure 3 18a: closely located inclusions (depicted as red circles) form regions of stress concentrations, which support most of the external load. Thus, that the strength of a composite material is not homogeneously distributed throughout its structure.

It is obvious that in the case when inclusions are more rigid than the matrix, an increase in the number and length of load-bearing chains will lead to an increase in specimen rigidity. In the framework of the present study, it was proposed to study location and number of potential load-bearing chains analyzing “surface of projections”, constructed by projecting inclusions on a certain plane of the cube. At each point, the magnitude of such surface is defined as the number of inclusions projected to this point (Figure 3 18b).

Construction of such surfaces for three main planes of the cube (XY, XZ and YZ) allows comparing rigidity of the specimen in different directions on a theoretical basis. Surfaces of projections were built with a resolution of 0.25 mm (Figure 3 18b). It must be noted that the presented method does not take into account the distance between inclusions in the potential load-bearing chain.

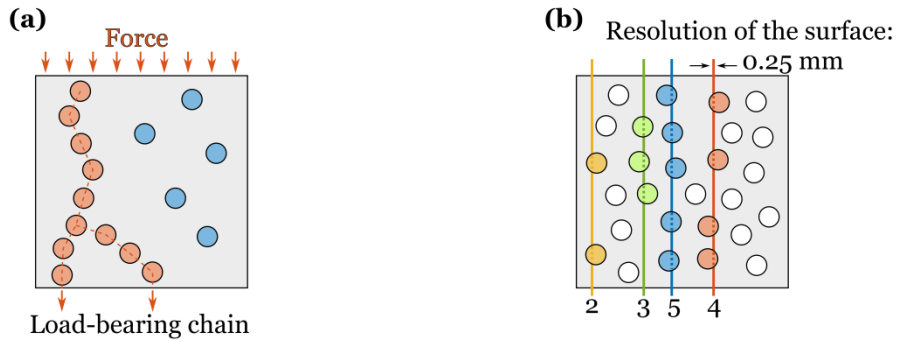


Figure 3.18: Schematic representation of a load-bearing chain in a composite material (a); construction of a surface of projections (b)

Figure 3.19a-f represents surfaces of projections for studied specimens containing inclusions. The number of inclusions n projected in a certain point (magnitude of a surface) is denoted by a colour map. For the reason of simplification of data representation, all magnitudes of each surface of projections were separated and plotted against the zero-value background. For example, first image in each row represents regions, in which at least one inclusion was projected. Particular region in the following text will be referred by variable n (= 1 for one projected inclusion, = 2 for two projected inclusions, etc.). The maximum magnitude for a certain surface of projections will be denoted as n_{max} .

During analysis of obtained surfaces of projections, two types of load-bearing chains can be distinguished. “Vertical” chains combine inclusions, which centres are located close to some common vertical line. On a surface of projections, these load-bearing chains form round contours of the size close to the dimension of inclusions. The other shape contours (thin ovals or formless constructions) observed on surfaces of projections can be referred to “shear” load-bearing chains. Load-bearing chains of this type are generated by inclusions, which centres are located aside from an average vertical line.

It can be assumed that the maximal vertical length L_{chain}^{max} of potential load-bearing chains is proportional to the inclusions diameter and the maximum magnitude of a surface of projections n_{max} . In this way, between two specimens V0075-D08 ($n_{max} = 4$) and V0075-D12 ($n_{max} = 3$) with the same inclusions’ volume fraction and different inclusions’ size, the last one has a higher value of $L_{chain}^{max} \sim Dn_{max}$ ($32 < 36$). Although it is impossible to define the number of load-bearing chains from the present analysis, calculation of the total area covered by each of n colour contours allows to study isotropy of a specimen and perform comparison between specimens. For a this purpose, fraction S_{fr}^n of a 60×60 square surface area covered by each of n colour contours was calculated for each of three main directions X, Y and Z.

Additionally, variation of the value S_{fr}^n calculated for different directions was analyzed using variation coefficient C_{var} , defined as follows:

$$C_{var} = \frac{1}{\mu} \sqrt{\frac{(S_{fr}^n(X) - \mu)^2 + (S_{fr}^n(Y) - \mu)^2 + (S_{fr}^n(Z) - \mu)^2}{3}} \quad (3.6)$$

were $\mu = \frac{1}{3} [S_{fr}^n(X) + S_{fr}^n(Y) + S_{fr}^n(Z)]$ is an average value of S_{fr}^n for a certain n . The value of S_{fr}^n calculated for the contour with number $n = n_{max}$ will be denoted in the following text as S_{fr}^{max} . Obtained data is presented in Table 3.3a-c.

 Table 3.3a: S_{fr}^n [%] calculated for each of the main directions and for different n

Number of projected inclusions (n)	V7.5-D8				V7.5-D12			
	$S_{fr}^n(X)$	$S_{fr}^n(Y)$	$S_{fr}^n(Z)$	C_{var} [%]	$S_{fr}^n(X)$	$S_{fr}^n(Y)$	$S_{fr}^n(Z)$	C_{var} [%]
1	47.53	52.03	54.58	5.7	46.8	45.18	39.49	7.2
	22.78	22.32	21.07	3.3	9.71	9.76	14.86	21.1
	11.01	8.33	8.14	14.3	0.0	1.53	2.17	73.8
	2.48	1.13	0.02	83.4	0.0	0.0	0.0	--
	0.0	0.0	0.0	--	0.0	0.0	0.0	--
	0.0	0.0	0.0	--	0.0	0.0	0.0	--

 Table 3.3b: S_{fr}^n [%] calculated for each of the main directions and for different n

Number of projected inclusions (n)	V22.5-D8				V22.5-D12			
	$S_{fr}^n(X)$	$S_{fr}^n(Y)$	$S_{fr}^n(Z)$	C_{var} [%]	$S_{fr}^n(X)$	$S_{fr}^n(Y)$	$S_{fr}^n(Z)$	C_{var} [%]
1	88.87	88.39	87.69	0.6	85.30	84.49	82.16	1.6
	74.58	74.90	74.57	0.2	60.01	57.85	57.38	2.0
	53.53	53.15	54.49	1.1	21.86	24.67	25.72	6.8
	28.11	26.92	27.22	1.9	2.41	2.56	4.39	28.9
	7.43	8.58	8.15	5.9	0.00	0.05	0.00	--
	0.10	0.75	0.55	57.9	0.00	0.00	0.00	--

 Table 3.3c: S_{fr}^n [%] calculated for each of the main directions and for different n

Number of projected inclusions (n)	V15-D10				V30-D10			
	$S_{fr}^n(X)$	$S_{fr}^n(Y)$	$S_{fr}^n(Z)$	C_{var} [%]	$S_{fr}^n(X)$	$S_{fr}^n(Y)$	$S_{fr}^n(Z)$	C_{var} [%]
1	68.88	65.90	71.87	3.5	90.32	90.27	93.09	1.4
	42.94	45.72	42.99	3.0	80.89	79.05	83.97	2.5
	19.39	18.13	17.40	4.5	62.07	59.83	61.30	1.5
	4.06	5.50	3.03	24.1	31.54	33.36	26.95	8.8
	0.00	0.00	0.00	0.00	5.11	7.39	4.81	20.0
	0.00	0.00	0.00	0.00	0.51	0.63	0.32	26.38

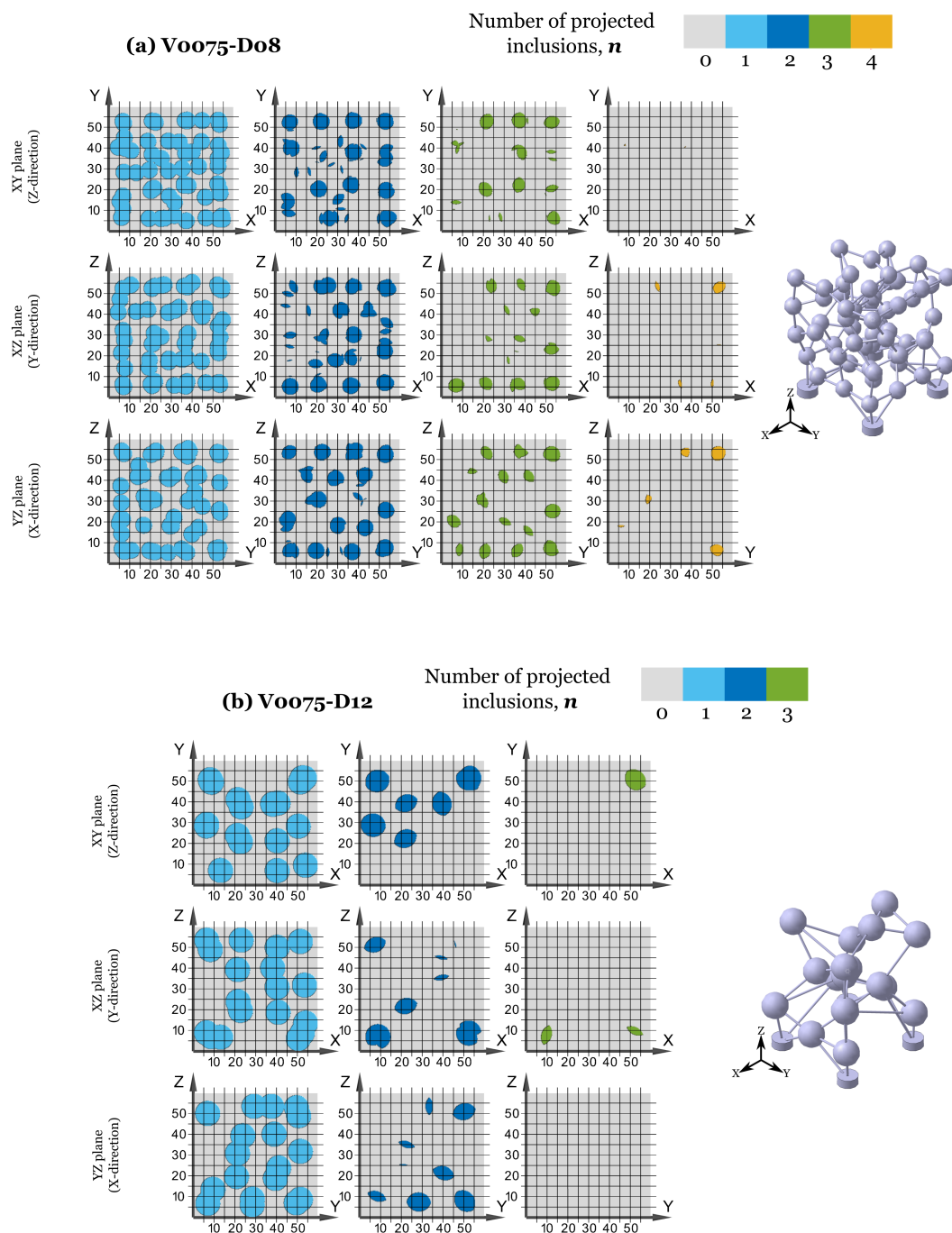


Figure 3.19 a-b: Surfaces of projections for specimens Voo75-Do8 (a) and Voo75-D12 (b)

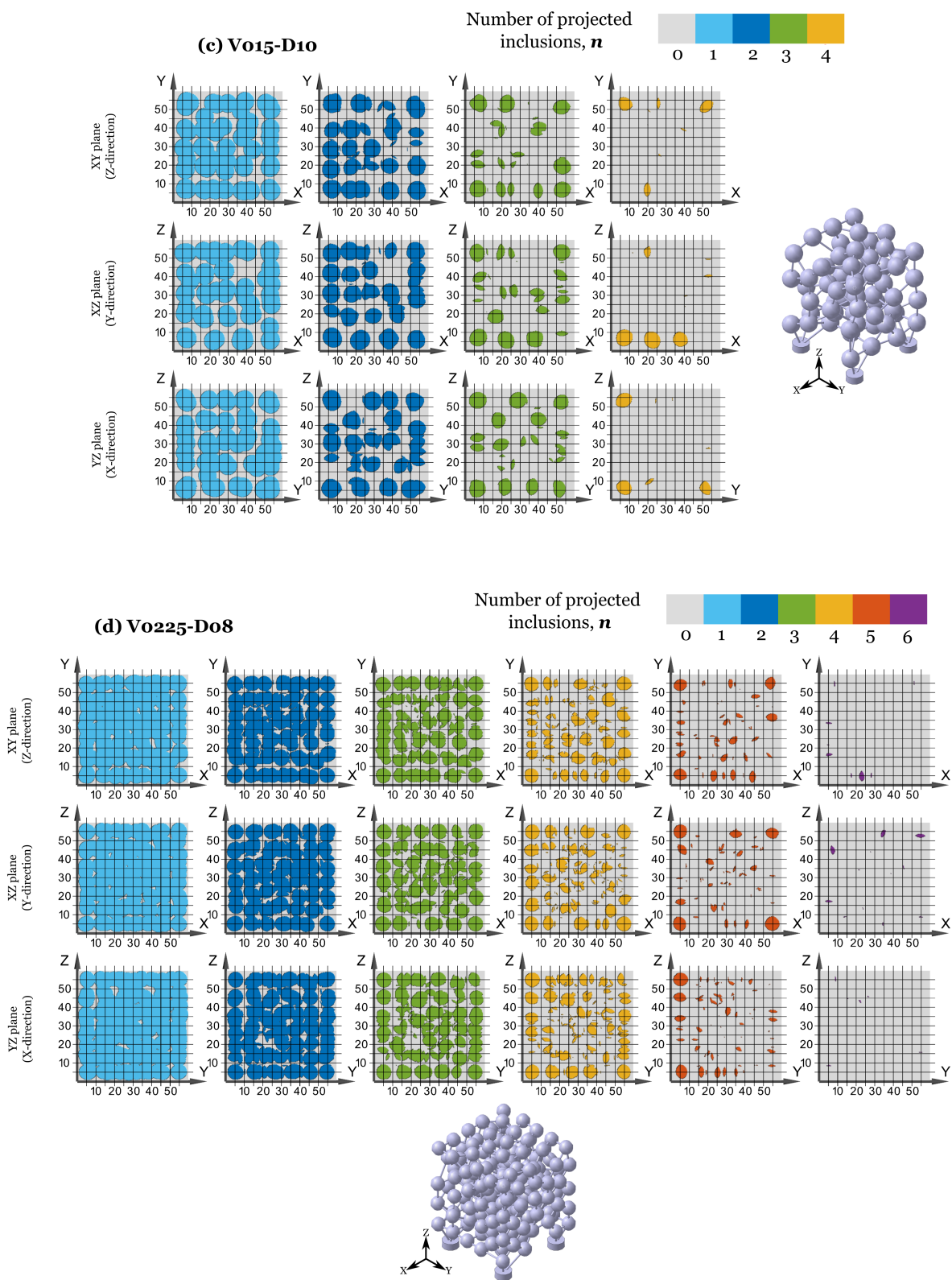


Figure 3.20 c-d: Surfaces of projections for specimens Vo15-D10 (c) and Vo225-Do8 (d)

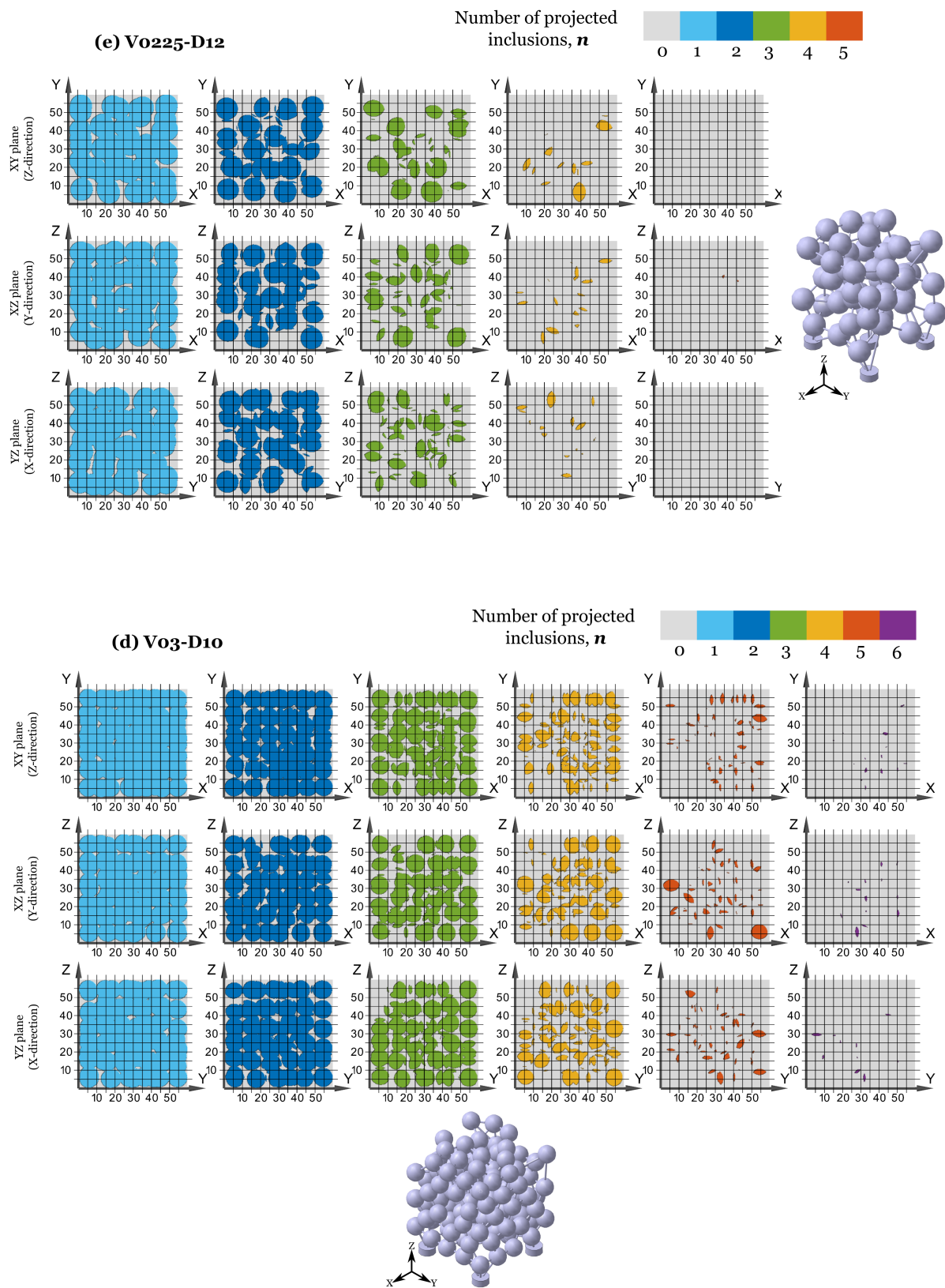


Figure 3.20 e-f: Surfaces of projections for specimens Vo225-D12 (e) and Vo3-D10 (f)

First of all, it is seen that an increase in a volume fraction, as well as a decrease in the size of inclusions, lead to an increase in load-bearing chains number (an increase in S_{fr}^n for each n) and lengths (and increase in n_{max}).

It can be seen from Figure 3.19a-f and Table 3.3a-c that certain differences can be found between main directions of studied specimens. For example, the value of n_{max} obtained for V0225-D12 specimen in the Y-direction (XZ-plane) is equal to 5, while for other two directions this value is equal to 4. It means that potentially Y-direction of the specimen can have a higher rigidity. Similarly it was found that for the case of V0075-D12 specimen n_{max} equals to 2 in the X-direction and to 3 in the other directions. It is also seen that the value of C_{var} grows with an increase in contour number n . It means that the difference between values of S_{fr}^n calculated for X-, Y- and Z- directions becomes more distinct for high values of n , and, thereby, it can be assumed that the stiffest direction can be found by the highest value of S_{fr}^{max} .

Concluding, it can be said that a preferred direction for each specimen can be suggested on the base of the presented analysis of surfaces of projections (*e.g.* X for V7.5-D8, Y for V22.5-D8, Z for V22.5-D12, etc.). However, it must be noted, that the significant difference in the value of S_{fr}^n , calculated for different directions, can be found only at $n = n_{max}$, which always corresponds to a very small values of S_{fr}^n and, consequently, to a negligible contribution to the rigidity of a specimen.

c) Links orientation and number. Total volume fraction of links

In this section, the influence of the presence of rigid links connecting inclusions on the mechanical behaviour of VM specimens was studied. Links can be considered as randomly oriented rigid fillers inside the matrix. Thus, the volume fraction of links as well as their orientation can be analyzed in order to estimate their contribution to the mechanical behaviour of the specimens. The value of volume fraction calculated relatively to 60x60x60 cubic RVE volume (used as the reference for the definition of inclusions' volume fraction) is presented in the first column of Table 3.4. It is seen that the volume fraction of links is negligibly small compared with the volume fraction of inclusions. This statement is especially applicable for specimens with higher inclusions' volume fraction and size.

Fibers oriented with the direction of load can sufficiently increase the rigidity of a composite

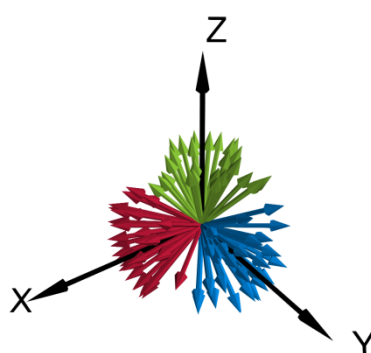


Figure 3.20: Orientations of links of the specimen V7.5-D8 inclined by less than 45° towards coordinate axes

material. By analogy, the orientation of links relative to the main directions of the cubic specimen can influence isotropy of the behaviour of a specimen. It was assumed that only links inclined by less than 45° towards main axes influence the mechanical behaviour of a specimen. As an example, Figure 3.20 represents orientations of all links of the V7.5-D8 specimen by vectors plotted from the same point (orientation vectors were calculated only for links inclined by less than 45° towards coordinate axes). A number of links oriented in each of three main directions can be found in Table 3.4. It is seen that for each specimen direction with the highest number of oriented links can be found. However, it must be admitted that the difference between directions does not exceed 10 % from the average for most of the structures under study.

Summarizing the above discussion, small volume fraction and absence of the primary orientation allow expecting the negligible influence of links presence on the mechanical behaviour of studied specimens.

Thus, it can be concluded that isotropy of the mechanical response of VM specimens, observed during the experimental investigation, is based on homogeneity of the internal structure. Homogeneity of the internal structure allows to confirm one more time the correctness of the choice of the specimen size characteristic size.

Table 3.4: Links volume fraction (calculated relative to the volume of RVE and the volume of inclusions) and orientation

	Links' volume fraction [%]	Links volume compared to inclusions volume [%]	Number of links oriented by less than 45° towards:		
			X-direction	Y-direction	Z-direction
V0075-D08	0.27	3.63	25	31	34
V0075-D12	0.13	1.72	8	7	7
V015-D10	0.21	1.39	35	35	31
V0225-D8	0.34	1.51	102	105	90
V0225-D12	0.12	0.53	30	29	23
V03-D10	0.18	0.60	67	63	71

3.4. Finite element simulation

Finite element simulation of VM specimens subjected to a loading-unloading cycle in the mode of compression was carried out. The following aspects are covered in this section:

- Identification of material models for the matrix and inclusions
- Description of the finite element model (meshing, boundary conditions, etc.)
- Investigation of the macroscopic response of VM specimens
- Study of internal structure and local stress concentrations

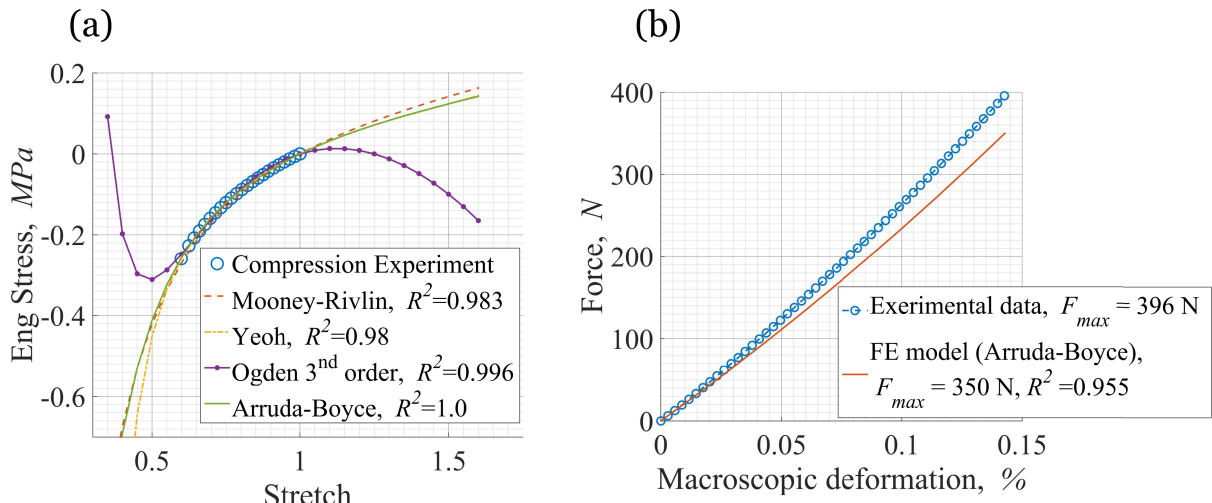


Figure 3.21: (a) Fitting of different hyperelastic models to QS compression data of a cylindrical silicone specimen; (b) prediction by FE simulation of the mechanical behaviour of Voo-D10 specimen using previously fitted Arruda-Boyce hyperelastic model

3.4.1. Material models

Inclusions were modelled using the elastic material approach with parameters of Young's modulus and Poisson's ratio identified in accordance with ABS material specifications (2150 MPa and 0.4 respectively).

Fitting of a hyperelastic material model of the matrix was carried out using two different approaches: 1) standard fitting process (described in Chapter 2: Section 3.3) using cylindrical specimen and 2) inverse-identification method using experimental data obtained for the Voo-D10 specimen.

a) Fitting to QS uniaxial compression experimental data

Figure 3.21a presents fitting results for 4 different hyperelastic models. It is seen that all models can be successfully used to fit experimental data. However, only Mooney-Rivlin, Yeoh and Arruda-Boyce models show good stability for the big range of possible stretch values in a uniaxial direction (poor stability would mean non-physical growth or decay of stress with an increase in a strain like in the case of Ogden model). It can be concluded from Figure 3.21a that the Arruda-Boyce hyperelastic model has the best fit with $R^2=1$.

Performance of the adjusted Arruda-Boyce model was verified by using FE simulation of the Voo-D10 specimen subjected to a compression load. Comparison between results of FE simulation and experimental data has revealed the insufficient accuracy of the model at high values of macroscopic strain (Figure 3.21b). Inverse-identification method was implemented in order to increase the accuracy of the material model.

b) Inverse Identification method

Inverse identification method was based on minimization of a mean square difference between Force vs Displacement curves obtained for Voo-D10 specimen during the experimental study and FE simulation (see Section 3.4.2 for the description of the FE model).

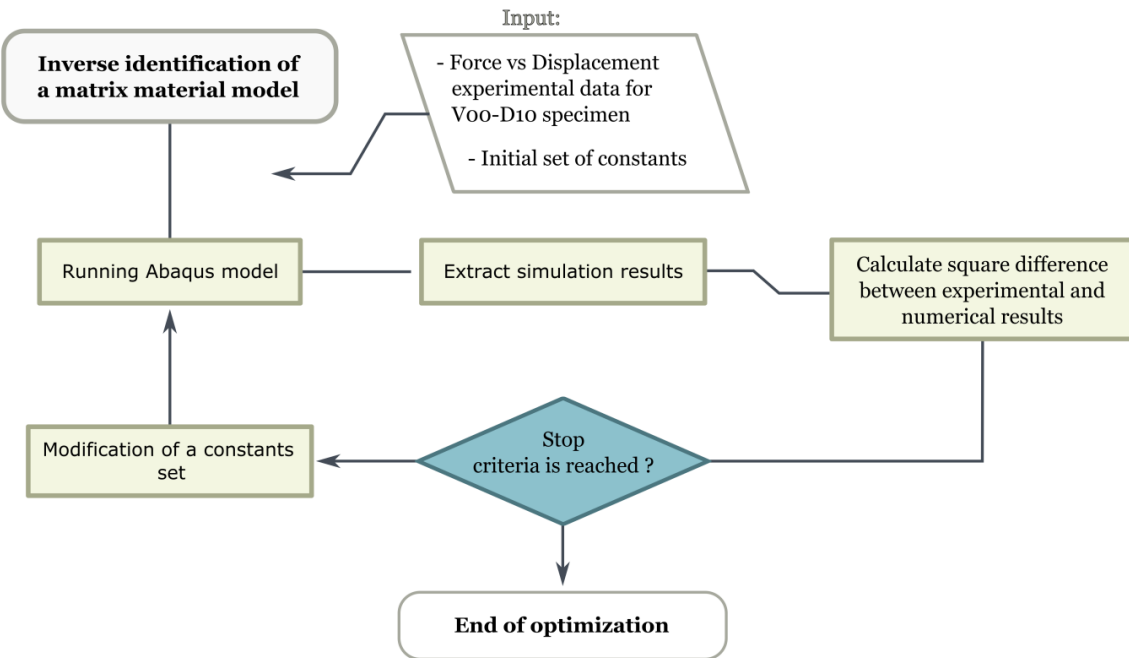


Figure 3.22: Scheme of inverse identification process

As in the case of a direct material identification, a medium response of the specimen was considered, in order to exclude friction influence from consideration. An iterative algorithm was developed using Python programming language to control optimization process. Constants of the material model were modified in each iteration step and a new simulation was performed afterwards (Figure 3.22). In this way, inverse identification method allows fitting of the material model using mechanical response of the material subjected to a multiaxial state of load (due to the geometry of the specimen and applied boundary conditions). Inverse identification of constants set was performed for the Arruda-Boyce hyperelastic model only, as its capabilities to describe the behaviour of the studied material was proved.

Constant sets identified by classical and inverse-identification fitting algorithms are presented in Table 3.5.

3.4.2. Finite element model of VM specimens

a) Meshing

The complex geometry of VM specimens requires additional attention during meshing process. A big difference between macroscopic and local characteristic sizes of a specimen

Table 3.5: Constants of Arruda-Boyce hyperelastic model

	C1 [MPa]	N
a) Fitting to QS uniaxial compression experiment data	0.115	6.2
b) Inverse Identification method	0.132	6.549

$$W_{AB} = C_1 \sum_{i=1}^5 \alpha_i \beta^{i-1} (I_B^{-i} - 3^i) \quad \text{with} \quad \beta = \frac{1}{N}; \quad \alpha = \left[\frac{1}{2}, \frac{1}{20}, \frac{11}{1050}, \frac{19}{7000}, \frac{519}{673750} \right]$$

(i.e. an edge of the cubic specimen $L + \Delta L = 70$ mm is much higher than the minimal distance between inclusions $a = 1$ mm) makes complicated to choose the best method of meshing and an element size without causing numerical problems. For example, a very fine mesh can be very accurate in repeating geometry of a specimen near inclusions, however it, can lead to generation of a huge number of elements and, as a result, a very long calculation time and low computational efficiency. On the opposite, a very coarse mesh will cause problems to describe a specimen's internal geometry, which can result in bad shaped elements and convergence issues afterwards.

Standard meshing algorithms available in Abaqus software are not effective enough, so capabilities of HyperMesh software were used instead. HyperMesh software allows to create mesh both accurately repeating specimens geometry (by mesh-refinement in certain regions) and consisting of the optimal number of elements (by increasing element size in certain regions). The second big advantage of HyperMesh is a powerful mesh-analyzing algorithm implemented in the software, which help to find poor-shaped elements and re-build them. An example of obtained mesh for the matrix and inclusions is presented in Figure 3.23a-b.

b) Boundary conditions

Any finite element model implies a certain number of assumptions and simplifications. Simulation of compression plates would allow the increasing accuracy of the model and bring it closer to the real case of the study. However, resolution of the contact problem established between specimen and compression plates can be complicated and time-consuming, especially when the big number of nodes/elements is involved in this problem. As it was mentioned above, the complex structure of VM specimen requires a high number of elements

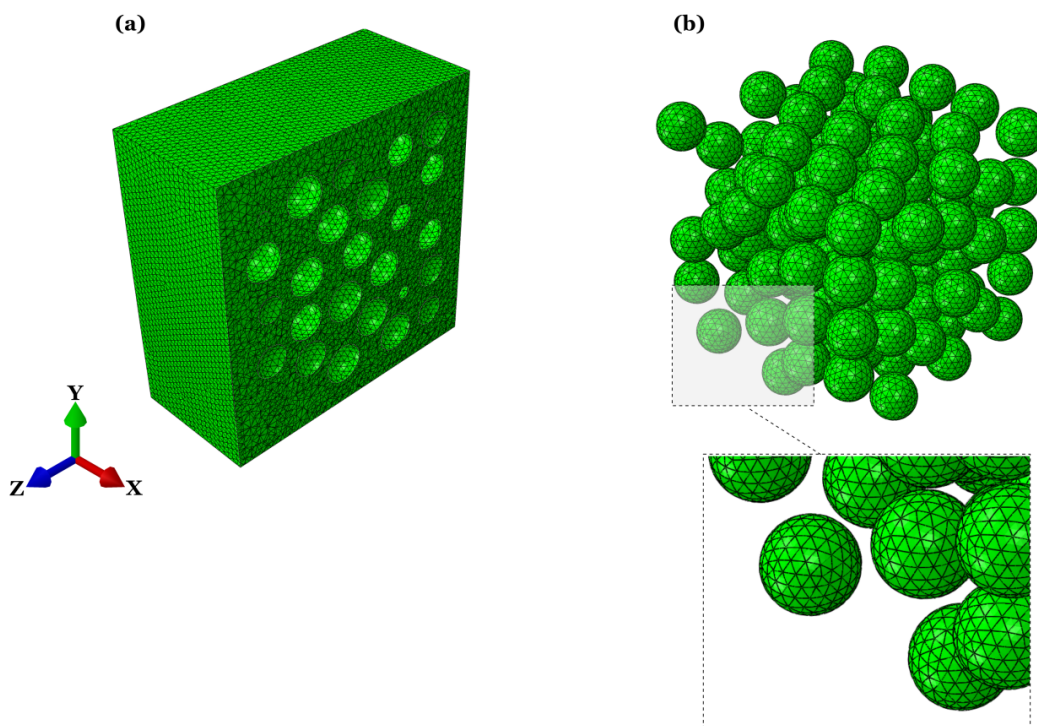


Figure 3.23: Meshing of the matrix (a) and the inclusions skeleton (b) of Vo3-D10 specimen

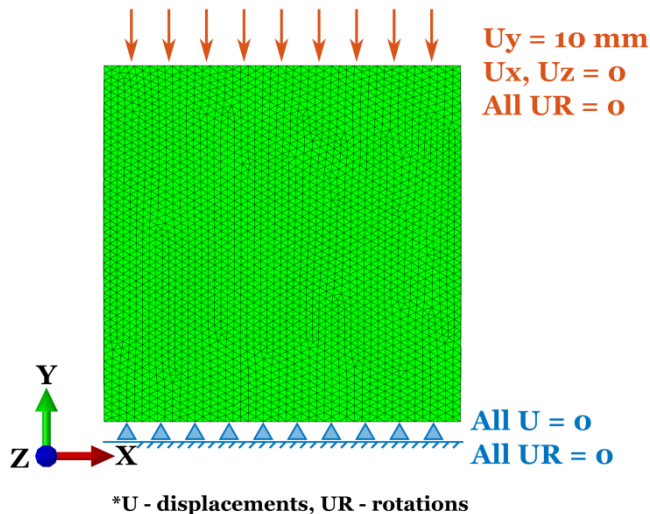


Figure 3.24: Boundary conditions for VM finite element model

to create appropriate meshing.

Thus, in order to simplify the studied case and reduce the computational time it was decided to model compression of the specimen by applying displacement boundary conditions directly on the top surface of the specimen (respectively to the direction of load). Nodes on the top surface were rigidly coupled together and all rotations, as well as displacements perpendicular to the direction of load, were prohibited. Nodes on the bottom surface (respectively to the direction of load) were also coupled and fully constrained in all directions of freedom (DOF). These boundary conditions (BC) allow to reduce the complexity of the numerical problem by eliminating resolution of the contact problem between specimen and compression plates. However, this corresponds to a “glued” top and bottom surfaces of a specimen, which can be accepted as an approximation of a real case. Boundary conditions are schematically presented in Figure 3.24.

c) Contact type influence; influence of the friction value

Modeling of a composite structure requires the definition of a contact law between matrix and inclusions. In general, this contact must be defined either as a tie constraint contact (an effect of inclusions “glued” to the matrix) or as a frictional contact (relative displacements and disconnection of contact surfaces are allowed).

It was found during the experimental investigation that VM specimens dissipate energy during cyclic loading. It was proved that silicone material of the matrix has hyperelastic behaviour and doesn't dissipate energy by itself. Thus, energy dissipation during cyclic loading of VM specimens was caused by friction between inclusions and matrix.

Thus, frictional contact type was chosen. In order to find appropriate value of friction coefficient, preliminary simulations were carried out. Influence of the value of friction coefficient on the mechanical behaviour of the structure was studied using Vo15-D10 specimen. This specimen was chosen due to its sufficient inhomogeneity along with an average computational complexity. Force vs Deformation curves obtained during compression experiment and FE simulations are presented in Figure 3.25.

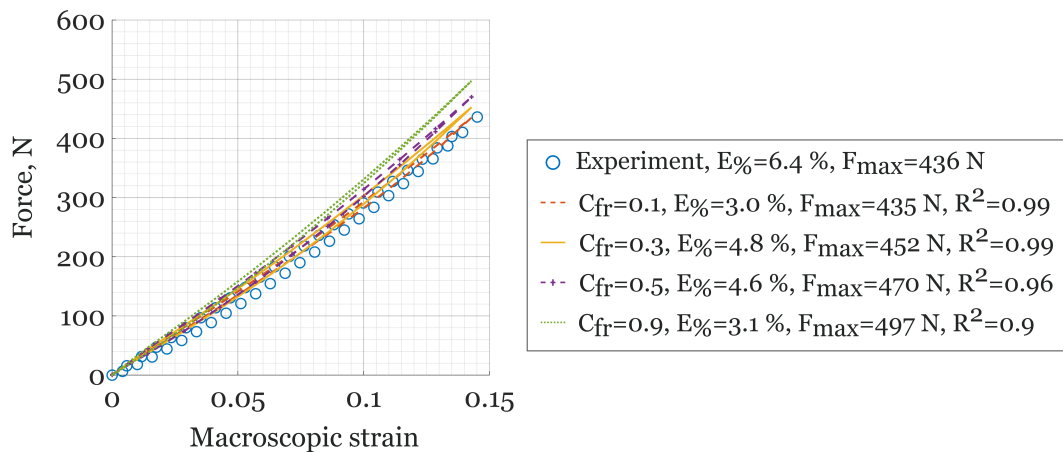


Figure 3 25: Influence of a friction coefficient value on the mechanical response of the FE model of V15-D10 specimen

It is seen that a decrease in the value of friction coefficient leads to a decrease in the value of F_{max} . The value of dissipated energy, on the opposite, has a non-monotonic dependence on friction coefficient value. Concerning maximum force, the value of friction coefficient equal to 0.1 provides the best fit to experimental data. However, a decrease in friction coefficient value leads to higher relative displacements between contacting surfaces, which increases numerical complexity of the finite element problem. For example, a decrease of a friction coefficient from 0.3 to 0.1 increases the time of calculation on 40 % (from ~19.5 hours to ~48 hours). Thus, following the compromise between accuracy and computational efficiency, the value of a friction coefficient equal to 0.3 was chosen for FE simulation.

3.4.3. Global Force vs Displacement/Deformation behaviour

The macroscopic mechanical behaviour of FE models of VM specimens was investigated following the strategy similar to the one used in the experimental study. First of all, isotropy of VM specimens was verified. Secondly, surfaces of response were defined. Finally, the global comparison between the macroscopic response of all specimens was carried out.

For the reasons of resources and time spends optimization it was decided to reduce the number of performed FE simulations. Thereby, verification of VM specimens' isotropy was based on simulation of only certain geometries for only certain loading directions. In this way, compression in all directions was simulated only for V0075-D08, V0075-D12 and V015-D10 specimens; simulation of V0225-D08 specimen (the highest number of inclusions) subjected to full (loading-unloading) cycle in Y-direction and half-(only loading and as a result no dissipation energy data) cycle in X-direction was carried out.

The rest of specimens were modelled considering only Y-direction of compressive load. Summary of all macroscopic data (F_{max} and $E\%$ [%]) obtained during FE simulation campaign is summarized in Table 3.6.

Analysis of the data presented in Table 3.6 shows that observed anisotropy of the specimen's behaviour does not exceed 0.5 % from an average value of F_{max} and can be neglected. Further, study of the VM specimens' behaviour will be based on data obtained for Y-loading direction only.

Recalling the discussion from Section 3.3 of the present chapter, it can be additionally highlighted, that the stiffest direction, found using FE approach, corresponds to a direction with the highest value of S_{fr}^{max} in Table 3.3a-c.

Table 3.6: Maximum force and Dissipated energy fraction data obtained during FE simulation of VM specimens subjected to compression load

	F_{max} [N]			$E\%$ [%]		
	X	Y	Z	X	Y	Z
Voo-D10	---	399.6	---	---	0.0	---
Voo75-Do8	426.6	426.2	425.8	2.4	2.4	2.2
Voo75-D12	428.2	427.6	428.5	2.3	2.4	2.4
Vo15-D10	451.1	452.5	450.5	4.7	4.8	4.6
Vo225-D8	---	475.6	475.9	---	7.3	---
Vo225-D12	---	480.1	---	---	7.5	---
Vo3-D10	---	515.9	---	---	10.3	---

3.4.4. Response surfaces (FEM)

Response surfaces were constructed on the base data obtained during of FE simulation of VM specimens subjected to compression loading in the Y-direction (Figure 3.26). Expressions for these surfaces were obtained using equation (3.3) and are as follows:

$$F_{max}(\hat{V}_{fr}, \hat{D}) = 452.49 + 54.96\hat{V}_{fr} + 1.71\hat{D} + 1.77\hat{V}_{fr}\hat{D} + 6.4\hat{V}_{fr}^2 - 2.32\hat{D}^2 \quad (3.7a)$$

$$E\%(\hat{V}_{fr}, \hat{D}) = 4.772 + 5.107\hat{V}_{fr} + 0.088\hat{D} + 0.092\hat{V}_{fr}\hat{D} + 0.398\hat{V}_{fr}^2 + 0.015\hat{D}^2 \quad (3.7b)$$

where \hat{V}_{fr} and \hat{D} are standardized variables V_{fr} and D respectively.

It is seen from Figure 3.27a-d that in the opposite to the experimental case (see Section 3.3.1) both F_{max} and $E\%$ parameters grow monotonically with the value of V_{fr} . It was also found that both parameters have negligible dependency on the value of inclusions' size D .

3.4.5. Comparison between specimens

Figure 3.27 presents Force vs Macroscopic strain curves obtained during FE simulations of VM specimens subjected to compression load in the Y-direction. It is seen that an increase in inclusions' volume fraction leads to an increase in values of F_{max} and $E\%$. In the opposite of volume fraction parameter, inclusions' size has no influence on macroscopic response of a specimen.

Indeed, no significant difference can be found in values of F_{max} and $E\%$ obtained for specimen pairs Voo75-Do8/12 and Vo225-Do8/12. The insignificant difference in values of F_{max} and

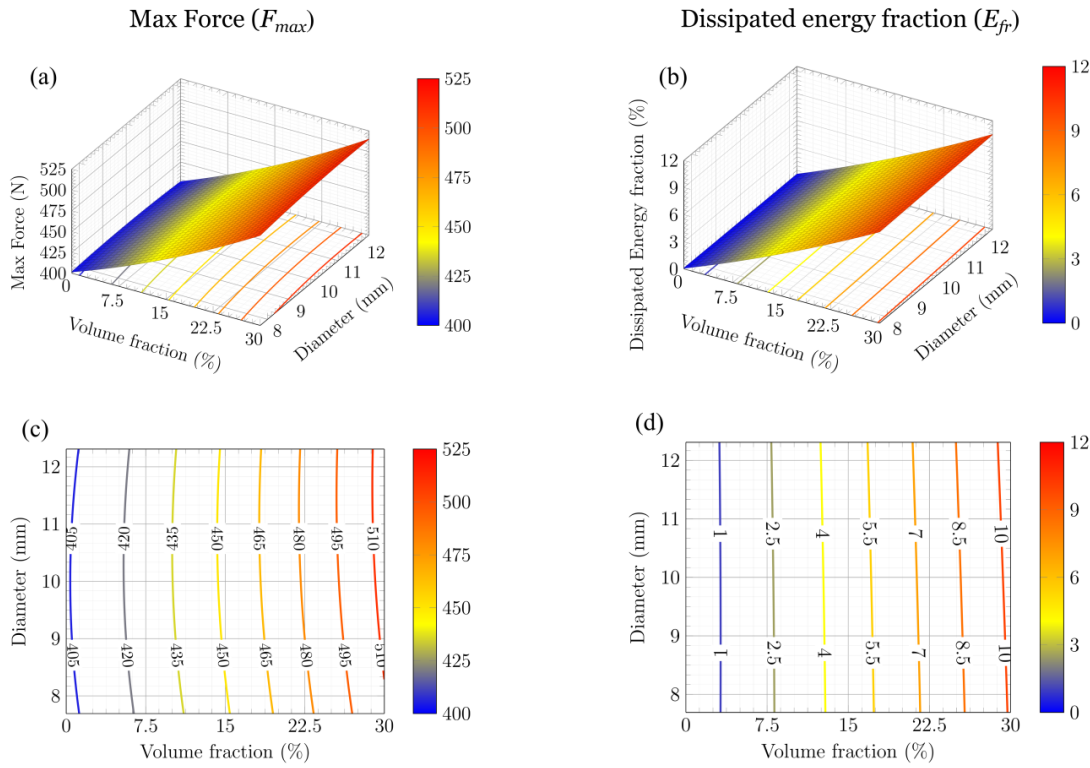


Figure 3.26: F_{max} (a) and $E_{\%}$ (b) output parameters obtained during FE simulations as functions of inclusions' volume fraction and diameter

$E_{\%}$, calculated for specimen pairs V0075-D08/12 and Vo225-D08/12, can be easily explained by the difference in resulted volume fraction indicated in Table 3.1.

Let us recall from the discussion in Section 3.3.3 that inclusion's volume fraction influences both number and length of load-bearing chains. At the same time, the size of inclusions affects, for the most part, only the length of load-bearing chains. The connection between the value of L_{chain}^{max} and specimens' rigidity was not proven during the present study. However, results of FE simulation along with observations made during analytical study of structures of VM specimens in Section b) allow assuming that the value of L_{chain}^{max} has no principal influence on specimens' rigidity.

3.4.6. Local stress concentrations

Continuing the analytical study of the internal structure of VM specimens, described in Section 3.3.3, finite element method allows investigation of specimen's internal mechanics during compression experiment. Stress/strain concentrations localized in the matrix material, confined between inclusions, can be presented by taking sections of a specimen in a direction perpendicular to the direction of load. Such stress/strain maps allow to find and visualize load-bearing chains going through the matrix. Cross sections' positions were proposed in accordance with the location of potential load-bearing chains (determined in Section 3.3.3). This allows to find the most representative regions of a specimen.

An example of stress concentrations analysis is presented on the base of data obtained during FE simulation of Vo225-D08 specimen (Figure 3.28). A similar approach can be used for the rest of the specimens. For simplicity reasons, surfaces of projections of Vo225-D08 specimen

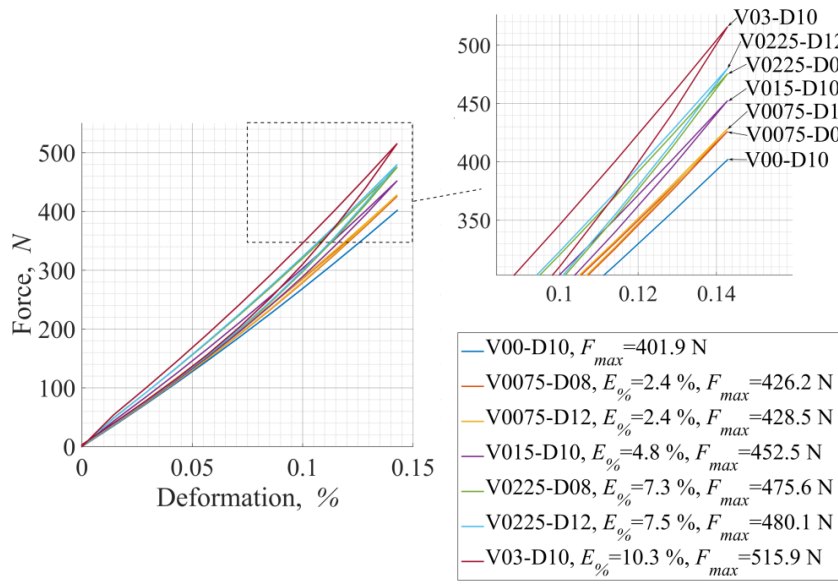


Figure 3.27: Force vs Macroscopic strain curves obtained during FE simulations of VM specimens subjected to compression load in the Y-direction

calculated in the Y direction (XZ plane) are duplicated in this section on the top of Figure 3.28.

It is seen that the biggest “Vertical” load-bearing chains ($n=5$) can be found close to the corners of XZ-plane (lines $x=5$ and $x=55$). As it is seen from Figure 3.28, the longest

“Shear” load-bearing chains ($n=6$) are located near lines $x=5$, $x=7.5$, $x=35.5$ and $x=55$. Von Mises, Y-uniaxial and YZ-shear stress maps, calculated in two cross sections at $x=5$ and $x=35.5$, are presented in Figure 3.28a-c. Inclusions’ geometries were removed from the figures for a better view of the stress state of the matrix material.

Von Mises stress, computed from the Cauchy stress tensor components, can be considered as an integral parameter of a material stress state. In this way, a map of Von Mises stress values can represent stress concentrations regardless the prevailing loading type (uniaxial, shear, etc.). Chains of Von Mises stress concentrations going from the top to the bottom of the specimen can be seen in Figure 3.28a. As it was assumed earlier, it is seen that a higher number of inclusions in the section leads to an increase in a number and length of load-bearing chains. It can be also noted that the value of Von Mises stress in the present cross sections reaches ~ 0.56 MPa, while the average value in the matrix is about 0.045 MPa (~ 12.5 times lower).

The similar picture can be found for the Y-true strain map: distinct chains of strain concentrations can be found in the present section (Figure 3.28b). It can be found that the magnitude of strain reaches values 3-5 times higher than the average in the matrix and 5-7 times higher than the applied strain (10 mm of applied load ~ 0.15 of true strain).

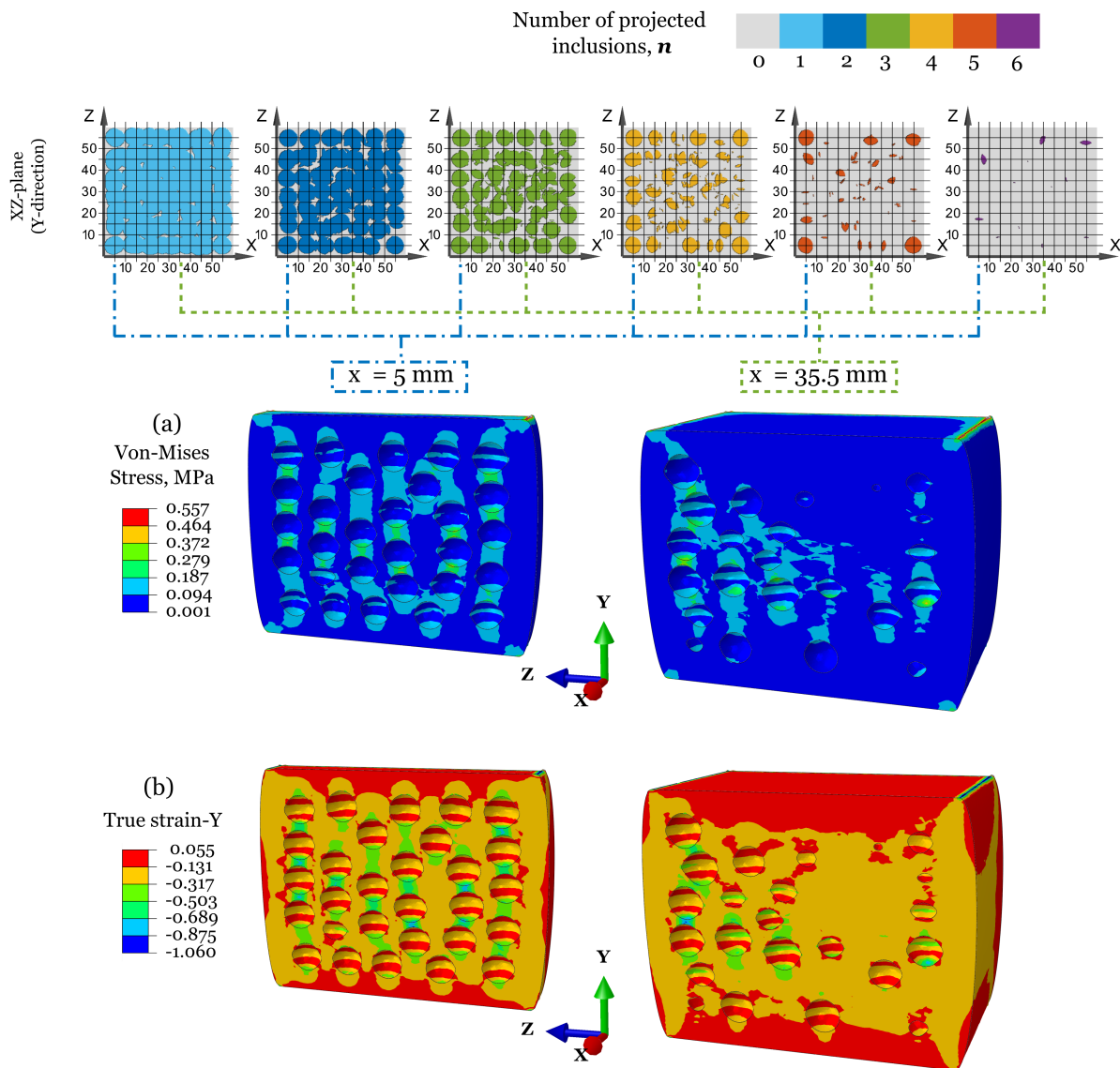


Figure 3.28: Maps of (a) Von Mises stress and (b) Y-uniaxial true strain at $x = 5 \text{ mm}$ and $x = 35.5 \text{ mm}$ cross sections (relatively to the central, $60 \times 60 \times 60 \text{ mm}^3$, part) of V22.5-D8 FE model subjected to compression displacement of 10 mm

3.5. Comparison between FE and experimental results. Discussion

Comparison between the results of the experimental investigation and FE simulation was carried out. For this purpose values of F_{max} and $E\%$ obtained during experiment and FE simulation of a VM specimens subjected to compression load in the Y-direction were plotted against total inclusions' surface area S_{total} (Figure 3.29a-b). It is seen from Figure 3.29a that a non-monotonic dependence of F_{max} on S_{total} observed during experimental investigation of VM specimens is not repeated for the case of FE models. It was already discussed in Section 3.4.4b that in the case of FE simulation the value of F_{max} grows monotonically with an increase in inclusions' volume fraction. It can be noted that the relative difference between values of F_{max} for specimens Voo-D10, Voo75-D08, Vo15-D10 and Vo3-D10 calculated using experimental and FE simulation data is small and varies from 0 to 5 %.

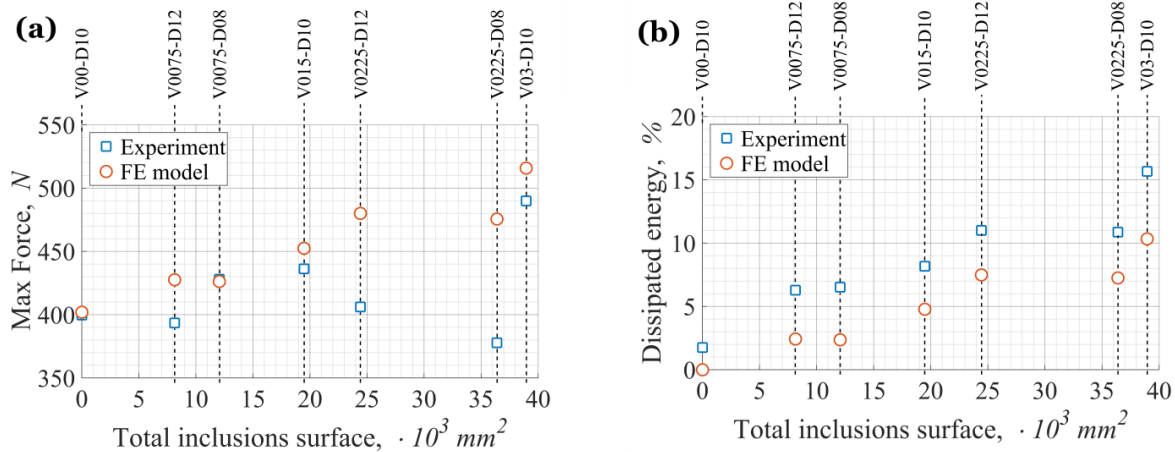


Figure 3.29: Dependences of F_{max} (a) and $E\%$ (b) on total inclusions' surface area obtained during experimental and FE investigations

Both experimental and FEM results show monotonic dependency of E_{fr} on S_{total} . Figure 3.29b shows that the value of $E\%$ obtained during experimental investigation of Voo-D10 specimen is 1.8 % higher than the correspondent value obtained during FE simulation. Obviously, due to established boundary conditions and chosen material behaviour, Voo-D10 specimen does not dissipate energy during FE simulation. On the opposite, presence of friction between the specimen and compression plates results in energy dissipation ($E\% = 1.8\%$) during experimental study.

In the case of specimens with inclusions, additional energy dissipation takes place due to friction between inclusions' and matrix surfaces. Moreover, the difference in the value of $E\%$ calculated for experimental and FE data is higher at the presence of inclusions. For example $E\%^{exp} - E\%^{FEM} = 3.6\%$ for V0225-D08 specimen, which is two times higher than the corresponding value for the specimen without inclusions. The following explanations can be found. Additional energy dissipation observed during experimental investigation can be connected with a stair-like surface of 3D printed geometries (inclusions and links, see Figure 3.7c). This influence can be non-uniform and can depend on relative the location of inclusions and the level of applied load.

4. Conclusions to Chapter 3

Influence of size (from 8 to 12 mm) and volume fraction (from 0 % to 30 %) of monodisperse spherical inclusions, randomly packed into a cubic matrix, on the mechanical behaviour of the obtained composite structure were investigated using “Virtual Material” approach. This approach allows the numerical study of a theoretical case without losing connection with results of a real experiment.

In the framework of “Virtual Material,” method 7 real and numerical specimens with different parameters of inclusions' size and volume fraction were developed. Direct geometrical correspondence between real and numerical specimens with the same parameters was ensured. Parameters of inclusions were chosen in accordance with Doehlert experimental design, which allowed to use obtained experimental and numerical data for construction “response surfaces”.

Inclusions skeletons obtained as a result of packing and links arrangement algorithms were analyzed analytically. It was shown on a theoretical basis that no preferential direction can be found for the inclusions arrangements, and the moment of inertia of developed specimens is close to a case of homogeneous cubic geometry.

A new method based on a theoretical analysis of potential load-bearing chains in a composite material was developed. It was shown that the length and a number of these chains can be approximated, which allows to compare rigidity of different specimens and different main directions of each specimen (on a qualitative basis).

The macroscopic mechanical behaviour of obtained VM specimens was studied experimentally and numerically (finite element simulation). It was found during experimental study that rigidity of material (F_{max} parameter) non-monotonically depends on both volume fraction (V_{fr}) and size (D) parameters of inclusions. This was explained by two possibilities: nucleation of porosities near inclusions (no adhesion between inclusions and matrix was found) and/or a slight difference in the mechanical behaviour of a silicone matrix for different specimens due to lack of material specification. Dissipative properties ($E\%$ parameter) of experimentally studied specimens, on the opposite, has shown a monotonic dependence on the value of V_{fr} and almost no dependence on the value of D .

In contradiction to the experimental study, FE simulation results have shown the similar qualitative behaviour of both F_{max} and $E\%$ parameters: monotonic dependence on the value of V_{fr} and small negligible dependence on the value of D .

Quantitative comparison between results of experimental and FE studies was also carried out. It was found that the relative difference between values of F_{max} for specimens Voo-D10, Voo75-Do8, Vo15-D10 and Vo3-D10 calculated using experimental and FE simulation data is small and varies from 0 to 5 %. It was shown that dependences of $E\%$ obtained during experimental and FE investigations have a similar qualitative behaviour. It was also found that the values of $E\%$ obtained during experimental investigation are always higher than ones obtained during FE simulation. Moreover, the difference in the value of $E\%$ calculated for experimental and FE data is higher at the presence of inclusions.

Finally, mechanics of the internal structure of VM specimens subjected to compression load was analyzed using capabilities of a finite element method. It was shown in the example of Vo225-Do8 specimen that visualization of stress/strain concentrations localized in the matrix material, confined between inclusions, allow to find and to visualize load-bearing chains going through the matrix. Analysis of a Von-Mises stress maps has proved a theoretical suggestion that a higher number of inclusions in the section leads to an increase in a number and length of load-bearing chains. It was also found that the value of Von Mises stress in load-bearing chains is almost 8 times higher than the average in the matrix.

Following methods described in the present chapter, the study of a more general case, in terms of problem discretization, can be performed (more than one fraction of inclusions, different inclusions' shapes, the visco-hyperelastic behaviour of the matrix etc.). In this way, the "Virtual Material" approach can allow the precise study of parameters of a bituminous mixture (BM) material by varying inclusions sizes, fractions (considering few fractions), shapes and the mechanical behaviour of the matrix material. The recent progress in additive manufacturing technologies shows potential to increase the precision of developed

specimens. For example, the possibility of 3D printing by few permanent materials allows excluding necessity in rigid links [16]. An additional increase in polymeric materials, available for 3D printing, would greatly extend the variety of compositions to study.

General conclusions. Remarks and perspectives

Nowadays, railway transportation is a fast developing field with a high demand for new technologies, approaches. The construction of a ballasted railway track did not evolve a lot of significant changes for the last 40 years and do not fully meet requirements for the modern high-speed trains, the speed of which, as a result, must be limited. The recent progress in computational capabilities allow for extended understanding and reconsider some of the already existing practices in order to increase bearing capacities of a ballasted railway track. As compared with experimental investigations (performed both in laboratory and *in-situ*), the numerical approach provides a flexible tool, allowing reduce costs and time of the investigation, while giving access to a wide range of information about the mechanics of a railway track as a whole, as well as by parts.

In the present study rail pad and bituminous mixture (BM) sub-ballast layers of a standard ballasted railway track were considered for investigation. These parts of the track were chosen for their similarities in the mechanical behaviour (nonlinearity and energy dissipation) and function (reduction of the dynamic part of the load, an influence on the load distribution).

Firstly, the literature review of basic approaches, appropriate for experimental study and modelling of different aspects of the mechanical behaviour of elastomeric materials was carried out in the first Chapter of the present work. Additionally, two approaches (CI-model and IV-model) extending the theory of linear viscoelasticity to the domain of finite strains were reviewed. The CI-model approach was chosen to represent the mechanical behaviour of a rail pad material as a natural extension of the theory of linear viscoelasticity, based on an extension of the well-established Boltzmann Superposition Principle.

The aims of the second chapter were to study the elastomeric material of a rail pad and to develop a finite element model, capable to predict the nonlinear behaviour and dissipative properties of a real rail pad structure, subjected to compressive load. Experimental measurements of a rail pad compression displacement carried out *in-situ* by the engineering department of SNCF railway company, allow to conclude that the macroscopic strain rate ($\dot{\lambda}$) of a compressive load does not exceed a quasi-static values of $1\text{--}2 \text{ s}^{-1}$. The fact the CI-model explicitly takes into account strain rate dependency (by the $d\varepsilon(s)/ds$ term in its formulation), allows to consider only one quasi-static strain rate for experimental investigation of the elastomeric material of rail pad, which significantly decreases the complexity of the modelling process.

The FE model, proposed in this chapter, is capable, in general, to describe the quasi-static and dynamic behaviour of a rail pad structure, while prediction of the residual compression displacement remains poor, especially in the first loading cycle. Adaptation of a more advanced model, capable to describe the nondestructive Mullins softening effect, can, probably, resolve this problem (e.g. [89]–[91]). Finite element analysis of the rail pad structure allowed to detect accumulation of high shear stress concentrations, when the rail

pad is subjected to a compression load. We must note that possible ways to simplify the numerical model, discussed in the second chapter of the present work, generally lead to high overestimation (2D plane strain and 3D grooveless models) or underestimation (2D plane stress model) of the rail pad mechanical behaviour.

Engineering characteristics of a rail pad structure (*e.g.* stiffness, loss modulus, etc), required for simplified models of a railway track can be identified on the basis of FE model for a variety of proposed geometries and materials. Finally, the numerical optimization of a rail pad geometry/material can be carried out in order to find the best compromise between sufficient level of energy dissipation, an acceptable rigidity of the structure and complexity of the model realization.

Investigation of heterogeneous media, such as BM, cannot be full apart from the mesoscopic approach. Analysis of the material behaviour on a meso-scale level allows a precise study of the internal structure and its influence on the macroscopic behaviour. Significant progress in computational capacities allowed the use of numerical approaches to study internal mechanics of composite materials. The contribution to the study of heterogeneous materials was carried out in the course of the third chapter of the thesis using the new “Virtual Material” approach. This approach allows the generalized study without losing a connection with a real, experimental case, by ensuring a direct geometrical correspondence between numerical and real specimens. Within the framework of the present study the more general problem was reduced and an influence of size and volume fraction of monodisperse spherical inclusions, randomly packed into a cubic hyperelastic matrix, on the mechanical behaviour of the obtained composite structure was investigated. Total 7 real and numerical specimens with different parameters of inclusions’ size (D) and volume fraction (V_{fr}) were developed. Parameters of specimens were chosen in accordance with the Doehlert experimental design. This allowed to perform a qualitative study of the specimens response variation, while identifying the most influencing input parameter.

Experimental and numerical investigations have shown that, despite the pure hyperelastic (non-dissipative) behaviour of the matrix material, VM specimens with inclusions dissipate energy. This can be explained by the frictional interaction between inclusions and matrix contact surfaces. During experimental and numerical investigations, it was found that both rigidity of specimens and their capacity for energy dissipation have a strong dependence on the value of V_{fr} and negligible dependence on the value of D . Finite element method allowed to visualize stress/strain concentrations in the matrix of VM specimens subjected to compression load. It was found, that these concentrations form so-called load-bearing chains going through the matrix. Analysis of a Von-Mises stress maps has proved a theoretical suggestion that a higher number of inclusions in the section leads to an increase in a number and length of load-bearing chains. It was also found that the value of Von Mises stress in load-bearing chains is almost 8 times higher than the average in the matrix.

The presented method can be generalized in terms of problem discretization (more than one fraction of inclusions, different inclusions’ shapes, visco-hyperelastic matrix behaviour, etc.), which allows to study complex heterogeneous materials, such as bituminous mixture (BM).

Bibliography

- [1] P. A. Ferreira, “PhD Thesis: Modelling and prediction of the dynamic behaviour of railway infrastructures at very high speeds,” Universidade Técnica de Lisboa, Instituto superior técnico, 2010.
- [2] B. Indraratna, W. Salim, and C. Rujikiatkamjorn, *Advanced Rail Geotechnology – Ballasted Track*. London: Taylor&Francis Group, 2011.
- [3] C. F. Bonnett, *Practical Railway Engineering*, 2nd Editio. London: Imperial College Press, 2005.
- [4] D. R. Cardona, “PhD Thesis: Characterisation of thermomechanical properties of bituminous mixtures used for railway infrastructures,” l’Universite de Lyon, 2016.
- [5] V. Ziae Rad, N. Nouri, S. Ziae Rad, and M. Abtahi, “A numerical study on mechanical performance of asphalt mixture using a meso-scale finite element model,” *Finite Elem. Anal. Des.*, vol. 57, pp. 81–91, 2012.
- [6] L. T. Mo, M. Huurman, S. P. Wu, and A. A. A. Molenaar, “2D and 3D meso-scale finite element models for ravelling analysis of porous asphalt concrete,” *Finite Elem. Anal. Des.*, vol. 44, no. 4, pp. 186–196, 2008.
- [7] A. Caballero, C. M. López, and I. Carol, “3D meso-structural analysis of concrete specimens under uniaxial tension,” *Comput. Methods Appl. Mech. Eng.*, vol. 195, no. 52, pp. 7182–7195, 2006.
- [8] Y. Xu and S. Chen, “A method for modeling the damage behavior of concrete with a three-phase mesostructure,” *Constr. Build. Mater.*, vol. 102, pp. 26–38, 2016.
- [9] J. Wimmer, B. Stier, J. W. Simon, and S. Reese, “Computational homogenisation from a 3D finite element model of asphalt concrete-linear elastic computations,” *Finite Elem. Anal. Des.*, vol. 110, pp. 43–57, 2016.
- [10] P. Wriggers and S. O. Moftah, “Mesoscale models for concrete: Homogenisation and damage behaviour,” *Finite Elem. Anal. Des.*, vol. 42, no. 7 SPEC. ISS., pp. 623–636, 2006.
- [11] Z. Q. Yue, S. Chen, and L. G. Tham, “Finite element modeling of geomaterials using digital image processing,” *Comput. Geotech.*, vol. 30, no. 5, pp. 375–397, 2003.
- [12] Q. Dai and Z. You, “Micromechanical finite element framework for predicting viscoelastic properties of asphalt mixtures,” *Mater. Struct.*, vol. 41, no. 6, pp. 1025–1037, 2007.
- [13] T. You, R. K. Abu Al-Rub, M. K. Darabi, E. A. Masad, and D. N. Little, “Three-dimensional microstructural modeling of asphalt concrete using a unified viscoelastic-viscoplastic-viscodamage model,” *Constr. Build. Mater.*, vol. 28, no. 1, pp. 531–548, 2012.
- [14] T. Schüler, R. Jänicke, and H. Steeb, “Nonlinear modeling and computational homogenization of asphalt concrete on the basis of XRCT scans,” *Constr. Build. Mater.*, vol. 109, pp. 96–108, 2016.
- [15] Y. Huang, D. Yan, Z. Yang, and G. Liu, “2D and 3D homogenization and fracture

- analysis of concrete based on in-situ X-ray Computed Tomography images and Monte Carlo simulations," *Eng. Fract. Mech.*, vol. 163, pp. 37–54, 2016.
- [16] Y. Ju *et al.*, "Visualization of the three-dimensional structure and stress field of aggregated concrete materials through 3D printing and frozen-stress techniques," *Constr. Build. Mater.*, vol. 143, pp. 121–137, 2017.
 - [17] I. M. Ward and J. Sweeney, *Mechanical Properties of Solid Polymers*, 3rd ed. John Wiley & Sons Ltd, 2012.
 - [18] R. M. Christensen, *Theory of viscoelasticity. An introduction*, Second. New York: Academic Press, 1982.
 - [19] J. Diani, B. Fayolle, and P. Gilormini, "A review on the Mullins effect," *Eur. Polym. J.*, vol. 45, no. 3, pp. 601–612, 2009.
 - [20] G. A. Holzapfel, *Nonlinear Solid Mechanics A Continuum Approach for Engineering*. John Wiley & Sons Ltd, 2000.
 - [21] R. W. Ogden, G. Saccomandi, and I. Sgura, "Fitting hyperelastic models to experimental data," *Comput. Mech.*, vol. 34, no. 6, pp. 484–502, Aug. 2004.
 - [22] T. Beda, "An approach for hyperelastic model-building and parameters estimation a review of constitutive models," *Eur. Polym. J.*, vol. 50, pp. 97–108, Jan. 2014.
 - [23] G. Marckmann and E. Verron, "Comparison of hyperelastic models," *Rubber Chem. Technol.*, vol. 79, no. 5, pp. 835–858, 2006.
 - [24] P. Steinmann, M. Hossain, and G. Possart, "Hyperelastic models for rubber-like materials: consistent tangent operators and suitability for Treloar's data," *Arch. Appl. Mech.*, vol. 82, no. 9, pp. 1183–1217, Feb. 2012.
 - [25] G. R. Strobl, *The Physics of Polymers*, 3rd ed. Leipzig: Springer-Verlag Berlin Heidelberg, 2007.
 - [26] R. Hill, "Constitutive inequalities for isotropic elastic solids under finite strain," *Proc. R. Soc. London. Ser. A, Math. Phys.*, vol. 314, no. 1519, pp. 457–472, 1970.
 - [27] H. Khajehsaeid, J. Arghavani, and R. Naghdabadi, "A hyperelastic constitutive model for rubber-like materials," *Eur. J. Mech. A/Solids*, vol. 38, pp. 144–151, 2013.
 - [28] A. Nguessong-Nkenfack, T. Beda, Z. Q. Feng, and F. Peyraud, "HIA: A Hybrid Integral Approach to model incompressible isotropic hyperelastic materials - Part 1: Theory," *Int. J. Non. Linear. Mech.*, vol. 84, pp. 1–11, 2016.
 - [29] B. Rivlin and D. W. Saunders, "Large Elastic Deformations of Isotropic Materials. VII. Experiments on the Deformation of Rubber," *Philos. Trans. R. Soc. London. Ser. A, Math. Phys. Sci.*, vol. 243, no. 865, pp. 251–288, 1951.
 - [30] L. R. G. Treloar, "The elasticity of a network of long chain molecules. I," *Trans. Faraday Soc.*, vol. 36, pp. 36–41, 1943.
 - [31] L. R. G. Treloar, "Stress-strain data for vulcanised rubber under various types of deformation," *Trans. Faraday Soc.*, vol. 40, pp. 59–70, 1944.
 - [32] R. S. Rivlin, "Large elastic deformations of isotropic materials. IV. Further developments of the general theory," *Philos. Trans. R. Soc. London. Ser. A, Math. Phys. Sci.*, vol. 241, no. 835, pp. 379–397, 1948.

- [33] M. Mooney, "A Theory of Large Elastic Deformation," *J. Appl. Phys.*, vol. 11, no. 9, pp. 582–596, 1940.
- [34] O. H. Yeoh, "Characterization of Elastic Properties of Carbon-Black-Filled Rubber Vulcanizates," *Rubber Chem. Technol.*, vol. 63, no. 5, pp. 792–805, 1990.
- [35] E. M. Arruda and M. C. Boyce, "A three-dimensional constitutive model for the large stretch behavior of rubber elastic materials," *J. Mech. Phys. Solids*, vol. 41, no. 2, pp. 389–412, 1993.
- [36] R. W. Ogden, "Large deformation isotropic elasticity - on the correlation of theory and experiment for incompressible rubberlike solids," *Proc. R. Soc. Lond. A. Math. Phys. Sci.*, vol. 326, no. 1567, pp. 565–584, 1972.
- [37] K. Miller, "Testing Elastomers for Hyperelastic Material Models in Finite Element Analysis," *Axel Products, Inc.* pp. 1–8, 2000.
- [38] D. J. Charlton, J. Yang, and K. K. Teh, "A Review of Methods to Characterize Rubber Elastic Behavior for Use in Finite Element Analysis," *Rubber Chem. Technol.*, vol. 67, no. 3, pp. 481–503, 1994.
- [39] M. A. Hassan, A. Abouel-Kasem, M. a. El-Sharief, and F. Yusof, "Evaluation of the material constants of nitrile butadiene rubbers (NBRs) with different carbon black loading (CB): FE-simulation and experimental," *Polymer (Guildf.)*, vol. 53, no. 17, pp. 3807–3814, Aug. 2012.
- [40] A. D. Drozdov, "Constitutive equations in finite elasticity of rubbers," *Int. J. Solids Struct.*, vol. 44, no. 1, pp. 272–297, Jan. 2007.
- [41] L. Meunier, G. Chagnon, D. Favier, L. Orgéas, and P. Vacher, "Mechanical experimental characterisation and numerical modelling of an unfilled silicone rubber," *Polym. Test.*, vol. 27, no. 6, pp. 765–777, Sep. 2008.
- [42] P. Haupt and A. Lion, "On finite linear viscoelasticity of incompressible isotropic materials," *Acta Mech.*, vol. 159, pp. 87–124, 2002.
- [43] A. Kossa and S. Berezvai, "Visco-hyperelastic Characterization of Polymeric Foam Materials," *Mater. Today Proc.*, vol. 3, no. 4, pp. 1003–1008, 2016.
- [44] J.-C. Petiteau, E. Verron, R. Othman, H. Le Sourne, J.-F. Sigrist, and G. Barras, "Large strain rate-dependent response of elastomers at different strain rates: convolution integral vs. internal variable formulations," *Mech. Time-Dependent Mater.*, vol. 17, no. 3, pp. 349–367, Sep. 2012.
- [45] D. Wollscheid and A. Lion, "Predeformation- and frequency-dependent material behaviour of filler-reinforced rubber: Experiments, constitutive modelling and parameter identification," *Int. J. Solids Struct.*, vol. 50, no. 9, pp. 1217–1225, May 2013.
- [46] A. F. M. S. Amin, A. Lion, S. Sekita, and Y. Okui, "Nonlinear dependence of viscosity in modeling the rate-dependent response of natural and high damping rubbers in compression and shear: Experimental identification and numerical verification," *Int. J. Plast.*, vol. 22, no. 9, pp. 1610–1657, Sep. 2006.
- [47] J. M. Martinez, A. Boukamel, S. Mo, and S. Lejeunes, "Statistical approach for a hyper-visco-plastic model for filled rubber: Experimental characterization and numerical modeling," *Eur. J. Mech. A/Solids*, vol. 30, no. 6, pp. 1028–1039, 2011.
- [48] J. Shim and D. Mohr, "Rate dependent finite strain constitutive model of polyurea,"

- Int. J. Plast.*, vol. 27, no. 6, pp. 868–886, Jun. 2011.
- [49] H. Abdul-Hameed, T. Messager, F. Zaïri, and M. Naït-Abdelaziz, “Large-strain viscoelastic-viscoplastic constitutive modeling of semi-crystalline polymers and model identification by deterministic/evolutionary approach,” *Comput. Mater. Sci.*, vol. 90, pp. 241–252, 2014.
 - [50] G. Ayoub, F. Zaïri, M. Naït-Abdelaziz, J. M. Gloaguen, and G. Kridli, “A visco-hyperelastic damage model for cyclic stress-softening, hysteresis and permanent set in rubber using the network alteration theory,” *Int. J. Plast.*, vol. 54, pp. 19–33, 2014.
 - [51] B. Bernstein, E. A. Kearsley, and L. J. Zapas, “A Study of Stress Relaxation with Finite Strain,” *J. Rheol. (N. Y. N. Y.)*, vol. 7, no. 1, pp. 391–410, 1963.
 - [52] R. I. Tanner, “From A to (BK)Z in Constitutive Relations,” *J. Rheol. (N. Y. N. Y.)*, vol. 32, no. 7, pp. 673–702, 2006.
 - [53] G. A. Holzapfel, “On large strain viscoelasticity: continuum formulation and finite element applications to elastomeric structures,” *Int. J. Numer. Methods Eng.*, vol. 39, no. December 1995, pp. 3903–3926, 1996.
 - [54] J. Ciambella, A. Paolone, and S. Vidoli, “A comparison of nonlinear integral-based viscoelastic models through compression tests on filled rubber,” *Mech. Mater.*, vol. 42, no. 10, pp. 932–944, Oct. 2010.
 - [55] J. S. Bergstrom and M. C. Boyce, “Constitutive modeling of the large strain time-dependent behavior of elastomers,” *J. Mech. Phys. Solids*, vol. 46, no. 5, pp. 931–954, May 1998.
 - [56] B. D. Coleman and W. Noll, “The thermodynamics of elastic materials with heat conduction and viscosity,” *Arch. Ration. Mech. Anal.*, vol. 13, no. 1, pp. 167–178, 1963.
 - [57] N. Huber and C. Tsakmakis, “Finite deformation viscoelasticity laws,” *Mech. Mater.*, vol. 32, no. 1, pp. 1–18, 2000.
 - [58] V. A. Profillidis, *Railway Management and Engineering*, 4th ed. Farnham: Ashgate Publishing Limited, 2014.
 - [59] I. G. Giner, A. R. Alvarez, S. S. C. García-Moreno, and J. L. Camacho, “Dynamic Modelling of High Speed Ballasted Railway Tracks: Analysis of the Behaviour,” *Transp. Res. Procedia*, vol. 18, no. June, pp. 357–365, 2016.
 - [60] I. A. Carrascal, J. A. Casado, J. A. Polanco, and F. Gutiérrez-Solana, “Dynamic behaviour of railway fastening setting pads,” *Eng. Fail. Anal.*, vol. 14, no. 2, pp. 364–373, Mar. 2007.
 - [61] S. Kaewunruen and A. M. Remennikov, “An Experimental Evaluation of the Attenuation Effect of Rail Pad on Flexural Behaviour of Railway Concrete Sleeper under Severe Impact Loads,” in *Australasian Structural Engineering Conference*, 2008, no. 51, pp. 26–27.
 - [62] J. Maes, H. Sol, and P. Guillaume, “Measurements of the dynamic railpad properties,” *J. Sound Vib.*, vol. 293, no. 3–5, pp. 557–565, Jun. 2006.
 - [63] M. Sol-Sánchez, L. Pirozzolo, F. Moreno-Navarro, and M. C. Rubio-Gámez, “A study into the mechanical performance of different configurations for the railway track section : A laboratory approach,” *Eng. Struct.*, vol. 119, pp. 13–23, 2016.
 - [64] E. Arlaud, S. Costa D’Aguiar, and E. Balmes, “Receptance of railway tracks at low

- frequency: Numerical and experimental approaches," *Transp. Geotech.*, vol. 9, pp. 1–16, 2016.
- [65] H. Chebli, D. Clouteau, and L. Schmitt, "Dynamic response of high-speed ballasted railway tracks: 3D periodic model and in situ measurements," *Soil Dyn. Earthq. Eng.*, vol. 28, no. 2, pp. 118–131, Feb. 2008.
 - [66] J. Park, S. Ahn, J. Kim, H. I. Koh, and J. Park, "Direct determination of dynamic properties of railway tracks for flexural vibrations," *Eur. J. Mech. A/Solids*, vol. 61, pp. 14–21, 2017.
 - [67] Q. Y. Xu, X. Ou, F. T. K. Au, P. Lou, and Z. C. Xiao, "Effects of track irregularities on environmental vibration caused by underground railway," *Eur. J. Mech. A/Solids*, vol. 59, pp. 280–293, 2016.
 - [68] P. A. Costa, R. Calçada, A. S. Cardoso, and A. Bodare, "Influence of soil non-linearity on the dynamic response of high-speed railway tracks," *Soil Dyn. Earthq. Eng.*, vol. 30, no. 4, pp. 221–235, Apr. 2010.
 - [69] S. G. Koroma, M. F. M. Hussein, and J. S. Owen, "Influence of Preload and Nonlinearity of Railpads on Vibration of Railway Tracks under Stationary and Moving Harmonic Loads," *J. Low Freq. Noise, Vib. Act. Control*, vol. 34, no. 3, pp. 289–306, 2015.
 - [70] A. V. Metrikine, A. R. M. Wolfert, and A. C. W. M. Vrouwenvelder, "Steady-state response of periodically supported structures to a moving load," *Heron*, vol. 44, no. 2, pp. 91–107, 1999.
 - [71] P. Szurgott and K. Bernyś, "Numerical Analysis of Load Distribution in Railway Track Under Wheelset," *J. KONES Powertrain Transp.*, vol. 20, no. 3, pp. 405–410, 2013.
 - [72] W. M. Zhai, K. Y. Wang, and J. H. Lin, "Modelling and experiment of railway ballast vibrations," *J. Sound Vib.*, vol. 270, pp. 673–683, 2004.
 - [73] J. H. Zicha, "High-speed rail track design," *J. Transp. Eng.*, vol. 115, no. 1, pp. 68–83, 1989.
 - [74] M. Oregui, Z. Li, and R. Dollevoet, "An investigation into the vertical dynamics of tracks with monoblock sleepers with a 3D finite-element model," *Proc. Inst. Mech. Eng. Part F J. Rail Rapid Transit*, vol. 230, no. 3, pp. 891–908, 2015.
 - [75] M. Oregui, Z. Li, and R. Dollevoet, "An investigation into the modeling of railway fastening," *Int. J. Mech. Sci.*, vol. 92, pp. 1–11, 2015.
 - [76] SNCF Département Etudes Voies - Section Mesures, "Mesures d'enfoncement de travers et d'écrasement de semelle au CAI89," 2005.
 - [77] B. J. Van Dyk, J. R. Edwards, M. S. Dersch, C. J. Ruppert, and C. P. Barkan, "Evaluation of dynamic and impact wheel load factors and their application in design processes," *Proc. Inst. Mech. Eng. Part F J. Rail Rapid Transit*, vol. 231, no. 1, pp. 33–43, 2016.
 - [78] E. T. Selig and D. Li, "Track Modulus: Its Meaning and Factors Influencing It," *Transp. Res. Rec. J. Transp. Res. Board*, vol. 1, no. 1470, pp. 47–54, 1994.
 - [79] NF EN 13146-9+A1:2011-12, *Railway applications. Track. Test methods for fastening systems. Determination of stiffness*. AFNOR, 2011.
 - [80] M. Hetenyi, *Beams on Elastic Foundation: Theory with applications in the fields of*

- civil and mechanical engineering.* London: Ann Arbor, 1946.
- [81] P. Viot, "Hydrostatic compression on polypropylene foam," *Int. J. Impact Eng.*, vol. 36, no. 7, pp. 975–989, 2009.
- [82] R. W. Ogden, *Non linear elastic deformations*. Mineola, New York: Dover, 1984.
- [83] H. Draper, N. R.; Smith, *Applied Regression Analysis*. Wiley-Interscience, 3rd ed. New-York: Wiley-Interscience, 1998.
- [84] R. W. Ogden, "Large deformation isotropic elasticity : on the correlation of theory and experiment for compressible rubberlike solids," *Proc. R. Soc. Lond. A. Math. Phys. Sci.*, vol. 328, no. 1575, pp. 567–583, 1972.
- [85] O. H. Yeoh, "Hyperelastic material models for finite element analysis of rubber," *J. Nat. Rubber Res.*, vol. 12, no. 3, pp. 142–153, 1997.
- [86] DS SIMULIA Corp, *Abaqus 6.11. User's Documentation*. Providence, RI, USA, 2011.
- [87] DS SIMULIA Corp, *Abaqus 6.11. Theory manual*. Providence, RI, USA, 2011.
- [88] T. Hoang, D. Duhamel, G. Foret, H. P. Yin, P. Joyez, and R. Caby, "Calculation of force distribution for a periodically supported beam subjected to moving loads," *J. Sound Vib.*, vol. 388, pp. 327–338, 2017.
- [89] Q. T. Nguyen, V. Tinard, and C. Fond, "The modelling of nonlinear rheological behaviour and Mullins effect in High Damping Rubber," *Int. J. Solids Struct.*, vol. 75–76, no. December 2015, pp. 235–246, 2015.
- [90] A. Dorfmann and R. W. Ogden, "A constitutive model for the Mullins effect with permanent set in particle-reinforced rubber," *Int. J. Solids Struct.*, vol. 41, no. 7, pp. 1855–1878, 2004.
- [91] A. Andriyana, M. S. Loo, G. Chagnon, E. Verron, and S. Y. Ch'Ng, "Modeling the Mullins effect in elastomers swollen by palm biodiesel," *Int. J. Eng. Sci.*, vol. 95, pp. 1–22, 2015.
- [92] National Academies of Sciences, *A Manual for Design of Hot Mix Asphalt with Commentary*. Washington, D.C: The National Academies Press, 2011.
- [93] D. Mounier, H. Di Benedetto, and C. Sauzéat, "Determination of bituminous mixtures linear properties using ultrasonic wave propagation," *Constr. Build. Mater.*, vol. 36, pp. 638–647, Nov. 2012.
- [94] M. Pasetto and N. Baldo, "Numerical visco-elastoplastic constitutive modelization of creep recovery tests on hot mix asphalt," *J. Traffic Transp. Eng. (English Ed.)*, vol. 3, no. 5, pp. 390–397, 2016.
- [95] F. Olard and H. Di Benedetto, "General '2S2P1D' Model and Relation Between the Linear Viscoelastic Behaviours of Bituminous Binders and Mixes," *Road Mater. Pavement Des.*, vol. 4, no. 2, pp. 185–224, 2003.
- [96] A. El Moumen, T. Kanit, A. Imad, and H. El Minor, "Effect of reinforcement shape on physical properties and representative volume element of particles-reinforced composites: Statistical and numerical approaches," *Mech. Mater.*, vol. 83, pp. 1–16, 2015.
- [97] J. Segurado and J. Llorca, "A numerical approximation to the elastic properties of sphere-reinforced composites," *J. Mech. Phys. Solids*, vol. 50, no. 10, pp. 2107–2121,

2002.

- [98] P. Sheng, J. Zhang, and Z. Ji, "An advanced 3D modeling method for concrete-like particle-reinforced composites with high volume fraction of randomly distributed particles," *Compos. Sci. Technol.*, vol. 134, pp. 26–35, 2016.
- [99] T. Kanit, S. Forest, I. Galliet, V. Mounoury, and D. Jeulin, "Determination of the size of the representative volume element for random composites: Statistical and numerical approach," *Int. J. Solids Struct.*, vol. 40, no. 13–14, pp. 3647–3679, 2003.
- [100] Z. Guo, X. Shi, Y. Chen, H. Chen, X. Peng, and P. Harrison, "Mechanical modeling of incompressible particle-reinforced neo-Hookean composites based on numerical homogenization," *Mech. Mater.*, vol. 70, pp. 1–17, 2014.
- [101] S. Kari, H. Berger, R. Rodriguez-Ramos, and U. Gabbert, "Computational evaluation of effective material properties of composites reinforced by randomly distributed spherical particles," *Compos. Struct.*, vol. 77, no. 2, pp. 223–231, 2007.
- [102] Z. F. Khisaeva and M. Ostoja-Starzewski, "On the size of RVE in finite elasticity of random composites," *J. Elast.*, vol. 85, no. 2, pp. 153–173, 2006.
- [103] J. Moraleda, J. Segurado, and J. LLorca, "Finite deformation of incompressible fiber-reinforced elastomers: A computational micromechanics approach," *J. Mech. Phys. Solids*, vol. 57, no. 9, pp. 1596–1613, 2009.
- [104] J.-J. Droesbeke, J. Fine, and G. Saporta, *Plans d'expériences: applications à l'entreprise*. Société de statistique de France, 1997.
- [105] G. E. P. Box, J. S. Hunter, and W. G. Hunter, *Statistics for Experimenters: Design, Innovation, and Discovery*, Second. Wiley-Interscience, 2005.
- [106] D. H. Doehlert and V. L. Klee, "Experimental designs through level reduction of the d-dimensional cuboctahedron," *Discrete Math.*, vol. 2, no. 4, pp. 309–334, 1972.
- [107] "GranOO's wiki." [Online]. Available: <http://www.lamef.bordeaux.ensam.fr/~granoo/wiki/doku.php>.
- [108] S. M. R. García-Rojo, H.J. Herrmann, *Powders and Grains 2005, Two Volume Set: Proceedings of the International Conference on Powders & Grains 2005, Stuttgart, Germany, 18-22 July 2005..*
- [109] V. A. PROFILLIDIS, *Railway Management and Engineering*, 4th ed. Farnham: Ashgate Publishing Limited, 2014.
- [110] B. J. Van Dyk, J. R. Edwards, M. S. Dersch, C. J. Ruppert, and C. P. Barkan, "Evaluation of dynamic and impact wheel load factors and their application in design processes," *Proc. Inst. Mech. Eng. Part F J. Rail Rapid Transit*, vol. 0, no. 0, pp. 1–11, 2016.
- [111] A. D. Kerr, "On the determination of the rail support modulus k," *Int. J. Solids Struct.*, vol. 37, no. 32, pp. 4335–4351, 2000.
- [112] ASTM D0412 - 98a: 2002, *Standard Test Methods for Vulcanized Rubber and Thermoplastic Elastomers*. 2002.

Appendix

Appendix A

The expression for the deflection $U(x, t)$ can be derived from the classical beam theory (Euler–Bernoulli theory) using the following equation:

$$EJ_x \frac{d^4 U(x, t)}{dx^4} + \rho \frac{d^2 U(x, t)}{dt^2} + kU(x, t) = -Q_w \delta(x - vt) \quad (\text{A.1})$$

Equation (A.1) can be solved using a double Fourier transformation of the function $U(x, t)$:

$$U^*(\omega, \gamma) = \int_{-\infty}^{\infty} \int_{-\infty}^{\infty} U(x, t) e^{-i\omega x} e^{-i\gamma t} dx dt \quad (\text{A.2a})$$

$$U(x, t) = \frac{1}{4\pi^2} \int_{-\infty}^{\infty} \int_{-\infty}^{\infty} U(\omega, \gamma) e^{ix\omega} e^{it\gamma} d\omega d\gamma \quad (\text{A.2b})$$

Applying (A.2a) in (A.1) and taking $2a = \rho/EJ_x$ and $b^4 = k/EJ_x$ leads to:

$$\omega^4 U^*(\omega, \gamma) - 2a\gamma^2 U^*(\omega, \gamma) + b^4 U^*(\omega, \gamma) = -\frac{2\pi Q_w \delta(\omega v + \gamma)}{EJ_x} \quad (\text{A.3})$$

Solving the linear equation (A.3) and taking the inverse Fourier transformation (A.2b) gives:

$$U(x, t) = -\frac{Q_w}{2\pi EJ_x} \int_{-\infty}^{\infty} \frac{e^{i(x-vt)\omega}}{\omega^4 - 2a\omega^2 v^2 + b^4} d\omega \quad (\text{A.4})$$

The integral in Equation (A.4) can be solved using methods of a contour integration. Firstly, assume that $x - vt > 0$. Consider the contour C_1 on the complex plane that goes from $-R$ to R along the real line and then counterclockwise along a semicircle with a centre at 0 and radius R (Figure A.1). Now consider a contour integral as follows:

$$\oint_{C_1} F(\omega) = \oint_C \frac{e^{i(x-vt)\omega}}{\omega^4 - 2a\omega^2 v^2 + b^4} d\omega \quad (\text{A.5})$$

According to Cauchy's residue theorem, the integral (A.5) is equal to $2\pi i$ times the sum of residues of $F(\omega)$ at its poles ω_i :

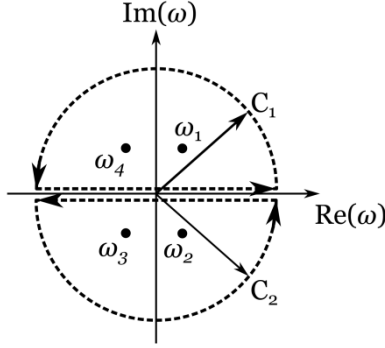


Figure A.1: Contours C_1 and C_2 on the complex plane around poles ω_i of a complex function $F(\omega)$

$$\oint_{C_1} F(\omega) = 2\pi i \sum \text{Res}(F, \omega_i) \quad (\text{A.6})$$

$F(\omega)$ has singularities at four points:

$$\omega^2_{1,2,3,4} = av^2 \pm \sqrt{b^4 - (av^2)^2} \quad (\text{A.7})$$

Assuming that $v < v_{cr} = b/\sqrt{a}$ we obtain:

$$\omega^2_{1,3} = av^2 + i\sqrt{(av^2)^2 - b^4}, \quad \omega^2_{2,4} = av^2 - i\sqrt{(av^2)^2 - b^4} \quad (\text{A.8})$$

Taking square roots in (A.7), poles of the function $F(\omega)$ can be finally written as follows:

$$\omega_{1,3} = \pm(s + iq), \quad \omega_{2,4} = \pm(s - iq) \quad (\text{A.9a})$$

with

$$s = \sqrt{0.5(b^2 + av^2)}, \quad q = \sqrt{0.5(b^2 - av^2)} \quad (\text{A.9b})$$

Returning to the integral (A.5) and formula (A.6) and taking into account that only poles ω_1 and ω_4 are inside the contour C_1 we get after some basic algebraic manipulations

$$\oint_{C_1} F(\omega) = 2\pi i [\text{Res}(F, \omega_1) + \text{Res}(F, \omega_4)] = \frac{\pi e^{-q(x-vt)} \cos(s(x-vt) - \arctg(q/s))}{2sq\sqrt{s^2+q^2}} \quad (\text{A.10})$$

The contour integral (A.5) can be split into two parts: an integral over the straight part of the contour C_1 (which is going along the rational axis of the complex plane) and an integral over a curved part of C_1 .

$$\oint_{C_1} F(\omega) = \int_{-R}^R F(\omega) + \int_{arc} F(\omega) \quad (\text{A.11})$$

It is easy to show using the estimation lemma that the integral over the arc region tends to zero if R tends to infinity:

$$\left| \oint_{arc} \frac{e^{i(x-vt)\omega}}{\omega^4 - 2a\omega^2v^2 + b^4} d\omega \right| < \oint_{arc} \left| \frac{e^{i(x-vt)\omega}}{\omega^4 - 2a\omega^2v^2 + b^4} \right| d\omega < \oint_{arc} \frac{1}{|\omega^4 - 2a\omega^2v^2 + b^4|} d\omega < \dots \quad (\text{A.12})$$

$$\dots < \oint_{arc} \frac{1}{R^4 - 2aR^2v^2 + b^4} d\omega = \frac{\pi R}{R^4 - 2aR^2v^2 + b^4} \rightarrow 0 \text{ as } R \rightarrow \infty$$

Thus, from (A.10), (A.11) and (A.12) we get

$$\int_{-\infty}^{\infty} F(\omega) d\omega = \lim_{R \rightarrow \infty} \int_{-R}^R F(\omega) = \frac{\pi e^{-q(x-vt)} \cos(s(x-vt) - \arctg(q/s))}{2sq\sqrt{s^2+q^2}} \quad (\text{A.13})$$

If $x - vt < 0$, then considering the contour C_2 (Figure A.1) and following the similar strategy as for the contour C_1 we can obtain:

$$\int_{-\infty}^{\infty} F(\omega) d\omega = \lim_{R \rightarrow \infty} \int_{-R}^R F(\omega) = \frac{\pi e^{q(x-vt)} \cos(s(x-vt) + \arctg(q/s))}{2sq\sqrt{s^2+q^2}} \quad (\text{A.14})$$

Finally combining (A.13) and (A.14) and substituting the result to (A.4) we get:

$$U(x) = -\frac{Q_w b^3 e^{-q|x-vt|}}{4sqk} \cos(r|x-vt| - \arctg(q/s)) \quad (\text{A.15})$$

Appendix B

Abaqus allows application of a static force/displacement boundary condition taking into account creep/relaxation phenomena. In this way, the second loading step can be applied to a fully relaxed structure.

It was mentioned in the main part of this chapter that installation of the “Nabla” fastening system results in a constant compression displacement d_{cd}^{nabla} instead of a constant clamping force F_{cf}^{nabla} and leads to relaxation of the clamping force with time. On the opposite, the weight of the rail provides a constant value of the force, which results in the creep phenomena. Both of these static preloads continue acting in the second step, when the dynamic force signal is applied. For the numerical application, consistency between types (displacement or force boundary condition) of all applied loads must be respected. Thus, the corresponding constant force F_{cf}^{nabla} , ensuring after the creep the same state of a rail pad structure as after force relaxation under a constant compression displacement d_{cd}^{nabla} , must be identified. It was done following an assumption that the same “relaxed” point can be reached by the force relaxation at a constant displacement d_{cd}^{nabla} or by creep at a constant force F_{cf}^{nabla} (Figure B.1).

The relaxed value of clamping force F_{cf}^{nabla} was obtained in two steps. Firstly FE model was

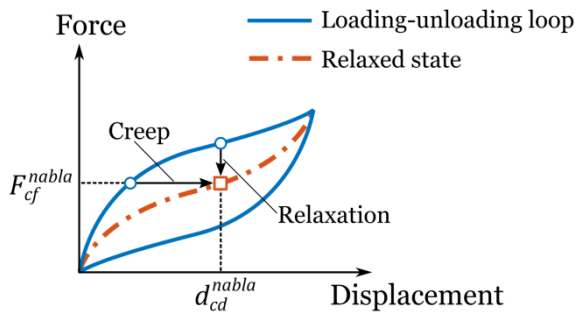


Figure B.1: The same “relaxed” state can be reached either by force relaxation at a constant displacement d_{cd}^{nabla} or by creep at a constant force F_{cf}^{nabla}

subjected to preload force F_{pr} , thus, the value of d_{cd}^{nabla} was found. In the second step, FE simulation of a rail pad structure subjected to the force relaxation at a constant value of a compression displacement d_{cd}^{nabla} was carried out. The value of force, obtained in the second step, was accepted as the value of F_{cf}^{nabla} .

2017-ENAM-0039



École doctorale n° 432 : Sciences des Métiers de l'ingénieur

Doctorat ParisTech

THÈSE

pour obtenir le grade de docteur délivré par

l'École Nationale Supérieure d'Arts et Métiers

Spécialité “ Mécanique-Matériaux ”

présentée et soutenue publiquement par

Roman ZHURAVLEV

le 14 décembre 2017

Contribution à l'étude du comportement mécanique de voies ferrées

Composants à caractère dissipatif non-linéaire : semelle sous rail et sous-couche de grave bitumineuse

Document résumé en français du manuscrit de thèse

Directeur de thèse : **Philippe VIOT**

Co-encadrement de la thèse : **Sandra GUERARD, Catherine FROUSTEY**

Jury

M. Oleg B. NAIMARK, Professeur des universités, RAS UB Continuum Mechanics Institute

M. Erwan VERRON, Professeur des universités, GeM, Centrale Nantes

M. Moussa NAIT-ABDELAZIZ, Professeur des universités, LMSFC, Polytech Lille

M. Philippe VIOT, Professeur des universités, I2M, Arts et Métiers - ParishTech

Mme. Sandra GUERARD, Maître de conférences, I2M, Arts et Métiers - ParishTech

Mme. Catherine FROUSTEY, Maître de conférences HdR, I2M, Université de Bordeaux

M. Pierre-Emmanuel LAURENS, Ingénieur, Direction Ingénierie & Projets SNCF

Président

Rapporteur

Rapporteur

Examinateur

Examinateur

Examinateur

Invité

T
H
È
S
E

Introduction générale

Les voies ferrées peuvent être endommagées par les chargements dynamiques répétés issus du passage des trains, en particulier pour les trains à grandes vitesses. L'étude du comportement mécanique d'une voie ferrée (de chaque composant à la structure entière) est donc étroitement liée à l'amélioration de la sécurité ferroviaire, ainsi qu'à l'efficacité de ce mode de transports.

Les voies ferrées modernes correspondent à des structures multicouches complexes, constituées de différents matériaux, définies pour augmenter la durabilité des voies. La structure d'une voie ferrée ballastée classique est représentée Figure 1. Elle est constituée successivement :

- 1) De rails longitudinaux en acier inoxydable, dont le rôle est de guider, de supporter les roues des trains et de distribuer la charge correspondante aux traverses inférieures ;
- 2) De semelles en élastomère destinées à amortir les vibrations et diminuer la composante dynamique du chargement issu des roues ;
- 3) De traverses de béton uniformément réparties, dont le rôle est de soutenir le rail et de transmettre le chargement correspondant au passage d'un train à la couche de ballast ;
- 4) D'une couche de ballast, qui supporte les traverses, assure la transmission de l'effort à un niveau réduit, apporte élasticité et résilience à la voie.

L'ensemble de cette structure s'appuie sur une sous-couche ; cette dernière est constituée de roches concassées, mais des récents travaux ont montré que l'utilisation de grave bitumineuse (asphalte) pour constituer cette sous-couche augmente les propriétés mécaniques de la voie ainsi que sa durée de vie.

La mise en place d'expérimentations pour évaluer les performances d'une voie, qu'elles soient faites en laboratoire ou *in-situ*, sont classiquement longues, difficiles et onéreuses. L'utilisation d'approches numériques dans l'étude du comportement d'une voie ferrée, que ce soit dans son ensemble [64]–[73] ou pour chacun de ses constituants pris séparément [5], [6], [74], [75], s'est donc développée récemment .

Ce travail de thèse se focalise sur l'étude des semelles sous rail et de la sous-couche en grave bitumineuse (GB). Ces deux composants ont été choisis pour leurs similarités en termes de comportement mécanique non linéaire et capacité de dissipation d'énergie. Ce manuscrit est divisé en trois chapitres.

Le premier chapitre présente une revue détaillée des principaux aspects du comportement mécanique des matériaux de type élastomères : les approches théoriques classiques et le choix d'un modèle numérique adapté sont abordés. Cette étude préalable est ensuite exploitée dans les chapitres deux et trois.

Le deuxième chapitre concerne l'étude du comportement mécanique du matériau élastomérique qui compose les semelles sous-rail : un modèle phénoménologique pour représenter le caractère non linéaire du comportement du matériau et ses capacités de dissipation d'énergie est présenté et ses paramètres identifiés. Ce modèle est ensuite utilisé

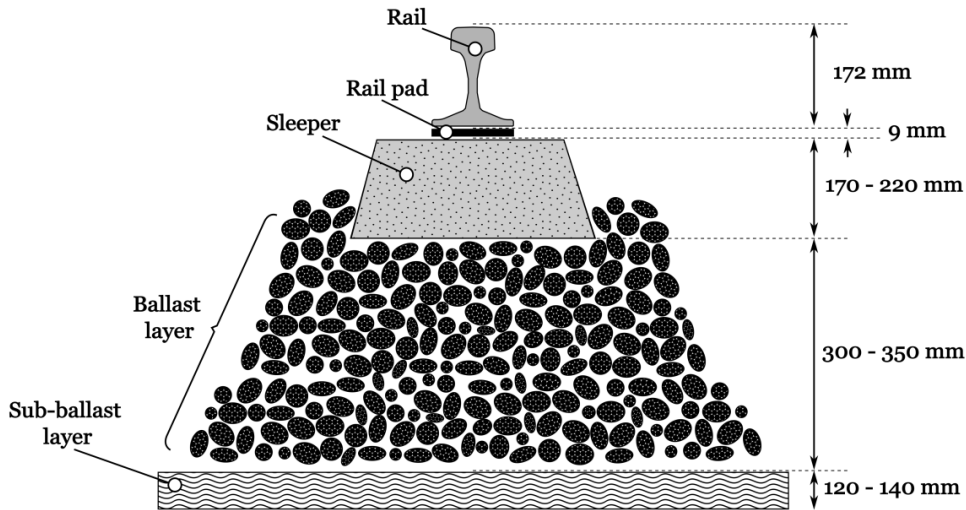


Figure 1: Coupe d'une structure de voie ferrée

pour la modélisation numérique de la réponse mécanique de la semelle sous-rail lors du passage d'un train à grande vitesse. Le chargement correspondant est évalué en amont et imposé à la semelle. Les résultats des simulations numériques sont finalement comparés aux résultats expérimentaux (essais sur coupons et essais *in-situ*).

Le troisième chapitre se focalise sur l'étude de la grave bitumineuse utilisée pour la couche sous-ballast. Constituée d'une matrice hyperélastique et d'inclusions rigides, l'influence de la taille des inclusions et de leur fraction volumique sur la réponse mécanique est étudiée. Pour cela, un concept de « matériau virtuel » est développé : des éprouvettes avec taille, position et fraction volumique des inclusions ont été réalisées par fabrication additive, puis testées mécaniquement, et enfin modélisées numériquement. Finalement, les résultats expérimentaux et numériques sont comparés.

Chapitre 1: Lois de comportement des matériaux élastomères. Approche théorique

1. Introduction

Les propriétés mécaniques (et par conséquent le comportement physique observé) d'une semelle sous-rail est fonction de sa géométrie et du matériau (élastomère) utilisé [17]. Tous les élastomères ont un comportement qualitatif tout à fait semblable, qui, en général, peut être décrit par : 1) l'élasticité non-linéaire (hyper-élasticité); 2) la dépendance à la fréquence et à la vitesse de déformation (viscoélasticité) ; 3) la dépendance à la température ; 4) l'incompressibilité. Naturellement, les matériaux élastomères soumis à une charge cyclique présentent une boucle d'hystérésis significative et, en conséquence, dissipent de l'énergie au cours de chaque cycle de charge.

Dans cette thèse, toutes les études expérimentales ont été faites à température constante contrôlée et les résultats sont considérés après pré-cyclage. La dépendance à la température et l'effet Mullins [19] propres aux élastomères ne sont donc pas pris en compte. Le présent chapitre passe en revue les principales approches théoriques développées pour la modélisation du comportement des élastomères, en dehors de ces deux propriétés.

2. Non-linéarité élastique (Hyper-élasticité)

2.1. Théorie générale de l'hyper-élasticité

La modélisation du comportement non-linéaire des matériaux élastomères dans le domaine des grandes déformations est généralement basée sur l'approche de l'hyper-élasticité. Cette approche implique l'existence d'une fonction de densité d'énergie de déformation (ou potentiel) W dépendant de l'état actuel de la déformation [20]. La contrainte actuelle est calculée comme la dérivée partielle de W par le tenseur de déformation. En particulier, le tenseur des contraintes de Cauchy $\underline{\sigma}$ pour un matériau incompressible s'exprime [20]:

$$En terme d'invariants: \underline{\sigma} = -p\underline{1} + 2 \left(\frac{\partial W}{\partial I} \underline{\underline{B}} - \frac{\partial W}{\partial II} \underline{\underline{B}}^{-1} \right) \quad (1a)$$

$$En terme d'elongations principales: \sigma_i = \lambda_i \frac{\partial W}{\partial \lambda_i} - p \quad (1b)$$

ou I et II sont invariant du tenseur de déformation de Cauchy–Green gauche $\underline{\underline{B}}$, λ_i sont les valeur propres du tenseur gradient de la transformation $\underline{\underline{F}}$, $\underline{1}$ est le tenseur identité et p est un multiplicateur de Lagrange, homogène à une pression, permet de prendre en compte l'incompressibilité du matériau.

2.2. Modèles hyper-élastiques

Les modèles hyper-élastiques traduisent la réponse quasi-statique des matériaux. Ils sont indépendants de l'histoire de chargement, de la fréquence et de la vitesse de déformation. Les formulations du potentiel W sont principalement développées en utilisant des approches phénoménologiques et/ou micro-mécaniques [22]–[24]. Les premières décrivent le comportement macroscopique observé par des équations mathématiques. Les secondes sont basées sur la mécanique statistique et la représentation idéalisée des chaînes moléculaires de la structure du matériau. Dans les deux cas, la connexion d'un modèle hyper-élastique à la théorie de l'élasticité doit être définie sous la forme de contraintes mathématiques.

Les caractéristiques d'un modèle hyper-élastique efficace et réaliste sont par exemple discutées dans [22]. Il y est montré que le choix d'un bon modèle doit être un compromis entre ses capacités à traduire le comportement matériau et sa complexité mathématique.

L'analyse de tous les modèles hyper-élastiques existants n'est pas l'objet de la présente étude (les travaux de Marckmann et Verron [23], Steinmann *et al.* [24] et Beda [22] présentent des études comparatives très complètes de la plupart des modèles). Nous nous intéressons ici aux modèles les plus connus et couramment utilisés.

La plupart de ces modèles peuvent être considérés comme des versions simplifiées du modèle de Rivlin (ou modèle polynomial) généralisé [29]. La forme polynomiale rend le modèle très flexible et permet un bon ajustement des données expérimentales, mais nécessite un grand nombre de paramètres (C_{pq}):

$$W_R = \sum_{p,q=0}^N C_{pq} (I - 3)^p (II - 3)^q \quad (2)$$

On peut citer :

- Le modèle Neo-Hookean (1948) [30]: dépendance linéaire au premier invariant du tenseur des contraintes ; une constante est requise.
- Le modèle de Mooney-Rivlin (1940-1948) [16,17]: dépendance linéaire aux premier et deuxième invariants ; deux constantes sont requises.
- Le modèle de Yeoh (1990) [34]: dépendance d'ordre trois au premier invariant; trois constantes sont requises.
- Le modèle de Arruda-Boyce (1993) [35]: dépendance polynomiale (ordre ~5) au premier invariant ; deux constantes sont requises.
- Le modèle de Ogden (1972) [36]: fonction puissance des élongations principales ; $2N$ constantes sont requises (N est l'ordre du modèle).

Il faut souligner que Steinmann *et al.* [24] ont montré, en utilisant les données expérimentales obtenues par Treloar [31], que les modèles Yeoh et Arruda-Boyce, ajustés pour un type d'expérience (par exemple traction uniaxiale), ont des capacités de prédiction raisonnables pour les modes de déformation complémentaires (cisaillement pur, traction biaxiale).

2.3. Identification des paramètres des modèles hyper-élastiques

L'identification des paramètres d'un modèle hyper-élastique est classiquement effectuée en ajustant l'équation contrainte-déformation correspondant aux données expérimentales. Une sollicitation conduisant à un état de déformation homogène permet de simplifier à la fois la procédure expérimentale et la forme des équations mathématiques. Les essais typiques pour les matériaux incompressibles sont : traction/compression uniaxiale ($\sigma_3 = \sigma$, $\sigma_1 = \sigma_2 = 0$), traction (équi-)biaxiale ($\sigma_3 = 0$, $\sigma_1 = \sigma_2 = \sigma$) et cisaillement pur ($\sigma_1 = 0$, $\sigma_1 \neq 0$, $\sigma_2 \neq 0$) [31], [36]–[38] (Figure 1a-d).

Notons qu'il est important d'utiliser des données expérimentales quasi-statiques pour l'identification des paramètres afin de s'affranchir du phénomène de viscoélasticité, dépendant de la vitesse de déformation [21], [36], [39]–[41].

3. Viscoélasticité linéaire

La théorie de la viscoélasticité est principalement basée sur des lois de comportements qui représentent la réponse macroscopique du matériau, lorsque le temps est pris en compte.

La viscoélasticité linéaire est la première approche du comportement viscoélastique d'un matériau. Une relation linéaire entre l'histoire de la déformation et la valeur actuelle de la contrainte est considérée. De plus, on se place dans le domaine des petites déformations.

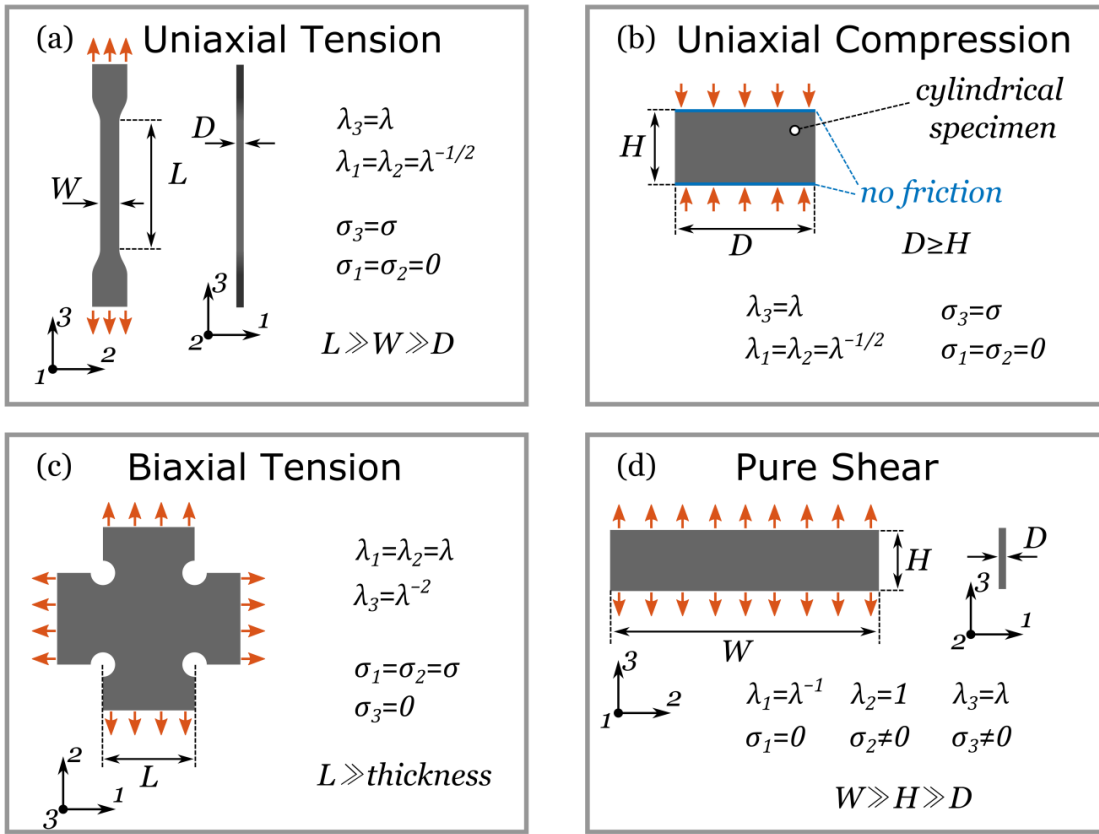


Figure 2: Essais typiques pour obtenir un état de déformation homogène pour un matériau incompressible : (a) traction uniaxiale, (b) compression uniaxiale, (c) traction biaxiale, (d) cisaillement pur [37].

3.1. Fluage et relaxation

La viscoélasticité peut être quantifiée macroscopiquement par des essais de fluage ou de relaxation. Les modules viscoélastiques du matériau sont définis (Figure 3a-b): 1) le module de fluage $J(t)$ qui donne la variation de la déformation à contrainte constante ($J(t) = \varepsilon(t)/\sigma_0$; et 2) le module de relaxation $G(t)$, qui donne la variation de la contrainte à déformation constante ($G(t) = \sigma(t)/\varepsilon_0$).

Dans la pratique, les fonctions $G(t)$ et $J(t)$ sont souvent représentées par une fonction

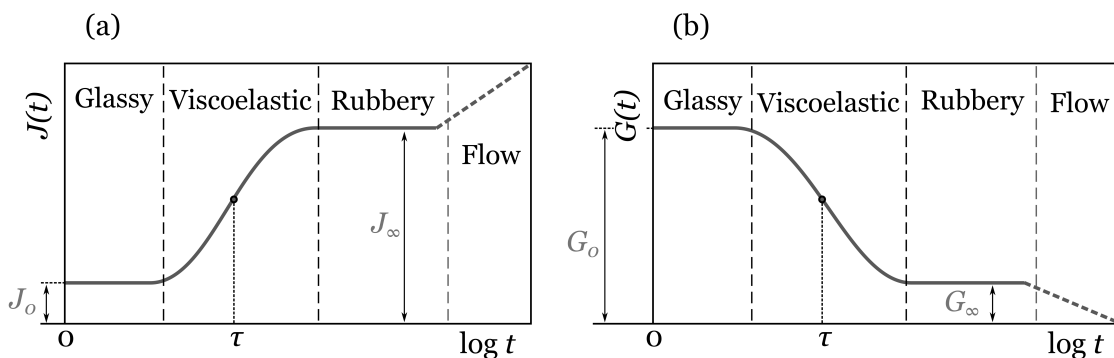


Figure 3: Module de fluage (a) et module de relaxation (b) en fonction du temps

exponentielle ou une série de fonctions (séries de Prony ou modèle de Maxwell généralisé [17]).

3.2. Principe de superposition de Boltzmann

Le principe de superposition de Boltzmann postule que : 1) la relaxation (et le fluage) est fonction de l'histoire entière du chargement ; 2) chaque étape de chargement contribue indépendamment à la déformation finale (ou à la contrainte finale) [17]. La contrainte dans un matériau viscoélastique linéaire peut s'exprimer sous la forme de l'intégrale de Duhamel :

$$\sigma(t) = \int_{-\infty}^t G(t-s) \frac{d\varepsilon(s)}{ds} ds \quad (3)$$

3.3. Modèles mécaniques de viscoélasticité linéaire

Une alternative pour représenter la viscoélasticité linéaire est de considérer la dépendance contrainte-déformation sous forme d'une équation différentielle linéaire [17]:

$$a_0\sigma + a_1 \frac{d\sigma}{dt} + a_2 \frac{d^2\sigma}{dt^2} + \dots = b_0\varepsilon + b_1 \frac{d\varepsilon}{dt} + b_2 \frac{d^2\varepsilon}{dt^2} + \dots \quad (4)$$

Cette équation généralise la classe des modèles rhéologiques qui tentent de décrire le comportement des matériaux viscoélastiques par un ensemble de ressorts élastiques et d'amortisseurs visqueux.

Classiquement, trois modèles phénoménologiques sont considérés dans la littérature : 1) le modèle de Maxwell (un ressort et un amortisseur en série) qui représente bien le phénomène de relaxation mais échoue à décrire le phénomène de fluage; 2) le modèle de Kelvin-Voigt (un ressort et un amortisseur en parallèle) capable de décrire le fluage, mais inapproprié pour la description de la relaxation ; 3) le modèle de Zener (un ressort en parallèle avec le modèle de Maxwell) qui peut décrire les deux phénomènes. Des modèles plus complexes (plusieurs éléments de Maxwell en parallèle ou plusieurs éléments de Kelvin-Voigt en série) peuvent être utilisés afin d'augmenter la capacité de prédiction [17].

3.4. Module de conservation et module de perte

La viscoélasticité d'un matériau peut être également observée lors d'un essai dynamique (DMA) : l'échantillon est soumis à un signal de déformation sinusoïdal alterné et la contrainte est mesurée. La contrainte varie également sinusoïdalement à la même fréquence que la déformation mais avec un déphasage.

Ce type d'essai permet de déterminer le module complexe du matériau $\tilde{G} = G_1 + iG_2$. La partie réelle G_1 (module de conservation) définit l'énergie stockée dans l'échantillon au cours de la déformation. La partie imaginaire G_2 (module de perte) définit la dissipation de l'énergie.

4. Viscoélasticité non-linéaire ou hyper-viscoélasticité

Dans le cadre d'applications réelles, les grandes déformations sont à considérer. Le comportement viscoélastique des élastomères dans le domaine des grandes déformations peut être décrit par l'extension de la théorie de viscoélasticité linéaire à ce domaine.

Les modèles visco-hyperélastiques sont généralement dérivés de deux approches : l'approche par intégrale de convolution (modèle-CI) [42]–[45] ou l'approche par variables internes (modèle-IV) [44], [46]–[48].

4.1. Approche par intégrale de convolution (modèle-CI)

Cette première approche est basée sur l'extension du principe de superposition de Boltzmann de la théorie de la viscoélasticité linéaire au domaine des grandes déformations non-linéaires. Elle peut être décrite comme une séparation de la contrainte totale en une partie hyper-élastique et une partie viscoélastique. La partie hyper-élastique correspond à la réponse du matériau, indépendante du temps. La partie viscoélastique décrit l'écart de comportement du matériau à un état hyper-élastique pur. Elle dépend de la vitesse de déformation et de l'histoire du chargement. L'expression finale de la contrainte de Cauchy est la suivante [44] :

$$\underline{\underline{\sigma}}(t) = \underline{\underline{\sigma}_0}(t) + \int_{-\infty}^t \frac{\dot{G}(s)}{G_0} \underline{\underline{F}_{t-s}}(t) \underline{\underline{\sigma}_0}(t-s) \underline{\underline{F}_{t-s}^T}(t) ds \quad (5)$$

La valeur de $\underline{\underline{\sigma}_0}(t)$ est donnée par l'équation (1a).

Dans le cas de l'incompressibilité du matériau elle devient:

$$\underline{\underline{\sigma}}(t) = -p \cdot \underline{\underline{1}} + [\underline{\underline{\sigma}}(t)]^D + dev \left\{ \int_0^t \left(\frac{\dot{G}(s)}{G_0} \underline{\underline{F}_{t-s}}(t) [\underline{\underline{\sigma}_0}(t-s)]^D \underline{\underline{F}_{t-s}^T}(t) \right) ds \right\} \quad (6)$$

ou $[\cdot]^D = dev(\cdot)$ et $[\cdot]^H = tr(\cdot)$ sont les parties déviatoriques et sphériques du tenseur, respectivement.

Comme points positifs au modèle CI, on peut mettre en évidence sa simplicité numérique (seule l'intégrale doit être calculée numériquement) et sa connexion directe avec le principe de superposition de Boltzmann. De plus, cette stratégie de séparation de la contrainte est en accord avec les observations de plusieurs auteurs [48], [55] lors d'essais de multi-relaxation de contrainte. Selon ces travaux, la partie purement hyper-élastique de la contrainte définit la limite de relaxation pour la contrainte, pour chaque niveau de déformation. Ces valeurs limites forment une courbe intermédiaire à l'intérieur de la boucle Contrainte-Déformation, cette courbe correspond au comportement hyper-élastique pur, à long terme, du matériau.

Comme points faibles à cette approche, on peut mentionner une forte erreur de prédiction du comportement dans le cas de relaxation à long terme si une fonction exponentielle est prise dans l'expression du module de relaxation (équation (5)). En utilisant les séries de Prony, une augmentation de l'ordre de la série peut, en général, améliorer la réponse du modèle ;

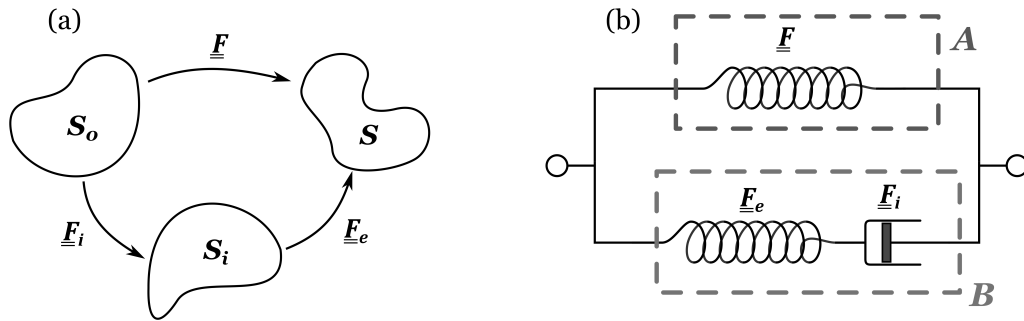


Figure 4: Représentation schématique de la division de la déformation dans l'approche du modèle-IV

cependant, cela entraîne un grand nombre de constantes à identifier. Ce problème peut être résolu en proposant une expression différente pour $G(t)$ [42].

4.2. Approche par variables internes (modèle-IV)

Cette deuxième approche (modèle-IV) postule que la déformation totale est composée de deux états indépendants : un état viscoélastique pur et un état hyper-élastique pur. En termes de mécanique non-linéaire, on suppose que le gradient de la déformation totale $\underline{\underline{F}}$ est composé d'une partie élastique (F_e) et d'une partie inélastiques (F_i) (Figure 4a-b).

Le tenseur des contraintes de Cauchy peut alors être obtenu en résolvant les équations suivantes [44]:

$$\underline{\underline{\sigma}} = 2 \frac{\partial W_1}{\partial \underline{\underline{B}}} \cdot \underline{\underline{B}} - 2 \frac{\partial W_2}{\partial \underline{\underline{B}}_e} \cdot \underline{\underline{B}}_e \quad (7a)$$

$$\dot{\underline{\underline{B}}}_e = \underline{\underline{L}} \cdot \underline{\underline{B}}_e + \underline{\underline{B}}_e \cdot \underline{\underline{L}}^T - \frac{2}{\eta} \underline{\underline{B}}_e \cdot \left[\frac{\partial W_2}{\partial \underline{\underline{B}}_e} \cdot \underline{\underline{B}}_e \right]^D \quad (7b)$$

ou $\underline{\underline{L}}$ est les tenseur gradient des vitesses. L'avantage principal du modèle-IV est sa cohérence avec le deuxième principe de la thermodynamique, les équations du modèle en dérivent directement.

L'approche modèle-IV suppose pour le matériau l'existence d'un état d'équilibre viscoélastique pur. Cependant, cette hypothèse n'est basée sur aucune considération physique ou évidence expérimentale.

4.3. Identification des paramètres des modèles hyper-visco-élastiques

Plusieurs auteurs proposent d'identifier séparément les paramètres relatifs au comportement à long terme et ceux relatifs à la relaxation de contrainte (e.g. [17], [47], [49]). Cette stratégie peut fournir un moyen plus facile d'identifier les constantes du modèle en utilisant différentes données expérimentales.

Cependant, en réalité, les mécanismes de viscoélasticité et d'hyper-élasticité agissent simultanément et un état pur pour le matériau ne peut être obtenu en cours d'essai. Selon Kossa *et al.* [43], l'ajustement séparé des parties hyper-élastiques et viscoélastiques peut conduire à de multiples erreurs:

- La position intermédiaire de la réponse hyperélastique sur la courbe Contrainte-Déformation est approximative et ne peut pas être clairement identifiée par un essai ;
- L'équation qui décrit la relaxation de contrainte suppose un chargement échelon, cela signifie que l'échantillon est chargé instantanément. L'essai de relaxation, au contraire, est fait avec un chargement de l'échantillon à vitesse de déformation constante. Donc, le point de départ de la courbe de relaxation dans l'expérience dépend de la vitesse de déformation et ne coïncide pas avec la contrainte initiale théorique.

En conclusion, les paramètres d'un modèle visco-hyperélastique doivent être identifiés à partir des données expérimentales, sans séparation du comportement à long terme et à la relaxation du matériau.

5. Conclusions du Chapitre 1

Dans le cadre de cette thèse, le modèle-CI est utilisé pour modéliser le comportement mécanique du matériau élastomère de la semelle. Cette approche a été choisie par les raisons suivantes : le modèle-CI est une extension naturelle de la théorie de la viscoélasticité linéaire, car basé sur l'extension du principe de superposition Boltzmann ; la séparation des contraintes proposée par ce modèle, a été observée expérimentalement par de nombreux auteurs. Au contraire, l'approche par le modèle-IV suppose l'existence d'un état d'équilibre viscoélastique pur, qui ne peut être prouvé expérimentalement ou justifié par des considérations physiques.

Chapitre 2: Étude expérimentale et numérique du comportement d'une semelle sous-rail en élastomère soumise à un chargement de compression

1. Introduction

Une semelle sous-rail est située entre le rail et la traverse (Figure 1). Son rôle est de favoriser un contact lisse entre le rail et la traverse, de réduire le bruit, les vibrations et la composante dynamique provoquée par la charge des roues. La rigidité de la semelle influence le niveau de flexion du rail qui, à son tour, influe sur la distribution de la charge sur les traverses [58].

Les études sur le rôle de la semelle sur le comportement mécanique d'une voie ferrée sont principalement limitées à des études expérimentales [60]–[63]. Les études numériques dans le domaine de l'ingénierie des voies sont généralement consacrées à la modélisation de la structure entière de voie, et sont principalement réalisées en utilisant une représentation simplifiée de la semelle. On ne recense pas dans la littérature d'études numériques concernant la semelle.

L'objectif de ce chapitre est de proposer une stratégie complète de modélisation d'une semelle en élastomère soumise à un chargement de compression. Il sera montré l'importance de considérer la géométrie 3D entière de cette structure.

2. Étude du chargement en service de la semelle

Les conditions de chargement de la semelle ont été définies en utilisant des données expérimentales obtenues *in-situ* et en faisant une approximation analytique.

2.1. Mesures *in-situ* et approche expérimentale

Nous disposons de la valeur des efforts agissant sur le rail et de la valeur de l'enfoncement de la semelle lors du passage d'un train à grande vitesse. Ces mesures ont été réalisées *in-situ* par la SNCF entre 2005 et 2009 sur voie réelle (SNCF Département Études Voies - Section Mesures, 2005-2009). Les efforts sont mesurés par jauge d'extensométrie et l'enfoncement de semelle à l'aide d'un capteur de déplacement laser placé sur la traverse.

Le passage d'un wagon de TGV à une vitesse de 316 km/h, provoque une charge moyenne de 72.7 kN par roue (Figure 5a) et un enfoncement moyen de semelle de 0.2 mm (Figure 5b). Compte tenu du fait que l'épaisseur d'une semelle de 9-10 mm, il est possible d'estimer la vitesse de déformation macroscopique (λ) à 1-2 s⁻¹.

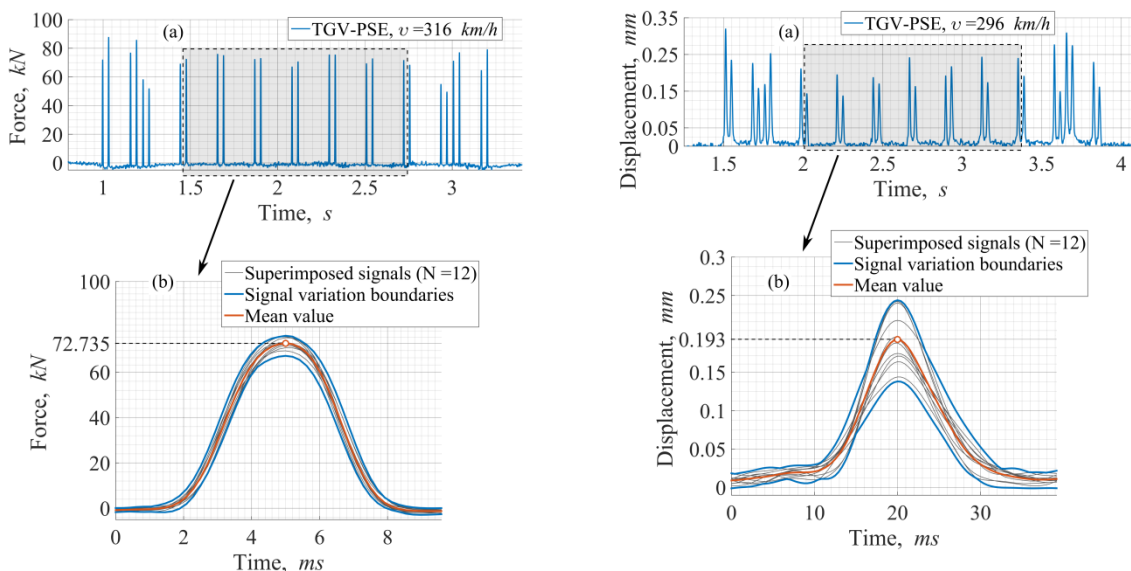


Figure 5: Passage d'un wagon de TGV-PSE : (a) charge de roue moyenne ; (b) enfoncement moyen de semelle

2.2. Détermination analytique du chargement de la semelle

Pour une étude numérique, le profil du chargement vu par la semelle est nécessaire. Il peut être déterminé analytiquement en faisant la somme de toutes les forces qui agissent sur la semelle à un instant donné. Ces forces peuvent être divisées en une partie statique et une partie dynamique. La partie statique combine le poids du rail et la force de serrage du système de fixation rail-traverse. La partie dynamique représente la charge générée par les roues en mouvement.

La charge statique peut être approximée en utilisant le principe fondamental de la statique. La détermination de la charge dynamique est plus complexe : elle comprend les forces inertielles provoquées par la masse des roues en mouvement (faciles à calculer) et les forces liées à la masse des voitures et aux imperfections de la zone de contact roue-rail (ondulations, soudures, défauts de planéité des roues, etc...) qui sont difficilement quantifiables. Différentes méthodes de calcul de cette composante dynamique sont proposées dans la littérature ([2], [109], [110]).

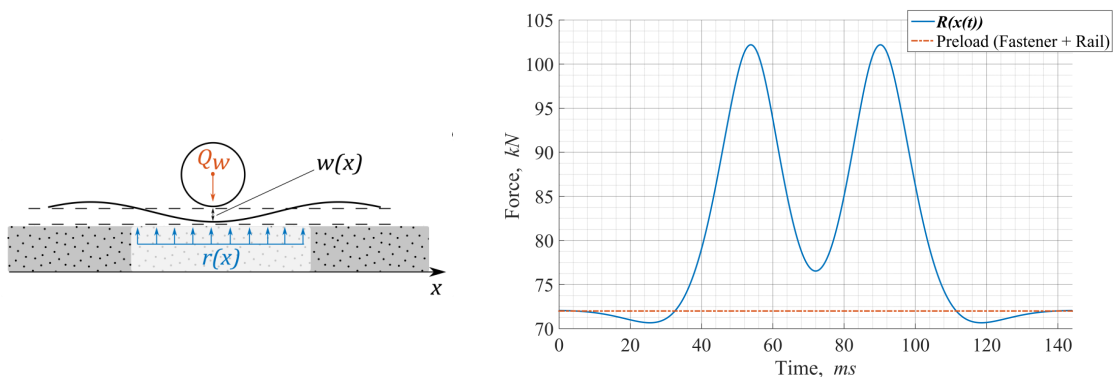


Figure 6: (a) Force de contre-réaction provoquée par la déflexion du rail ; (b) Profil Force-Temps final calculé pour la semelle

A partir des données mesurées *in-situ*, la charge statique sur la semelle peut être raisonnablement estimée à 15-20 kN. La charge dynamique est approximée à l'aide de la solution du problème de fondation de Winkler (théorie des poutres d'Euler-Bernoulli) qui donne la déflexion d'une poutre (rail) soumise à une charge en mouvement (roue) [80]. La déflexion du rail provoque une déformation de la fondation élastique et par conséquent, une force de contre-réaction qui agit sur ce rail (Figure 6a). La discrétisation de cette force en un certain nombre de charges concentrées (qui représentent les forces de réaction des traverses) permet de définir le profil de chargement sur la semelle. En utilisant la même stratégie, la charge générée par un bogie de TGV est obtenue. Le profil Force-Temps final pour la semelle est représenté Figure 6b. C'est ce profil qui sera utilisé pour la simulation Éléments Finis de la structure semelle soumise à un chargement dynamique.

3. Matériaux et méthodes

3.1. Matériaux et éprouvettes

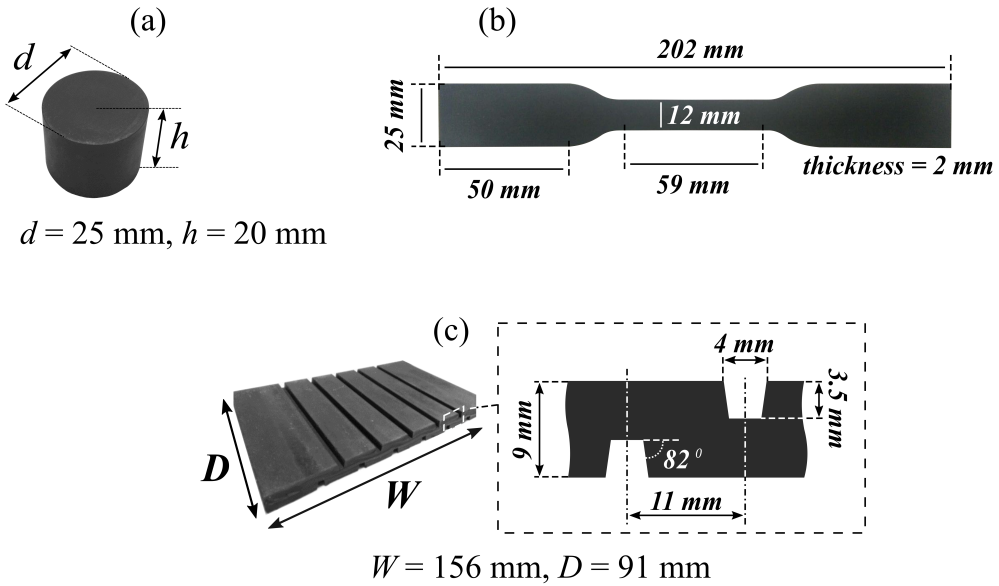


Figure 7: Dimensions des échantillons : (a) cylindrique; (b) haltère [112]; (c) demi-semelle de rail

Expérimentalement, on cherche à déterminer d'une part la loi de comportement du matériau constitutif de la semelle (caoutchouc styrène-butadiène chargé en noir de carbone de 27 phr (SBR)), et d'autre part le comportement de la structure semelle. Pour le premier point, des échantillons cylindriques (Figure 7a) et de géométrie haltère (Figure 7b) sont utilisés respectivement en compression et en traction. Pour le second point, une moitié de semelle rainurée (Figure 7c) est utilisée.

3.2. Machine et Instrumentation

Tous les essais sont effectués sur une machine de traction-compression conventionnelle Instron 5969 (Instron Ltd, High Wycombe, Royaume-Uni). Cette machine est équipée d'une cellule de force de 50 kN.

Les mesures des déformations (en traction) et du déplacement vertical relatif des plateaux de compression (pour les cylindres et les semelles en compression) sont réalisées en utilisant un extensomètre laser.

La fréquence d'acquisition des signaux de force, déplacement et déformation est de 10 Hz. Tous les essais sont faits à température ambiante (25°C).

De plus, l'incompressibilité du matériau a été vérifiée en utilisant une cellule de compression hydrostatique [81]. Le matériau SBR peut être considéré comme incompressible.

3.3. Traitement des données et procédure d'identification des paramètres des modèles

La procédure d'identification et d'optimisation des paramètres des modèles est effectuée par minimisation par la méthode des moindres carrés, en utilisant le logiciel MatLab®.

4. Modélisation du comportement du matériau élastomère

4.1. Essais de traction / compression à faible vitesse de déformation

Ces essais sont réalisés à une vitesse de déformation de $\dot{\lambda} = 0.01 \text{ s}^{-1}$. Deux cycles de chargement-déchargement sont effectués : le premier cycle à un niveau d'effort plus élevé que le second pour s'affranchir de l'effet Mullins [19]. Les données obtenues au cours du second cycle sont utilisées pour : 1) l'identification d'un modèle hyper-élastique approprié, 2) l'identification des paramètres du modèle-CI.

4.2. Choix d'un modèle hyper-élastique

Les paramètres de l'ensemble des modèles présentés au Chapitre 1 ont été déterminés et optimisés en utilisant la partie chargement des courbes de traction et de compression. Seuls les modèles de Yeoh, Arruda Boyce et Ogden peuvent représenter la courbe contrainte-déformation en forme de S, caractéristique du matériau ; et c'est le modèle de Yeoh qui donne une prédiction avec la plus faible erreur relative (coefficient de corrélation $R^2 = 0.995$ [83]). C'est donc le modèle hyper-élastique de Yeoh ($C_1 = 1.41 \text{ MPa}$, $C_2 = -0.8 \text{ MPa}$, $C_3 = 0.46 \text{ MPa}$ dans l'équation (8)) qui est choisi pour décrire la non-linéarité du matériau SBR étudié.

$$W_Y = \sum_{p=1}^3 C_p (I - 3)^p \quad (8)$$

4.3. Identification des Constantes du modèle visco-hyper-élastique (modèle-CI)

L'identification des constantes du modèle-CI est faite en utilisant simultanément les parties chargement et déchargement des courbes de traction et de compression. Le modèle-CI avec des séries de Prony de premier ordre donne une bonne représentation des données expérimentales et l'augmentation de l'ordre des séries ne fournit aucune amélioration significative. A noter que le modèle a une réponse légèrement imprécise en fin de déchargement (déformation supérieure à 0.2 pour une contrainte nulle). La précision du modèle-CI optimisé a été caractérisée par $R^2 = 0.99$ (compression) et $R^2 = 0.85$ (traction) (Figure 2.22).

Tableau 1 : Paramètres du modèle-CI identifiés par la méthode des moindres carrés

Paramètre	$C_1 \text{ [MPa]}$	$C_2 \text{ [MPa]}$	$C_3 \text{ [MPa]}$	$g_1 \text{ [MPa]}$	$\tau_1 \text{ [s]}$
Valeur	2.5264	-0.9177	0.4711	0.5688	2.635

5. Essais expérimentaux et numériques sur la structure semelle

Les résultats des essais expérimentaux seront comparés aux résultats des essais numériques pour valider (ou non) la capacité du modèle-CI à fournir une prédiction raisonnable du

comportement mécanique de la structure semelle, soumise à des chargements de compression.

5.1. Essais expérimentaux sur la semelle

Expérimentalement, la semelle est soumise à deux cycles de chargement-déchargement de niveaux 45 kN et 40 kN respectivement (le premier cycle a pour objectif de s'affranchir de l'effet Mullins). La vitesse de chargement est de 6 mm/min, ce qui correspond à un vitesse de déformation macroscopique de 0.01 s^{-1} .

Les résultats (Figure 9) montrent que la semelle a un comportement non-linéaire significatif et qu'elle dissipe une grande quantité d'énergie (boucle d'hystéresis).

Le champ de déplacement sur une face de l'échantillon est mesuré par corrélation d'images (DIC) ; ces données seront utilisées dans la procédure de validation du modèle éléments finis.

5.2. Modélisation Éléments Finis de la semelle

La simulation des essais est faite sous le logiciel ABAQUS®. En premier lieu, un modèle 3D de la semelle, qui représente sa géométrie exacte, est construit et utilisé pour vérifier la validité du modèle-CI. Un modèle géométrique 2D est également construit et les simulations sont faites en déformations planes et en contraintes planes pour juger de la capacité d'une modélisation simplifiée à reproduire le comportement de la semelle. L'influence des rainures sur le comportement mécanique de la semelle est également étudiée par une simulation sur un modèle 3D sans rainure.

Le maillage 3D est réalisé avec des éléments briques linéaires à 8-nœuds et une intégration réduite (C3D8RH). Pour le maillage 2D, des éléments carrés linéaires à 4-nœuds et une intégration réduite (CPE4RH et CPS4R) sont utilisés. Une attention particulière est apportée au raffinement du maillage près des rainures (Figure 8c). Dans ces zones, le matériau est fortement déformé ; on observe du contact entre les 3 bords des rainures ainsi qu'avec les plateaux de compression.

Les plateaux de compression sont considérés infiniment rigides. Pour simuler le chargement

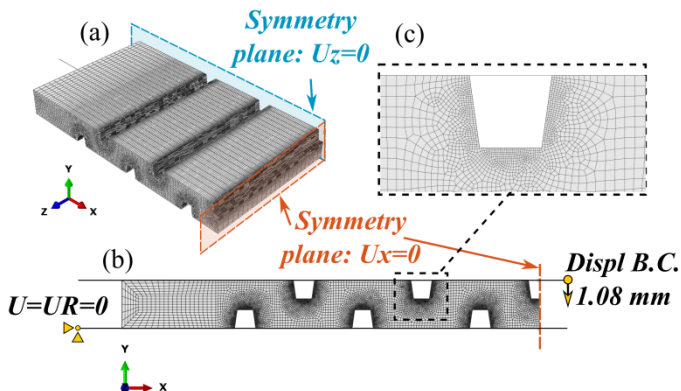


Figure 8: (a-b) Modèles géométriques 2D et 3D de la semelle; plans de symétrie ; (b) conditions aux limites appliquées ; (c) raffinement du maillage (rainures)

et le déchargement de la semelle, une condition limite en déplacement est appliquée sur le plateau supérieur (Figure 8b).

5.3. Résultats de simulation pour le modèle géométrique 3D

Plusieurs simulations sont faites avec des coefficients de frottement (entre l'échantillon et les plateaux de compression) compris entre 0.17 et 0.3. En comparant les résultats de simulation et les données expérimentales, on voit que les meilleurs résultats sont obtenus pour une valeur du coefficient égale à 0.225 (Figure 9).

Pour valider la valeur du coefficient de frottement, on utilise le fait que le champ de déplacement dans la structure ne dépend pas du modèle matériau mais uniquement du frottement entre l'échantillon et les plateaux de compression (et du chargement). Sur la face de l'échantillon, pour un coefficient de frottement de 0.225, les cartes de déplacement obtenues par simulation et mesurées expérimentalement par corrélation d'images (DIC) sont en bon accord qualitativement et quantitativement.

Des semelles avec une géométrie rainurée sont couramment utilisées sur les voies ferrées en raison de la rigidité réduite de ce type de structure. Cela permet d'utiliser des caoutchoucs plus rigides, plus résistants aux processus de vieillissement et de fatigue. Cependant, pendant une compression uniaxiale (par exemple dans la direction Y), les rainures alignées dans la direction Z permettent au matériau de se dilater librement dans les directions X et Y. Cela crée près des rainures des zones de haute concentration de contraintes et déformations.

La Figure 10 présente les cartes des déformations logarithmiques, calculées dans la direction Y (direction de chargement), pour quatre sections droites perpendiculaires à la direction Z. Le champ de déformation à l'intérieur de la semelle est très hétérogène dans la direction Z : les déformations sont presque uniformes sur la face de la semelle (section 1, Figure 10), ce qui n'est pas le cas, en particulier à proximité des rainures, au milieu de l'échantillon (section 4, Figure 10).

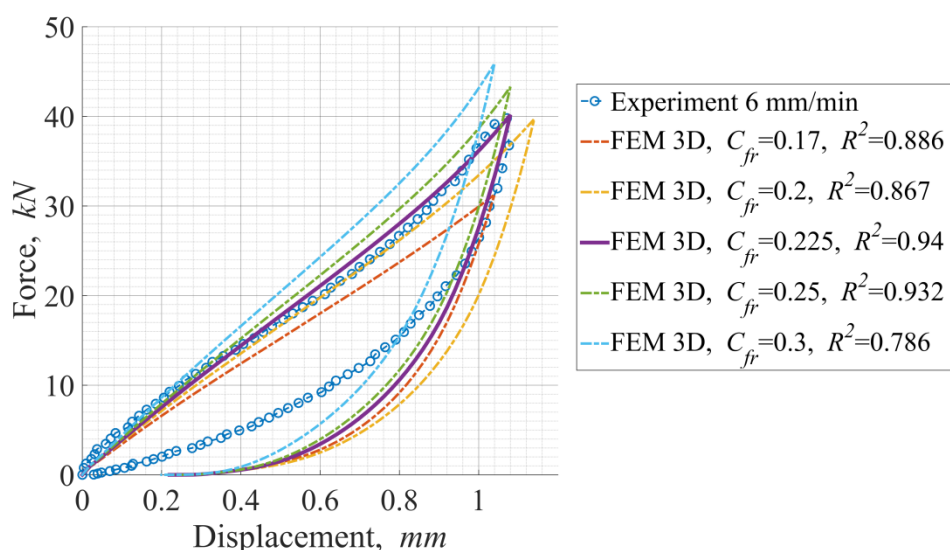


Figure 9: Courbes Force-Déplacement expérimentale et obtenues par simulation avec des coefficients de frottement compris entre 0.17 et 0.3

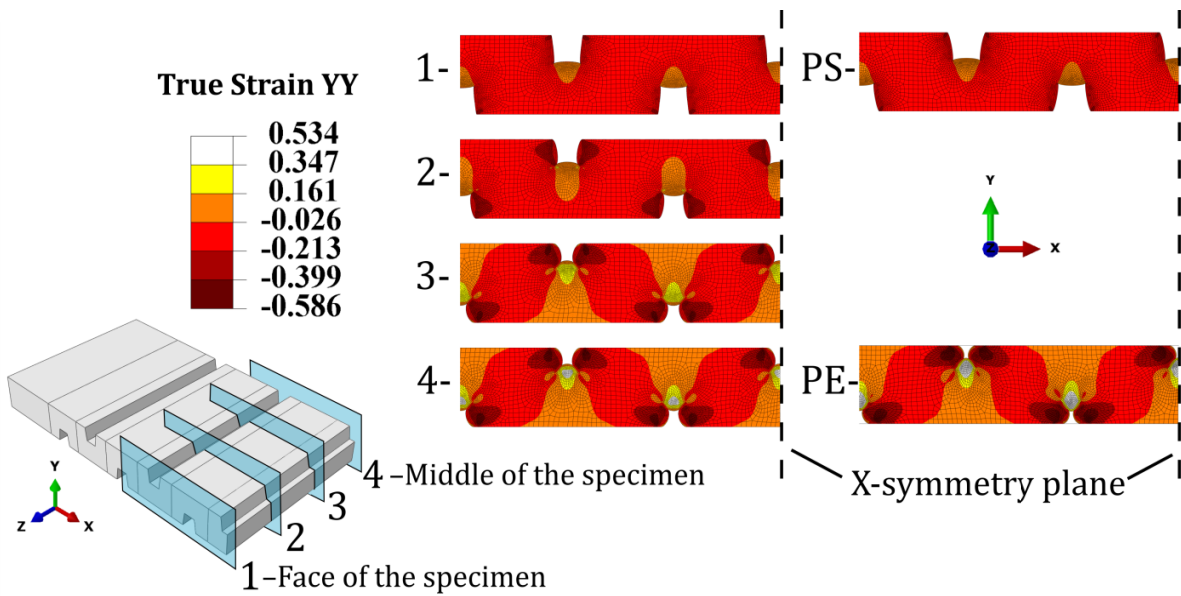


Figure 10: Déformations longitudinales (YY) pour différentes sections droites de normale Z (du bord libre au centre de la semelle) et champs de déformation obtenus en 2D (PE=déformations planes, PS= contraintes planes). L'écrasement de la semelle est de 1.08 mm.

Si on regarde la valeur des déformations longitudinales (déformations YY, Figure 10) et celle des distorsions (déformations XY, Figure 11) au milieu de l'échantillon, on constate que :

- les déformations longitudinales maximales sont du même ordre de grandeur que celles utilisées pour ajuster le modèle-CI (le modèle-CI a été ajusté avec des données expérimentales de déformation comprises entre - 0.55 et 0.31).
- pour les distorsions maximales (XY), leur valeur est presque deux fois supérieure à celle atteinte lors des essais de traction ou compression pour l'identification du modèle. Cela peut

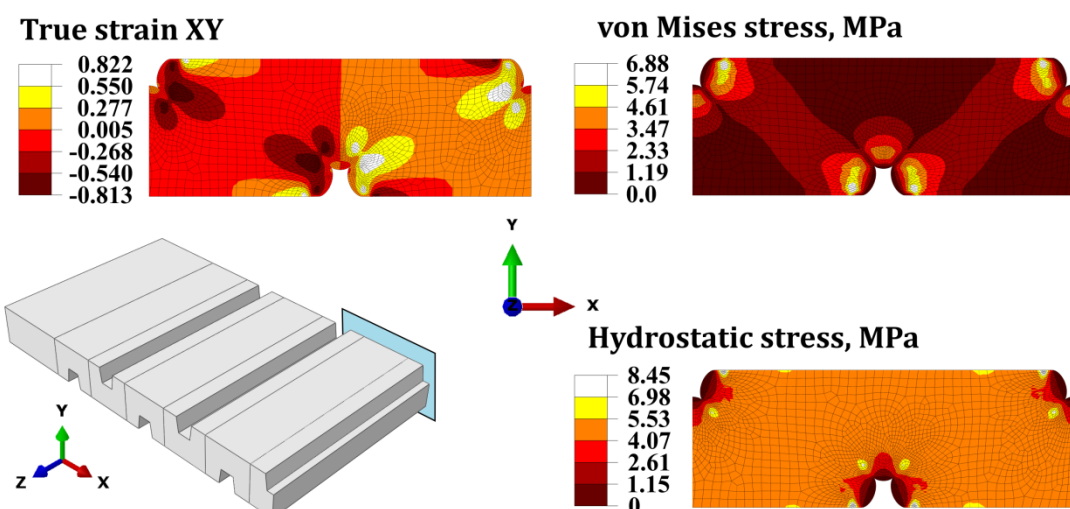


Figure 11: Champs de déformation vraie (transverses XY) et contraintes de Von Mises et hydrostatique calculés sur la section droite de la semelle. Déplacement : 1.08 mm

être une source d'erreur dans la représentation du comportement macroscopique de la semelle. La Figure 11 présente également les contraintes équivalentes au sens de Von Mises et les valeur de la pression hydrostatique au milieu de l'échantillon. Les zones où les contraintes de Von Mises sont le plus élevées révèlent les régions où la géométrie de la semelle pourrait être optimisée. Quant à la cartographie des pressions, elle montre qu'elles sont relativement uniformes et restent à des valeurs pour lesquelles l'incompressibilité du matériau est vérifiée.

La valeur de l'énergie dissipée au cours d'un cycle peut être définie comme la surface de la boucle chargement-déchargement du tracé Force-Déplacement. Les données expérimentales donnent une dissipation de 9.45 J alors que les résultats de simulation (modèle géométrique 3D) donnent 12.96 J. Cet écart de 37.5% vient du fait que le modèle ne reproduit pas correctement la phase de déchargement.

5.4. Résultats des simulations pour les modèles simplifiés (2D et 3D sans rainure)

L'approche 2D en déformation plane conduit à une réponse beaucoup plus raide qu'expérimentalement et à une valeur maximale de force deux fois plus élevée que celle mesurée (Figure 12a). À l'inverse, l'approche 2D en contrainte plane conduit à une réponse très douce de la structure et à une valeur maximale de force deux fois moins élevée que celle mesurée (Figure 12a).

Le modèle 3D sans rainures donne un comportement très rigide : la force maximale est trois fois supérieure à celle de l'expérience. Comme mentionné ci-dessus, la présence des rainures dans la structure semelle entraîne évidemment une réponse beaucoup plus douce.

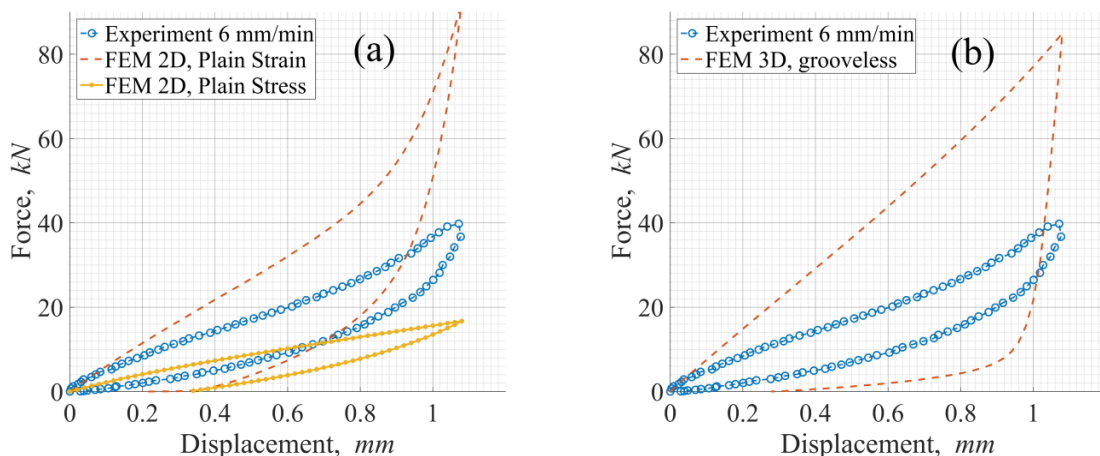


Figure 12: Comparaison entre les données expérimentales et la réponse du modèle FE de la semelle: (a) 2D en déformation plane et en contrainte plane; (b) 3D sans rainures FE

6. Simulation de la réponse de la semelle soumise à un chargement répété

Le modèle EF (Paragraphe 5) et le profil Force-Temps (Paragraphe 2) sont utilisés pour étudier le comportement de la semelle soumise à un chargement réel (passage d'un train). Ces résultats sont comparés aux mesures faites *in-situ*.

Un chargement statique de 17.3 kN est en premier lieu appliqué, il représente le poids du rail et l'effort de serrage rail-traverse. Le chargement dynamique Force-Temps est ensuite appliqué et la réponse Déplacement-Temps est récupérée de la simulation (Figure 13a). Sur cette figure, on voit que la symétrie du chargement d'entrée ne se retrouve pas en sortie et on observe un déplacement résiduel non négligeable (environ 20 % du déplacement maximum).

Sur la Figure 13b sont portés les résultats de la simulation et les résultats des mesures *in-situ* (l'échelle de temps est adimensionnée car les mesures d'effort et de déplacement *in-situ* ont été faites pour des vitesses de trains quelque peu différentes). Les différences majeures entre simulation et mesures apparaissent pour la pente et les valeurs du déplacement dans la première partie du "M". Ces différences peuvent être dues à l'approximation faite sur le chargement imposé en simulation à la semelle : en effet, ce chargement imposé est déduit analytiquement des mesures *in-situ* faites sur le rail, et il y a également une incertitude sur la valeur du paramètre k (module de voie) [78], [111]; il est donc difficile de savoir si l'approximation faite est acceptable. La pente moins raide conduit à une légère sous-estimation du déplacement maximum (repère 2, 10% inférieur à la mesure *in-situ*). La surestimation du déplacement résiduel (repère 3, à la fin de la première partie du "M") était plus attendue car on sait que le modèle CI ne reproduit pas parfaitement la fin de la décharge. Cette surestimation du déplacement se répercute sur le reste des résultats de simulation (repères 4 et 5). La seconde partie du "M" est donc correctement reproduite.

Globalement, on peut donc dire que la simulation EF donne une bonne prédiction du comportement de la structure semelle soumise à un chargement dynamique.

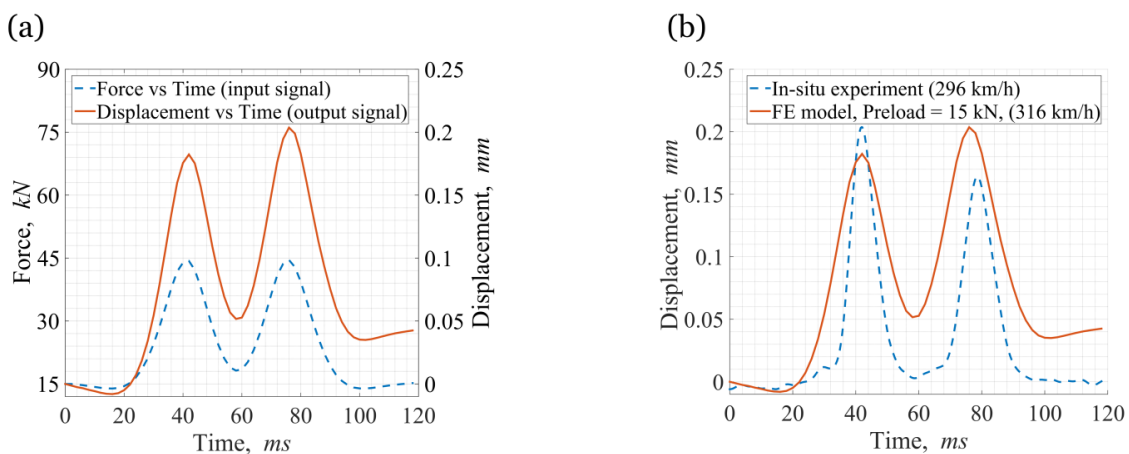


Figure 13: Chargement dynamique Force-Temps appliqué et réponse Déplacement-Temps récupérée de la simulation (a) ; comparaison des courbes Déplacement-Temps obtenues par simulation et par mesures *in-situ* (échelle de temps adimensionnée) (b).

7. Conclusion du Chapitre 2

Dans ce chapitre, une stratégie de modélisation pour prédire le comportement non-linéaire et la capacité d'absorption d'énergie d'une structure semelle a été présentée. Des approches simplifiées (2D, semelle sans rainure) ont également été testées et discutées.

Le modèle de comportement (modèle-CI) permet de représenter de façon très fiable la partie chargement de la semelle (erreur de 1 % pour la rigidité). Pour la partie déchargement, la représentation est un peu moins bonne : la déformation résiduelle "numérique" est de 2,2 % alors qu'expérimentalement elle n'est que de 0,4 %, ce qui conduit à une erreur de prédition sur l'énergie dissipée de 37,5 %.

Ce modèle-CI doit être utilisé sur le modèle géométrique 3D complet de la semelle, les approches simplifiées conduisent à des prédictions fortement erronées.

Les résultats de simulation peuvent être utilisés pour déterminer précisément les paramètres semelle (rigidité, facteur d'amortissement par exemple) à injecter dans des modèles plus complexes de simulation du comportement de voie ferrée dans son ensemble.

Cette stratégie de modélisation peut aussi servir à optimiser le choix du matériau constitutif et/ou la géométrie de la semelle.

La dernière partie du chapitre montre que le modèle utilisé permet de décrire assez correctement la réponse de la semelle au passage d'un train. Les écarts entre résultats de simulation et mesures *in-situ* peuvent provenir de nombreuses sources (imperfection du modèle à décrire la fin du déchargement, hypothèses sur le profil de l'effort, effort et déplacement mesurés sur des voies différentes et pour des vitesses de train différentes....) et sont finalement sûrement acceptables.

Chapitre 3: Influence de l'hétérogénéité du matériau sur ses propriétés mécanique. Concept de Matériau Virtuel

1. Introduction

Pour l'empilement complexe que représente une voie ferrée complète, le remplacement de la sous-couche de granulat par une sous-couche de grave bitumineuse (GB) améliore son comportement mécanique et entraîne une diminution significative des opérations de maintenance [4].

Le comportement mécanique macroscopique des matériaux hétérogènes (tels que la GB) dépend directement des caractéristiques de sa composition : matériaux constitutifs et

fraction volumique. Pour les applications d'ingénierie, les paramètres macroscopiques sont généralement étudiés par des approches expérimentales [92]. Des lois de comportement sont également proposées et caractérisées sur la base du comportement macroscopique du matériau [93]–[95]. Cependant, une étude approfondie des matériaux hétérogènes ne peut être effectuée en dehors d'une approche mésoscopique qui permet d'étudier précisément l'influence des paramètres de la structure interne sur le comportement macroscopique.

Les techniques expérimentales qui donnent accès à la structure interne du matériau sont très limitées (par exemple, la tomographie aux rayons X) et impliquent souvent des restrictions sur les conditions d'essais. Des approches numériques, par éléments finis (FEM) ou par éléments discrets (DEM), sont alors souvent utilisées. Ces méthodes, cependant, augmentent les sous-tâches qui doivent être résolues:

- Discrétisation du problème étudié : dimensions (2D ou 3D) ; géométrie, taille et fraction volumique des inclusions ; géométrie et taille d'un échantillon numérique.
- Taille du échantillon : le choix d'une taille de échantillon influe à la fois sur la complexité numérique du modèle et sur ses capacités de prédiction [96], [100]–[102].
- Remplissage numérique d'un volume donné par des agrégats (ou inclusions).
- Recherche de modèles matériau appropriés pour les agrégats et la matrice.

La plupart des travaux concernant la modélisation numérique des matériaux composites peuvent être répartis en deux groupes. Les travaux du premier groupe sont consacrés à l'étude d'un cube théorique utilisant des approches 2D [5], [6] ou 3D [6]–[10]. Ces travaux manquent généralement de connexion avec les cas réels et fournissent des résultats théoriques et qualitatifs à l'échelle mésoscopique.

Un certain nombre d'auteurs a choisi de travailler avec un cube numérique (2D et/ou 3D) défini à l'aide de tomographie ou de scan optique de la surface [11]–[15]. Dans ce cas, les travaux sont consacrés à l'étude d'un cas concret et sont difficilement généralisables.

Dans le cadre de ce travail, un nouveau concept de «Matériel virtuel» (VM) est proposé pour étudier l'influence de l'hétérogénéité d'un matériau à deux composants sur son comportement mécanique. Ce VM permet de faire le parallèle entre les échantillons numériques et réels.

2. Concept de Matériau Virtuel

Les idées principales du concept de VM sont les suivantes : 1) développement d'un matériau artificiellement hétérogène avec un niveau d'hétérogénéité contrôlé par des paramètres choisis a priori; 2) correspondance géométrique directe entre les échantillons numériques et réels afin d'exclure l'influence de l'emplacement et de la distribution des inclusions dans la matrice; 3) les modèles matériau pour l'échantillon numérique sont basés sur le comportement mécanique des matériaux constitutifs de l'échantillon réel.

Parmi tous les paramètres qui influent le comportement mécanique du VM, les éléments suivants peuvent être soulignés:

- Propriétés mécaniques de la matrice
- Propriétés mécaniques des inclusions

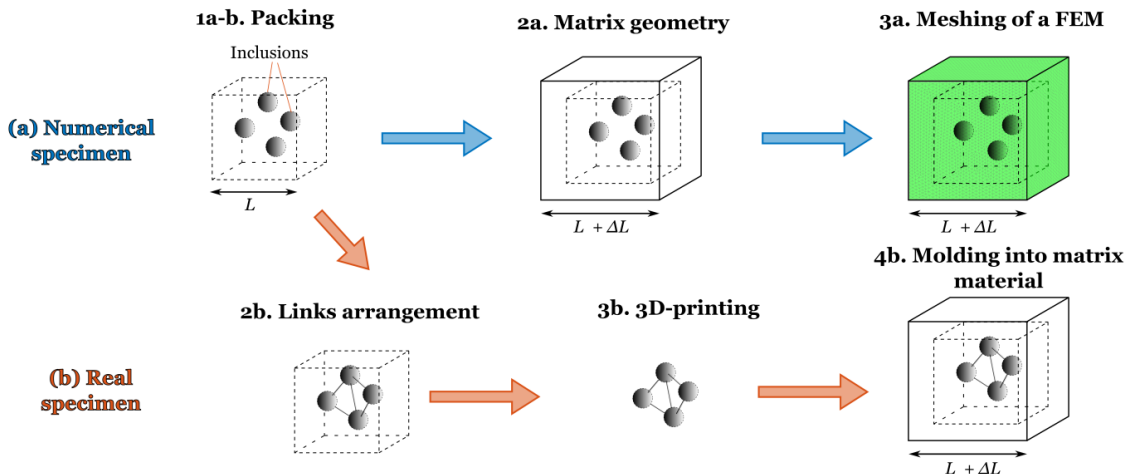


Figure 14: Représentation schématique du procédé de construction des échantillons numériques et réels.

- Distribution des tailles et formes d'inclusions
- fraction volumique totale des inclusions
- Distribution (emplacement) des inclusions dans la matrice

Dans le cadre de la présente étude, il a été choisi de réduire le problème très général mentionné ci-dessus. Ainsi, on a étudié l'influence de la taille et de la fraction volumique d'inclusions sphériques, dispersées aléatoirement dans une matrice, sur le comportement mécanique de la structure composite obtenue. Les inclusions sont infiniment rigides par rapport à la matrice. La matrice a un comportement hyperélastique.

2.1. Approche Générale

Le procédé de construction des échantillons de VM pour chaque couple (diamètre-fraction volumique) est schématiquement représenté Figure 14.

Pour l'échantillon numérique :

- (Étape 1a) Remplissage aléatoire d'un cube de taille L avec des inclusions sphériques, en préservant une distance minimale entre les particules,
- (Étape 2a) Construction de la géométrie de la matrice (cube de taille $L + \Delta L$) avec des vides pour les inclusions,
- (Étape 3a) Importation de la géométrie numérique obtenue vers un logiciel éléments finis et génération du maillage.

Pour l'échantillon réel : (Étape 1b on considère le cube de l'Étape 1a) :

- (Étape 2b) Création et arrangement de liens entre les inclusions (pour les maintenir dans leur emplacement d'origine),
- (Étape 3b) Impression 3D du squelette d'inclusions,
- (Étape 4b) Moulage du squelette d'inclusions dans la matrice.

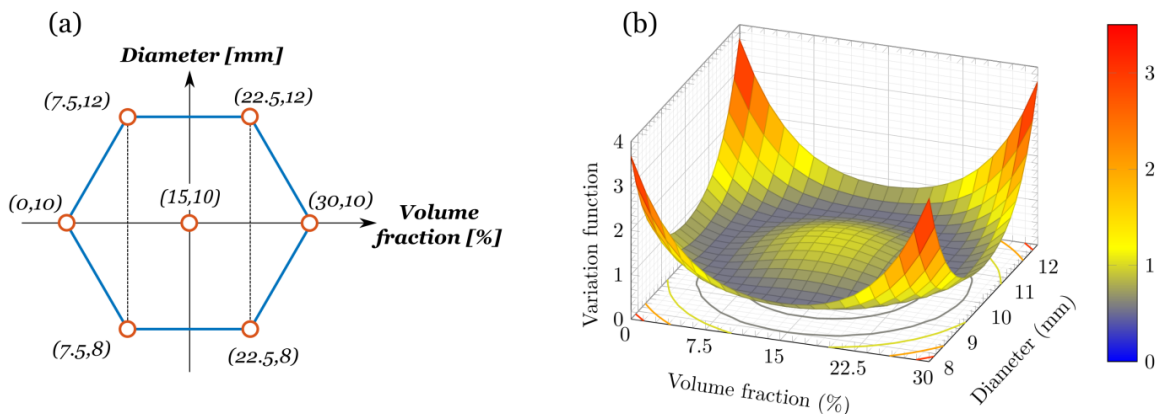


Figure 15: Caractéristiques des éprouvettes déduites du plan d'expériences de Doehlert (a) ; fonction variance (b)

2.2. Plan d'expériences de Doehlert et caractéristiques des échantillons VM

Les trois objectifs principaux de la méthode des plans d'expériences sont les suivants :

- l'identification des facteurs d'entrée qui ont l'influence la plus importante sur la réponse étudiée
- l'étude qualitative de la variation de la réponse par interpolation polynomiale des données expérimentales et construction d'une "surface de réponse"
- la minimisation des essais expérimentaux requis

Le plan d'expériences de Doehlert à deux facteurs d'entrée (Figure 15a) est choisi pour déterminer les caractéristiques des échantillons. Le plan d'expériences de Doehlert a les avantages suivants:

- distribution uniforme des points expérimentaux : la qualité de l'interpolation de la surface de réponse dépend de tous les points expérimentaux,
- possibilité d'étendre le domaine de validité par ajout de nouveaux points expérimentaux,
- possibilité d'augmenter le nombre de paramètres d'entrée,
- qualité de la prédiction sur tout le domaine de validité (Figure 15b)

Les couples (fraction volumique- diamètre) obtenus et notés (V_{fr} [%]; D [mm]) sont : (0; 10), (7.5; 8), (7.5; 12), (15; 10), (22.5; 8), (22.5; 12) et (30; 10).

Un plan de Doehlert à deux facteurs d'entrée utilise un modèle polynomial du deuxième degré pour prédire la valeur de la réponse :

$$y_{mod}(z) = b_0 + b_1 z_1 + b_2 z_2 + b_3 z_1 z_2 + b_4 z_1^2 + b_5 z_2^2 \quad (9)$$

Les paramètres du modèle (9) sont identifiés en utilisant les résultats de 7 expériences.

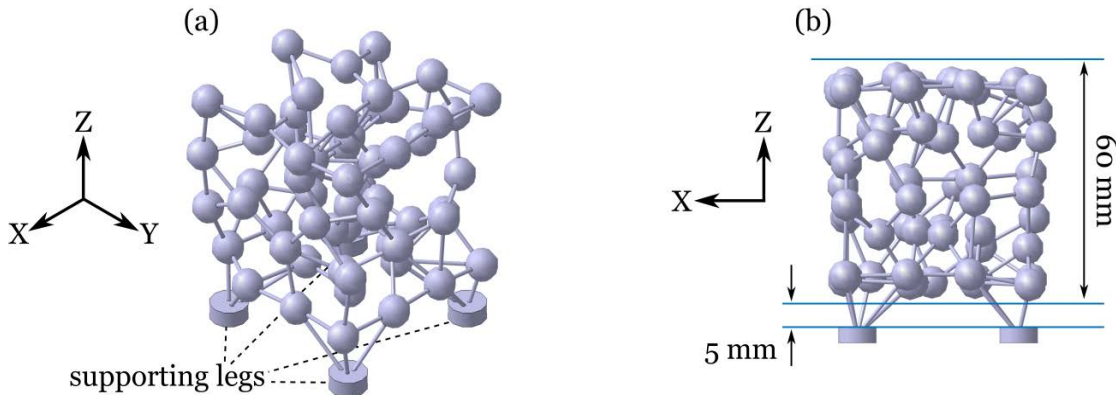


Figure 16: Squelette d'inclusions de l'échantillon V0075-Do8 renforcé de liens pour l'impression 3D : (a) vue isométrique, (b) vue du plan XZ

2.3. Développement numérique du squelette d'inclusions

Un cube de côté $L = 60$ mm est rempli d'inclusions sphériques de manière aléatoire en utilisant le logiciel open source GranOO [107]. Une distance minimale de 1 mm entre les inclusions est imposée. La fraction volumique ciblée et résultante ainsi que le nombre d'inclusions placées dans le cube sont présentés Tableau 2.

Des liens rigides sont créés et arrangés entre les inclusions en utilisant la méthode de triangulation 3D de Delaunay. Pour réduire l'influence de la présence des liens sur le comportement des échantillons, un algorithme qui minimise le nombre de liens a été développé sous Python.

Des liens de diamètre 1 mm conduisent à une rigidité suffisante de la structure, sans augmenter excessivement la fraction volumique. Un exemple de structure obtenue après toutes les manipulations décrites est présenté Figure 16a-b.

Tableau 2 : Paramètres du squelette d'inclusions ciblés et obtenus

	V00-D10	V0075-Do8	V0075-D12	V015-D10	V0225-D8	V0225-D12	V03-D10
Fraction volumique ciblée [%]	0.0	7.5	7.5	15	22.5	22.5	30
Fraction volumique résultante [%]	0.0	7.45	7.54	15.03	22.46	22.62	30.06
Nombre d'inclusions	0	60	18	62	181	54	124

2.4. Analyse numérique des structures d'inclusions

Une étude analytique des squelettes d'inclusions est effectuée pour caractériser l'homogénéité de la distribution des inclusions, estimer la fraction volumique de liens et l'influence de leurs orientations.

L'isotropie de la distribution des inclusions est analysée selon la procédure proposée par Segurado et Llorca [97]: 1) calcul des coordonnées du barycentre du squelette d'inclusions; et 2) calcul du moment d'inertie du squelette par rapport aux trois axes perpendiculaires dont l'origine est le centre du cube. Résultats : le barycentre est toujours proche du centre du cube. Pour chaque échantillon les 3 moments d'inertie ont des valeurs très proches de l'ordre de $I_m = \frac{1}{3}(I_X + I_Y + I_Z)$. L'écart-type ne dépasse pas 1% de I_m pour les échantillons avec $V_{fr} \geq 0.15$ et 6.5% de I_m pour les échantillons avec $V_{fr} = 0.075$. Enfin, si on considère un cube homogène de même masse et dimension que l'enveloppe du squelette, le moment d'inertie de ce cube est très proche de I_m ($\sim 7\%$ de la différence en moyenne).

La transmission inhomogène d'une charge axiale externe par les chaînes de charge (ou chemins de force) est bien connue pour les poudres/matériaux granulaires [108]. Un mécanisme similaire est supposé exister pour nos échantillons et pour le vérifier, une méthode basée sur l'analyse théorique des chemins de force potentiels est développée. Ainsi, la longueur et le nombre de ces chemins peuvent être estimés. Ceci permet de comparer la rigidité des différents échantillons dans chacune de leurs directions principales (qualitativement). Par exemple, on constate que, malgré l'isotropie générale, une petite différence entre les trois directions principales pour chaque échantillon existe. Cela peut entraîner une petite variation de la rigidité en fonction des directions, mais qui reste non significative à l'échelle de l'essai mécanique.

Enfin, la fraction volumique des liens est négligeable par rapport à la fraction volumique des inclusions pour tous les échantillons et aucune orientation privilégiée des liens n'est observée.

2.5. Fabrication des échantillons réels

La fabrication des échantillons réels sur la base de la géométrie numérique est effectuée en deux étapes: 1) fabrication additive 3D du squelette d'inclusions; 2) moulage du squelette dans une matrice hyperélastique pour former un cube.

La machine de fabrication additive est une imprimante Stratasys® uPrint SE Plus et la matière plastique utilisée est de l'ABS (Acrylonitrile butadiène styrène, de module d'Young $E \approx 2100$ MPa). La résolution d'impression est 0.25 mm. Pour assurer une certaine répétabilité, tous les échantillons sont imprimés dans la direction X. A noter que les échantillons obtenus par la technique d'impression 3D ont une surface non lisse, présentant des marches d'escaliers. Cela peut avoir un rôle sur leur réponse mécanique.

Les squelettes sont moulés dans un matériau élastomère (silicone Soloplast™, $E \approx 0.5$ MPa) en utilisant des boîtes de moulage de dimension intérieure 70x70x70 mm³. A noter que les bulles d'air sont retirées des moules par dégazage à l'aide d'une chambre à vide.

A noter également, il n'y a aucune adhérence entre le silicone séché et le plastique ABS des inclusions.

3. Comportement mécanique des échantillons de VM

L'isotropie, la rigidité et la capacité à dissiper l'énergie des échantillons VM sont étudiées expérimentalement et numériquement (éléments finis). Les résultats des deux approches sont comparés.

3.1. Comportement mécanique du matériau élastomère silicone

Pour déterminer le comportement mécanique du silicone, la même procédure que pour l'élastomère de la semelle sous-rail est suivie (Chapitre 2 : Paragraphe 3.2).

Le silicone peut être considéré comme incompressible. Son comportement peut être décrit comme hyper-élastique pur (aucune dissipation d'énergie ni dépendance à la vitesse de déformation).

L'Identification de la loi de comportement du silicone est effectuée par l'optimisation des paramètres d'un modèle hyper-élastique, qui est fait par deux méthodes. Premièrement, on utilise le processus d'ajustement standard (décrit au Chapitre 2) pour choisir le modèle approprié et déterminer ses constantes. Les données expérimentales utilisées sont celles obtenues en compression uniaxiale pour un échantillon cylindrique (Figure 17a). C'est le modèle hyper-élastique d'Arruda-Boyce qui offre les capacités de prédiction les plus satisfaisantes :

$$W_{AB} = C_1 \sum_{i=1}^5 \alpha_i \beta^{i-1} (I_B^{-i} - 3^i), \quad (11)$$

avec $\beta = \frac{1}{N}$; $\alpha = [\frac{1}{2}, \frac{1}{20}, \frac{11}{1050}, \frac{19}{7000}, \frac{519}{673750}]$

Deuxièmement, on fait une identification inverse (par la méthode des moindres carrés) à

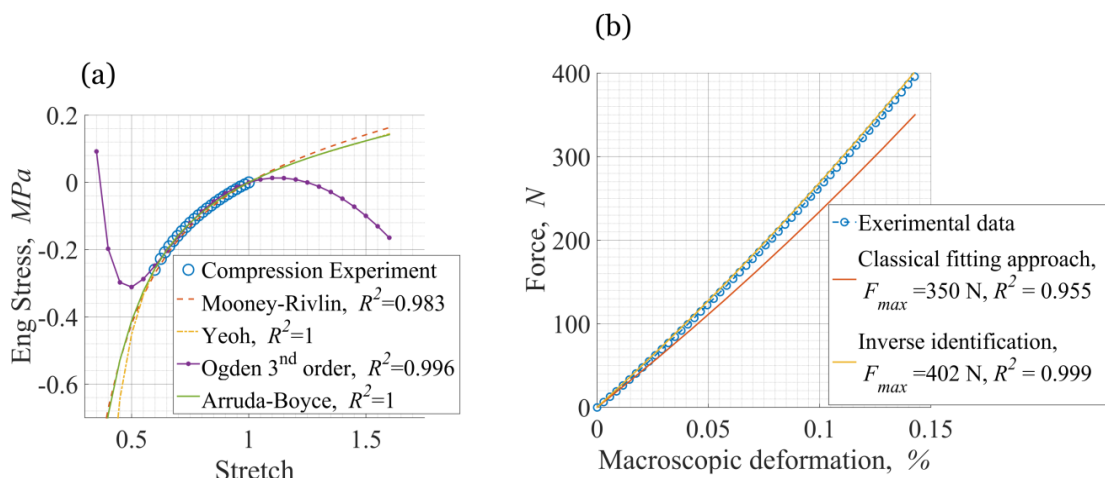


Figure 17: (a) Comparaison entre modèles hyper-élastiques et données expérimentales obtenues sur une éprouvette cylindrique en silicone testée en compression QS ; (b) le modèle d'Arruda-Boyce pour échantillon Voo-D10 simulé par éléments finis

partir des données obtenues sur l'échantillon VM en silicium pur.

Les 2 jeux de constantes du modèle d'Arruda-Boyce identifiés par les deux méthodes sont données Tableau 3. On conserve les paramètres obtenus par identification inverse par la simulation EF (Figure 17b).

3.2. Essais expérimentaux sur les échantillons VM

Tous les essais sont effectués sur une machine de traction-compression conventionnelle Instron 5969 (Instron Ltd, High Wycombe, Royaume-Uni). Cette machine est équipée d'une cellule de force de 50 kN. La fréquence d'acquisition des signaux de force, déplacement et déformation est de 10 Hz. Tous les essais sont faits à température ambiante (25 °C).

Afin de diminuer l'influence des liens sur le comportement mécanique, tous les échantillons sont préalablement soumis à un chargement cyclique d'amplitude de 15 mm, dans chacune des directions primaires (X, Y et Z).

Le programme de chargement est identique pour chaque échantillon VM et est présenté Figure 18a. Chaque échantillon est soumis à un chargement de compression à déplacement contrôlé à une vitesse de 8,4 mm/min soit $2 \cdot 10^{-3} \text{ s}^{-1}$. Le pré-cyclage élimine les effets permanents (liens brisés et/ou déplacés) et temporaires (effet Mullins). A titre d'exemple, l'effet du pré-cyclage est présenté par les courbes expérimentales Force-Déplacement obtenues pour l'échantillon Vo3-D10 (Figure 18b). Les données expérimentales exploitées

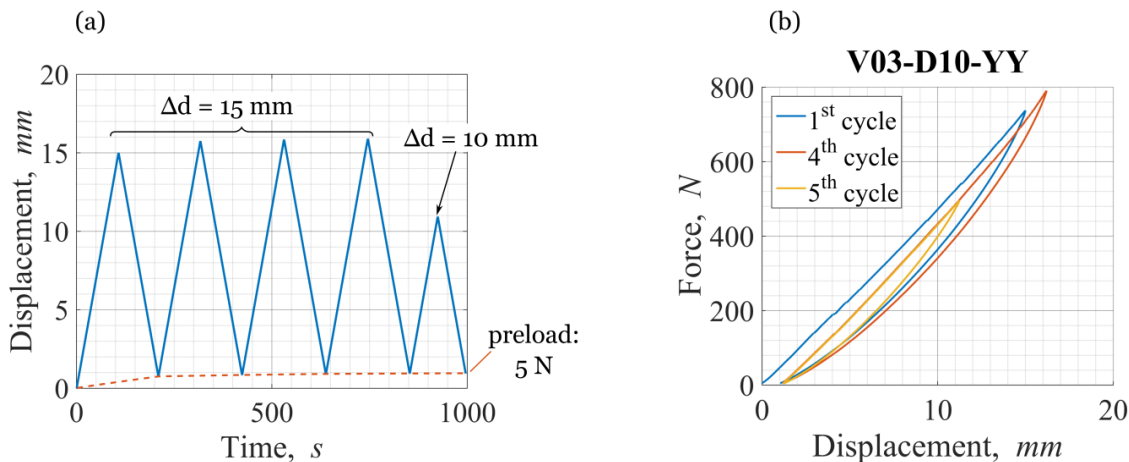


Figure 18: Programme de chargement d'un échantillon VM (a) et effet du pré-cyclage (b)

Tableau 3 : Les 2 jeux de constantes du modèle d'Arruda-Boyce identifiés par les deux méthodes

Optimisation des paramètres du modèle:	C1 [MPa]	N
a) à partir des données expérimentales en compression uniaxiale d'un échantillon cylindrique	0.115	6.2
b) par identification inverse	0.132	6.549

$$W_{AB} = C_1 \sum_{i=1}^5 \alpha_i \beta^{i-1} (I_B^i - 3^i) \quad \text{with} \quad \beta = \frac{1}{N}; \quad \alpha = \left[\frac{1}{2}, \frac{1}{20}, \frac{11}{1050}, \frac{19}{7000}, \frac{519}{673750} \right]$$

sont celles du 5ème cycle.

Le comportement mécanique macroscopique des échantillons est analysé en termes de force maximale F_{max} (valeur de la force pour le niveau maximal du déplacement de compression) et en terme de fraction d'énergie $E\%$ (énergie dissipée par rapport à l'énergie totale accumulée):

$$E\% = \frac{L'énergie dissipée}{L'énergie accumulée} \cdot 100 \% \quad (12)$$

Les valeurs de F_{max} et $E\%$ pour l'ensemble des échantillons et pour les différentes directions de chargement sont portées Tableau 4.

Tableau 4: Force maximale et fraction d'énergie dissipée obtenues expérimentalement pour l'ensemble des échantillons VM et pour les différentes directions de chargement

	F_{max} [N]			$E\%$ [%]		
	X	Y	Z	X	Y	Z
Voo-D10	398.2	399.6	371.9	$E\%^{fr} = 2.2$	$E\%^{fr} = 1.8$	$E\%^{fr} = 5.2$
Voo75-Do8	427.2	428.1	401.1	6.6	6.5	7.8
Voo75-D12	394.4	393.4	378.6	6.0	6.3	7.2
Vo15-D10	430.4	436.2	413.6	8.3	8.2	9.3
Vo225-D8	395.6	377.7	388.1	12.4	10.9	11.4
Vo225-D12	397.3	406.2	406.4	12.1	11.0	12.6
Vo3-D10	479.8	489.9	475.5	15.6	15.7	16.5

A partir de ce tableau, on constate que la direction Z est presque toujours caractérisée par une valeur plus faible de F_{max} et une valeur plus élevée de $E\%$, comparé aux directions X et Y. Cela s'explique par la différence dans les conditions de contact : le processus de moulage provoque la formation d'un ménisque concave sur la surface supérieure des échantillons qui modifie les conditions limites de contact échantillon-plateau de compression. La contribution de ce ménisque ne peut être estimée de façon fiable ; la comparaison entre les directions Z et X ou Z et Y n'est donc pas faite. Pour un échantillon donné, la comparaison entre les données obtenues dans les directions X et Y, ne fait pas apparaître d'anisotropie marquée.

L'analyse des données expérimentales montre que la dépendance de la rigidité du matériau (le paramètre F_{max}) à la fraction volumique (V_{fr}) et au diamètre (D) des inclusions n'est pas monotone. Ceci peut s'expliquer par deux faits : la nucléation de porosités près des inclusions (il n'y a pas adhésion entre inclusions et matrice) et/ou une faible disparité de comportement mécanique du silicium (différents lots utilisés).

Pour les propriétés dissipatives (paramètre $E\%$) au contraire, on constate une dépendance monotone à la valeur de V_{fr} et presque aucune dépendance à la valeur de D .

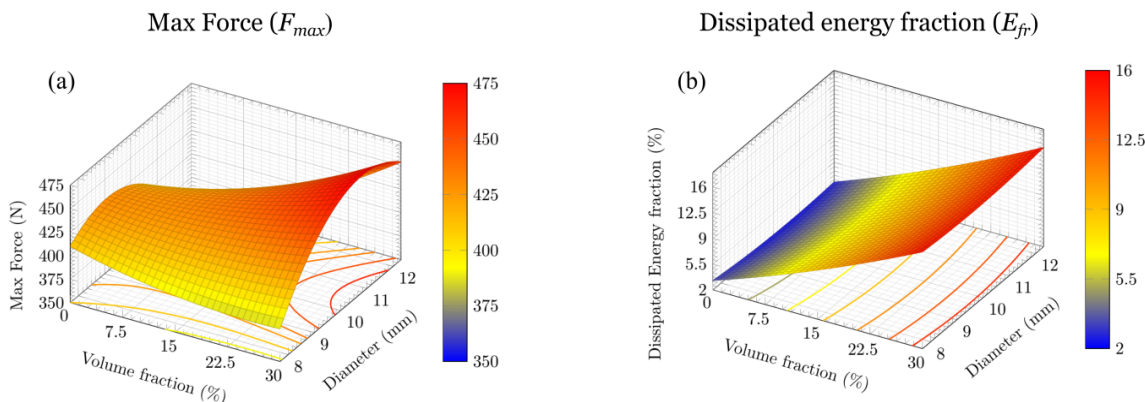


Figure 19: Surfaces de réponses expérimentales pour F_{max} (a) et E (b) en fonction de la fraction volumique et du diamètre des inclusions

Des conclusions similaires sont trouvées à partir de l'analyse des surfaces de réponse (Figure 19a-d) construites en utilisant les équations suivantes:

$$F_{max}(\hat{V}_{fr}, \hat{D}) = 436.18 + 23.82\hat{V}_{fr} - 1.79\hat{D} + 36.44\hat{V}_{fr}\hat{D} + 8.57\hat{V}_{fr}^2 - 49.3\hat{D}^2 \quad (13a)$$

$$E\%(\hat{V}_{fr}, D) = 8.18 + 6.15\hat{V}_{fr} - 0.035\hat{D} + 0.208\hat{V}_{fr}\hat{D} + 0.53\hat{V}_{fr}^2 + 0.483\hat{D}^2 \quad (13b)$$

où \hat{V}_{fr} et \hat{D} sont des variables centrées réduites de V_{fr} et D respectivement.

3.3. Simulation par éléments du comportement finis des échantillons VM

La simulation par la méthode des éléments finis du comportement des échantillons VM soumis à une charge de compression cyclique est effectuée. Les étapes suivantes sont décrites ici :

- Description du modèle éléments finis (maillage, conditions limites etc...)
- Étude de la réponse macroscopique des échantillons VM
- Étude de la structure interne et des concentrations de contraintes locales

Les inclusions sont modélisées par un matériau élastique de module d'Young de 2150 MPa et de coefficient de Poisson de 0.4 (conformément aux spécifications des matériaux ABS).

Le maillage des géométries des échantillons est réalisé en utilisant le logiciel commercial HyperMesh. Il permet de créer un maillage de bonne qualité avec un nombre optimal d'éléments (zones de raffinement du maillage et zones d'augmentation de la taille des éléments).

Pour la simulation du comportement en compression, les conditions limites en déplacement sont appliquées directement sur les surfaces supérieure et inférieure de l'échantillon (Figure 20). Cette approche permet de réduire le temps de calcul en éliminant la nécessité de résoudre le problème du contact échantillon-plateaux de compression.

Un échantillon VM est constitué d'une matrice hyper-élastique et d'inclusions élastiques (infiniment rigides par rapport à la matrice). La dissipation d'énergie pendant le chargement

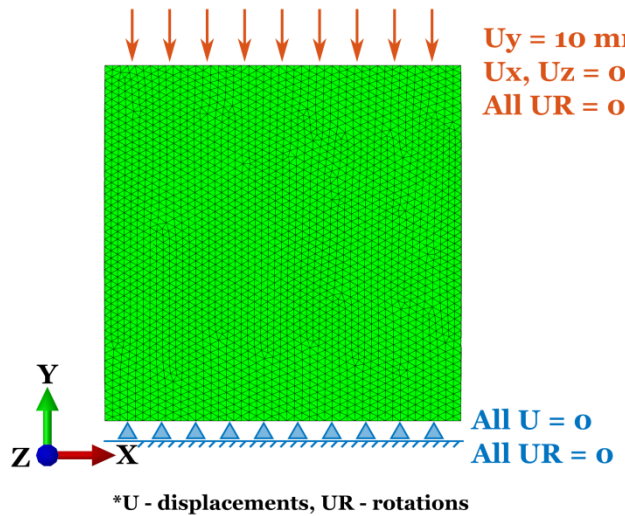


Figure 20: Conditions limites en déplacement appliquées sur les échantillons VM pour la simulation par EF

cyclique ne peut être causée que par le frottement entre les inclusions et la matrice. Une loi de contact par frottement est choisie pour décrire l'interaction mécanique matrice-inclusions.

L'influence de la valeur du coefficient de frottement sur le comportement mécanique est étudiée sur l'échantillon Vo15-D10 qui est suffisamment hétérogène et conduit à des temps de calcul acceptables. Les calculs sont faits pour des coefficients compris entre 0,1 et 0,9. Un coefficient faible diminue la rigidité de la réponse (alors plus proche de la réalité expérimentale) mais augmente drastiquement la complexité numérique. Un coefficient de 0,3 est un bon compromis entre précision des résultats et temps/complexité des calculs (Figure 21).

Pour des raisons d'optimisation des ressources et des temps de calcul, toutes les simulations ne sont pas faites. Les données macroscopiques (F_{max} et $E\%$) calculées sont portées Tableau 5.

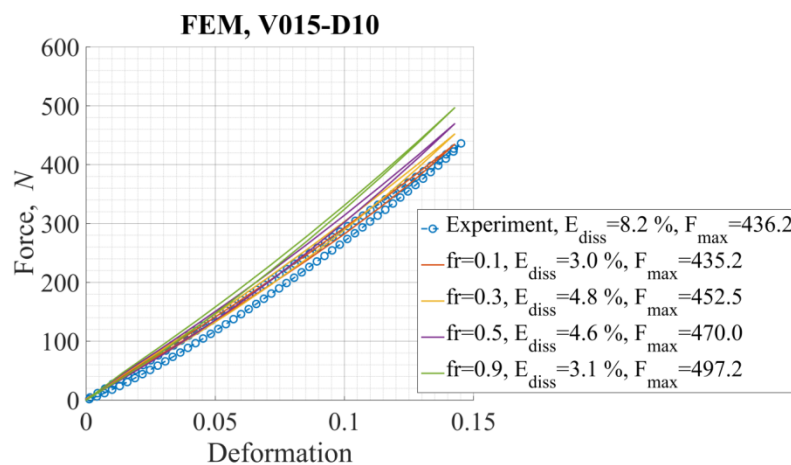


Figure 21: Influence du coefficient de frottement sur le comportement mécanique (échantillon Vo15-D10)

Table 5: Force maximale et fraction d'énergie dissipée obtenues par simulation EF

	F_{max} [N]			$E\%$ [%]		
	X	Y	Z	X	Y	Z
Voo-D10	---	399.6	---	---	0.0	---
Voo75-Do8	426.6	426.2	425.8	2.4	2.4	2.2
Voo75-D12	428.2	427.6	428.5	2.3	2.4	2.4
Vo15-D10	451.1	452.5	450.5	4.7	4.8	4.6
Vo225-D8	---	475.6	475.9	---	7.3	---
Vo225-D12	---	480.1	---	---	7.5	---
Vo3-D10	---	515.9	---	---	10.3	---

Les résultats de simulation pour les échantillons Voo75-Do8, Voo75-D12, Vo15-D10 obtenus pour les 3 directions de chargement (X, Y et Z) et ceux pour l'échantillon Vo225-D8 (directions Y et Z) permettent de conclure que le comportement du VM est isotrope, quel que soit le couple (V_{fr} , D).

Comme expérimentalement, les résultats de simulation montrent que les paramètres F_{max} et $E\%$ ont une dépendance monotone à la fraction volumique V_{fr} et une dépendance négligeable au diamètre D .

L'analyse des surfaces de réponse, construites avec les résultats de simulation FE pour les cas de chargement suivant la direction Y, conduit à la même conclusion (Figure 22a-d). Les équations de ces surfaces sont :

$$F_{max}(\hat{V}_{fr}, \hat{D}) = 452.49 + 54.96\hat{V}_{fr} + 1.71\hat{D} + 1.77\hat{V}_{fr}\hat{D} + 6.4\hat{V}_{fr}^2 - 2.32\hat{D}^2 \quad (14a)$$

$$E\%(\hat{V}_{fr}, \hat{D}) = 4.772 + 5.107\hat{V}_{fr} + 0.088\hat{D} + 0.092\hat{V}_{fr}\hat{D} + 0.398\hat{V}_{fr}^2 + 0.015\hat{D}^2 \quad (14b)$$

Enfin, la simulation numérique permet d'avoir une cartographie des états de contraintes et de

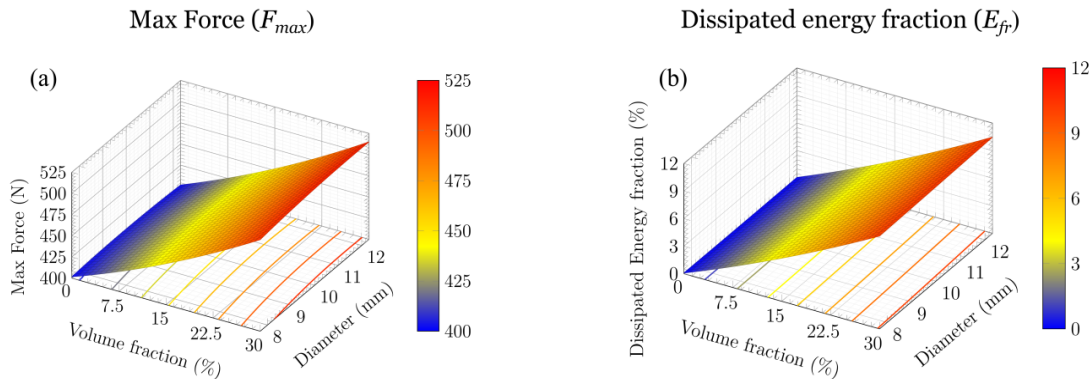


Figure 22: Surfaces de réponses construites à partir des résultats de simulation pour F_{max} (a) et $E\%$ (b) en fonction de la fraction volumique et du diamètre des inclusions

déformations à l'intérieur de la structure. Pour l'échantillon Vo225-Do8 et pour 2 sections droites perpendiculaires à X, la Figure 23a-c montre : les contraintes équivalentes au sens de Von-Mises, les déformations longitudinales dans la direction de chargement (YY) et les déformations de distorsions (XY).

Cette visualisation est faite pour un déplacement de 10 mm et les 2 sections sont choisies à partir de l'étude analytique de la géométrie de l'échantillon. Les concentrations de contraintes dans la matrice confinée entre les inclusions, permet de trouver et de visualiser les chemins de force. La cartographie des contraintes de Von-Mises est en accord avec le postulat qu'un nombre élevé d'inclusions dans une section mène à une augmentation du nombre et de la longueur des chemins de force. Sur ces chemins, la contrainte de Von-Mises est environ 8 fois supérieure à celle dans la matrice.

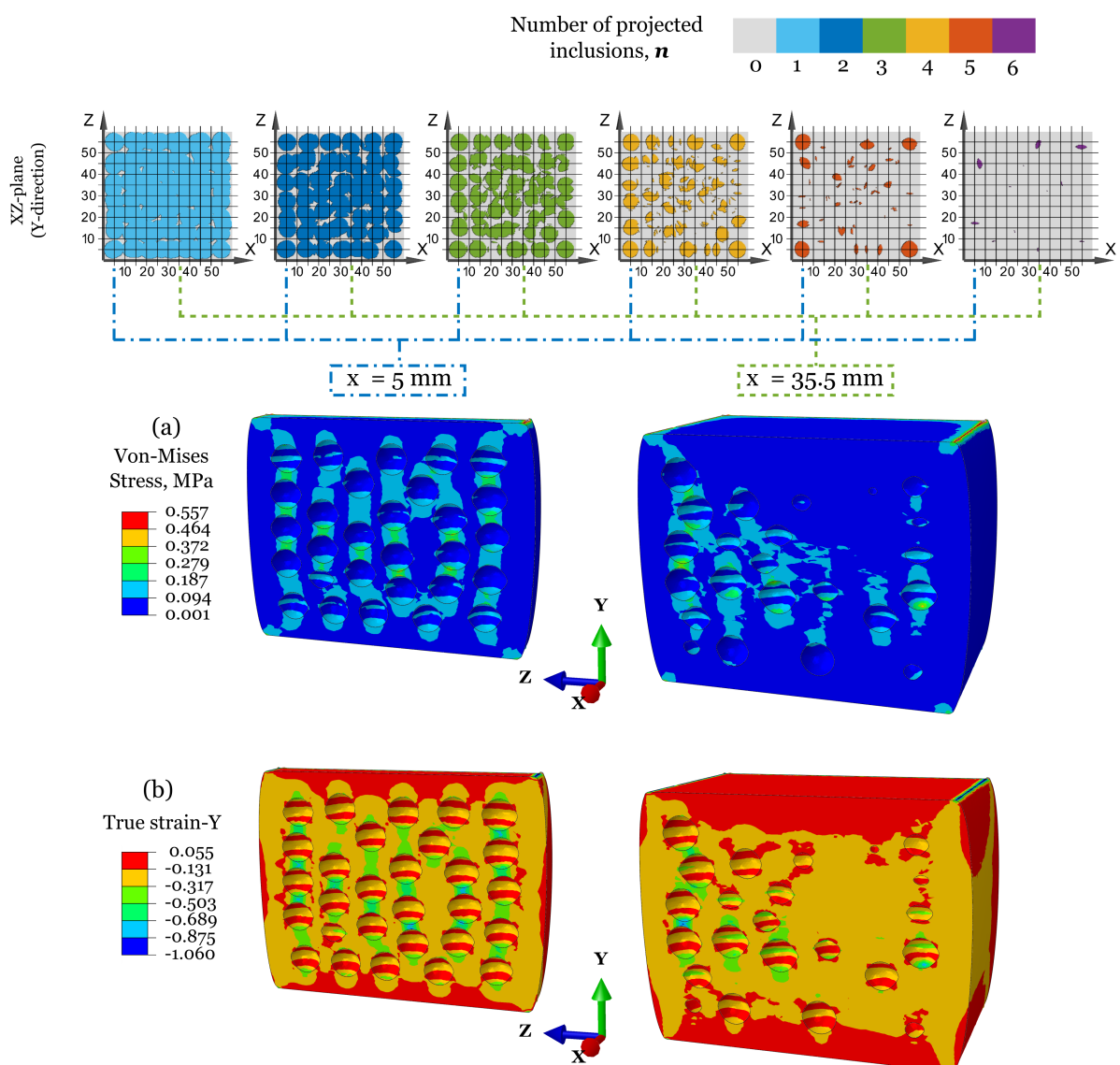


Figure 23: a-c: Échantillon Vo225Do8 sous 10 mm de compression : Contrainte de Von Mises (a) et déformation vraie YY (b) pour les sections à $x = 5 \text{ mm}$ et $x = 35,5 \text{ mm}$

3.4. Comparaison des résultats expérimentaux et numériques – discussion

Une comparaison quantitative de l'ensemble des résultats expérimentaux et des simulations numériques montre que pour F_{max} , la différence est inférieure à 5 %. Les valeurs de $E\%$ sont quant à elles toujours supérieures en expérimental et plus élevées en présence d'inclusions. Mais globalement, essais et simulations conduisent à la même dépendance de $E\%$ à la fraction volumique (et indépendance au diamètre).

4. Conclusion du Chapitre 3

Des cubes de "Matériaux Virtuels" ont été réalisés en disposant aléatoirement des inclusions sphériques rigides dans un volume de matrice au comportement hyper-élastique. L'influence du diamètre et de la fraction volumique de ces inclusions sur le comportement mécanique d'une structure a été étudiée numériquement et expérimentalement en utilisant un plan d'expérience de type Doehlert. Cette approche de « Matériaux Virtuels » a permis d'avoir une correspondance exacte entre les géométries des spécimens numériques et expérimentaux sur les 7 échantillons testés.

La répartition spatiale des inclusions et l'orientation des liens rigides entre inclusions ont été étudiées analytiquement : cette analyse a montré qu'il n'y avait pas d'orientation préférentielle des liens et que les moments d'inertie des échantillons réalisés étaient proches de ceux d'un cube homogène.

Une nouvelle méthode basée sur l'analyse théorique des chemins de force potentiels a été mise en place et a montré que la longueur et le nombre de ces chemins pouvaient être approximés, ce qui permet de comparer la rigidité des différents spécimens dans chacune de leurs directions principales (qualitativement).

Une comparaison quantitative des résultats numériques et expérimentaux du comportement macroscopique des échantillons a été effectuée. La différence entre les valeurs de F_{max} pour les spécimens Voo-D10, Voo75-Do8, Vo15-D10 et Vo3-D10 reste inférieure à 5%. Par ailleurs, l'évolution qualitative de $E\%$ observée numériquement et expérimentalement est similaire, même si les valeurs expérimentales restent supérieures aux valeurs numériques.

L'analyse des surfaces de réponses a montré que les deux paramètres observés F_{max} et $E\%$ sont fortement corrélés aux valeurs de V_{fr} . L'influence du diamètre des inclusions, par contre, est très faible.

Enfin, les simulations par éléments finis ont permis d'étudier la répartition interne des contraintes et déformations. Les résultats ont été présentés pour l'échantillon Vo225-Do8 : la chaîne d'effort a été visualisée à l'intérieur de la matrice et présente des contraintes de Von Mises jusqu'à 8 fois celles obtenues dans la matrice.

Dans l'étude proposée, le diamètre et la forme des inclusions ont été fixés. Il serait intéressant de faire varier ces paramètres en utilisant la même méthodologie. Par ailleurs, les récentes avancées en termes de fabrication additive permettent d'imaginer la construction d'échantillons hétérogènes complexes.

Conclusion générale. Perspectives.

Le transport ferroviaire est un domaine en constant développement avec un fort besoin en nouvelles technologies et nouvelles approches. Les progrès récents en modélisation et calcul permettent de comprendre et de reconsidérer certaines des pratiques déjà existantes visant à améliorer les performances d'une voie ferrée.

Dans la présente étude, on s'est intéressé aux semelles sous-rail et sous-couche de grave bitume (GB) d'une voie ferrée. Ces parties de l'empilement complexe que constitue une voie ont été choisies pour leurs similitudes de comportement mécanique (non linéarité et dissipation d'énergie) et similitudes de fonction (répartition du chargement et atténuation de sa partie dynamique).

Le premier chapitre est consacré à l'étude bibliographique des modèles proposés pour traduire les différents aspects du comportement mécanique de matériaux élastomères (hyper-visco-élasticité). L'approche par intégrale de convolution (modèle-CI) qui est une extension de la théorie de la viscoélasticité linéaire au domaine des grandes déformations, basée sur le principe de superposition de Boltzmann, a été retenue.

L'objectif du deuxième chapitre était d'étudier le comportement du matériau élastomère qui constitue la semelle et de proposer une modélisation éléments finis de cette structure, capable de prédire son comportement non linéaire et ses propriétés dissipatives. Les mesures d'écrasement de la semelle réalisées *in-situ* par la SNCF ayant montré que la vitesse de déformation ($\dot{\lambda}$) n'excède pas 1 à 2 s^{-1} d'une part, et le fait que le modèle CI prenne explicitement en compte la dépendance à la vitesse de déformation (par le terme $d\varepsilon(s)/ds$ dans sa formulation) d'autre part, nous ont conduit à ne considérer qu'un seul taux de déformation pour l'étude expérimentale du matériau et l'identification de tous les paramètres du modèle hyper-visco-élastique. La simulation du comportement de la structure semelle donne des résultats très encourageants. Les résultats de simulation et les résultats expérimentaux sont confondus (sauf en fin de chargement) pour un cycle de chargement-déchargement en compression. Pour le chargement réel (précharge statique plus chargement dynamique en forme de M), les résultats de simulation et les relevés de mesures *in-situ* sont un peu plus éloignés et expliqués par cette mauvaise représentation par le modèle de la fin de la phase de décharge. Cependant, la stratégie de modélisation proposée montre son potentiel pour fournir à un modèle plus complexe de voie des paramètres précis de la semelle (comme la rigidité ou le module de perte). Elle peut aussi être utilisée pour les optimiser, en jouant autant d'un point de vue matériau que géométrique, pour atteindre un bon compromis entre rigidité et énergie dissipée. Dans cette partie, nous avons également montré qu'un modèle géométrique simplifié de la semelle (2D en contraintes planes, 2D en déformations planes ou encore 3D sans présence de rainures) ne peut convenir.

Le troisième chapitre est une contribution à l'étude de l'influence d'hétérogénéités (comme celles présentes dans la grave bitumineuse) sur les propriétés mécaniques d'un matériau en utilisant le concept de matériau virtuel. Cette approche permet de conserver une parfaite adéquation entre échantillon réel et échantillon numérique. Dans le cadre de ce travail, nous nous sommes limités à l'étude de l'influence de la taille et de la fraction volumique d'inclusions sphériques placées aléatoirement dans une matrice hyper-élastique. Sept échantillons réels (squelette d'inclusions obtenu en impression 3D) et numériques ont été

créés. La fraction volumique et le diamètre des sphères ont été choisis à partir d'un plan d'expériences de Doehlert. Cela nous a permis de faire une étude qualitative de la réponse des échantillons en fonction de ces paramètres d'entrée. Les études expérimentales et numériques montrent que malgré le comportement purement hyper-élastique de la matrice et élastique rigide des inclusions, l'échantillon dissipe de l'énergie sous chargement-déchargement de compression. La raison de cette dissipation d'énergie est certainement due au frottement matrice-inclusions. Elles montrent aussi que la rigidité et la dissipation d'énergie sont fonction de la fraction volumique et ne dépendent pas de la taille des inclusions. De plus, la modélisation numérique permet d'accéder aux concentrations de contraintes locales dans la matrice et de mettre en évidence des chemins d'effort dans l'échantillon. Dans ces zones, la contrainte équivalente au sens de Von Mises peut être jusqu'à 8 fois supérieure à la valeur de la contrainte moyenne dans la matrice.

La méthode présentée peut bien évidemment s'appliquer à des modèles plus complexes (réels et numériques). Les progrès récents en fabrication additive permettent de créer des échantillons hétérogènes avec une grande précision. Par exemple, la possibilité d'utiliser simultanément plusieurs matériaux peut éviter la nécessité de mettre des liens entre les inclusions [16]. De plus, la variété des matériaux disponibles en impression 3D ouvre largement la variété de matériaux hétérogènes à étudier.

Contribution à l'étude du comportement mécanique de voies ferrées.

Composants à caractère dissipatif non-linéaire : semelle sous rail et sous-couche de grave bitumineuse.

RESUME :

Les voies ferrées sont endommagées par les chargements dynamiques répétés issus du passage des trains, en particulier des trains à grande vitesse. Structures multicouches complexes, ces voies sont constituées : de rails en acier, de semelles en élastomère, de traverses en béton, d'une couche de ballast et d'une sous-couche.

Ce travail de thèse se focalise sur l'étude des semelles et de la sous-couche en grave bitumineuse (GB), choisies pour leur comportement mécanique non linéaire et leur capacité de dissipation d'énergie similaires.

Une modélisation éléments-finis de la semelle à comportement visco-hyper-élastique est effectuée et les résultats numériques et expérimentaux sont comparés.

La GB est étudiée à l'aide d'un « matériau virtuel » constitué d'un squelette d'inclusions rigides issu de fabrication additive et d'une matrice hyper-élastique. L'influence des paramètres géométriques sur le comportement mécanique macroscopique est analysé, numériquement et expérimentalement.

Mots clés : Hyperélasticité, viscoélasticité, dissipation d'énergie, comportement quasi-statique, comportement dynamique, matériaux hétérogènes

Contribution to the study of the mechanical behaviour of railway track.

Components with non-linear and dissipative behaviour: rail pad and bituminous mixture sub-ballast.

ABSTRACT:

Repetitive dynamic loads caused by passing trains can damage a railway track, especially at high speeds. Investigation of the mechanical behaviour of the railway track structure (as the whole and by parts) can have a great importance for the improvement of safety and efficiency of railway transportation.

In the present study rail pad and bituminous mixture (BM) sub-ballast layers were considered for investigation, due to their similarities in the mechanical behaviour (nonlinearity and energy dissipation).

A finite element model of a rail pad structure was developed using visco-hyperelastic material model. Results of the simulation were compared with experimental study.

The BM was studied using a new “Virtual Material” approach: the skeleton of rigid inclusions (of predefined size and volume fraction), produced using additive manufacturing, is moulded into the hyperelastic matrix. Influence of geometrical parameters on the mechanical behaviour was studied experimentally and numerically.

Keywords: Hyperelasticity, viscoelasticity, energy dissipation, quasi-static behaviour, dynamic behaviour, heterogeneous media

